

Obsah:

21	<b>BIM CONTROL METHOD FOR HIDDEN QUALITY COST OF PREFABRICATED BUILDING CONSTRUCTION PROJECT</b> <i>Zhao Heng, Zhana Ningning</i>
22	<b>DETECTION METHOD OF TUNNEL SURROUNDING ROCK LEAKAGE CHANNEL BASED ON IMPROVED CHAOTIC PARTICLE SWARM OPTIMIZATION ALGORITHM</b> <i>Lei Zhu, Peixuan Qiao, Fuyu Jiang, Caihua Shen, Yuke Jiang</i>
23	<b>SEISMIC INVESTIGATION OF REINFORCED SOIL WALLS WITH GEOGRIDS</b> <i>Hongliang Yue, Xiaoyong Liang</i>
24	<b>APPLICATION OF L-SHAPED MAST CLIMBING WORK PLATFORM(MCWP) IN FAÇADE RENOVATION OF HIGH-RISE BUILDINGS: A CASE STUDY</b> <i>Yin Ni, Yuchao Zhang, Pengbo Li</i>
25	<b>EXPERIMENTAL STUDY ON QUALITY LOSS AND MICROSTRUCTURAL CHARACTERISTICS OF REINFORCED CONCRETE IN BRIDGE DECK PANELS AFTER SALT</b> <i>Xilong Zheng; Di Guan; Honglei Zhang</i>
26	<b>POLYURETHANE CEMENT REINFORCEMENT FOR SEISMIC TESTING OF CURVED BEAM BRIDGES PIERS</b> <i>Longyi Wang, Quansheng Sun, Haoyang Zhang, Yong Huang</i>
27	<b>PREVENTION AND DRAINAGE TECHNOLOGY FOR ANTI-STUCK AND DISCHARGING DURING SHIELD TUNNELING IN COMPLEX RED ROCK STRATA WITH ULTRA-LARGE DIAMETER UNDER NORMAL AND PRESSURIZED CONDITIONS</b> <i>Kexin Zhang, Xin Dong, Qingcheng Zeng, Jian Ouyang, Dawei Hu, Xingwei Xue</i>
28	<b>DYNAMIC PERFORMANCE ANALYSIS OF CABLE DAMAGE IN PRESTRESSED <math>\Pi</math>-SHAPED BEAM CABLE-STAYED BRIDGE</b> <i>Xilong Zheng, Honglei Zhang</i>
29	<b>FRACTURE ENERGY OF UNSTABILIZED RAMMED EARTH: INFLUENCE OF CLAY TYPE AND CONTENT IN THE MIXTURE</b> <i>Barbora Mužíková, Pavel Padevět, Tereza Plaček Otcovská</i>
30	<b>DUST DISTRIBUTION PATTERN AND OPTIMIZATION OF TUNNEL VENTILATION SYSTEM</b> <i>Xuhui Zhang, Hanwen Lai, Zeren Peng, Hengxing Zhong, Yashi Liao, Jingping Liao</i>

# BIM CONTROL METHOD FOR HIDDEN QUALITY COST OF PREFABRICATED BUILDING CONSTRUCTION PROJECT

*Zhana Ningning<sup>1</sup> and Zhao Heng<sup>2</sup>*

1. *Henan Technical College of Construction, Zhengzhou, Henan 450064, China; zhangning2024624@163.com*
2. *School of Civil Engineering, Neijiang Normal University, Neijiang, Sichuan, 641000, China*

## ABSTRACT

At present, the hidden quality cost in the construction process of prefabricated building projects in China is too high. If it is not controlled, there will inevitably be a "benefit funnel". Based on the construction of cost BIM control model, the information integration platform of prefabricated construction project is designed. Utilizing the details provided regarding the model and platform, the technique of constrained machine learning is employed for managing the concealed expenses related to quality in prefabricated construction ventures. By optimizing cost control, the ultimate objective of managing expenses is achieved. The outcomes of experiments illustrate that this approach has the capability to proficiently govern the covert quality expenses linked with prefabricated construction projects. It significantly enhances the focused and efficient management of comprehensive and evolving oversight of quality-related expenses throughout the construction process.

## KEYWORDS

Prefabricated building, Hidden quality cost, BIM Technology, cost control

## INTRODUCTION

In recent years, with the deepening of globalization and the sustained growth of economies in various countries, the construction industry has become an important pillar in promoting world economic prosperity. However, at the same time, engineering quality accidents are also on the rise globally, which not only poses a serious threat to people's life and property safety, but also brings a heavy burden to the economies of various countries. More seriously, some projects have clearly failed to meet the mandatory international quality standards, which reflects that negligence and inadequate quality control have become an urgent problem to be solved in the global construction process. Governments, construction industries, and relevant regulatory agencies around the world are actively seeking effective solutions to strengthen quality control and ensure the safety and reliability of construction projects [1]. In this scenario, if left unchecked, these costs are bound to create a "benefit funnel," which hampers the comprehensive oversight of project expenses.

Reference [2] is to effectively control the production cost of prefabricated components and thus reduce the total construction cost of prefabricated buildings. This method analyzes the production characteristics of prefabricated components, and establishes the production scheduling optimization model of prefabricated components aiming at minimizing the production cost. An improved differential evolution algorithm is designed to solve the model. Reference [3] design the cost control scheme of prefabricated building construction regarding BIM Technology. This method discusses the collection and collection mode of assembly construction cost under BIM platform, combines BIM with earned value method, analyzes the deviation of cost, and puts forward corrective measures. Reference [4] sorted out 13 representative influencing factors, constructed an

Interpretative Structural Modeling (ISM) based impact index system for prefabricated construction cost, analyzed the relationship between factors, and obtained the weight of each influencing factor by combining Analytic Hierarchy Process (AHP) and entropy method. The analysis shows that component price, integrity of industrial chain, prefabrication rate and assembly rate, project management experience and system have great influence on the cost of prefabricated buildings. Based on the research results, reasonable cost control measures and suggestions are put forward to provide reference for the development of prefabricated buildings. These studies mainly focus on the establishment of qualitative control measures, and the quantitative data analysis is obviously insufficient.

Prefabricated building (also known as prefabricated building) is a method of constructing buildings by prefabricating components in a factory and assembling them on the construction site. This construction method has many advantages, such as high construction efficiency, controllable quality, and minimal environmental impact. In order to achieve dynamic and holistic control of implicit quality costs in construction projects, this article proposes a method for controlling implicit quality costs in construction projects based on the characteristics of multiple influencing factors and high uncertainty, combined with BIM technology. The research includes establishing cost analysis models, project cost models, and BIM based information integration platforms, while using extreme learning machine methods to optimize and control implicit quality costs. The novelty of the research lies in the combination of BIM technology and cost management, which improves the accuracy and real-time performance of cost analysis. At the same time, a BIM based information integration platform is used to achieve collaborative work and data sharing between different units. In addition, using extreme learning machine methods to process complex nonlinear data helps optimize the cost control process, improve the effectiveness and accuracy of cost control. Through these innovative methods and technologies, this study aims to solve the problem of implicit quality cost in prefabricated building construction projects and improve the efficiency and quality of the projects.

## **BIM COST CONTROL MODEL**

### **Cost analysis**

Firstly, the cost analysis of prefabricated buildings [5, 6] is carried out based on BIM Technology. Implement virtual construction of buildings through BIM Technology. Building BIM model is built, and cost analysis of each stage is implemented in the cycle construction process of the model.

#### **(1) Theoretical basis**

BIM, as a technology covering the whole life cycle of buildings [7, 8], will also keep BIM modeling until the building is completed. Therefore, it is necessary to build the most appropriate BIM modeling according to the life cycle of the building, rather than building the BIM model in a hurry. The specific steps are as follows:

##### *Step 1: establish network and floor line*

When architects create architectural and construction drawings, the layout of networks and floors serves as a crucial foundation. Accurate placement and positioning of columns depend on reference grids, facilitating on-site construction teams in locating precise points on the foundation. The floor line is essential for indicating floor heights and delineating the placements of beams, columns, wall heights, and floor positions. Typically, architects design floors and beams situated below the floor line, while walls are positioned beneath the beams or floors.

##### *Step 2: import CAD documents*

Importing CAD files into BIM software [9, 10] can make it convenient to directly select the drawing surface or draw according to the drawing when building column beam slab wall in the next

step. When importing CAD, pay attention to whether the unit and grid line are consistent with the CAD drawing.

*Step 3: establish column beam slab*

Position columns, beams, plates, walls, and other elements within the model in accordance with the drawing's surface. Choose suitable shapes corresponding to the distinct characteristics of each component for accurate representation.

*Step 4: color display*

Color rendering is an important tool for visual communication. When the architect discusses the design with the owner, the three-dimensional model can be used to discuss the building shape, spatial image and whether the architect's design meets the owner's requirements.

*Step 5: output to CAD drawing and detail table*

In BIM modeling, it is not necessary to build all the contents in one step, but to continuously improve the accuracy of the model according to the steps. From conceptual design to a built design, Level of Detail (LOD) is defined as five levels, namely lod100 to lod500. LOD 100 – conceptual conceptualization. At this stage, referred to as the conceptual design phase, the model represents the building's overall form and structure. Typically, it portrays the building's volume and provides an analysis of various aspects such as volume itself, building orientation, and cost per square meter. At LOD 200, which entails an approximate geometric representation of components, the model reflects both schematic and expanded design elements. This level of detail is comparable to the conceptual and expanded design stages. The model at this stage contains the approximate quantity, size, shape, position, direction and other information included in the universal system. LOD 300 – precise geometry precise component (construction drawing and detailed construction drawing). This level corresponds to the traditional construction drawing stage and the further detailed construction drawing phase. The model at this point should encompass details like component properties and parameters outlined by the owner in the BIM submission standard. It has proven highly effective for tasks such as accurate cost estimation and facilitating construction coordination, which encompasses collision inspections, construction scheduling, and visual representation. LOD 400 – fabrication processing. The model at this stage can be used for the processing and installation of model units, such as the processing and manufacturing of project components by specialized contractors and manufacturers. LOD 500 – as built. The model at this stage represents the completion of the project. The model will contain the complete component parameters and properties specified in the owner's BIM submission instructions. The model will be integrated into the building operation and maintenance system as a central database.

Based on the above analysis, this paper analyzes the hidden cost of lod100 in BIM.

## **(2) Cost analysis results**

The concealed quality cost pertains to the potential loss arising from subpar quality in the delivered products or services. This type of cost isn't captured in financial records and is only assessable through estimation methods [11]. It represents an actual loss that does not find expression in financial accounting, and its worth remains uncompensated. It's an intangible and latent form of loss.

In the categorization of quality expenses, hidden quality costs emerge within the consumer phase of the product's lifecycle expenditure. These costs share the common trait of detaching from the internal value chain of the enterprise. If the enterprise allows certain quality defects out of the consideration of cost saving, the image of the product trademark will be damaged due to the flow of defective products into the market, which will further affect the future market share and reduce the sales income. This possibility not only exists, but will continue for a long time, and the loss amount is difficult to estimate. Some scholars call the loss caused by such quality problems exposed in the process of consumer use "hidden quality cost". On the surface, the hidden quality cost is the

manifestation of the external loss cost of the manufacturer, but in fact, it is caused by insufficient investment in prevention and identification, which is manifested as the sum of various quality costs that violate the "applicability". It may not only mean the costs borne by manufacturers, but some costs that consumers have to bear temporarily will eventually bring incalculable losses to enterprises. Although the hidden cost is not actually paid, it is virtually equivalent to increasing the product cost after it occurs. Therefore, attaching importance to and controlling the occurrence of hidden quality costs will fundamentally improve the economic benefits of enterprises. This aspect is more and more important in the modern industrial society with "user satisfaction" as the leading and restricting factor.

Hidden quality costs mainly include meeting costs, procurement costs [12], talent flow costs, and other costs. See Table 1 for details.

*Tab. 1 - Hidden quality cost*

Cost type	Influence factor
Meeting costs	Unscientific construction organization design
	Catch up with the construction period and neglect the quality problem
	Backward process method
	The quality inspection is not conducted carefully
	Defective design documents
	Blindly reduce costs and sacrifice quality
	Quality standards lag
Procurement costs	The quality of building materials is not up to standard
	Material and equipment factors: Equipment maintenance is not in place [13, 14]
	Material degradation
Talent flow costs	The owner is not responsible
	Dereliction of duty by supervisors
	Lack of training for labor personnel
	Low quality of construction management personnel
Other costs	Restriction of natural conditions
	Environmental factors (force majeure)
	Operation environment impact
	Market and policy impact

### Project cost model

In the cost management of construction projects, quality cost is an important part that cannot be ignored. It is divided into two levels: explicit quality cost and implicit quality cost. Explicit quality costs refer to costs that can be directly recorded in accounting accounts, such as repair costs and compensation costs incurred due to quality issues. These costs are relatively transparent and easy to calculate and calculate. However, the implicit quality cost is not the case, as it often drifts away from accounting accounts and is difficult to quantify directly, making it easy for people to overlook. Implicit quality costs include indirect costs such as reputation loss, customer loss, and project delays caused by quality issues. Although these costs are not directly reflected in the financial statements, their existence and impact are tangible. If not controlled, the implicit quality cost can easily form a

"benefit funnel", meaning that as the project progresses, quality problems accumulate, ultimately leading to a decline in overall project benefits. This not only hinders the comprehensive management of project costs, but may also have a serious impact on the long-term development of the enterprise. Therefore, in order to ensure real-time and dependable access to project information for Party A throughout the project construction journey, a hidden quality cost control framework for prefabricated construction projects is established, drawing on BIM [15–17]. This framework is designed to effectively manage the concealed quality costs associated with the project. The structure of this model is depicted in Figure 1.

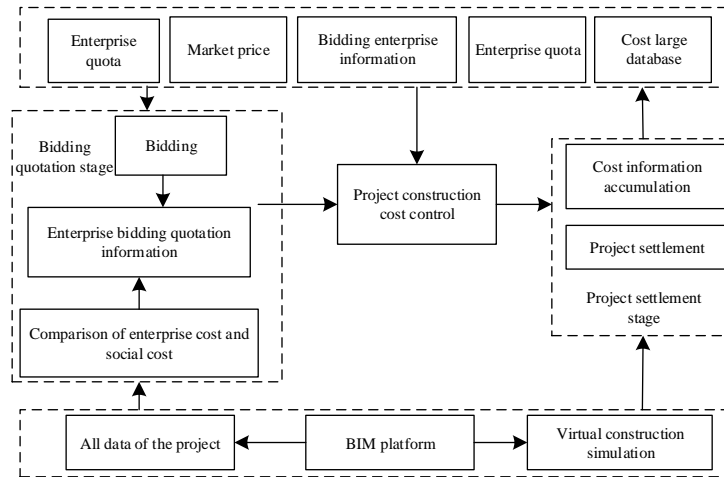


Fig. 1 – Hidden quality cost control model of prefabricated building construction project based on BIM

The model shown in Figure 1 is implemented in combination with BIM. In the model, the cost big data includes data information of multiple entities and levels. Party A integrates all information for the whole project from construction to completion. Cost big data has obvious hierarchical characteristics, and this kind of data is selective in the updating process, which can realize efficient information updating. Using BIM, Party A can carry out a virtual construction simulation of the project. This simulation encompasses the construction advancement and expenses for each construction phase of the project. It compiles the expense outcomes for each construction element, leading to more precise cost data compilation.

### BIM based prefabricated building construction project information integration platform

The core of BIM is information, and the efficient mutual use of information is the core value of BIM. The prefabricated building construction project is an industry involving many parties and a large number of associations, and the construction period is relatively long. Therefore, in the whole life cycle, it generates a huge amount of information. In order to make this information fully, quickly and reliably used and play its value, Party A takes the leading position to complete the information integration of the prefabricated building construction project [18–20], According to the integrated information, the construction conditions of the prefabricated building construction project are simulated to provide reliable data basis for cost control. The architecture of BIM based information integration platform for prefabricated construction projects is shown in Figure 2.

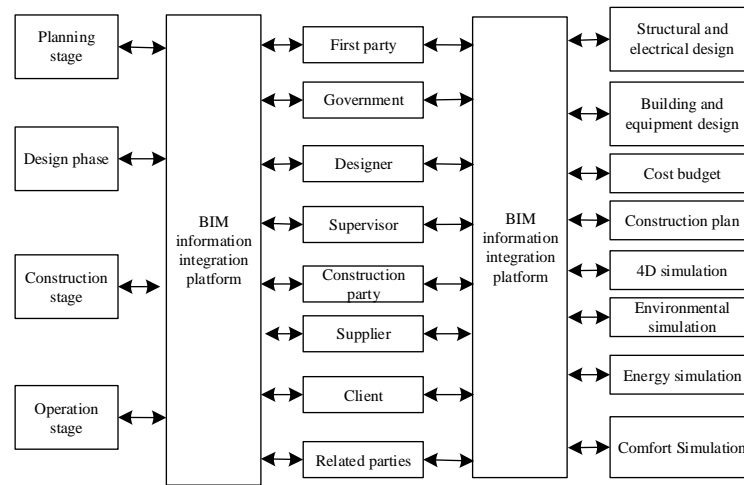


Fig. 2 – BIM based information integration platform architecture of prefabricated building construction project

BIM has a good integration function. The processing of various information of the project can be completed through information loading source and conversion standard. The former is in multi-interface state and the latter is a unified standard. It also supports the management and sharing of comprehensive and dynamic information of the project.

## PROJECT HIDDEN QUALITY COST CONTROL METHOD

In construction projects, there is usually an initial budget or bid, which is estimated based on factors such as project design, scale, material costs, labor costs, etc. However, in the actual execution process of the project, due to various reasons (such as design changes, market fluctuations, changes in construction conditions, etc.), the actual cost may deviate from the budget. Therefore, the goal of the engineering cost control method in this article is to make the actual cost as close to or within the budget as possible through reasonable management and strategic adjustments during the project execution process. On the basis of building the above cost control model, this paper uses the typical technology of big data analysis, namely Extreme Learning Machine (ELM) [21, 22], to complete the hidden quality cost control of prefabricated construction projects.

### Theoretical basis of limited learning machine

ELM represents a feedforward neural network characterized by a single hidden layer. It has significant advantages in operation efficiency and can ensure the reliability of cost control results. The implicit quality cost data of prefabricated building construction project is expressed by  $(x_i, t_i)$ , and its quantity is  $N$ , which is taken as the input of elm, where  $x_i = [x_{i1}, x_{i2}, \dots, x_{in}]^T \in R^n$  and  $t_i = [t_{i1}, t_{i2}, \dots, t_{im}]^T \in R^m$ .  $\bar{N}$  represents the number of nodes in the hidden layer,  $g(x)$  represents the activation function, then the elm control model is:

$$t_j = \sum_{i=1}^{\bar{N}} \beta_i g(w_i \cdot x_j + b_i) \quad (1)$$

Where:  $j = 1, 2, \dots, N$ ;  $\beta_i$  and  $w_i$  denotes the weight. The former belongs to the node between the hidden layer and the input layer, and the latter belongs to the node between the hidden layer and the output layer;  $b_i$  represents the offset value [23, 24], belonging to the node and located in the hidden layer.

During the learning and training of the model, in order to achieve the maximum approximation of the model to  $(x_i, t_i)$  with the number of  $N$ , it is necessary to ensure that formula (2) is established, which is:

$$\sum_{i=1}^{\bar{N}} \beta_i g(w_i \cdot x_j + b_i) = t_j \quad (2)$$

At this time, formula (2) is the output result of cost control. If  $x_1, x_2, \dots, x_N$  is the input, under its influence, the output of the  $i$ -th node in the hidden layer can be represented by the  $i$ -th column in the matrix. To complete the training of the model:

$$E = \sum_{j=1}^N \left( \sum_{i=1}^{\bar{N}} \beta_i g(w_i \cdot x_j + b_i) - t_j \right)^2 \quad (3)$$

When  $g(x)$  is infinitely differentiable,  $w_i$  and  $b_i$  can be randomly allocated. At this time, the formula (1) is trained, and the training result can be regarded as the solution of the least square solution of formula (3). The formula is:

$$\hat{\beta} = H^+ T \quad (4)$$

Where:  $H^+$  represents the generalized inverse matrix, belonging to  $H$ . Thereby completing BIM control.

### BIM based cost control

Take the control results output by the model as the basis for BIM based cost control. To ascertain the interrelation and comparative significance of diverse indicators concerning the concealed quality expenses in prefabricated construction projects, separate hidden quality cost models for these projects are established utilizing the rough set theory. In order to obtain the Rule Association between the sub cost and the total cost, the association between each indicator is arranged; Formulate cost control strategies according to the obtained rules association results, complete cost control through the transfer of cost models, and provide cost control results to Party A.

The cost dynamics is generated by the construction activities of the prefabricated building construction project. The dynamic model of the hidden quality cost control of the prefabricated building construction project is constructed in combination with BIM. The model formula is:

$$s = (U, A, V, f) \quad (5)$$

Where: the cost information expression system is represented by  $U$ ; Information sets and functions are represented by  $A$  and  $f$  respectively, and the former cannot be empty and finite; The total attribute is represented by  $V$ .  $(x_1, x_2, \dots, x_n)$  represents the universe; Each attribute is represented by  $a_m$ ; The attribute is represented by  $a_j$  and its value range is represented by  $V_{a_j}$ . If  $A \in C \in D$  is the condition that  $U$  needs to meet, and in  $f$ ,  $C$  and  $D$  represent attributes, the former corresponds to the condition, and the latter corresponds to the decision.

The growth of the total set shall be based on the premise of controlling the growth of the subset cost. The discernible matrix is represented by  $M = n \times n$ , which is used to describe the quantification of the cost deviation. If it is input into formula (5), the elements in  $M = n \times n$  are described by formula (6):

$$m_{ij} = \begin{cases} c \in C & c(x_i) \neq c(x_j), d(x_i) \neq d(x_j) \\ 0 & d(x_i) = d(x_j) \end{cases} \quad (6)$$

Where:  $x_i$  represents cost data, and its value on  $c$  is represented by  $c(x_i)$ ; The value of  $D$  after solution is expressed by  $d(x_i)$ . The higher the frequency of attributes in the matrix, the better the representation effect; The more attributes exist, the more important they are. Attribute is the core element of cost control. Formula (7) is used to measure the relative importance of cost indicators:

$$sig(c) = \sum_{i=1}^n \sum_{j=1}^n \frac{\lambda_{ij}}{|m_{ij}|} \quad (7)$$

Where: the relative importance of each indicator of cost is expressed by  $sig(c)$ ; The number of attributes is represented by  $|m_{ij}|$ ; The global effect of attributes is represented by  $\sum_{j=1}^n$ ; Quantitative attribute benefit is expressed by  $\lambda_{ij}$ . After the normalization is applied to the formula (7), the corresponding factor importance can be obtained. The formula is:

$$W = (w_1, w_2, \dots, w_n) \quad (8)$$

Where:  $w_1, w_2, \dots, w_n$  represents cost factor.

Simplify the cost attribute and remove redundant information. Rough sets contain upper and lower similar sets, respectively corresponding to the primary merge set of  $X$  and the intersection set of  $X$ , and all elements in the two sets belong to  $X$ .  $H$  denotes a non-empty set, which is given, and its equivalence relation is represented by  $R$ , and  $X \in U$ ; The similarity space is represented by  $K$ , and  $K = \{U, R\}$ , the association between elements is obtained according to formula (8), and in each index element belonging to the cost, the formula is:

$$R(X) = \{X \in U: [X]_R \subseteq X\} \quad (9)$$

$$(X) = \{X \in U: [X]_R \cap X \neq \emptyset\} \quad (10)$$

The above two formulas respectively represent the lower and upper similarity sets, which belong to  $R$  and are located in  $X$ ;  $[X]_R$  represents a set, which is composed of  $X$  and its equivalent relationship. Formula (11) ~ (13) for the edge domain, positive domain and negative domain respectively:

$$B_{nR}(X) = R^-(X) - R_-(X) \quad (11)$$

$$P_{POS_R}(X) = R_-(X) \quad (12)$$

$$N_{Neg_R}(X) = U - R_-(X) \quad (13)$$

Where: the former belongs to  $X$ , and the latter two belong to  $R$  and are located in  $X$ .

According to the association between each indicator of cost, the ranking is implemented. Based on the rough set theory, the cost control decision-making and probability rules are obtained, which are located in the order structure. The rules between costs are related, and the acquisition is simplified according to the attributes. The cost control is completed according to the Rule Association, as shown in formula (14):

$$P_{POS_{R-C}}(D) = \frac{\lambda_{ij} \sum_{i=1}^n P_{POS_R}(D)}{N_{Neg_R}(X)} \quad (14)$$

Where:  $P_{POS_{R-C}}$  represents the negative field and belongs to the total cost set.

## Optimization of hidden quality cost control of prefabricated building construction project

The statistical analysis model for the hidden quality expenses in prefabricated construction projects is formulated, and the characteristic attributes of the association rule pertaining to the hidden quality cost within these projects are derived as follows:

$$S_{i,j}(t) = p_{i,j}(t) - \lambda_{ij} p_{i,j}(t) \quad (15)$$

In the provided expressions,  $p_{i,j}(t)$  denotes the fuzzy evaluation feature of the hidden quality cost in the context of prefabricated building construction projects, while  $T_{i,j}(t)$  stands for the feature set encompassing the operations related to the hidden quality cost within these projects, presented as:

$$T_{i,j}(t) = \frac{|p_{i,j}(t) - \Delta p(t)|}{P_{POS_{R-C}}(D)} \quad (16)$$

In this context:  $\Delta p(t)$  represents the gain coefficient. The approach of multiple regression analysis is employed to actively uncover the hidden quality cost dynamics within prefabricated construction projects. The outcome is the acquisition of the quantitative characteristic distribution function for the hidden quality cost within these prefabricated construction ventures, illustrated as follows:

$$U_{i,j}(t) = \exp(-T_{i,j}(t) z_i(t)) \quad (17)$$

Where  $z_i(t)$  signifies the ambiguity function associated with the hidden quality cost of the prefabricated construction project [25].

Employing the big data information fusion technique facilitates the operational management and statistical oversight of the hidden quality cost within prefabricated construction projects. This leads to the establishment of the training function  $s_i = \{x_j : d(x_j, y_i) \leq d(x_j, y_i)\}$  for controlling the hidden quality cost of such projects. Under the influence of fuzzy information, the quantitative measure of the fuzzy degree in relation to the control of hidden quality cost within prefabricated construction projects is achieved.

$$\min z_i(t) = \min \{U_{i,j}(t), N_{Neg_R}(X)\} \quad (18)$$

Using the limit learning machine, the weight vector  $\mu_{ik}$  of the hidden quality cost control of the prefabricated construction project is obtained. Under the guidance of association rules, the optimization objective function of hidden quality cost control of prefabricated construction projects is obtained as follows:

$$J = \sum_{k=1}^n \sum_{i=1}^c \mu_{ik} \min z_i(t) \quad (19)$$

Solve formula (19) to complete the hidden quality cost control of the prefabricated building construction project:

$$V_i = \frac{x_k \sum_{k=1}^m \mu_{ik}}{J} \quad (20)$$

According to the above analysis, we can realize the hidden quality cost control of prefabricated construction project.

## TEST ANALYSIS

### Project overview

The prefabricated building in the experiment is a student apartment. The building structure of the apartment is a frame shear assembly structure. The project contracting mode is general contracting. The overall building area can reach 25000 square meters, and it is divided into two buildings. In the given context, Building A consists of seven above-ground floors and two below-ground floors, encompassing a combined area of 4200 square meters. On the other hand, Building B features eighteen above-ground floors and two below-ground floors, with a total area of 20800 square meters. The project is priced in the form of list, except for the following adjustments: adjustments allowed by the contract, various rewards and penalties, economic visas, design changes, changes in the manufacturer or brand of equipment and materials, risk adjustment in the price of commercial concrete and reinforcement, and provisional price adjustment of equipment and materials. No adjustment will be made due to rate changes, technical measures costs, machinery costs, material prices, labor costs and other reasons. In this paper, the prefabricated building construction project is selected as the case study object. According to the requirements of Party A, the cost control of the project is carried out through MATLAB software according to the cost control method proposed in this paper, and the overall application of this method is tested.

### Result analysis

In the experiment, the running time and relative error data of the method are obtained, and the control effect is reflected by these two parameters. The calculation formula of relative error is as follows:

$$\delta = \frac{y_i - \hat{y}_i}{y_i} \quad (21)$$

Where:  $\delta$  represents the relative error. The smaller the absolute value, the stronger the implicit quality cost control ability of the model. In the experiment, in order to enhance the contrast of the results and make the experimental data more abundant and detailed, the running time and relative error experimental data of the two methods are added as the comparative data in the experiment. These two methods are the implicit quality cost control method based on difference algorithm and ism. Firstly, the running time of the three experimental methods was tested.

For this method and the implicit quality cost control method based on difference algorithm and ism, the running time experimental data in cost control are shown in Table 2.

Tab. 2 - Operation time experimental data

Prefabricated building	Control iterations	Running time (s)		
		Methods in this paper	Method based on difference algorithm	Methods under ISM
Building A	5	1.42	1.84	2.13
	10	1.76	2.03	2.02
	15	1.74	1.92	2.07
	20	1.94	2.14	2.12
Building B	5	2.16	2.51	2.8
	10	2.15	2.58	2.84
	15	2.37	2.57	2.72
	20	1.97	2.88	3.1

The running time experimental data in Table 2 shows that, compared with the implicit quality cost control method based on the difference algorithm and ism, the design method takes less time to control the cost of building a or building B within the range of 5-20 control iterations, which proves that the designed implicit quality cost control method model has shorter running time than other methods.

The text method needs to control the project cost before controlling the cost. In this paper, elm is used to complete the cost control. During the control process, elm needs to determine the optimal number of hidden layer nodes, and take the time complexity of model training as the measurement standard to test the time complexity results of this method under different node numbers, as shown in Figure 3.

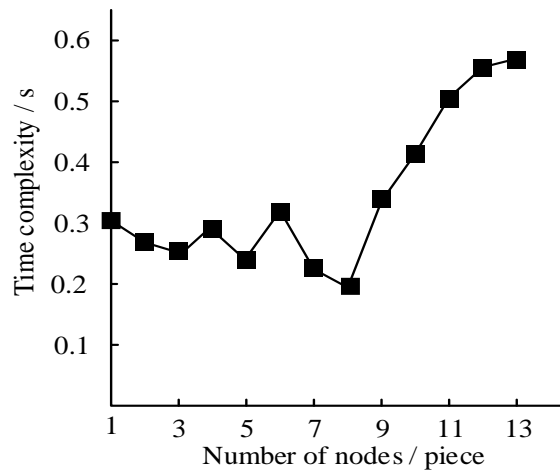


Fig. 3 – Test results of number and time complexity of hidden layer nodes

According to the test results in Figure 3, it can be seen that the model training time complexity fluctuates irregularly when the number of hidden layer nodes increases gradually, but the time complexity is the lowest when the number of nodes is 8. When the number of nodes exceeds 8, the time complexity increases significantly. This result is that the training time of the model will increase significantly due to the excessive number of nodes.

Then the relative error experimental results of the cost control results of the three experimental methods are obtained. The relative error between this method and the implicit quality cost control method based on difference algorithm and ISM is shown in Table 3.

Tab. 3 - Relative error test results

Prefabricated building	Control iterations	Relative error		
		Methods in this paper	Method based on difference algorithm	Methods under ISM
Building A	5	2.77	3.36	3.95
	10	2.65	3.65	3.01
	15	2.52	3.58	3.12
	20	3.45	3.9	3.52
Building B	5	2.45	3.52	3.05
	10	2.3	3.96	3.67
	15	2.85	3.48	3.41
	20	2.94	3.74	3.62

According to the relative error experimental results in Table 3, the relative error of the design method is smaller than the implicit quality cost control method based on the difference algorithm and ism, which proves that the design method has stronger implicit quality cost control ability.

The text method needs to control the project cost before controlling the cost. In this paper, elm is used to complete the cost control. During the control process, elm needs to determine the number of nodes in the best hidden layer, and take the root mean square error of model training as the measurement standard to test the root mean square error results of this method under different node numbers, as shown in Figure 4.

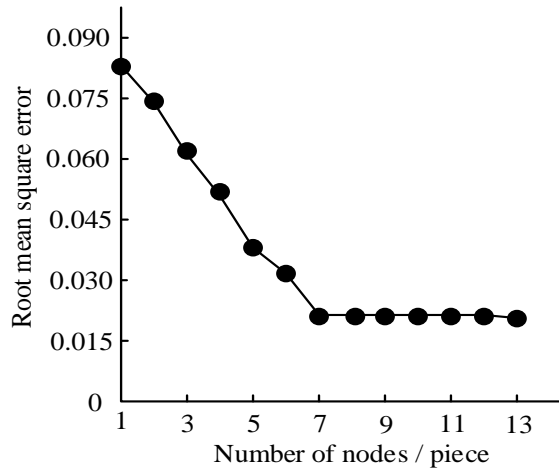


Fig. 4 – Root means square error test results of hidden layer nodes

According to the test results in Figure 4, with the gradual increase of the number of hidden layer nodes, the root mean square error shows a gradual downward trend. When the number of nodes is 7, the root mean square error is the smallest, which is 0.012. After the number of nodes exceeds 7, the root mean square error remains almost unchanged

Combined with the test results of time complexity (running time) and root mean square error (relative error), the number of hidden layer nodes is finally determined to be 8 and used in subsequent tests.

Test the change results of the model fitness function under different node numbers with the gradual increase of iteration times under the optimal number of hidden layer nodes to measure the convergence performance of this method. The results are shown in Figure 5.

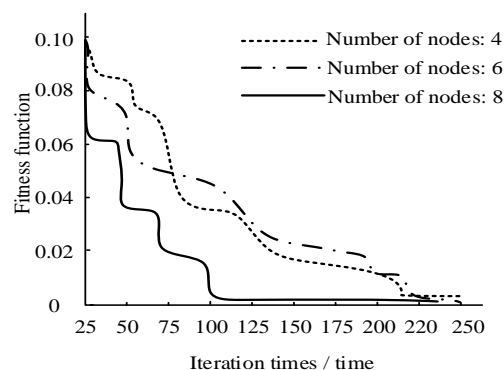


Fig. 5 – Convergence performance test results

As depicted in Figure 5, the test outcomes reveal that as the number of iterations increases gradually, the fitness function displays a consistent downward trajectory. Notably, when the node count is set at 4 and 6, the fitness function exhibits a gradual decline. Beyond 200 iterations, the fitness function reaches a state of stability without further fluctuations. Similarly, with 8 nodes and

100 iterations, the fitness function stabilizes. These findings underscore the method's commendable convergence capabilities, indirectly confirming the appropriateness of the 8-node configuration. In order to test the implicit quality cost control performance of the method in this paper, taking the seven project construction parts divided into the project as an example, the method in this paper is used to control each part and obtain the control results, as shown in Figure 6. Among them, the construction parts of 7 projects are represented by No. 1-7 construction respectively.

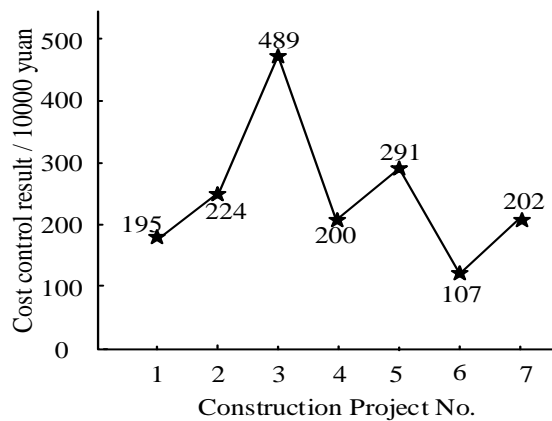


Fig. 6 – Cost control performance test results

According to the test results shown in Figure 6, this method can complete the hidden quality cost control of 7 project construction parts of the prefabricated building construction project, because BIM is used to control the cost of the project. BIM has information integration and virtual construction of the project, and can reliably grasp the progress of the project in different construction parts. Therefore, the construction cost of each part of the project can be controlled, good cost control performance of each project.

To evaluate the efficacy of this method in controlling hidden quality costs, a textual approach is employed to manage cost information post-control. This generates an overall assessment of cost control outcomes for the prefabricated building construction project. To ensure the impartiality of the control outcomes, the evaluation is conducted across three distinct scenarios.

The first scenario involves introducing 1dB noise to the cost information. The second scenario entails randomly selecting  $5 \times 10^4$  data entries. In the third scenario,  $20 \times 10^4$  erroneous data inputs are used. The resultant control outcomes for the overall cost of the prefabricated building construction project in these three conditions are contrasted against actual cost results. This comparison serves as a metric to gauge the effectiveness of the method's control capabilities. The outcomes of this analysis are presented in Figure 7.

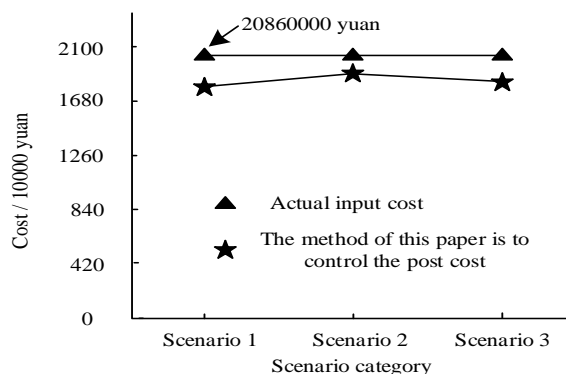


Fig.7 – Cost control results

According to the test results shown in Figure 7, under the three scenarios, the method in this paper can complete the cost control and control, and the cost after control is lower than the cost

used in the actual construction. The results show that the method in this paper can more reasonably complete the total cost control of the prefabricated building construction project and realize the cost control under different scenarios. The reason is that BIM has the information integration function and can complete the integration and analysis of comprehensive information, and the method in this paper has a large cost database, which can provide reliable reference data for cost control. Therefore, even if there is a certain degree of missing or error in data information. The cost control can still be completed, and the control result is still better than the actual cost result, which can ensure that the cost of all links of the prefabricated building construction project is the most reasonable state and better than the actual input cost.

## CONCLUSION

As the prefabricated building construction project mode is completed jointly by many parties, it is difficult for Party A to control the cost, and it is impossible to achieve information management and control. This paper analyzes the characteristics of a prefabricated building construction project, and puts forward the BIM control method of hidden quality cost of prefabricated building construction project to help party and complete the cost control of the project. This approach integrates BIM technology to effectively manage the cost aspects of prefabricated building construction projects. The conducted testing demonstrates that the method presented in this paper is capable of controlling costs within such projects. Additionally, it achieves the control of hidden quality costs across each construction facet within the entirety of the project. The application of BIM facilitates the consolidation of all pertinent project information, establishing a dependable foundation for Party A's cost control efforts and ensuring cost optimization.

## FUNDING

This work supported by Project "Research on the Inheritance and Popularization of Patriotic Spirit in Qi Jiguang's Poems and Essays" (2021-SKZZ-01); Stage achievements of Shandong Province Ideological and Political Education project "Innovation Research and Practice of Patriotism Education Mechanism for College Students from the Perspective of Qi Jiguang's Patriotism Spirit" (SSD-2021-046); The achievements of the stage of "Research on the Cultivation Path of Patriotism Spirit of Private College Students under the New Situation" (22SAQ096).

## REFERENCES

- [1] Dimitrantzou C, Psomas E, Vouzas F 2020 Future research avenues of cost of quality: a systematic literature review. *The TQM Journal* <https://doi.org/10.1108/TQM-09-2019-0224>
- [2] Chang C, Wang M, Wang S 2022 Production Scheduling Optimization of Prefabricated Components Based on Improved Artificial Fish Swarm Algorithm. In: *Proceedings of the 6th International Conference on Computer Science and Application Engineering*. pp 1–5 <https://doi.org/10.1145/3565387.3565427>
- [3] Huang B, Lei J, Ren F, et al 2021 Contribution and obstacle analysis of applying BIM in promoting green buildings. *J Clean Prod* 278:123946 <https://doi.org/10.1016/j.jclepro.2020.123946>
- [4] Tan T, Chen K, Xue F, Lu W 2019 Barriers to Building Information Modeling (BIM) implementation in China's prefabricated construction: An interpretive structural modeling (ISM) approach. *J Clean Prod* 219:949–959 <https://doi.org/10.1016/j.jclepro.2019.02.141>
- [5] Dashti MS, RezaZadeh M, Khanzadi M, Taghaddos H 2021 Integrated BIM-based simulation for automated time-space conflict management in construction projects. *Autom Constr* 132:103957 <https://doi.org/10.1016/j.autcon.2021.103957>
- [6] Hollberg A, Genova G, Habert G 2020 Evaluation of BIM-based LCA results for building design. *Autom Constr* 109:102972 <https://doi.org/10.1016/j.autcon.2019.102972>
- [7] Guo K, Li Q, Zhang L, Wu X 2021 BIM-based green building evaluation and optimization: A case study. *J Clean Prod* 320:128824 <https://doi.org/10.1016/j.jclepro.2021.128824>

- [8] Othman I, Al-Ashmori YY, Rahmawati Y, et al 2021 The level of building information modelling (BIM) implementation in Malaysia. *Ain Shams Engineering Journal* 12:455–463 <https://doi.org/10.1016/j.asej.2020.04.007>
- [9] Zhuang D, Zhang X, Lu Y, et al 2021 A performance data integrated BIM framework for building life-cycle energy efficiency and environmental optimization design. *Autom Constr* 127:103712 <https://doi.org/10.1016/j.autcon.2021.103712>
- [10] Bastos Porsani G, Del Valle de Lersundi K, Sánchez-Ostiz Gutiérrez A, Fernández Bandera C 2021 Interoperability between building information modelling (BIM) and building energy model (BEM). *Applied sciences* 11:2167 <https://doi.org/10.3390/app11052167>
- [11] Mariotto AB, Enewold L, Zhao J, et al 2020 Medical Care Costs Associated with Cancer Survivorship in the United States. *Cancer Medical Care Costs in the United States. Cancer Epidemiology, Biomarkers & Prevention* 29:1304–1312 <https://doi.org/10.1158/1055-9965.EPI-19-1534>
- [12] Bodendorf F, Lutz M, Michelberger S, Franke J 2022 An empirical investigation into intelligent cost analysis in purchasing. *Supply Chain Management: An International Journal* 27:785–808 <https://doi.org/10.1108/SCM-11-2020-0563>
- [13] Malhotra R, McLeod E, Alzahawi T 2020 Management and maintenance of electrical equipment in industrial facilities: procedures for improving safety while saving money. *IEEE Industry Applications Magazine* 27:48–54 <https://doi.org/10.1109/MIAS.2020.3024486>
- [14] Churruca K, Ellis LA, Long JC, et al 2022 An exploratory survey study of disorder and its association with safety culture in four hospitals. *BMC Health Serv Res* 22:530 <https://doi.org/10.1186/s12913-022-07930-6>
- [15] Potrč Obrecht T, Röck M, Hoxha E, Passer A 2020 BIM and LCA integration: A systematic literature review. *Sustainability* 12:5534 <https://www.mdpi.com/2071-1050/12/14/5534/>
- [16] Al-Ashmori YY, Othman I, Rahmawati Y, et al 2020 BIM benefits and its influence on the BIM implementation in Malaysia. *Ain Shams Engineering Journal* 11:1013–1019 <https://doi.org/10.1016/j.asej.2020.02.002>
- [17] Tam VWY, Zhou Y, Illankoon C, Le KN 2022 A critical review on BIM and LCA integration using the ISO 14040 framework. *Build Environ* 213:108865 <https://doi.org/10.1016/j.buildenv.2022.108865>
- [18] Quevedo-Martínez E, Cortés-Pérez JP, Coloma JF, et al 2022 Integration of Aerobiological Information for Construction Engineering Based on LiDAR and BIM. *Remote Sens (Basel)* 14:618 <https://doi.org/10.3390/rs14030618>
- [19] Zhu J, Wu P 2021 Towards effective BIM/GIS data integration for smart city by integrating computer graphics technique. *Remote Sens (Basel)* 13:1889 <https://doi.org/10.3390/rs13101889>
- [20] Jo C, Choi J 2021 BIM Information Standard Framework for Model Integration and Utilization Based on openBIM. *Applied Sciences* 11:9926 <https://doi.org/10.3390/app11219926>
- [21] Wang J, Lu S, Wang S-H, Zhang Y-D 2022 A review on extreme learning machine. *Multimed Tools Appl* 81:41611–41660 <https://doi.org/10.1007/s11042-021-11007-7>
- [22] Manoharan JS 2021 Study of variants of extreme learning machine (ELM) brands and its performance measure on classification algorithm. *Journal of Soft Computing Paradigm (JSCP)* 3:83–95
- [23] Rellstab C, Dauphin B, Exposito-Alonso M 2021 Prospects and limitations of genomic offset in conservation management. *Evol Appl* 14:1202–1212 <https://doi.org/10.1111/eva.13205>
- [24] Wang J, Wang A, Chen X, et al 2021 An All Fiber Mach-Zehnder Interferometer Based on Tapering Core-Offset Joint for Strain Sensing. *IEEE Photonics Technology Letters* 34:11–14 <https://doi.org/10.1109/LPT.2021.3132663>
- [25] Wang Y, Sun G-C, Wang Y, et al 2022 A Multi-Pulse Cross Ambiguity Function for the Wideband TDOA and FDOA to Locate an Emitter Passively. *Remote Sens (Basel)* 14:3545 <https://doi.org/10.3390/rs14153545>

# DETECTION METHOD OF TUNNEL SURROUNDING ROCK LEAKAGE CHANNEL BASED ON IMPROVED CHAOTIC PARTICLE SWARM OPTIMIZATION ALGORITHM

*Lei Zhu<sup>1</sup>, Peixuan Qiao, Fuyu Jiang<sup>3</sup>, Caihua Shen<sup>3</sup>, Yuke Jiang<sup>1</sup>*

1. *Zhongjiao Tunnel Bridge (Nanjing) Technology Co., Ltd., Jiangsu, Nanjing, 211800, China*
2. *Anhui Water Resources and Hydropower Survey and Design Research Institute Co., Ltd., Hefei, Anhui, 230088, China, huandengwoqiao2@163.com*
3. *School of Civil Engineering and Transportation, Hohai University, Nanjing, Jiangsu, 210098, China*

## ABSTRACT

Leakage channels in tunnel lining and surrounding rock can lead to water seepage on tunnel walls, significantly posing risks to the safety and stability of tunnel operations. Accurate detection of these leakage channels is important to block them and maintain safe operations of tunnels. Based on the theory of natural potential field detection, the potential distribution on the tunnel wall is studied. An improved particle swarm optimization algorithm is applied to invert the spatial charge distribution inside the tunnel lining and surrounding rock. The distribution of spatial charges is used to infer the location and direction of leakage channels within the tunnel lining and surrounding rock. The research results show that the variance of charge distribution is 1.58% in the forward modeling inversion and 7.6% in the inversion of measured data. The inverted result shows an area of charge anomaly consistent with the actual position of the leakage channel.

## KEY WORDS

Spontaneous potential method, Particle swarm optimization, Coupling of multiple physical fields, Tunnel seepage

## INTRODUCTION

Water seepage in the tunnel wall will affect the normal operation and lifespan of tunnel electromechanical equipment, leading to cracking or detachment of the tunnel lining, posing a threat to tunnel stability. In China, tunnel leakage is a significant issue. In 1995, a survey of 4855 railway tunnels revealed that 1428 tunnels had severe leakage, accounting for 29.4% of the total. According to the statistics of China's railway tunnel technical status in 1997, there were more than 5,000 railway tunnels in operation along the entire line. Among them, about 70% of the tunnels have leakages, and 1,502 tunnels were affected by cracking and water leakage, accounting for more than 30% of the total railway tunnels [1-2]. One of the main causes of these diseases is that the groundwater flows through the seepage channels in the surrounding rock and soil mass of the tunnel, continuously eroding the tunnel lining layer, leading to the breakage of the tunnel lining layer. The location detection of tunnel leakage channels has always been a challenging engineering problem. In practice, the method of repairing the leakage channel mostly adopts extensive excavation and then filling, which is blind, ineffective and wasteful. Therefore, it is necessary to detect the leakage channels

inside the tunnel lining and surrounding rock and to repair the leakage channels according to the detection results.

According to the flow potential effect, uneven distribution of positive and negative charges will occur in the leakage channel, causing abnormal distribution of potentials in the inner wall of the tunnel. In line with the principle of natural potential method exploration, it is possible to use the distribution of potentials in the inner wall of the tunnel as a known condition to detect the internal distribution of electric charges in the tunnel surrounding rock [3-5]. This article will study the detection method for the location of tunnel surrounding rock leakage channels based on the principles of flow potential effect and natural electrical exploration, striving to provide direction for the management of tunnel leakage water sections.

## MATERIALS AND METHODS

### Study on Forward Modeling of Electric Potential Distribution on Tunnel Walls

The essence of the abnormal distribution of natural electric field on the tunnel lining's inner wall is the selective adsorption of charged particles in the liquid by the surrounding rock and lining layers, leading to the directional separation of charged particles. This abnormal distribution of natural electric field is coupled with the seepage field, and there is a coupling relationship equation between the seepage field and the natural electric field under saturated conditions [6-8]. Under quasi-static conditions, the total current density  $j$  in saturated porous media can be represented as follows:

$$j = -\sigma_{sat}\nabla\varphi + j_s \quad (1)$$

where  $\varphi$ ,  $\sigma_{sat}$  and  $j_s$  are the potential, conductivity and flow current density, respectively. Under saturation conditions, the flow current density  $j_s$  is expressed as follows:

$$j_s = \sigma_{sat}C_{sat}\nabla P \quad (2)$$

where  $\sigma_{sat}$  is the conductivity of the pore water under saturated conditions;  $C_{sat}$  is the coupling coefficient of the flow potential under saturated conditions, and  $P$  is the pressure. Charge is conserved under quasi-static conditions, and the equation can be calculated as follows:

$$\nabla \cdot j = 0 \quad (3)$$

The governing equations of the flow potential can be obtained from Eqs.(1) and (3):

$$\nabla \cdot \sigma_{sat}\nabla\varphi = \nabla \cdot j_s \quad (4)$$

The coupled relationship equations between the seepage field and the natural electric field in the saturated state can be obtained by coupling Equations (2) and (4):

$$\nabla \cdot \sigma_{sat}\nabla\varphi = \nabla \cdot \sigma_{sat}C_{sat}\nabla P \quad (5)$$

Based on the above analysis, a three-dimensional coupled seepage field-natural electric field model is established within the Comsol multi-physics software for the analysis of the potential distribution on the inner wall of the tunnel. The model is shown in Figure 1. The boundary condition used for the model is the Delicacy boundary condition with a value of 0 at infinity.

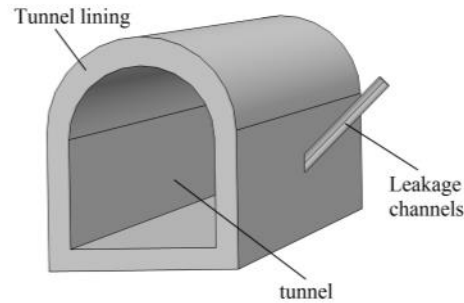


*Fig. 1 - Schematic diagram of tunnel forward model*

According to theoretical analysis, the low water pressure appears at the location of the leakage channel. Due to the variation of water pressure, the flow velocity and direction at the location of the leakage channel also change [9-11]. Based on the coupled relationship between the natural electric field and seepage field (Equation 5), the electric potential distribution at the leakage channel location can be calculated. It can be seen from Figure 2 that there is an obvious positive potential feature close to the inner wall of the tunnel, and a significant negative potential feature at a position away from the inner wall of the tunnel. Figure 3 illustrates the electric potential distribution on the tunnel walls.

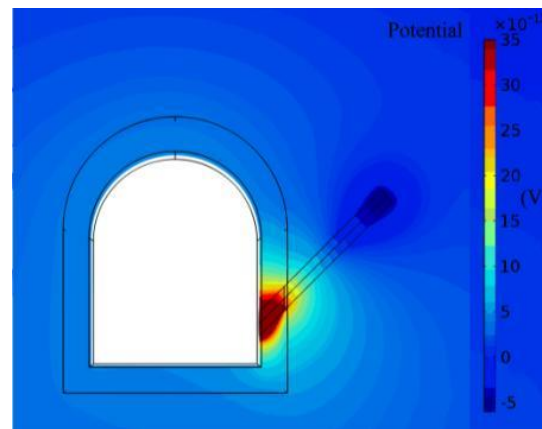


*Fig. 2 - Potential distribution diagram of leakage channel position*

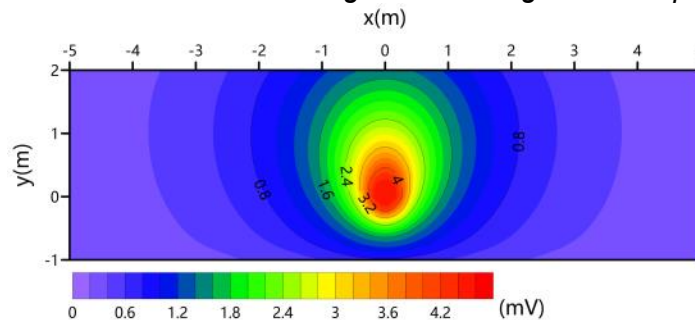


*Fig. 3 - Potential distribution of inner wall of tunnel*

## Inverse study of charge distribution in tunnel surrounding rock

In the inversion of the space charge distribution, the inversion can be divided into the following three steps:

- ① Construct the fitness function;
- ② Solve the solution when the fitness function takes the minimum value;
- ③ Output of results and graphical display;

In inversion, the establishment of the fitness function is the most important part, and the construction of fitness function can be divided into the following steps:

- (1) Randomly generate  $n$  points in the target inversion space, with the positions  $(x_i, y_i, z_i)$  and the charges of the point as  $q_i$ , where  $i = 1, 2, 3 \dots n$ .
- (2) Import the measured data. The position and potential of each point in the measured data is  $(x_j, y_j, z_j)$  and  $U_j$ , where  $j = 1, 2, 3 \dots m$ ,  $m$  is the number of measured data points.
- (3) The sum potential  $U_{merj}$  generated by all point charges in space at the location of the  $j$ th real point can be expressed as follows:

$$U_{merj} = \sum_{i=1}^n k \frac{q_i}{r_{ij}^2} \quad (6)$$

where  $k$  is the Coulomb constant,  $q_i$  is the charge of the  $i$ -th point charge, and  $r_{ij}$  is the distance from the  $i$ -th point charge to the  $j$ -th data point.

- (4) Use  $V_j$  as a parameter to measure the deviation between the measured potential at the location of the  $j$ -th data point and the combined potential  $U_{merj}$ ,  $V_j$  is expressed as follows:

$$V_j = \left| \frac{U_{merj} - U_j}{U_j} \right| \quad (7)$$

- (5) The average deviation  $\overline{V}_a$  from the measured value of the combined potential generated by all point charges in space at all measured point positions is as follows:

$$\overline{V}_a = \frac{\sum_{j=1}^m V_j}{m} \quad (8)$$

Construct the fitness function  $f_{ad}$  as follows:

$$f_{ad} = \overline{V}_a \quad (9)$$

$f_{ad}$  is a function of  $x_i, y_i, z_i, q_i$ .

Taking  $x_i, y_i, z_i$  and  $q_i$  as the unknowns of the fitness function  $f_{ad}$  for solution when the fitness function  $f_{ad}$  is minimized, these solutions can represent the position and charge of each point, and  $i = 1, 2, 3 \dots n$ . Since the fitness function may be underdetermined and unknowns are large, it is solved using a nonlinear optimization algorithm.

The particle swarm optimization algorithm is an evolutionary algorithm inspired by bird flocking behavior, and developed by Kennedy and Eberhart [12], and El Rassy et al. [13]. Particle swarm algorithm is an iterative optimization algorithm that firstly creates a set of random solutions in the solution space, i.e. the initial particle swarm. Then it takes the optimal solution in the initial particle swarm, allowing the remaining particles to follow the optimal particles for optimization in the solution space, and gradually approach to the better solution by adjusting the particle's moving speed and position [14-15].

The solution of the above fitness function belongs to the solution of multi-dimensional and multi-peak function. As can be seen from the previous studies [16-18], compared with other nonlinear solution methods, the particle swarm algorithm for multi-dimensional, multi-peak problems has the advantages of strong solving ability, good convergence, good stability, high computational efficiency, and simple parameters, which is very suitable for the solution of the minimum value of the above

fitness function. In this study, the particle swarm algorithm is used to solve the solution when the fitness function takes the minimum value.

### Improvements to the Particle Swarm Optimization (PSO)

Traditional PSO-based inversion algorithms has problems such as easy to fall into the local optimal solutions, the multiple solutions leads to mismatch between the inversion results and the actual situation, and difficulty in displaying the inversion results are difficult to display. In response to the above problems, the PSO-based inversion algorithm is improved.

### Adaptive Weight Method

In a traditional PSO algorithm, the inertia weight is a fixed value, typically between 0.4 and 0.9. A smaller inertia weight will weaken the global search capability of the PSO algorithm, while a larger one will weaken its local improvement ability [19-21]. To balance the global search and local improvement capabilities of the PSO algorithm, a nonlinear dynamic inertia weight coefficient formula can be expressed as follows (10):

$$\omega = \begin{cases} \omega_{min} - (\omega_{max} - \omega_{min}) \times (f - f_{min}) / (f_{avg} - f_{min}), & f \leq f_{avg} \\ \omega_{max}, & f > f_{avg} \end{cases} \quad (10)$$

where  $\omega_{max}$  and  $\omega_{min}$  are the maximum and minimum values of  $\omega$ , respectively  $f$  is the current fitness of the particle;  $f_{avg}$  are the average fitness of all current particles, and  $f_{min}$  is the minimum fitness of all current particles.

In the above equation, the inertia weight will automatically change with the objective function value of the particle, is hence called the adaptive weight [22-24].

When the objective value of each particle tends to be consistent or tends to be locally optimal it will increase the inertia weight; while when the objective value of each particle is more dispersed, it will decrease the inertia weight. Meanwhile, for particles whose objective function values are better than the average objective values, the corresponding inertia weight factor is smaller, protecting the particles. On the other hand, for particles whose objective function values worse than the average objective values, the corresponding inertia weight factor is larger, making the particles closer to the better search area.

### Chaos Mapping Method

When the PSO algorithm iterates to a certain extent, the traditional PSO algorithm is prone to getting stuck in local optima and unable to escape. When the PSO algorithm falls into a local optimum, if it can force some particles to break through the local optimum and continue global search, it can significantly improve the global search ability of the PSO algorithm.

Chaos is a widespread nonlinear phenomenon in nature. It may seem chaotic, but it has a complex internal structure, featuring randomness, ergodicity, and regularity. It is highly sensitive to initial conditions and can traverse all states within a certain range without repetition according to its own rules. Based on the properties of chaotic motion, optimization searches can be carried out [25-26]. The main idea of introducing chaotic optimization search techniques into the PSO algorithm is to incorporate the computation process of the PSO algorithm the main procedure. When the optimal fitness of the population changes very little in  $n$  iterations, indicating that it has fallen into local optima, chaotic optimization search is applied to particles with the optimal fitness. This drives the particle to escape the local optimum, thereby improving the trend of PSO algorithm falling into local optima in the later stages of evolution [27-29].

To improve computational efficiency, chaotic optimization search is not triggered in the early

stages of evolution due to the fast convergence speed of PSO algorithm. However, in the later stages, when the convergence of the PSO algorithm slows down, chaotic optimization search will be called multiple times for optimization.

The chaos mapping method used in this study is the Logistic-Sine-Cosine chaotic mapping, and the formula to generate chaotic sequences is as follows (11):

$$y_{i+1} = \cos\{\pi[4ry_i(1 - y_i) + (1 - r)\sin(\pi y_i) - 0.5]\}, r \in [0,1] \quad (11)$$

where  $y_1$  is a random number;  $y_2 - y_{i+1}$  is generated by the chaos mapping formula, and  $y_1 - y_i$  is the chaos mapping sequence.

The chaotic sequence is mapped into the  $x_i$ -centered domain by carrier wave, and expressed as follows (12):

$$x'_i = x_i + R(2y_i - 1) \quad (12)$$

where  $R$  is the chaotic search radius, and the value range of  $x'_i$  is as follows:

$$x'_i \in [x_i - R, x_i + R] \quad (13)$$

The update formula for particle swarm velocity is as follows:

$$v'_i = \frac{x'_i - x_i}{\|x'_i - x_i\|} \quad (14)$$

## Adaptive Outlier Filtering Method

When applying the traditional PSO algorithm to the inversion of leakage channels within the tunnel lining and surrounding rock in a three-dimensional space, the reliability of the inversion results will be inevitably affected by the multiple solutions. On one hand, the inversion results may significantly deviate from reality; on the other hand, the results from two different inversions may be entirely dissimilar. To address this issue, constraints need to be applied to the inversion process and results.

According to the basic geological distribution pattern, the distribution of charges is continuous and smooth, and it is unlikely that there will be a sudden change in charges. Therefore, this regularity can serve as a constraint to eliminate mutation points, reduce the existence of multiple solutions, and make the inversion results closer to reality.

To eliminate mutation points, this inversion algorithm adopts an outlier determination-correcting method based on the Pautacriterion to rectify mutation points. During the correction process, an adaptive weighting coefficient  $\delta$  is introduced to avoid data distortion and overcorrection.

The calculation steps are as follows:

- (1) Calculate the distance  $r_{km}$  from the data point  $k$  to all remaining data points in the solution space, where  $k = 1, 2, 3 \dots n$ ,  $m = 1, 2, 3 \dots n$ , and  $n$  is the total number of points in the group.
- (2) The sphere with the radius  $R$  is determined with the data point  $k$  as the center.
- (3) When the number of points with a distance to the data point  $k$  less than  $R$  is greater than  $l$ , the standard deviation and average value of all points in the sphere range with  $R$  as the radius are obtained. The value of the data point  $k$  is corrected according to Eq. (15) when the difference between the value of the data point  $k$  and the average of all points in the range is greater than  $q$  times the standard deviation; otherwise, the value of the data point  $k$  ( $val_k$ ) remains unchanged.

$$val_k = \sum_{i=1}^n \frac{r_{ki}}{\sum_{j=1}^n r_{kj}} \times val_i \times (1 - \delta) + val_k \times \delta, i = 1, 2, 3 \dots s, j = 1, 2, 3 \dots s, k = 1, 2, 3 \dots n \quad (15)$$

where  $s$  is the number of all points in the range except the data point  $k$ ;  $val_i$  is the amount of charge of the data point  $i$ ;  $r_{kj}$  and  $r_{ki}$  are the distance between data point  $k$  and data points  $i$  and  $j$ . The

coefficient  $\delta$  is determined as follows:

$$\delta = 1.2^{-(s-1)} \quad (16)$$

(4) When the number of points whose distance to the data point  $k$  is less than  $R$  is less than or equal to  $l$ , the standard deviation and the mean of these  $l$  points plus data point  $k$  are sought. The data point  $k$  is corrected according to Equation (17) when the difference between the data point  $k$  and the average of the sought  $l+1$  points is greater than  $q$  times the standard deviation; otherwise, the value of the data point  $k$  remains unchanged.

$$val_k = \sum_{i=1}^n \frac{r_{ki}}{\sum_{j=1}^n r_{kj}} \times val_i \times (1 - \delta) + val_k \times \delta, i = 1,2,3 \dots l, j = 1,2,3 \dots l, k = 1,2,3 \dots n \quad (17)$$

where  $val_i$  is the amount of charge of the data point;  $r_{kj}$  and  $r_{ki}$  are the distance between the data point  $k$  and data points  $i$  and  $j$ . The coefficient  $\delta$  is determined as follows:

$$\delta = 1.2^{-(l-1)} \quad (18)$$

### Four-Dimensional Discrete Data Point Grid Interpolation Method

In the inversion of leakage channels within the tunnel lining and surrounding rock in three-dimensional space, the output result of the PSO algorithm is represented as an  $n \times 4$  matrix. In the output matrix, the first three columns are the position of the data point, and the fourth column is the charge of the point  $val_i, i=1,2,3 \dots n$ . As the data points in the output result are sparsely distributed in three-dimensional space, it is challenging to visualize them directly. To address this, a four-dimensional discrete data point grid interpolation algorithm is designed to visualize the randomly distributed four-dimensional data points. The algorithm steps are as follows:

(1) Establish a uniformly distributed three-dimensional grid of points  $p_j$ , and set the charge corresponding to each three-dimensional grid point as  $dval_j$ , where  $j = 1,2,3 \dots m$ , and  $m$  is the number of three-dimensional grid points.

(2) Calculate the distance from all data points to the three-dimensional grid point  $p_j$  and indicate them by  $r_1, r_2, r_3 \dots r_n$ . In addition, when  $r_i$  is 0,  $r_i$  is changed to  $1.0 \times 10^{-100}$ ;

(3) Calculate the weight of all data points to 3D mesh point  $p_j$  according to Eq. (19),  $j = 1,2,3 \dots m$ :

$$weight_i = \frac{r_i}{\sum_{i=1}^n r_i}, i = 1,2,3 \dots n, \quad (19)$$

(4) Calculate the charge amount  $dval_j$  of the three-dimensional grid point  $p_j$  as follows:

$$dval_j = \sum_{i=1}^n weight_i \times val_i, i = 1,2,3 \dots n, j = 1,2,3 \dots m, \quad (20)$$

(5) The coordinates of the three-dimensional grid point  $p_j$  and the charge amount  $dval_j$  of the point are combined to form a meshed interpolation matrix.

## ANALYSIS AND RESULTS

### Comparison of Algorithm before and After Improvements

Taking a simple three-dimensional model as an example, as shown in Figure 4(a), the simple three-dimensional model is established as follows: a charged sphere with a radius of 0.6m is placed in a semi-infinite space. The center coordinates of the sphere are (0.5, 0.5, -1). The surface of the semi-infinite space is at  $Z=0m$ . The volume charge density of the sphere is  $1C/m^3$ . The surface potential distribution at  $Z=0m$  is shown in Figure 4(b).

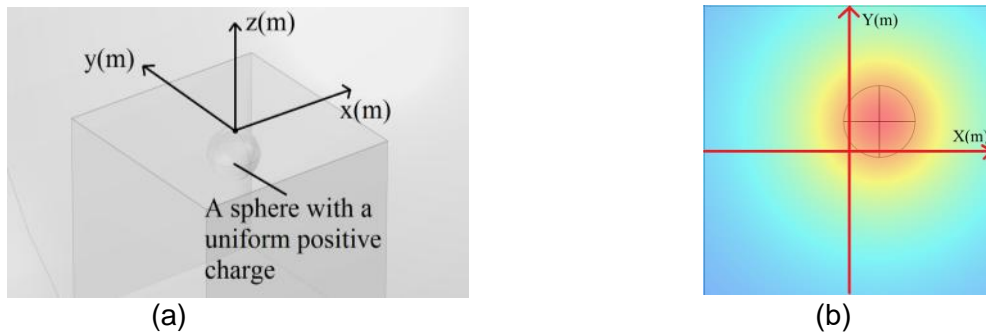


Fig. 4 - Surface potential distribution at  $z = 0m$

The standard particle swarm algorithm and the improved particle swarm algorithm are respectively used for inversion test, as shown in Figures 5 to 6. The direction of each axis of the coordinate system in Figures 5 to 6 is consistent with the direction of each axis of the coordinate system in Figure 4, but the coordinate origin in Figures 5 to 6 is located at (0, 0, -2) in the coordinate system of Figure 4.

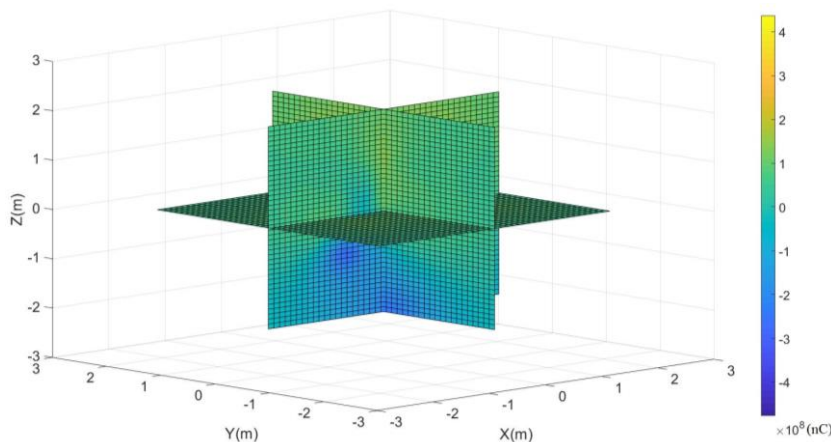


Fig.5 - Inversion result diagram of standard particle swarm optimization algorithm

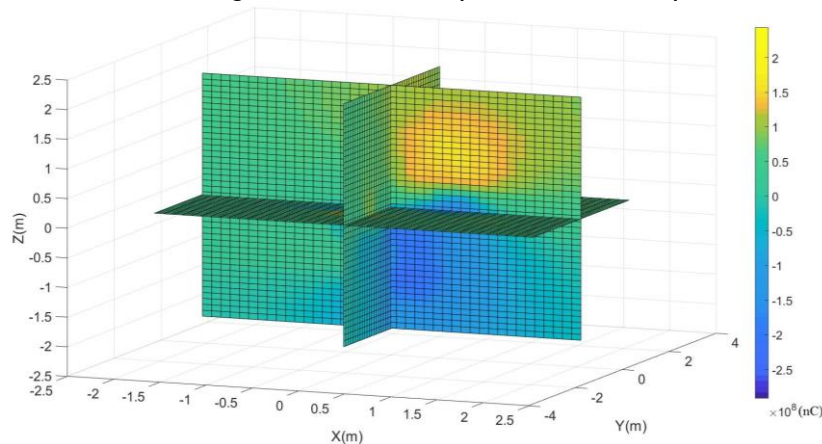
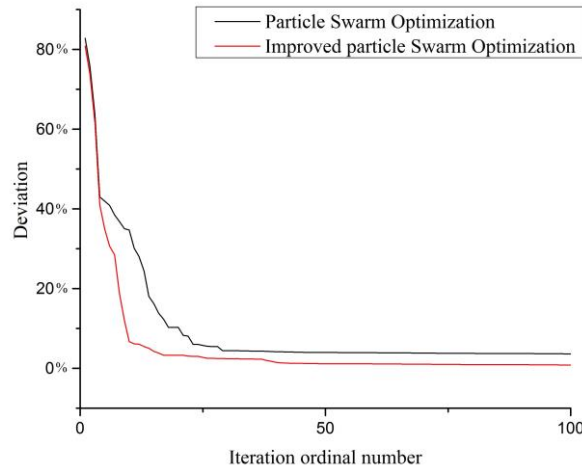


Fig.6 - Inversion Results of Improved Particle Swarm Optimization Algorithm

The convergence curves of the algorithms are shown in Figure 7.



*Fig. 7 Convergence curve of algorithm*

As shown in Figure 7, the inversion fitting variance of the improved PSO algorithm is significantly smaller than that of the standard PSO algorithm. Compared with the standard PSO algorithm, the inversion results of the improved PSO algorithm match the established model to a better extent, which shows better inversion effect.

### Forward Simulation Data Inversion

The basic steps of the algorithm are as follows:

- (1) Import raw data and set inversion parameters;
- (2) Apply adaptive outlier filtering to preprocess the original data and remove outliers;
- (3) Use the adaptive weighted particle swarm optimization algorithm to invert the preprocessed data;
- (4) When optimization stagnates, apply chaos mapping to the optimal solution to expand the search range;
- (5) Stop iteration when the objective fitness is reached, and apply adaptive outlier filtering to the discrete point cloud to make the results conform more to geological laws;
- (6) Export the data and create plots.

Taking the aforementioned three-dimensional coupled model of seepage field-natural electric field as an example, the inverse processing of the forward data is carried out in the following steps:

- (1) As shown in Figure 3, the potential distribution of the surrounding tunnel wall is obtained on the tunnel wall of the forward model centered on the seepage point;
- (2) Establish a square with a side length of 2 m as the inversion area, and take the center of the inversion area as the origin to establish a three-dimensional coordinate system, in which the Z-axis points beyond the inner wall of the tunnel, the Y-axis is upward, and the X-axis is to the right, so that the coordinates of the inner wall of the tunnel are Z=1 m, and the coordinates of the water seepage point are (0, 0, 1). The established coordinate system is shown in Figure 8.
- (3) Inversion parameter setting: a target fitting variance of 1%; a maximum number of iterations of 200, and an initial filtering parameter-filtering number of 1.

In this inversion trial, the variance of the inversion results from the forward data is 1.58%. The inversion results are shown in Figure 8.

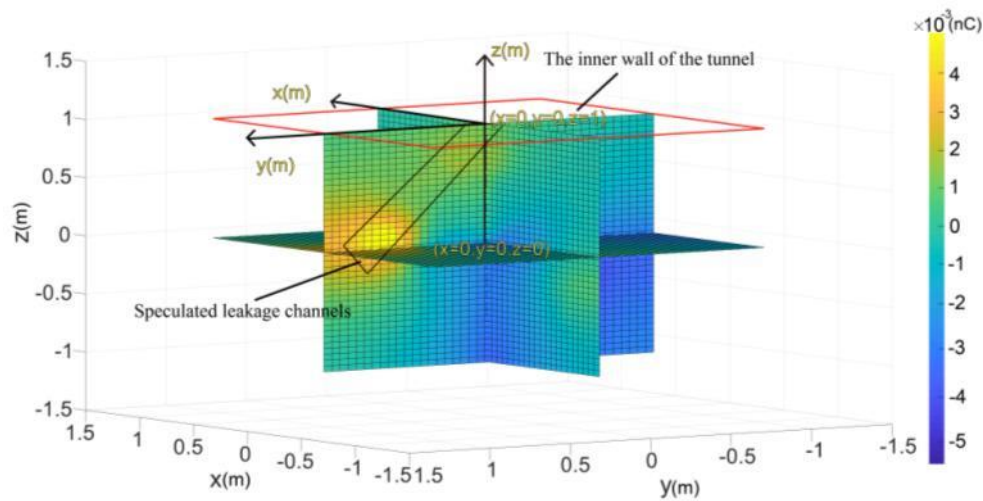


Fig. 8 - Inversion Results of Forward Model

It can be seen from Figure 8 of the inversion results that the position and morphology of the leakage channel in the forward model have a good correspondence with the position and morphology of the positive charge concentration distribution in the space charge inversion result diagram. Therefore, the spatial charge distribution inversion based on the forward data is reliable.

### Inversion Study of Measured Data

After long-term operation, water seepage occurs in the inner wall of a tunnel, and it is necessary to carry out leakage plugging construction on the seepage channel. Taking the seepage location of the tunnel as an example, the effectiveness of the detection method is further verified. As shown in Figure 9(a), the measuring points are arranged where water seepage occurs in the tunnel inner wall, and the distribution of measuring points is depicted as shown in Figure 9(b).

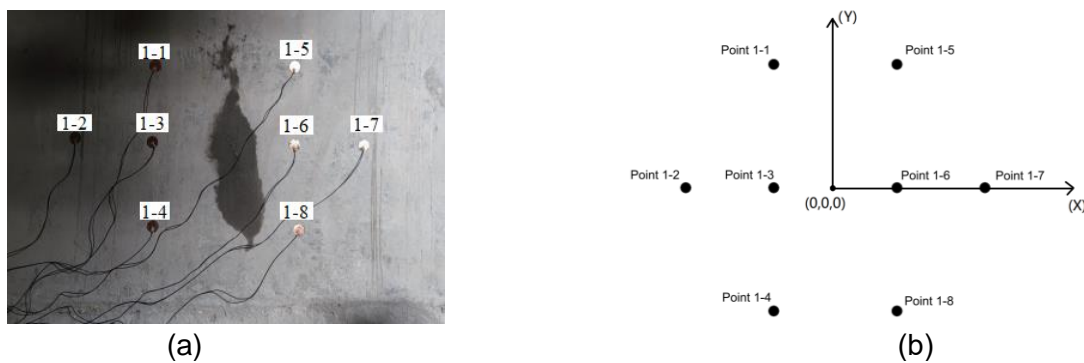


Fig.9 - Layout of Measuring Points for Measured Data

Based on the distribution of the measured points, a spatial coordinate system with the X and Y axes is established, as shown in Figure 9(b). The seepage point is the origin of the X-Y axis coordinate system. The Z-axis is set to point outward from the tunnel surface, where the Z-axis coordinate of the tunnel surface is 2m. Therefore, the origin of the coordinate system is 2m inside the tunnel lining, located at the intersection of the X and Y axes. Table 1 shows the coordinates and potential values of each measured point, and Figure 10 shows the potential distribution on the inner wall surface of the tunnel (interpolated using the Kriging method).

Tab. 1 - Measured Point Coordinates and Potential Values

Dot	X	Y	Z	potential(mV)
Point 1-1	-0.35	0.7	2	-14.8082
Point 1-2	-0.85	0	2	25.7779
Point 1-3	-0.35	0	2	27.4132
Point 1-4	-0.35	-0.7	2	5.4714
Point 1-5	0.35	0.7	2	-27.6113
Point 1-6	0.35	0	2	-32.2695
Point 1-7	0.85	0	2	1.4756
Point 1-8	0.35	-0.7	2	-27.3133

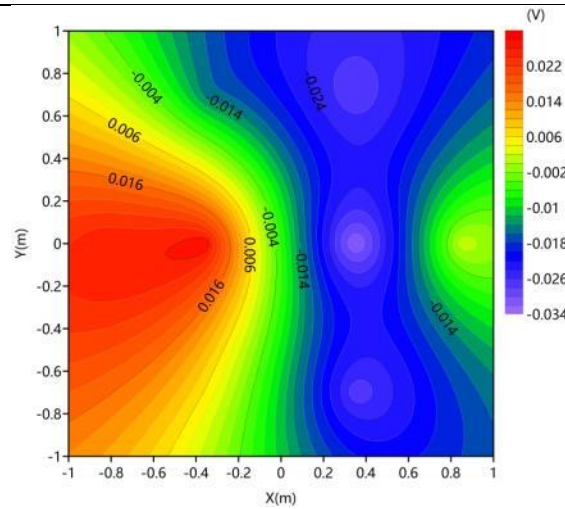


Fig. 10 Potential distribution of inner wall surface of tunnel

The inversion process utilizes parameters such as a target fitting variance of 5%, maximum iteration times of 200 and initial filtering parameters - filtering times of 1. The inversion variance is 7.6%. The inversion result is shown in Figure 11.

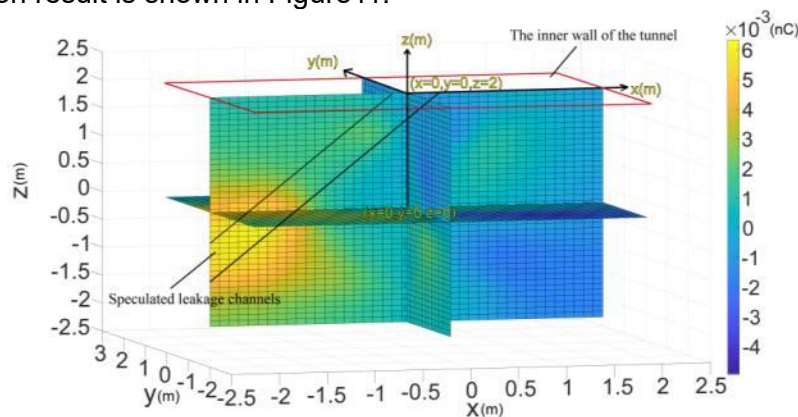


Fig. 11 Inversion Results of Measured Data

From the inversion result in Figure 11, it can be observed that the spatial charge distribution inversion based on the measured data corresponds to the actual situation of charge anomaly distribution caused by leakage channels. It can be inferred that the leakage channels in the external surrounding rock of the tunnel lining may exist at the location surrounded by the black wireframe in Figure 11. During the excavation process of the circled seepage channel, the excavation results

showed that at the abnormal position shown in Figure 11, the soil was loose and water seepage occurred. The loose part was excavated and replaced, and after treatment, there was no water seepage.

## CONCLUSION

The following points can be drawn:

- (1) When there are leakage channels in the tunnel lining and the external surrounding rock, the potential distribution on the inner surface of the tunnel lining near the leakage channels will be significantly affected by the flow potential, resulting in anomalies.
- (2) The inversion software based on the improved chaos particle swarm optimization algorithm achieves a variance of 1.58% in the inversion of the forward model and a variance of 7.6% in the inversion of the measured data. Moreover, the charge anomaly distribution areas in the inversion results of the forward model are well correlated with the locations of leakage channels in the established model. In the inversion of the measured data, the distribution of charge anomalies conforms to geological laws. Therefore, the improved chaos PSO algorithm demonstrates good convergence and high consistency in the inversion of three-dimensional spatial charge distributions.
- (3) Through the analysis of the inversion results of numerical simulation data and measurement data, it can be seen that the improved chaotic PSO algorithm is used to perform three-dimensional inversion of the leakage channel inside the tunnel surrounding rock using the potential distribution of the tunnel lining layer as the original data, which is consistent with the actual situation. The inversion algorithm has high reliability.

## REFERENCES

- [1] Fu, J.K. 2012. Study on the causes of water leakage and its impact on structures of highway tunnel [D]. Southwest Jiaotong University.
- [2] Yao, Z.Z., Yang, C.P. 2014. Rectification measures for leakage water leakage in tunnels in active operation of expressways (in Chinese). *Transportation Science & Technology*, no. 02, pp. 112-115.
- [3] Hunter, R. J. 2013. *Zeta Potential in Colloid Science: Principles and Applications*. Academic Press.
- [4] Chenyakin, Y., & Chen, D. D. Y. 2021. Characterization of capillary inner surface conditions with streaming potential. *Electrophoresis*, vol. 42, no. 20, pp. 2094-2102. <https://doi.org/10.1002/elps.202100167>
- [5] Siani, P., Frigerio, G., Donadoni, E., & Di Valentin, C. 2023. Modeling Zeta Potential for Nanoparticles in Solution: Water Flexibility Matters. *The Journal of Physical Chemistry C*, vol. 127, no. 19, pp. 9236-9247. <https://doi.org/10.1021/acs.jpcc.2c08988>
- [6] Hamlyn, J., Cottrell, R. J., Bird, C. L., & Kulesa, B. 2023. Observing water flow within an embankment dam using self-potential monitoring. *Dams and Reservoirs*, vol. 33, no. 1, pp. 19-26. <https://doi.org/10.1680/jdare.22.00085>
- [7] Bolève, A., Vandemeulebrouck, J., & Grangeon, J. 2012. Dyke leakage localization and hydraulic permeability estimation through self-potential and hydro-acoustic measurements: Self-potential 'abacus' diagram for hydraulic permeability estimation and uncertainty computation. *Journal of Applied Geophysics*, vol. 86, pp. 17-28. <https://doi.org/10.1016/j.jappgeo.2012.07.007>
- [8] Kukemilks, K., & Wagner, J. F. 2021. Detection of Preferential Water Flow by Electrical Resistivity Tomography and Self-Potential Method. *Applied Sciences*, vol. 11, no. 9, pp. 4224. <https://doi.org/10.3390/app11094224>
- [9] Wang, Y., Chung, E., & Sun, S. 2022. Physics-preserving IMPES based multiscale methods for immiscible two-phase flow in highly heterogeneous porous media. *arXiv preprint arXiv:2212.05942*. <https://doi.org/10.48550/arXiv.2212.05942>

- [10] Xu, R. 2023. Stability of surrounding rock in broken zone of the tunnel in rich water and mountains. *Desalination and Water Treatment*, vol. 290, pp. 170-176. Doi: 10.5004/dwt.2023.29419
- [11] Gambolati, G., & Freeze, R. A. 1973. Mathematical simulation of the subsidence of Venice: 1. Theory. *Water Resources Research*, vol. 9, no. 3, pp. 721-733. <https://doi.org/10.1029/WR009i003p00721>
- [12] Li, B. 2023. A Productivity Prediction Method Based on Artificial Neural Networks and Particle Swarm Optimization for Shale-Gas Horizontal Wells. *Fluid Dynamics & Materials Processing*, vol. 19, no. 10, pp. 2729-2748. DOI:10.32604/fdmp.2023.029649
- [13] Chatterjee, A., & Siarry, P. 2006. Nonlinear inertia weight variation for dynamic adaptation in particle swarm optimization. *Computers & Operations Research*, vol. 33, no. 3, pp. 859-871. <https://doi.org/10.1016/j.cor.2004.08.012>
- [14] Abualigah, L., Almotairi, K. H., AbdElaziz, M., Shehab, M., & Altalhi, M. 2022. Enhanced Flow Direction Arithmetic Optimization Algorithm for mathematical optimization problems with applications of data clustering. *Engineering Analysis with Boundary Elements*, vol. 138, pp. 13-29. <https://doi.org/10.1016/jenganabound.2022.01.014>
- [15] Shi, K., Cai, Y.G., Zou, G.S., Wang, T. 2005. Comparison between Ant Colony Algorithm and Particle Swarm Optimization and their application in VRP. *Proceeding of the 24<sup>th</sup> Chinese Control Conference*, Guangzhou, China, pp. 732-735.
- [16] Li, H. 2010. Inverse Problems of Partial Differential Equations Particle Swarm Algorithm [D]. Xi'an University of Technology.
- [17] Zou, S., Ji, J.M., Yang, X.D., He, Y.M. 2021. Application of Improved PSO Algorithm in Reactive Power Optimization of Power System. *Information & Computer*, vol. 33, no. 24, pp. 77-80.
- [18] Altinoz, O. T., Yilmaz, A. E., & Weber, G. W. 2010. Chaos Particle Swarm Optimized PID Controller for the Inverted Pendulum System. *2<sup>nd</sup> international conference on engineering optimization*, Lisbon, Portugal.
- [19] Kennedy, J., & Eberhart, R. 1995. Particle Swarm Optimization. *Proceedings of ICNN'95 - International Conference on Neural Networks*, Perth, WA, Australia, IEEE, vol. 4, pp. 1942-1948. DOI: 10.1109/ICNN.1995.488968
- [20] El Rassy, E., Delaroque, A., Sambou, P., Chakravarty, H. K., & Matynia, A. 2021. On the Potential of the Particle Swarm Algorithm for the Optimization of Detailed Kinetic Mechanisms. Comparison with the Genetic Algorithm. *The Journal of Physical Chemistry A*, vol. 125, no. 23, pp. 5180-5189. <https://doi.org/10.1021/acs.jpca.1c02095>
- [21] Dong, W. Y., & Zhang, R. R. 2022. Stochastic stability analysis of composite dynamic system for particle swarm optimization. *Information Sciences*, vol. 592, pp. 227-243. <https://doi.org/10.1016/j.ins.2021.12.095>
- [22] Wang, S., Liu, Y., Zou, K., Li, N., & Wu, Y. 2022. Multiobjective Particle Swarm Optimization Based on Ideal Distance. *Discrete Dynamics in Nature and Society*, vol. 2022, pp. 3515566. <https://doi.org/10.1155/2022/3515566>
- [23] Li, R., Yu, N., Li, R., Zhuang, Q., & Zhang, H. 2021. Transient electromagnetic inversion based on particle swarm optimization and differential evolution algorithm. *Near Surface Geophysics*, vol. 19, no. 1, pp. 59-71. <https://doi.org/10.1002/nsg.12129>
- [24] Zhang, J., Sun, Z., Qiu, N., Zhang, Y., & Li, F. 2019. 3-D effective elastic thickness inversion of subduction zone based on particle swarm optimization algorithm. *Chinese Journal of Geophysics*, vol. 62, no. 12, pp. 4738-4749. Doi: 10.6038/cjg2019M0247
- [25] Wardhana, S. G., & Pranowo, W. 2022. Rock-physics modeling by using particle swarm optimization algorithm. *Journal of Applied Geophysics*, vol. 202, pp. 104683. <https://doi.org/10.1016/j.jappgeo.2022.104683>
- [26] Liu, B., Wang, L., Jin, Y. H., Tang, F., & Huang, D. X. 2005. Improved particle swarm optimization combined with chaos. *Chaos, Solitons & Fractals*, vol. 25, no. 5, pp. 1261-1271. <https://doi.org/10.1016/j.chaos.2004.11.095>
- [27] Zeedan, M., Attiya, G., & El-Fishawy, N. 2022. A Hybrid Approach for Task Scheduling Based Particle Swarm and Chaotic Strategies in Cloud Computing Environment. *Parallel Processing Letters*, vol. 32, no. 01n02, pp. 2250001. DOI:10.1142/S0129626422500013
- [28] Gao, S., Yang, J.Y. 2006. Research on Chaos Particle Swarm Optimization Algorithm. *Pattern Recognition*

and Artificial Intelligence, vol. 19, no. 02, pp. 266-270.

[29] Yang, J.J., Zhou, J.Z., Yu, J., Wu, W. 2005. Particle swarm optimization algorithm based on chaos searching. Computer Engineering and Applications, no. 16, pp. 69-71.

# SEISMIC INVESTIGATION OF STRENGTHENED SOIL WALLS WITH GEOGRIDS

*Hongliang Yue and Xiaoyong Liang*

*School of Civil Engineering, Hebei University of Science and Technology,  
Shijiazhuang, 050018, China; lxy063019@163.com*

## ABSTRACT

This study explores the impact of various factors on the seismic behavior of geogrid-strengthened soil walls. The research involves modifying soil properties like friction angle, cohesion, elastic modulus, and Poisson's ratio. The aim is to comprehend the consequent effects on the wall's horizontal and vertical deformations, the lateral pressure applied to the wall's surface, and the peak pulling force encountered by strengthening under seismic states with a maximum acceleration of 0.3 g. The primary goal is to boost the seismic execution of such walls and analogous scenarios. To attain this goal, a two-dimensional numerical analysis is performed employing the finite difference method and FLAC software while accounting for strain considerations. The analysis findings reveal that increasing cohesion at the wall's height results in a nearly consistent peak pulling force on the reinforcements. However, the impact of cohesion on this force diminishes for wall heights exceeding 4 meters. Elevating the internal friction angle leads to a reduction in the peak pulling force on the reinforcements, particularly in the lower segment of the wall. Conversely, with increasing wall height, the decrease in horizontal pressure on the wall's rear surface becomes less noticeable, eventually stabilizing at around 1 kilopascal in the upper half of the wall. Altering the soil's elastic modulus demonstrates that once the value surpasses 35 MPa, the peak pulling force on the reinforcements remains stable, exhibiting no further alterations.

## KEYWORDS

Strengthened soil walls, Seismic analysis, FLAC numerical pattern, Finite difference method, Deformation, Soil cohesion, Soil friction angle

## INTRODUCTION

Strengthened soil walls have historically played a pivotal role in the evolution of geotechnical engineering. Their economical construction costs, minimal settlement, and effective resistance against seismic loads make them crucial subjects of study (Bao et al., 2023; Nunes et al., 2022). Presently, these structures are referred to as Mechanically Stabilized Earth Walls (MSEW) (Huang, 2019; Xu et al., 2020; Yang et al., 2023). The United States began employing strengthened soil techniques for retaining wall construction around 1972. Notably, more than 7,000 such walls were built between 1972 and 1996, with over 200,000 structures executed globally in the past two decades in 11 diverse countries (Bathurst & Hatami, 1998).

Initially, metal straps were used for wall reinforcement, later replaced by welded wire mesh. These frameworks faced issues such as susceptibility to corrosion and high costs. Consequently, the emergence of polymer geosynthetics offered an economically viable and corrosion-resistant solution. These geosynthetics are grouped into categories, including geotextiles, geogrids, geonets, and geocomposites. Geotextiles and geogrids are commonly used for soil reinforcement and

contribute to stability through functions like filtration, drainage, and separation (Changizi et al., 2022; Geng, 2021).

The introduction of geotextile reinforcement took place in France in 1972, marking a turning point in geotextile use for soil reinforcement, especially since the 1980s. Geogrids similarly gained prominence in this period and currently maintain a significant market presence (Holtz, 2017). Notably, geosynthetics exhibit superior tensile strength compared to metals, albeit with higher deformation. Additionally, geosynthetics display distinctive long-term behavior due to gradual "creep," causing increased deformation over time (Leshchinsky & Han, 2004).

Numerical studies on strengthened soil structures were historically limited due to information gaps and skepticism regarding numerical frameworks. However, recent years have witnessed a growing recognition of the potential of these frameworks. For instance, Cai and Bathurst (1995) utilized modified TARA-3 software to simulate earthquake-resistant walls with segmented geosynthetic facades. They employed the El Centro (1940) earthquake acceleration curve, applying maximum values of 0.125 and 0.25 g at a reduced scale. Segrestin and Bastick (1988) utilized the SUPER FLUSH finite element program, obtaining promising outcomes comparable to shake table tests. More recently, researchers like Zhang et al. (2020), Ling (2023), Ren et al. (2024), and Majumder et al. (2023) have delved into various aspects of numerical analysis to understand the seismic response and behavior of strengthened soil walls under various states (Fairless, 1989; Javdanian & Goudarzi, 2023; Murali Krishna & Madhavi Latha, 2009; Qian, 2023; Safaee et al., 2023; Zhou & Ding, 2021).

Despite these advances, laboratory investigations of diverse parameters, particularly under seismic states, pose challenges due to complexity and costs. Consequently, numerical frameworks offer an efficient alternative, providing detailed outcomes for accurate execution assessment and model validation. However, in the context of strengthened soil, few instances of actual earthquake-condition model outcomes can be found in the technical literature. To ensure numerical accuracy, comparisons were drawn between a one-meter-high instrumented laboratory model and a constructed seven-meter-high model subjected to earthquake loads in FLAC software. This study aims to contribute to understanding seismic behavior through the comparison and evaluation of constructed numerical frameworks against laboratory cases, emphasizing novel insights into the reaction of stabilized soil walls under seismic states.

## NUMERICAL PATTERN

In this study, the impactiveness of the FLAC software's execution is evaluated by comparing outcomes derived from a numerical pattern generated through this software with those obtained from an analogous model subjected to laboratory experimentation. To validate the precision of the FLAC software under seismic states, a series of shake table experiments carried out by Bathurst and his associates at the Royal Military College (RMC) in Canada were utilized. These tests were conducted using a one-meter-scale design of a stabilized soil geosynthetic wall with a continuous facade, based on the structure proposed by lai (1989). To faithfully replicate states resembling real-world scenarios, meticulous attention was given to factors such as the wall's physical dimensions, soil characteristics, and stiffness of the geosynthetic reinforcement. A visual representation of this wall's geometry on the shake table is depicted in Figure 1.

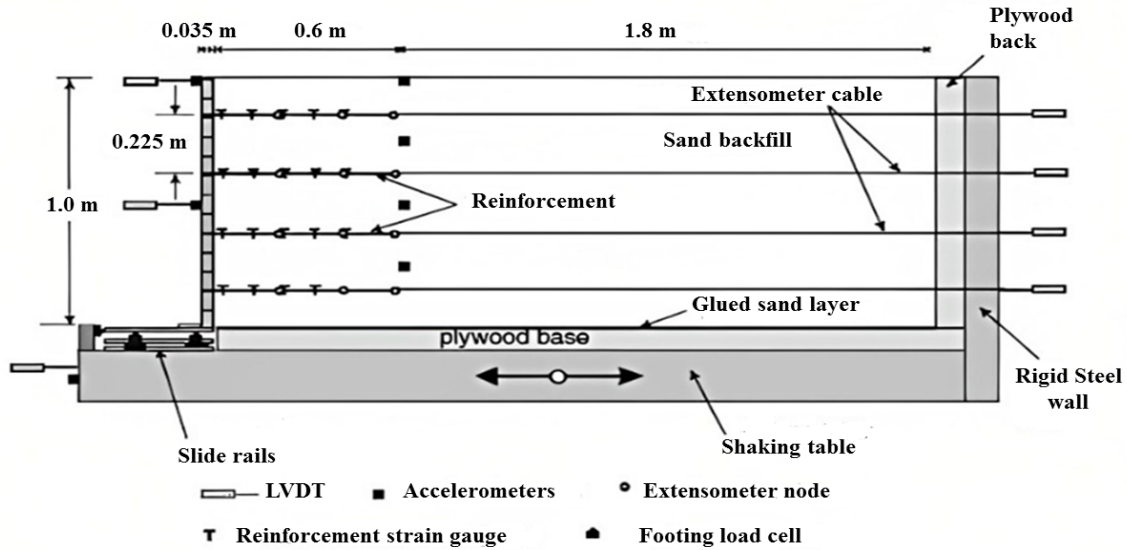


Fig.1- Wall-mounted tool model on a shaky table

A 5 Hz frequency wave with a constant amplitude every 5 seconds has been used to shake the wall to demonstrate it, as displayed in Figure 2

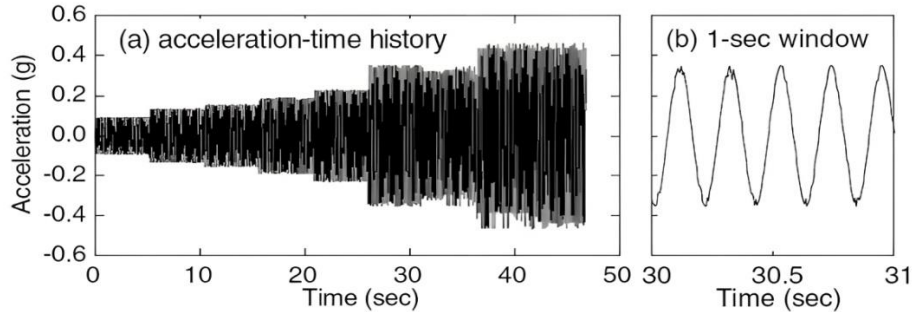


Fig. 2 - The base acceleration is used in the shaky table model.

Figure 3 depicts the finite difference model generated through FLAC, representing the RMC vibration table. The wall was composed of soil with a specific weight of 15.7 KN/m<sup>3</sup>, an inner friction angle of 46 degrees, a bulk modulus (K) of 6 MPa, and a shear modulus (G) of 7 MPa. For wall strengthening, a geogrid with a tensile strength (Tu) of 13 MPa, flexural strength (Tf) of 6.5 MPa, and an elasticity modulus (E) of 45 MPa was utilized. The behavioral model applied to both the strengthened soil and retained soil adheres to the principles of Mohr-Coulomb.

To ensure proper meshing of the model and alignment of existing zones with wave propagation states, equations from the Coulomb-Lee model were employed.

$$C_s = \sqrt{\frac{G}{\rho}} = 104 \quad \Delta l \leq \frac{C_s}{10f} = 2.1 \quad (1)$$

In Equation 1, Cs represents the shear wave velocity, G is the shear modulus, ρ denotes the density of the material, and f stands for the natural frequency of the soil layer. The modeling process imposes a maximum zone size limit of 2.1 meters. Therefore, constructing the model requires a mesh size smaller than this threshold. To ensure the accuracy of the results, mesh sizes of 0.1, 0.5,

and 1 meter were evaluated. The analysis runtime for a 0.1-meter mesh size exceeded 24 hours, which is the upper time limit. Similar outcomes were observed for the 0.5 and 1-meter mesh sizes.

Consequently, due to the impractical duration required for a 0.5-meter mesh model, a 1-meter mesh size was adopted for the intended model. The base soil and wall frontage were modeled with elastic frameworks. Cable elements were used to represent the reinforcements, while the interactions among the base and retaining soil, the frontage and retaining soil, and the retaining soil and interface element were simulated. An interface element was included to simulate the wall's foundation, enabling sliding states, simultaneous rotation, and displacement by assigning an internal friction angle of zero. The input wave used in FLAC is visualized in Figure 3.

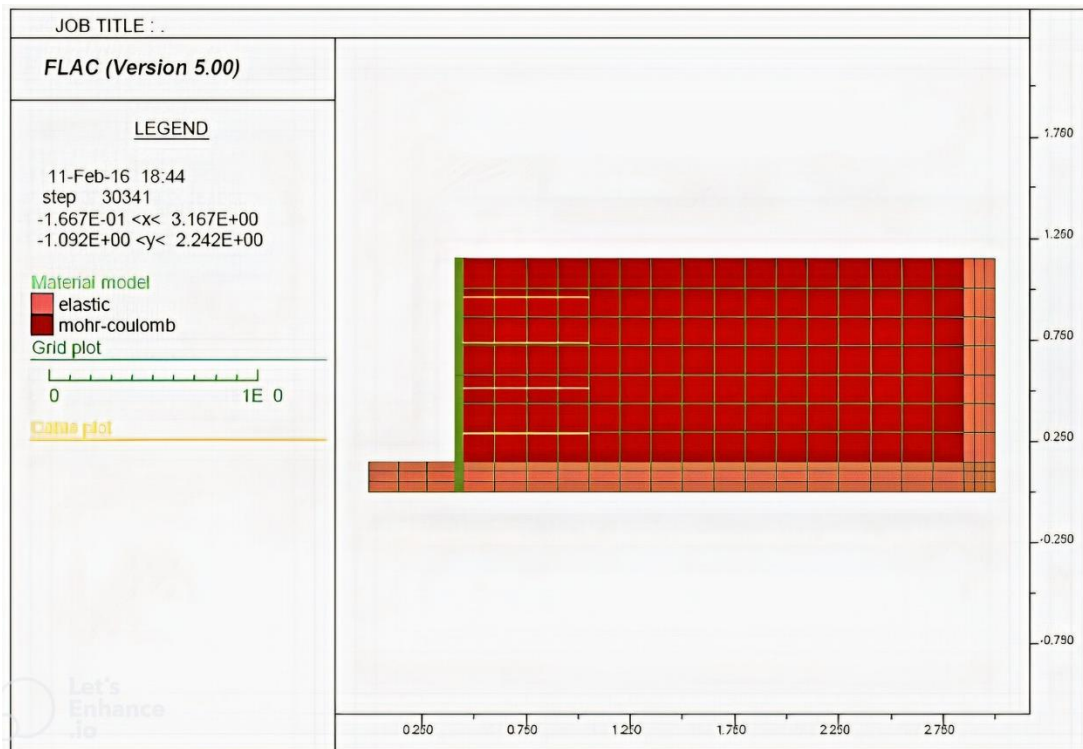


Fig. 3 - The finite difference mesh of the vibration table model

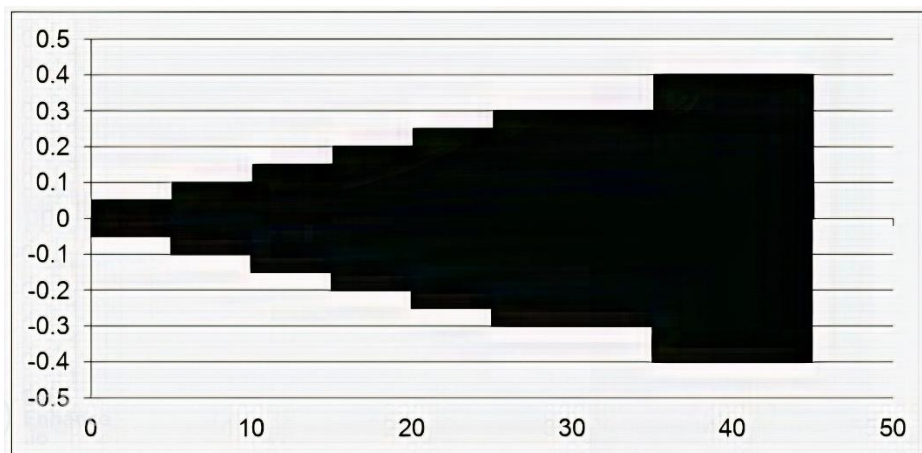


Fig. 4 - The base acceleration is used in the FLAC model.

In Figure 4, the term "base acceleration" refers to the fundamental level of acceleration integrated into the FLAC model. This essential parameter plays a crucial role in governing the

model's response and behavior during simulations. It serves as a foundational input that impacts various aspects of the model's dynamics and outcomes. By defining the base acceleration, the model can precisely simulate and analyze how structures or materials respond under diverse seismic states or loading scenarios. This ensures accuracy in predicting and comprehending the execution and stability of engineered systems under seismic forces.

Figure 5 displays that the FLAC outcomes demonstrate relatively good consistency with the measured parameters. As depicted in the figure, significant values are observed following a horizontal shift of the facade. The base acceleration utilized was 0.3 g.

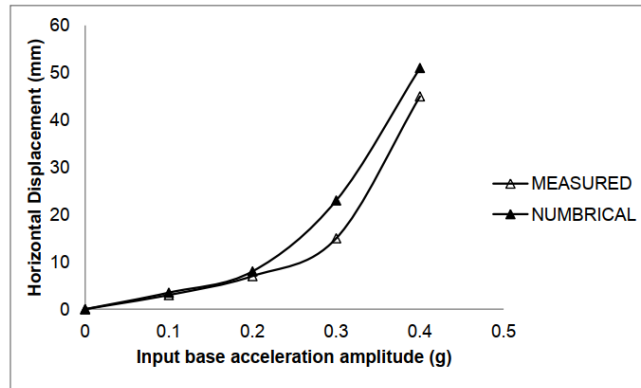


Fig. 5 - Estimated and quantified horizontal shift of the top of the wall against input acceleration.

Tab. 1 - Summary of the parameters

Parameter	Value/Description
Seismic Acceleration	0.3 g
Soil Properties	
Friction Angle ( $\phi$ )	34 °, 39 °, 44 °, 49°
Elastic Modulus (E)	20, 35, 50, 60 MPa
Poisson's Ratio (PR)	0.25, 0.3, 0.65
Reinforcement Properties	Geogrid

In this study, the following parameters were analyzed to evaluate the seismic behavior of geogrid-strengthened soil walls: The friction angle ( $\phi$ ) values were set at 34°, 39°, 44°, and 49° to explore the impact of soil shear strength on the wall's execution. The elastic modulus (E) values were varied at 20, 35, 50, and 60 MPa to assess how changes in soil stiffness influence the deformations and forces within the wall structure. Additionally, Poisson's ratio (PR) was considered at values of 0.25, 0.3, and 0.65 to understand its impact on the soil behavior under seismic loading. These parameters were systematically varied to comprehensively understand their effects on horizontal and vertical deformations, the lateral pressure exerted on the wall, and the peak pulling forces endured by the geogrid strengthening. The study aimed to offer robust insights into optimizing the structure and execution of geogrid-strengthened soil walls under seismic states by incorporating a range of values for these critical parameters.

## OUTCOMES AND DISCUSSION

Boundary States and Model Loading Under Seismic States: In this scenario, a sole horizontal seismic loading element is employed to the lowermost points of the model. This acceleration is

introduced when the system reaches a state of static equilibrium, with all point displacements held at zero (Sadighi et al., 2022). Consequently, the displacements witnessed during the seismic analysis are exclusively attributed to the impact of seismic loads. It's crucial to acknowledge that forces derived from combined static and seismic analyses deviate from those originating solely from static analysis. This deviation arises due to the persistence of forces, despite setting displacements to zero. Figure 6 depicts the 0.3 g acceleration utilized in the context of the discussed wall model.

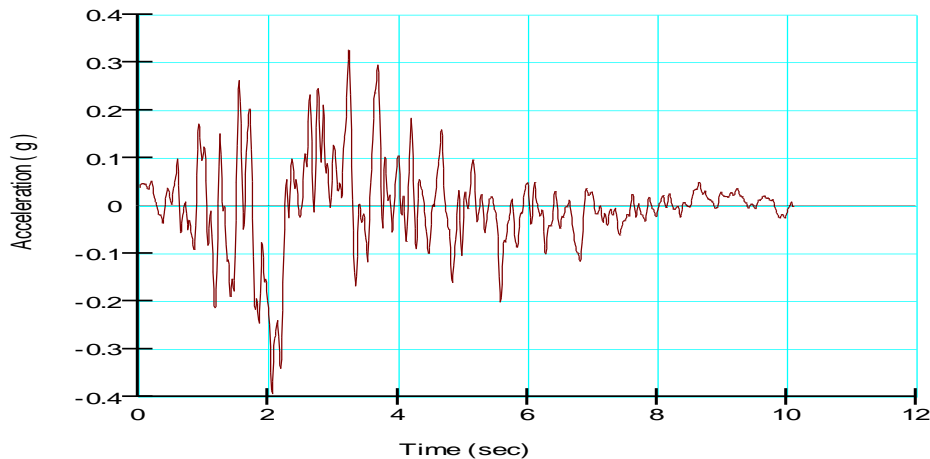


*Fig. 6 - The input wave in the seismic analysis of the numerical pattern for the strengthened soil wall*

### **Parametric Study on Strengthened soil Wall under Seismic States**

Subjecting the strengthened soil wall to seismic loading aims to investigate factors influencing its stability and the extent of its deformations. As part of this study, modifications have been implemented in the properties of the strengthened soil to assess their impact on the structure's behavior.

Findings with Fundamental Soil Properties: This segment centers on the strengthened soil wall with basic soil attributes— $C=0$ ,  $\nu=0.3$ ,  $E=35$  MPa, and  $\phi=34$ . The wall is exposed to a maximum speed gain of 0.3 g, and its conduct is observed under static and seismic scenarios.

#### **A) Peak Pulling force of Reinforcements:**

Figure 7 portrays alterations in the highest pulling force of reinforcements under static and seismic states, along with the total force. From the visual representation, it can be deduced that heightened pulling force within reinforcements primarily transpires in the lower portion of the wall, particularly at its base. This trend can be attributed to the augmented seismic loading, which significantly influences the reaction of the lower segment of the wall.

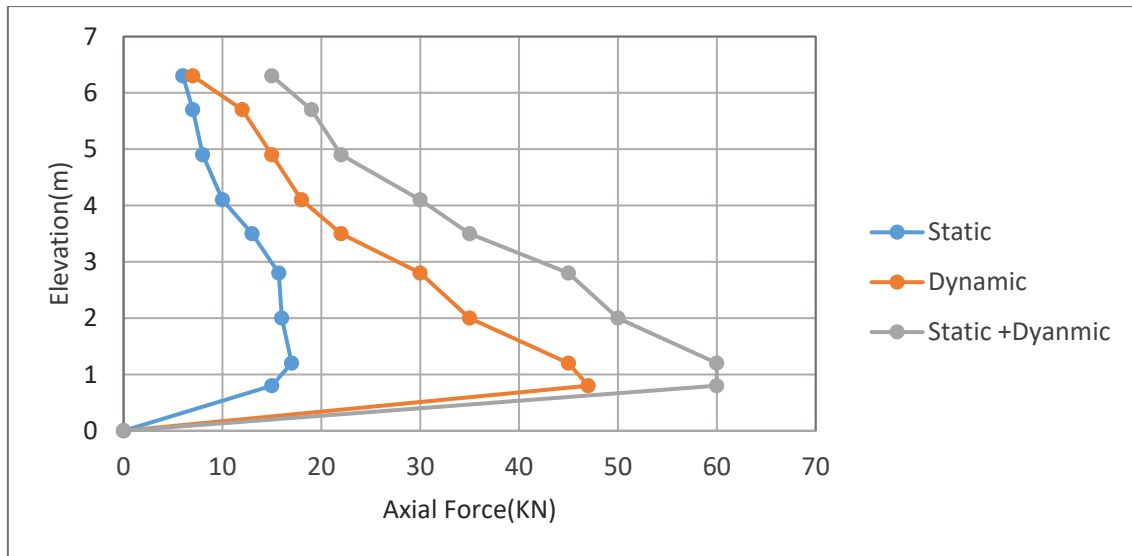


Fig. 7 - The highest pulling force of reinforcements with basic soil properties under static and seismic states at the end of the 0.3 g base acceleration

**B) Horizontal Pressure on the Rear of the Wall:**

Figure 8 illustrates the alterations in the horizontal pressure exerted on the rear side, considering basic soil characteristics under both static and seismic states. Notably, in seismic states, the horizontal pressure on the wall's rear side undergoes a more substantial augmentation in the lower half compared to the upper portion. This observation highlights that the impact of seismic loading is more pronounced in the lower segment of the wall. This phenomenon can be assigned to the increased weight and subsequent rise in lateral pressure at greater depths, particularly in seismic scenarios.

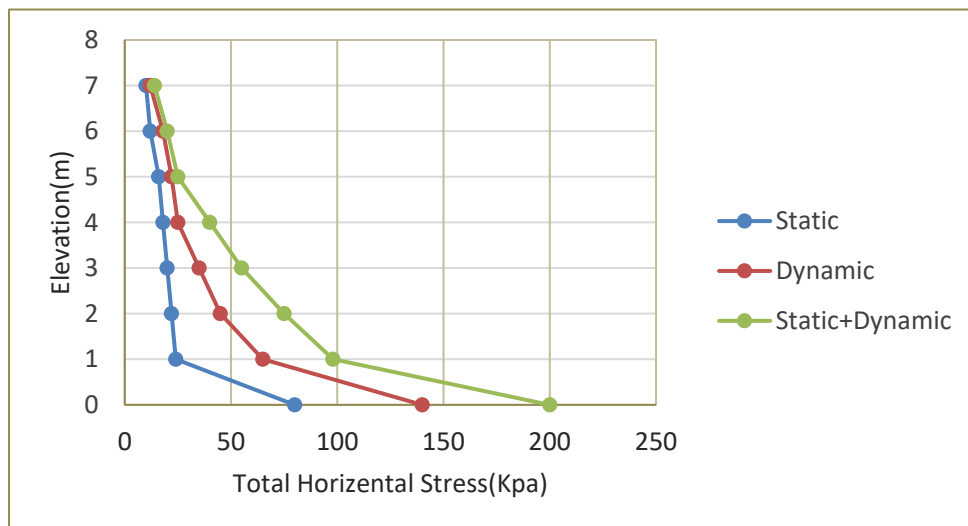


Fig. 8 - Horizontal pressure on the rear of the wall with basic soil properties under static and at the end of the 0.3 g base acceleration

**C) Horizontal shift of the Wall:**

Figure 9 presents the horizontal shifts of the wall relative to its height under static and seismic states. Evidently, the magnitude of horizontal shifts is amplified fourfold under seismic states in

comparison to static states. This stark contrast underscores the substantial impact of seismic activity on the wall's behavior.

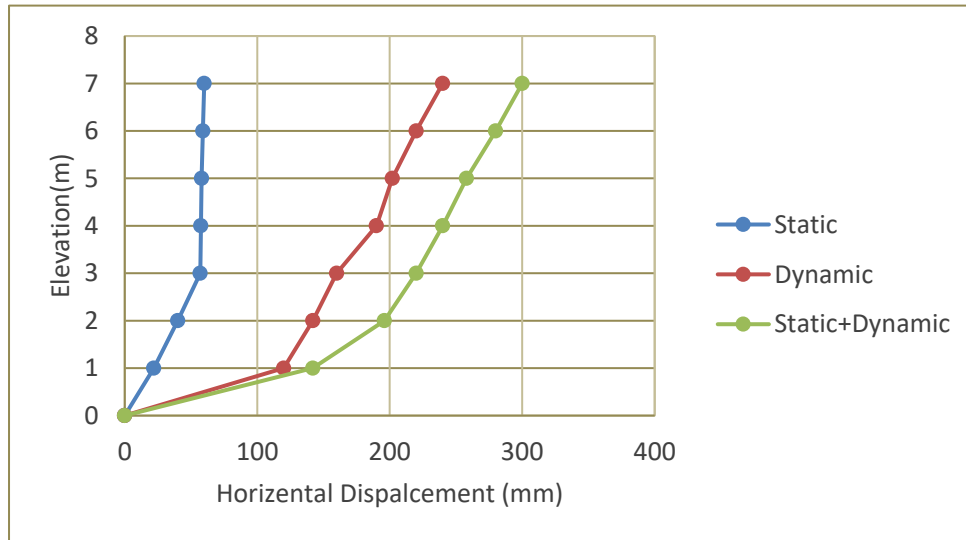


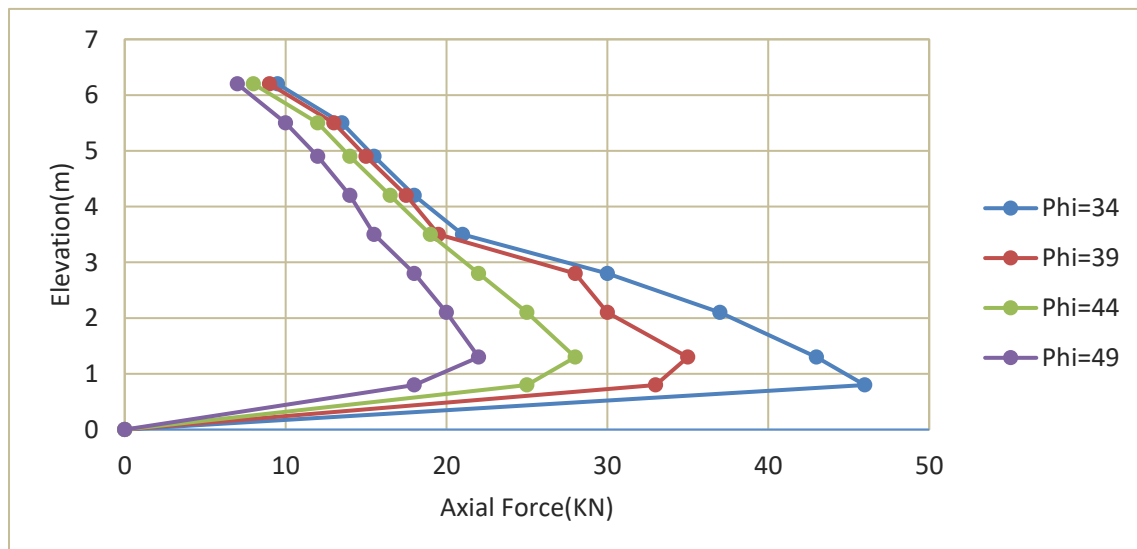
Fig. 9 - Horizontal shifts of the wall with basic soil properties under static and at the end of the 0.3 g base acceleration

### The impact of the Internal Friction Angle of Strengthened soil on the Response of the Structure

Within this segment, the structure's response is explored across various internal friction angle values of the strengthened soil. Throughout all analyses, cohesion is presumed to be absent, and a maximum acceleration of 0.3 g is employed to the system.

#### A) Peak Pulling force of Reinforcements:

Figure 10 portrays the impact of the internal friction angle on the peak pulling force experienced by the reinforcements. Notably, as it escalates, the highest pulling force of the reinforcements diminishes, particularly in the lower section of the wall. With escalating  $\phi$  values, the curves within Figure 10 converge, indicating a trend toward similarity.



**B) Horizontal Pressure on the Wall's Rear Surface**

Figure 11 illustrates the shifts in horizontal pressure on the wall's rear surface. The pressure diminishes as the internal friction angle of the strengthened soil rises. This decrease is especially prominent in the wall's lower half. With increasing height, the magnitude of this reduction wanes, eventually stabilizing at around 1 kPa in the upper portion of the wall. It's noteworthy that the spacing between the curves remains uniform as the  $\phi$  value increases.

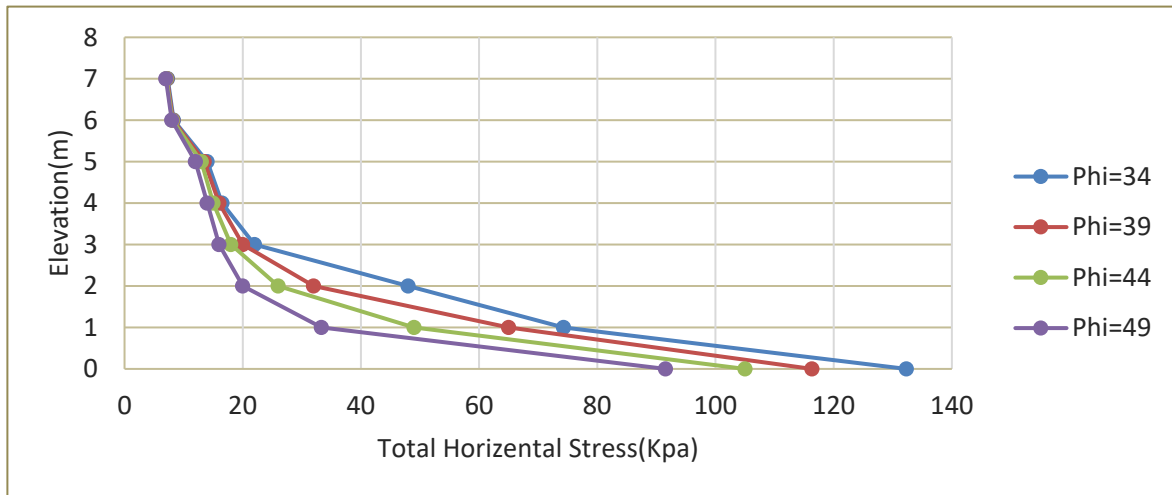


Fig. 11 - The impact of the internal friction angle of the strengthened soil on the horizontal pressure exerted on the rear of the wall at the conclusion of the 0.3 g base input acceleration

**C) Horizontal shift of the Wall:**

Figure 12 displays the trend of horizontal shifts with increasing internal friction angle. As observed, increasing  $\phi$  leads to a reduction in the magnitude of horizontal shifts of the wall. The distance between the curves becomes less than the other curves for  $\phi \geq 39^\circ$ .

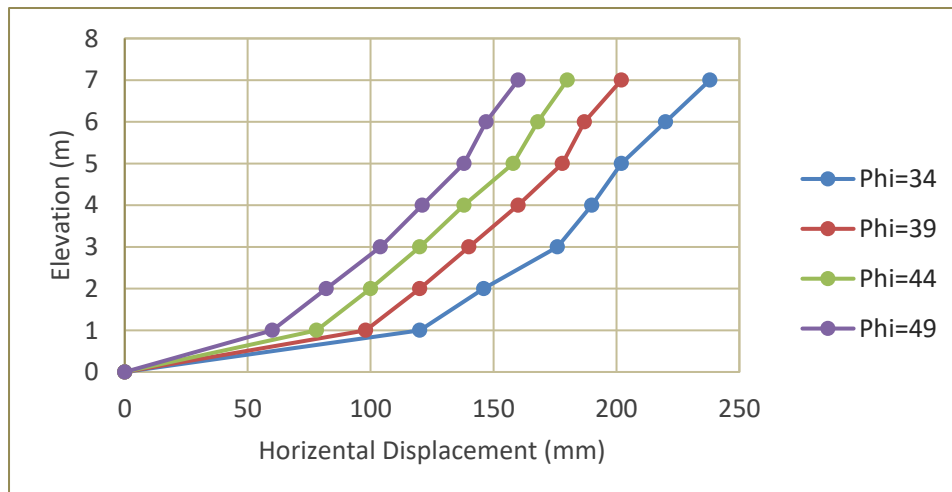


Fig. 12 - Effect of the internal friction angle of the strengthened soil on the horizontal shift of the wall at the end of the 0.3 g base input acceleration

**D) Vertical shift of the Top and Bottom of the Wall:**

Figure 13 displays that increasing the internal friction angle results in a reduction in the vertical shifts of the top and bottom of the wall.

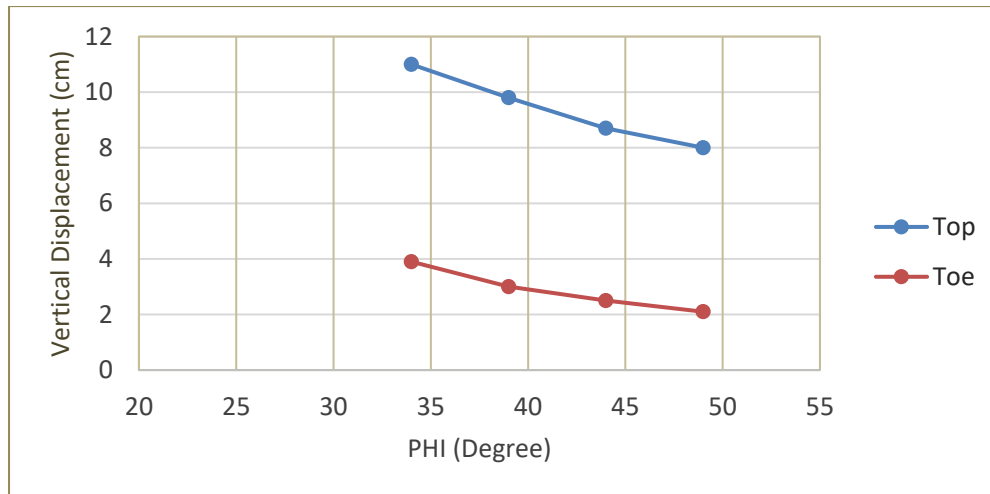


Fig. 13 - Effect of the internal friction angle of the strengthened soil on the vertical shifts of the top and bottom of the wall at the end of the 0.3 g base input acceleration

### The impact of the Elastic Modulus of the Strengthened soil on the Reaction of the Structure

In this section, the structural behavior is assessed through the manipulation of the strengthened soil's elastic modulus, ranging from 20 to 60 kPa. The repercussions of this variability are explored. It's important to highlight that across all analyses, the internal friction angle and cohesion remain constant at 34 and 0 degrees, respectively. Furthermore, a uniform maximum acceleration of 0.3 g is incorporated in all scenarios.

#### A) Peak Pulling force of Reinforcements:

Figure 14 visualizes the alteration in the peak pulling force endured by the reinforcements concerning height, considering diverse elastic modulus values for the strengthened soil (ES). Notably, these curves demonstrate that when the elastic modulus of the strengthened soil (ES) surpasses 35 MPa, the highest pulling force within the reinforcements stabilizes at a constant value, signifying the absence of further fluctuations.

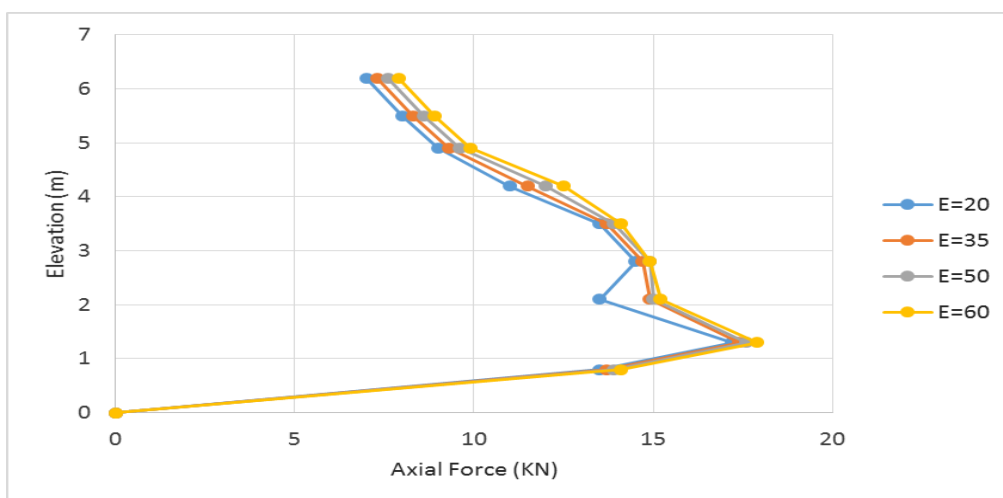


Fig. 14 - Effect of the elastic modulus of the strengthened soil on the highest pulling force of reinforcements at the end of the 0.3 g base input acceleration

**B) Horizontal Pressure on the Rear of the Wall:**

The changes in horizontal pressure on the wall's rear surface, corresponding to the rising elastic modulus of the strengthened soil, are illustrated in Fig. 15. When the elastic modulus (ES) elevates from 20 to 35 MPa, a decline in the horizontal pressure on the wall's rear side becomes evident. The bottom point of the wall manifests the most substantial reduction, amounting to 11.6 kPa. However, for ES values equal to or exceeding 35 MPa, notable shifts in horizontal pressure on the wall's rear surface are not discernible.

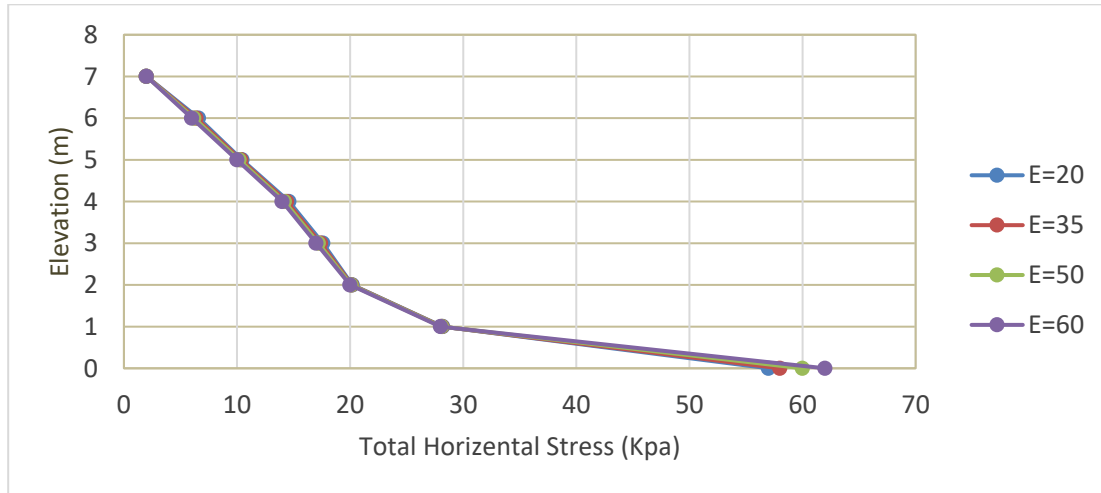


Fig. 15 - Effect of the elastic modulus of the strengthened soil on the horizontal pressure on the rear of the wall at the end of the 0.3 g base input acceleration

**C) Horizontal shift of the Wall:**

Figure 16 displays the variation of horizontal shifts of the wall with height for diverse values of the elastic modulus of the strengthened soil. With growing ES from 20 to 35 MPa, a sudden change occurs in the magnitude of horizontal shifts. Moreover, for  $ES \geq 35$  MPa, the distance between the curves becomes smaller, and for  $ES \geq 50$  MPa, the reduction in horizontal shifts is limited to a maximum of 11 mm.

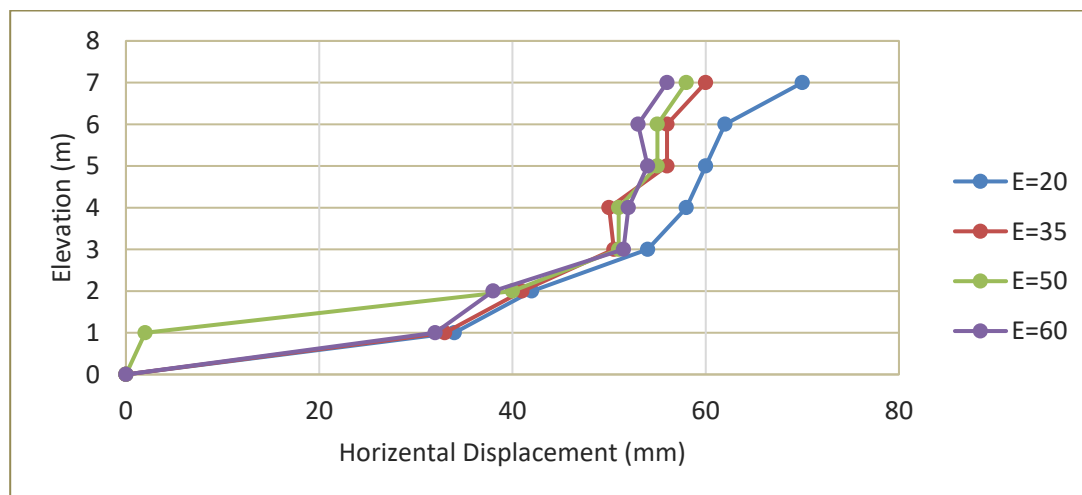


Fig. 16 - Effect of the elastic modulus of the strengthened soil on the horizontal shift of the wall at the end of the 0.3 g base input acceleration

**D) Vertical shift of the Top and Bottom of the Wall:**

Figure 17 presents the vertical shifts at both the top and bottom sections of the wall across diverse elastic modulus values. Elevating the elastic modulus of the strengthened soil results in reduced vertical shift at the wall's top. The maximum value observed is 9 mm for ES values greater than or equal to 35 MPa. Simultaneously, the vertical shift at the wall's bottom remains constrained within a maximum of 11.8 mm for elastic modulus values ranging from 20 to 35 MPa. Negligible changes are discernible for ES values exceeding 35 MPa. In summation, an upsurge in the elastic modulus of the strengthened soil has minimal impact on the vertical shifts at both the top and bottom of the wall.

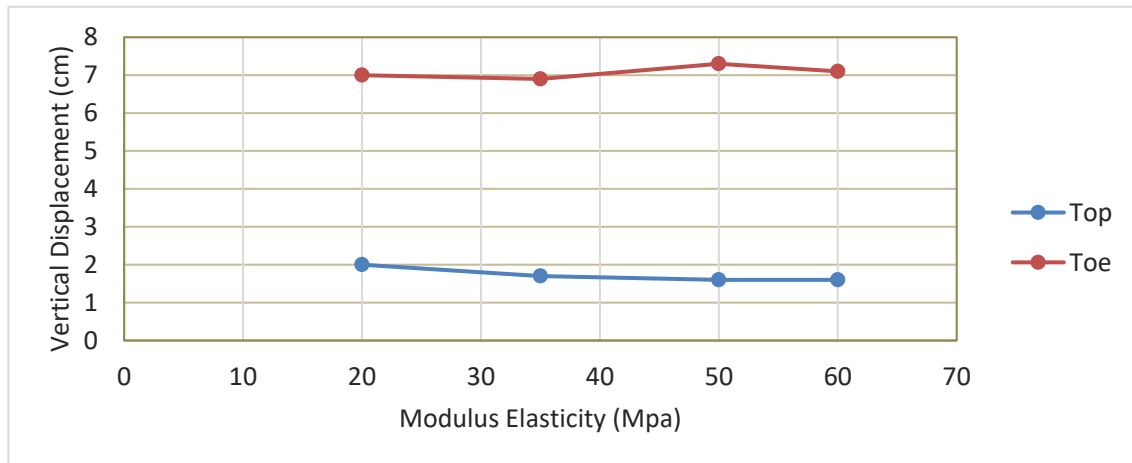


Fig. 17 - Effect of the elastic modulus of the strengthened soil on the vertical shifts of the top and bottom of the wall at the end of the 0.3 g base input acceleration

**The impact of the Poisson's Ratio on the Strengthened soil**

This section explores the impact of Poisson's ratio of the strengthened soil on the reaction of the strengthened soil structure.

**A) Highest pulling Force of Reinforcements:**

Figure 18 displays the fluctuation of the highest pulling force of reinforcements with height for diverse values of Poisson's ratio of the strengthened soil (PR). These curves indicate that the alteration in the value of Poisson's ratio has no significant impact on the increase or decrease in the highest pulling force of the reinforcements.

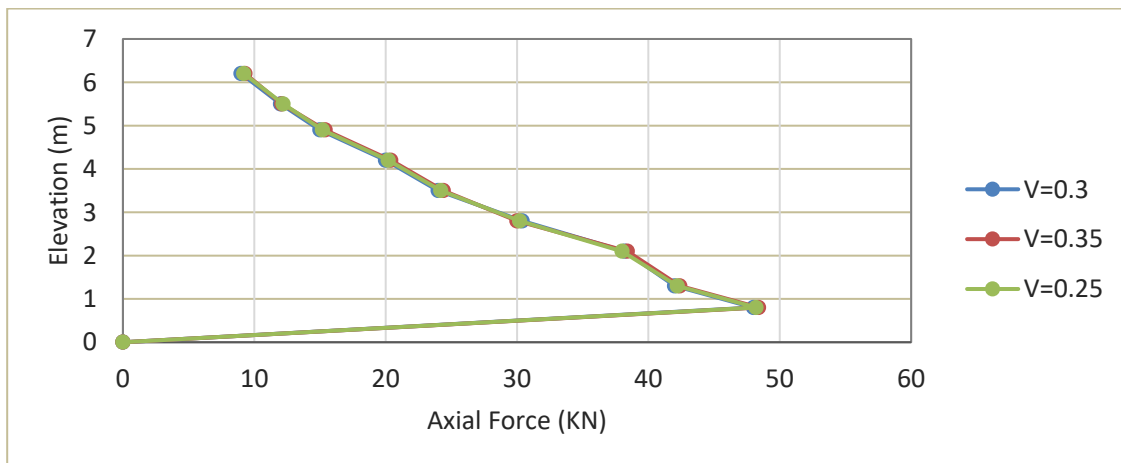


Fig. 18 - Effect of the Poisson's ratio of the strengthened soil on the highest pulling force of reinforcements at the end of the 0.3 g base input acceleration

**B) Horizontal Pressure on the Rear of the Wall:**

Figure 19 illustrates the impact of the change in Poisson's ratio on the horizontal pressure on the rear of the wall. As displayed in the figure, the change in Poisson's ratio has no crucial impact on the pressure.

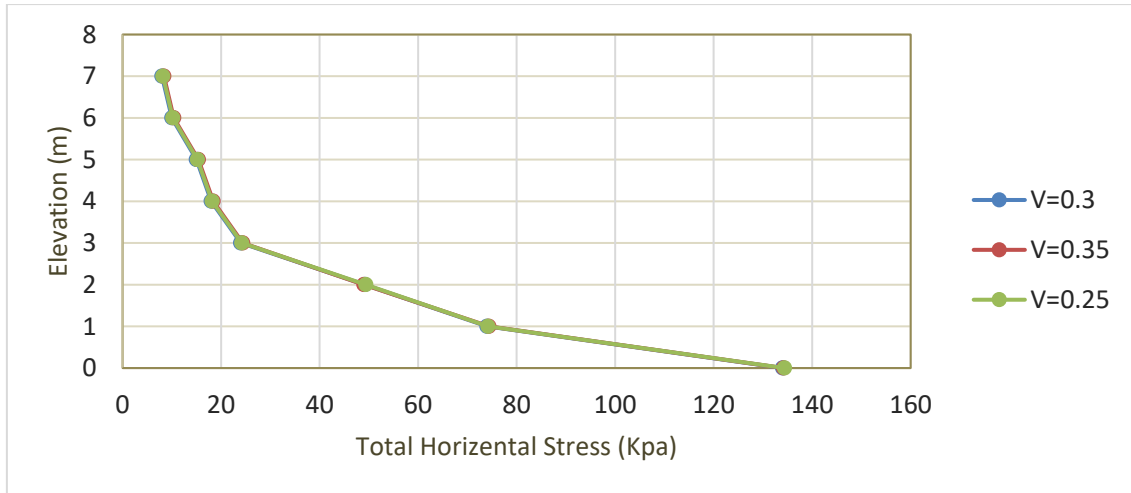


Fig. 19 - Effect of the Poisson's ratio of the strengthened soil on the horizontal pressure on the rear of the wall at the end of the 0.3 g base input acceleration

**C) Horizontal Shift of the Wall:**

Figure 20 displays the variation of horizontal shifts of the wall with height for diverse values of Poisson's ratio of the strengthened soil. Increasing the elastic modulus of the strengthened soil results in a slight escalation in the horizontal shifts, with the maximum escalation limited to 2.7 mm at a height of 7 meters of the wall.

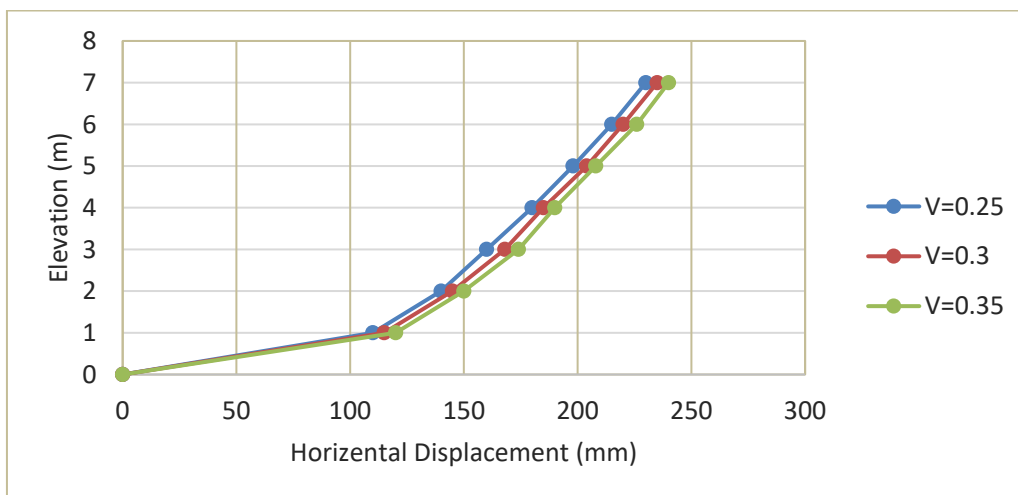


Fig. 20 - Effect of the Poisson's ratio of the strengthened soil on the horizontal shift of the wall at the end of the 0.3 g base input acceleration

**D) Vertical Shift of the Top and Bottom of the Wall:**

Figure 21 displays the vertical shift curves for diverse values of Poisson's ratio of the strengthened soil. The change in Poisson's ratio has no crucial impact on the vertical shifts of the top and bottom of the wall.

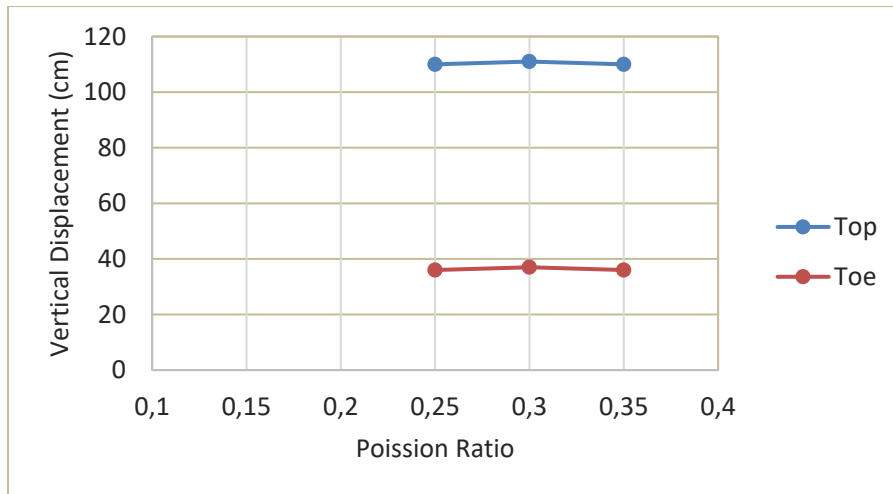


Fig. 21 - Effect of the Poisson's ratio of the strengthened soil on the vertical shifts of the top and bottom of the wall at the end of the 0.3 g base input acceleration

## CONCLUSION

This research explores the seismic reaction of geogrid-strengthened soil walls through a comprehensive study of various influencing factors. The study focuses on assessing the impacts of parameters including adhesion, internal friction angle, elastic modulus, and Poisson's ratio on the execution of these structures under seismic loading states. By analyzing vertical and horizontal shifts, maximum pulling forces in reinforcing bars, and horizontal pressure on the wall's rear surface, this study provides insights into optimizing the structure and execution of geogrid-strengthened soil walls for seismic resilience.

- Seismic loading predominantly affects the lower half of the wall, necessitating stronger reinforcing bars in this section and leading to a significant increase in horizontal deformation compared to static states.
- Increasing adhesion values up to  $c = 10$  kp effectively mitigate maximum pulling forces and horizontal pressure on the wall's rear surface. Beyond  $c = 40$  kp, maximum pulling forces across reinforcing bars stabilize at various heights.
- Higher adhesion values ( $c \geq 20$  kp) consistently reduce horizontal deformation, suggesting a minimum adhesion requirement for controlling seismic-induced deformations.
- Elevating the internal friction angle ( $\phi \geq 39^\circ$ ) reduces maximum pulling forces in reinforcing bars, horizontal pressure on the wall, and horizontal deformation, contributing to optimal deformation control.
- Changes in elastic modulus ( $E \geq 35$  MPa) have minimal impact on maximum pulling forces but significantly reduce horizontal deformation, making soil with  $E \geq 35$  MPa advisable for horizontal deformation control.
- Alterations in Poisson's ratio do not significantly influence the studied parameters—maximum pulling forces in reinforcing bars, horizontal pressure on the wall, and horizontal and vertical deformations.

## REFERENCES

- [1]. Bao Y, Hu H, Gan G (2023) Seismic response analysis of slope reinforced by pile-anchor structures under near-fault pulse-like ground motions. *Soil Dynamics and Earthquake Engineering* 164:107576
- [2]. Nunes GB, Portelinha FHM, Futai MM, Yoo C (2022) Numerical study of the impact of climate conditions on stability of geocomposite and geogrid reinforced soil walls. *Geotextiles and Geomembranes* 50:807–824

- [3]. Yang K-H, Wu H-M, Tseng T-L, Yoo C (2023) Model tests of geosynthetic-reinforced soil walls with marginal backfill subjected to rainfall. *Geotextiles and Geomembranes* 51:342–359
- [4]. Xu P, Hatami K, Jiang G (2020) Study on seismic stability and performance of reinforced soil walls using shaking table tests. *Geotextiles and Geomembranes* 48:82–97
- [5]. Huang C-C (2019) Seismic responses of vertical-faced wrap-around reinforced soil walls. *Geosynth Int* 26:146–163
- [6]. Bathurst RJ, Hatami K (1998) Seismic response analysis of a geosynthetic-reinforced soil retaining wall. *Geosynth Int* 5:127–166
- [7]. Geng M (2021) A short review on the dynamic characteristics of geogrid-reinforced soil retaining walls under cyclic loading. *Advances in Materials Science and Engineering* 2021:1–10
- [8]. Changizi F, Razmkhah A, Ghasemzadeh H, Amelsakhi M (2022) Behavior of geocell-reinforced soil abutment wall: A physical modeling. *Journal of Materials in Civil Engineering* 34:04021495
- [9]. Holtz RD (2017) 46th Terzaghi lecture: geosynthetic reinforced soil: from the experimental to the familiar. *Journal of Geotechnical and Geoenvironmental Engineering* 143:03117001
- [10]. Leshchinsky D, Han J (2004) Geosynthetic reinforced multitiered walls. *Journal of Geotechnical and Geoenvironmental Engineering* 130:1225–1235
- [11]. Segrestin P, Bastick MJ (1988) Seismic design of reinforced earth retaining walls-the contribution of finiteelements analysis. In: *International geotechnical symposium on theory and practice of earth reinforcement*. pp 577–582
- [12]. Zhang, R., Jiang, Y., & Zhang, Z. (2020). Numerical modeling of seismic behavior of reinforced soil walls considering soil-structure interaction. *Soil Dynamics and Earthquake Engineering*, 139, 106347.
- [13]. Ling, H. I., & Leshchinsky, D. (2023). Contributions of physical modeling and numerical analysis to seismic behavior of reinforced soil retaining structures. In *Smart Geotechnics for Smart Societies* (pp. 72-91). CRC Press.
- [14]. Ren, F., Huang, Q., Zhang, F., & Wang, G. (2024). Numerical study on seismic performance of tiered reinforced soil retaining walls. *Soil Dynamics and Earthquake Engineering*, 181, 108672.
- [15]. Majumder, M., Venkatraman, S., Bheda, M., & Patil, M. (2023). Numerical Studies on the Performance of Geosynthetic Reinforced Soil Walls Filled with Marginal Soil. *Indian Geotechnical Journal*, 53(4), 805-826.
- [16]. Javdanian H, Goudarzi N (2023) Seismic Analysis of Geogrid-Reinforced Soil Retaining Walls Under Decomposed Earthquake Records. *Iranian Journal of Science and Technology, Transactions of Civil Engineering* 1–13
- [17]. Zhou L, Ding G (2021) Seismic response of reinforced retaining walls with saturated calcareous sand backfill subjected to acid rain erosion. *Journal of Materials in Civil Engineering* 33:06021005
- [18]. Fairless GJ (1989) Seismic performance of reinforced earth walls
- [19]. Murali Krishna A, Madhavi Latha G (2009) Seismic behaviour of rigid-faced reinforced soil retaining wall models: reinforcement effect. *Geosynth Int* 16:364–373
- [20]. Safaee AM, Mahboubi A, Noorzad A (2023) Seismic behavior of tiered geogrid reinforced soil (GRS) using treated backfill soil. *Geosynth Int* 30:200–224
- [21]. Qian Y (2023) Maximum dry unit weight and optimum moisture content prediction of lateritic soils using regression analysis. *Advances in Engineering and Intelligence Systems* 2:
- [22]. Sadighi, H., Badiei, E., & Eslami Haghghat, A. (2022). Rational selection of pseudostatic seismic coefficient of slopes. *Iranian Journal of Science and Technology, Transactions of Civil Engineering*, 46(6), 4529-4541.

# APPLICATION OF MAST CLIMBING WORK PLATFORM(MCWP) IN FAÇADE RENOVATION OF HIGH-RISE BUILDINGS:A CASE STUDY

*Yin Ni<sup>1,2</sup>, Yuchao Zhang<sup>1,3</sup> and Pengbo Li<sup>1</sup>*

1. *Shanghai Pudong New Area Construction (Group) Co. Ltd, Shanghai, China*
2. *College of Civil Engineering, Tongji University, Shanghai, China*
3. *Department of Civil Engineering, Shanghai University, Shanghai, China, 13501973162@163.com*

## ABSTRACT

This paper introduces a typical mast climbing work platform (MCWP) as a novel construction machinery designed for facade renovation in high-rise buildings. The application of the MCWP is illustrated through a real-world facade renovation project, which utilizes a combination of linear and L-shaped MCWPs. Additionally, this study establishes a finite element method (FEM) model of the linear and L-shaped MCWPs and presents the obtained results. The findings indicate that the serviceability of both linear and L-shaped MCWPs meets the required standards. Furthermore, compared to a suspended basket method based on time duration and cost, the MCWP approach for facade repair demonstrates significantly higher construction efficiency and cost reduction.

## KEYWORDS

Facade Renovation, High-rise Building, Mast Climbing Work Platform, Construction Technology, Construction Machinery, Cost analysis

## INTRODUCTION

Currently, urban renewal projects, which involve maintenance and repair of building facades, are rapidly gaining momentum across the world [1-7]. Traditional facade renovation methods primarily rely on scaffolding and suspended baskets. However, these approaches present higher safety risks, longer setup times, and lower construction efficiency, making them unable to fully cater to the ever-increasing demand for safer and more efficient practices [8]. In response to the limitations of traditional methods, mast climbing work platforms (MCWPs) have gained widespread adoption. An MCWP represents a novel category of construction machinery, powered by gears and racks. It features a highly reliable electrical and mechanical system, enabling it to securely elevate itself to the specific elevation of the building. Moreover, the platform where workers stand can be extended or retracted according to varying requirements. The entire structure can be easily assembled and disassembled, and the position of the platform can be effortlessly adjusted.

The process of façade renovation using MCWPs involves the following stages: construction design, installation, inspection, use, and dismantling. Among these stages, construction design is the most critical. When addressing buildings with numerous concave and convex corners during the construction design phase, a combination of linear and L-shaped MCWPs is recommended. Although numerous standards and publications offer guidelines for the safe use of MCWPs [9-14], they predominantly concentrate on linear-type MCWPs. For example, Wimer et al. [13] examined the effects of fall-arrest systems on MCWP

stability; however, their findings are limited to single-column MCWPs and cannot be directly extrapolated to L-shaped twin-column MCWPs. Consequently, this restricts their widespread adoption in engineering practice. Nonetheless, considering that construction hoists and tower cranes are also attachment-type construction machinery, their stability analysis methods undoubtedly offer valuable insights for the research in this paper.

Numerical simulation has emerged as a widely adopted method to investigate the mechanical behavior of construction machinery [15-22]. For example, Zheng et al. [16] Calculated the stability of construction building hoist. Cheng et al. [18] assessed the safety and stability of tower cranes during operation. As building heights continue to rise, research on the anti-overturning capability of attachment-type machinery has become progressively more critical. In this context, the CFD (Computational Fluid Dynamics) method has been widely utilized to examine the anti-overturning capacity of attachment-type machinery, simulating the interplay between fluids and mechanical structures to offer more precise references for mechanical design and construction [20]. Simultaneously, with the advancement of test equipment, the incorporation of scaled model tests has also gained interest among scholars. For instance, Jiang et al. [21] demonstrated the stability variation patterns of tower cranes under incremental dynamic loads through a combination of numerical simulation and scaled model testing. Kenan et al. [22] similarly investigated the mechanical behavior of tower crane masts through scaled testing. In summary, the primary methods for investigating the stability of attachment-type machinery include numerical simulation, scaled model tests, and probability analysis based on data. Among these, numerical simulation is the most frequently employed method due to its efficiency and convenience. Nonetheless, scaled model tests entail higher experimental costs. In comparison to tower cranes and construction hoists, MCWPs are subjected to less complex external loads, which simplifies their stability research. Therefore, this article primarily utilizes numerical simulation to investigate the overall mechanical behavior of L-shaped MCWPs during the construction design stage.

After the dismantling step, in comparison to analogous repair methodologies (such as hanging basket and scaffolding), the cost-effectiveness of the MCWP approach remains to be substantiated. Nevertheless, given their efficiency and convenience, the potential applications of MCWPs in the repair sector merit further investigation and scholarly inquiry. As a result, this manuscript delineates the comprehensive process of employing linear and L-shaped MCWPs in a building renovation project, providing valuable insights and serving as a reference for analogous cases.

## PROJECT OVERVIEW

Due to the deterioration and detachment of the external facades, two high-rise buildings in the 5th Shang Gang residential community necessitated renovation. These two buildings are located adjacent to Metro Lines 7 and 13 in Shanghai, China. As shear wall-frame structures, the structures boast a standard floor height of 2.8m, reaching an overall height of 43.2m. The renovation area extends over 100,385 m<sup>2</sup>. The basic conditions of the buildings are also illustrated in Figure 1. These two buildings are nearly identical in design. As a result, the manager decided to employ a suspended basket method for one building and an MCWP method for the other. Although the MCWP method was introduced as a new technology to the company, the manager wanted to investigate whether its adoption improves efficiency and reduces cost.

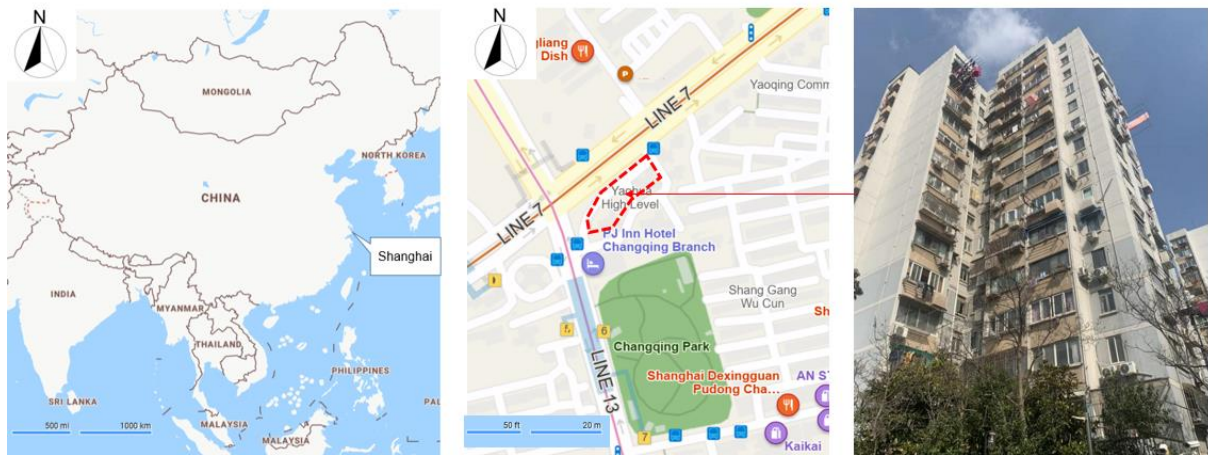


Fig. 1- Basic information about the building needed to be repaired

## CONSTRUCTION PRINCIPLE

### Components of the MCWP

The MCWP primarily comprises the following components: a base frame, columns, a working platform, a driving system, a control system, and mast tie equipment, as depicted in Figure 2. To avoid disrupting residents' communication, it's essential to predetermine the stacking location for these parts. Additionally, since the components need to be transported to the assigned site using a car crane, the load capacity of the outriggers must be considered. To alleviate stress concentration, wooden blocks should be placed beneath the outriggers. Prior to hoisting the components to the designated location, ensure that no one is in the vicinity of the car crane. Furthermore, it is crucial for the staff in charge to wear safety helmets throughout the entire operation to prevent potential safety incidents.

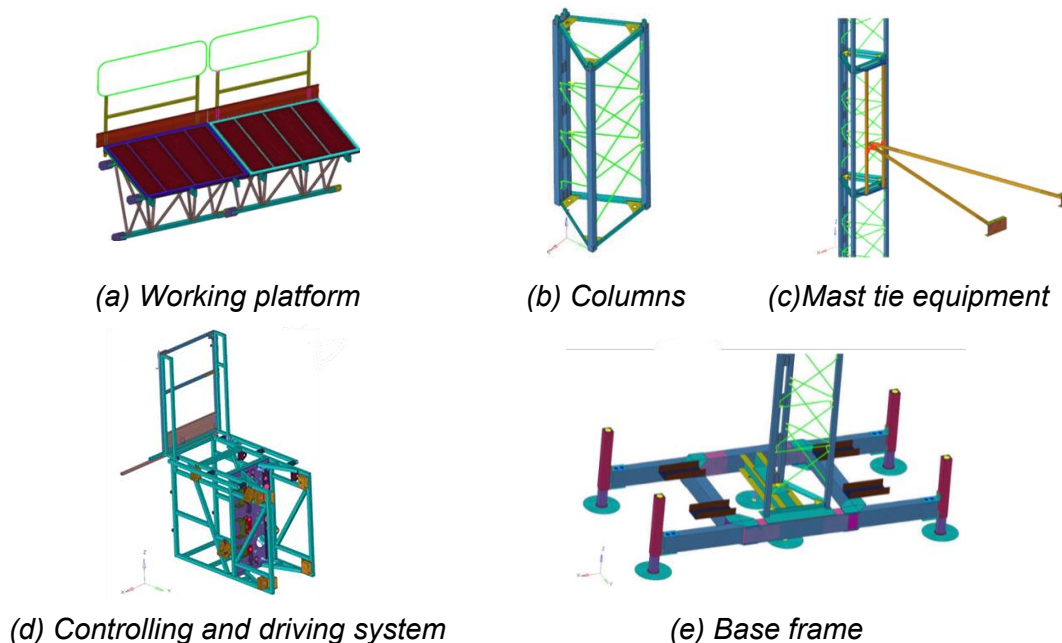


Fig. 2- Main Components of the MCWP

### Form of MCWP

MCWPs can be classified into two types based on the number of foundations: single-column and twin-column, as illustrated in Figure 3. The maximum span for single-column MCWPs is 9.8 meters, while for twin-column MCWPs, it is 27 meters. Additionally, the maximum span between adjacent columns in twin-column MCWPs is 18 meters. These specifications can be found in the specific regulations [23].

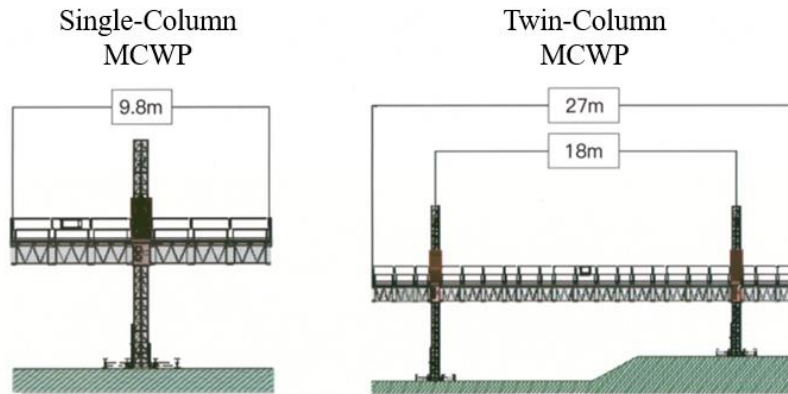


Fig. 3- Diagram of the single and twin-column WCWP

Twin-column MCWP can also be divided into linear, or L-shaped arrangements, as shown in Figure 4.



(a) Linear-type WCWP



(b) L-shaped WCWP

Fig. 4- Linear-type and L-type WCWP

### Process principle for the MCWP

Firstly, assemble the base frame, control system mast, and working platform. Subsequently, as the platform rises, connect the MCWP to the wall using the mast tie. Next, activate the motor to supply power, which propels the platform to ascend to the designated floor. Once the platform comes to a halt, workers can commence renovation tasks for the primary structure.

### OPERATION PROCESS FOR THE MCWP

#### Installation, Use, and Removal Process

As shown in Figure 5, the process of assembling and operating a WCWP undergoes



The spans for both the linear-shaped and L-shaped MCWPs are presented in Figure 7. However, these configurations have not undergone calculations, and the maximum deformations for these two types of MCWPs have not yet been determined. Consequently, it is essential to complete a structural analysis of the MCWP in advance.

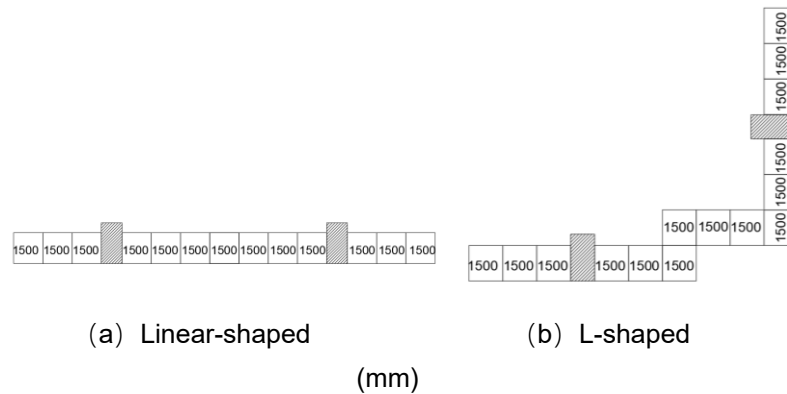


Fig. 7- Schematic diagram of double-column MCWP

Initially, SolidWorks was utilized to create a 3D model of the MCWP's components. Following this, these models were imported into the meshing software Hypermesh for discretization. Lastly, the meshed model was transferred to the large-scale finite element software Ansys for analysis. The component is crafted from Q345 steel, possessing an elastic modulus of 210 GPa and a Poisson's ratio of 0.33. Its yield strength is 345 MPa, and the ultimate tensile strength reaches 512 MPa. The calculated load was determined according to the specifications outlined in the standard [23].

Figure 8 and Figure 9 presents finite element analysis results for linear and L-shaped MCWPs, offering a comprehensive understanding and evaluation of their mechanical properties under specified design loads. Furthermore, Figure 8 distinctly demonstrates the deformation distribution of the linear-type MCWP under the design load, with the maximum deformation occurring in the mid-span area of the platform, measuring 20.55 mm. This value is within the deformation limits established by pertinent standards, indicating that the linear MCWP possesses exceptional resistance to deformation and structural stability under these loading conditions.

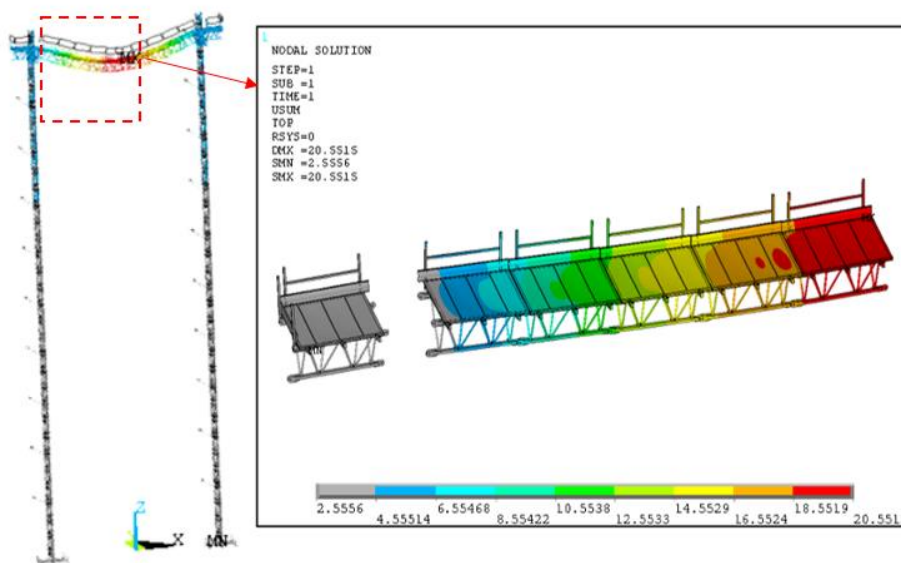


Fig. 8- Deformation cloud of Linear-MCWP

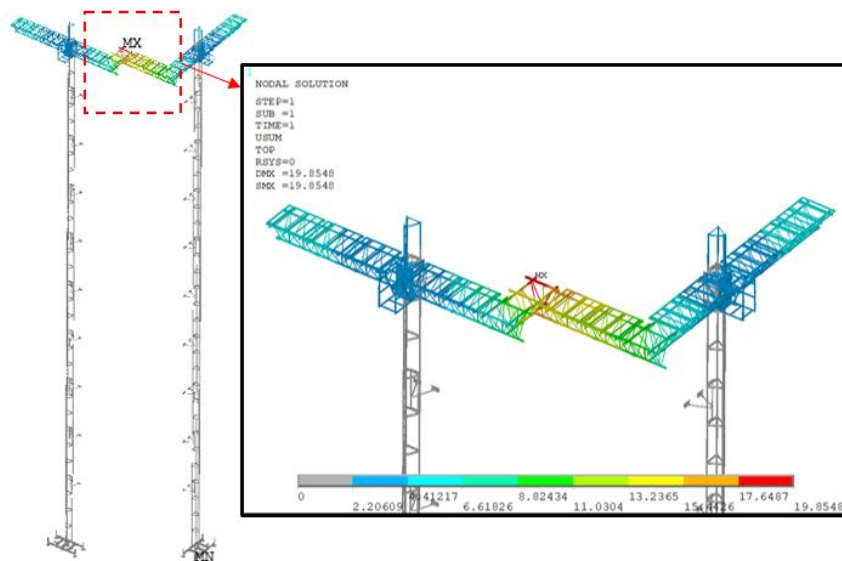


Fig. 9- Deformation cloud of L-shaped MCWP

At the same time, as a non-standard structure comprising two single-column MCWPs, the deformation characteristics of the L-shaped MCWP are not explicitly outlined in the current specifications. It is particularly crucial to precisely calculate and analyze the deformation of the L-shaped platform to ensure its safety and reliability in engineering practice. Moreover, Figure 9 indicates that the maximum deformation of the L-shaped MCWP was 19.85 mm, which also complies with the general specification requirements.

In summary, analyzing the deformation of these two types of platforms not only verifies their structural safety under design loads but also highlights the significance of deformation values as essential indicators for assessing the serviceability of MCWP. Specifically, steel structures inevitably experience deformation when subjected to loads, and the magnitude of this deformation directly impacts the safety and stability of the structure. When the deformation exceeds acceptable limits, it can lead to structural failure or safety incidents. Hence, precise calculation and control of deformation through finite element analysis are essential prerequisites for ensuring the safe operation of MCWP.

### Installation of foundation

The determination and installation process for the foundation is illustrated in Figure 10, which encompasses four scenarios:

1. When the foundation must be installed in a courtyard, negotiation with the homeowner is necessary. If negotiations are unsuccessful, adjustments to the construction plan and adoption of a suspended basket method become necessary.
2. When the foundation must be positioned on a flower bed or greenery with poor soil mechanical properties, the soil can be excavated and removed. If the soil exhibits good engineering properties, a dynamic compactor can be employed to ensure that the foundation's bearing capacity is not less than 60 kPa, by the standard [24].
3. When the foundation must be constructed on an asphalt road, merely adjusting the pedestal to the same level is required.
4. When encountering steps, the flatness of the MCWP can be aligned to the same height using a steel cushion.

The concrete slab in use measures 3 meters in length, 3 meters in width, and 0.2 meters

in thickness. It incorporates a reinforced grillage, with a spacing of 20 millimeters between the horizontal and vertical steel bars and a spacing of 0.1 meters between the upper and lower grillages. Upon completion of the installation, a fence should be erected within 1 meter of the foundation perimeter to deter people from approaching.

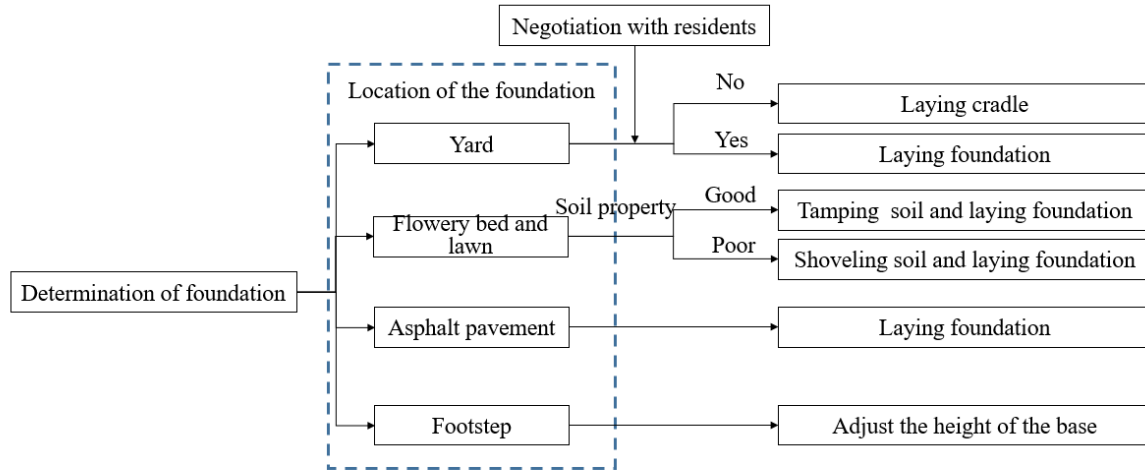


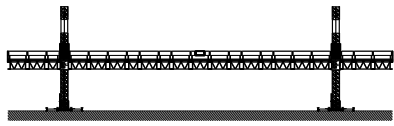
Fig. 10- Process flow for handling the foundation

### Installation of the main structure

The installation process for the primary components of a twin-column MCWP is detailed in Table 1. Despite the existence of various arrangements, the twin-column linear type remains the most prevalent and is extensively utilized in construction sites.

Tab. 1 - Process for installing a twin-column MCWP

Step	Diagram	Content
1		Install the base frame and driving system on the left side; Adjust the base's level and verticality and test it with a leveling device. After installing the bottom parts, install the first cantilever platform beam on both sides and fix them with several pins to the driving system.
2		Install the other base frame.
3		Install the driving system and the right-side overhanging platform using three pins.
4		Then install guardrails and safety gates. The mast tie is installed to the wall with the elevation of the platform.

5		<p>Install the ladder and bolt it tightly to the base.</p>
---	---	--

### Installation of the mast tie

When employing the MCWP method for high-rise buildings, wind load must be taken into consideration. To counteract lateral loads and provide stability to the structure under repair, a mast tie equipment is utilized. As depicted in Figure 11, the mast tie equipment comprises the following components: chemical bolts, high-strength bolts, anti-slip fasteners, oblique rods, mast tie rods, mast tie frames, and connecting bases. An oblique rod is added to the upper portion of the mast tie equipment, and the chemical bolt type is M16×180 mm, with a required bolt torque of 75 N·m. The angle of the steel tube should be kept within the range of 30°-55°. On-site pull-out tests are performed for the chemical bolts, ensuring that the drawing force exceeds the value specified by the standard.

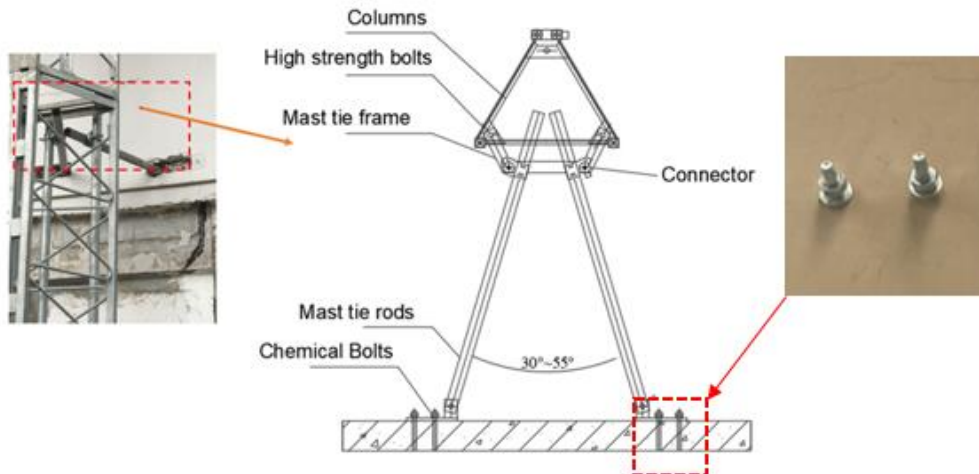


Fig. 11- Mast tie

### Installation of the other equipment

Other protective equipment is shown in Figure 12. The platform guardrail plays a crucial role in ensuring that neither materials nor individuals fall to the ground (Figure 12(a)). Additionally, safety ropes are tied to the platform to avert failures of the safety device (Figure 12(b)). To protect against high-altitude falling objects during the repair process, a protective shed is installed above the pedestrian walkway (Figure 12(c)).



(a) Guardrail

(b) Safety rope

(c) Protective shed

Fig. 12- Protective Equipment

Beyond these protective measures, special attention must be paid to the setup of the electrical system. The electric control box should be installed in the center of the platform and secured with bolts. After securing the power cable, workers should verify the input voltage and insert the cable of the driven motor into the electrical control box. The cable should be fastened to the platform beam, insulated, and securely tied. The power supply specification for the motor is a three-phase five-wire system, incorporating both grounding and zero connections. Each motor has a rated current of 3A and a starting current of 40A. It is imperative to confirm that grounding and zero connections are effectively established to prevent electric leakage. The installation of the electric control box and cables should be carried out by qualified electricians.

### COST ANALYSIS AND COMPARISON

The procedures for renovating walls typically involve waterproofing, primer painting, sanding, and coating. For one building in the same residential area, the general contractor utilized an MCWP, while for the other building, a hanging basket was employed. The construction cost comprises labour, machinery, and material expenses. In this case, machinery and material costs have been converted into labour costs. A comparison of the actual cost and duration between utilizing an MCWP and a suspended basket is presented in Table 2. The facade repair area is 5,000 square meters. The MCWP method took 104 days, whereas the suspended basket method required 196 days. Assuming a labour cost of 400 yuan per day for the MCWP method and 300 yuan per day for the suspended basket method, the total cost amounts to 41,600 yuan for the MCWP method and 58,800 yuan for the suspended basket method, respectively. As evidenced by the table, employing an MCWP method is more efficient and cost-effective compared to using a suspended basket.

*Tab. 2 - Renovation cost for using the MCWP and suspended basket*

	Procedure	Using an MCWP			Using a suspended basket		
		Number of workers (per person)	Time (per day)	Duration for each step	Number of workers (per person)	Time (per day)	Duration for each step
1	Whitewash	2	4	8	2	5	10
2	Exterior wall polishing	6	3	18	6	8	48
3	First-time whitewashing	6	3	18	6	8	48
4	Levering with plaster	6	2	12	6	6	36
5	Second-time whitewashing	6	3	18	6	10	60
6	Coating of the wall	6	5	30	6	11	66
	Total(days)	104			196		

### DISCUSSION

Based on the on-site practical application of the MCWP method, our findings indicate that it possesses notable advantages in terms of safety performance and construction

efficiency.

Firstly, the utilization of MCWP has significantly enhanced construction safety. Its integrated protective, electrical, and mechanical systems ensure safety and reliability throughout each phase of the construction process. This comprehensive approach to safety minimizes risks. Secondly, economic data from a comparable high-rise building in the same community, which was repaired using traditional basket methods, highlights that MCWP outperforms in terms of construction efficiency and cost reduction. This is primarily attributed to its innovative lifting mechanism and flexible platform design, enabling construction personnel to complete tasks more expeditiously and effectively.

The contribution of this paper lies in the refinement of construction design steps. Specifically, the platform selection process incorporates a blend of linear and non-standard platforms. To validate the structural stability and reliability of these platforms, finite element method (FEM) simulations were conducted. This flexible arrangement of platform types is made possible through a thorough understanding and meticulous consideration of the specific conditions at the construction site.

Nevertheless, this study acknowledges certain limitations and areas for improvement. For example, the sample size is confined to a single urban renewal project, which may not fully encapsulate the diverse performance capabilities of MCWP across varying environments. Future research should endeavour to expand the sample scope to more comprehensively assess the adaptability of MCWP. Furthermore, there is potential for incorporating cutting-edge technologies, such as the Internet of Things (IoT) and big data analytics, to achieve intelligent control and optimized management of the platform.

## CONCLUSION

This paper provides a detailed account of the application of MCWPs in urban renewal projects, with particular focus on the construction techniques used for the facade repair of high-rise buildings. By comparing the facade repair methods that utilize hanging baskets, this paper highlights the advantages of MCWP in terms of safety, efficiency, and cost. And the following key conclusions can be drawn:

- 1) A combination of linear and L-shaped MCWPs is suitable for buildings with concave and convex corners.
- 2) In comparison to traditional facade renovation methods, the MCWP approach offers improved safety, reliability, and performance.
- 3) The overall MCWP structure is simple to install and features a higher turnover rate.
- 4) Employing the MCWP method for high-rise buildings abbreviates the overall construction period and reduces total costs.

In summary, the MCWP is poised to assume a pivotal role in the future of urban construction. Currently, several forward-thinking companies are actively incorporating MCWP into their research and development initiatives, particularly in the realm of exterior wall plastering robots. These efforts are directed towards realizing the vision of unmanned facade repair construction, thereby addressing the challenges associated with traditional manual methods and fostering a new era of smart construction practices.

## REFERENCES

- [1] Madureira S., Flores-Colen I., Brito J., et al., 2017. Maintenance planning of facades in current buildings. *Construction and Building Materials*, vol. 47, p. 790-802. <https://doi.org/10.1016/j.conbuildmat.2017.04.195>
- [2] Pires R., De Brito J., Amaro B., 2014. Statistical survey of the inspection, diagnosis and repair of painted rendered facades. *Structure and Infrastructure Engineering*, vol. 11(5), p. 1-14. <https://doi.org/10.1080/15732479.2014.890233>
- [3] Pereira C., Silva A., de Brito J., et al., 2020. Urgency of repair of building elements: Prediction

- and influencing factors in facade renders. *Construction and Building Materials*, vol. 249, p.118743, <https://doi.org/10.1016/j.conbuildmat.2020.118743>
- [4] Pulley, D.M., Robison, E.C., 2004. Emergency repairs for historic facades. In: *BUILDING FACADE MAINTENANCE, REPAIR, AND INSPECTION: Symposium on Building Facade Maintenance, Repair and Inspection*. vol. 1444, pp. 91-105. <https://doi.org/10.1520/STP11463S>
- [6] Fong, K. L., Loieue, C., 2004. Facade ordinances and historic structures - Theoretical and practical conservation issues in inspection and repair. In: *BUILDING FACADE MAINTENANCE, REPAIR, AND INSPECTION. Symposium on Building Facade Maintenance, Repair and Inspection*, vol.1444, pp. 47-64. <https://doi.org/10.1520/STP11460S>.
- [7] De Gregorioi, S., 2019. The rehabilitation of buildings. Reflections on construction systems for the environmental sustainability of interventions. In: *VITRUVIO-INTERNATIONAL JOURNAL OF ARCHITECTURAL TECHNOLOGY AND SUSTAINABILITY*, vol. 4, p. 47-58. <https://doi.org/10.4995/vitruvio-ijats.2019.12634>.
- [8] Bucon, R., Czarnigowska, A., Kmiecik, P., et al., 2019. Qualitative and Quantitative Assessment of Scaffolding Used in Polish Cities: Focus on Safety. In: *3rd World Multidisciplinary Civil Engineering, Architecture, Urban Planning Symposium (WMCAUS)*, vol. 471(11), 112059. <https://doi.org/10.1088/1757-899X/471/11/112059>.
- [9] ANSI/SIAA92.9 – 2011: 2011. ANSI/SIA: Mast Climbing Work Platforms. 2011. Available from: [https://webstore.ansi.org/preview-pages/SIA-Scaffold/preview\\_ANSI+SIA+A92.9-2011.pdf](https://webstore.ansi.org/preview-pages/SIA-Scaffold/preview_ANSI+SIA+A92.9-2011.pdf)
- [10] BS 7981:2017. BS: Code of Practice for the Installation, Maintenance, Thorough Examination, and Safe Use of Mast Climbing Work Platforms. 2017. Available from: <https://webstore.ansi.org/standards/bsi/bs79812017>
- [11] USAO 07/10-002: 2006. USAO: Guidelines for the Safe Use of Mast Climbing Work Platforms. 2006. Available from: <https://www.mastclimbers.com/wp-content/uploads/Safe-Use-Guidelines-Mastclimbers.pdf>
- [12] Pan C. S., Ning X. P., and Wimer B. et al., 2021. Biomechanical assessment while using production tables on mast climbing work platforms. *Applied Ergonomics*, p. 103276. <https://doi.org/10.1016/j.apergo.2020.103276>
- [13] Wimer B., Pan C. S., Lutz T. et al., 2017. Evaluating the stability of a freestanding Mast Climbing Work Platform. *Journal of Safety Research*, vol. 62, p. 163-172. <https://doi.org/10.1016/j.jsr.2017.06.014>
- [14] Wu J. Z., Pan C. S., Wimer B., et al., 2023. A Finite Element Analysis of the Effects of Anchorage Reaction Forces and Moments on Structural Stability of Mast Climbing Work Platforms. *Journal of Multiscale Modelling*, vol.14(03). <https://doi.10.1142/S1756973723500099>
- [15] Qin X. R., Hong Y., Yue P. et al., 2014. Dynamic Stability Analysis of the Tower Structure of Construction Elevators. In: *Applied Mechanics and Mechanical Engineering IV, Applied Mechanics and Materials (ICAMME 2013)*, Singapore, vol. 459, p. 646-649, <https://doi.org/10.4028/www.scientific.net/AMM.459.646>.
- [16] Zheng P., Zhang Q., Lu Y. Z., 2009. Structural modeling and analysis of super-high building hoist. *Engineering Journal of Wuhan University*, vol. 42(3), p. 353-7, 381.
- [17] Cheng B., Yang B., Wang D., et al., 2023. Finite element analysis of complete structure of tower cranes. In: *Journal of Physics: Conference Series*, (UK), Proceedings of the 2022 2nd International Conference on Mechanical Automation and Electronic Information Engineering (MAEIE2022), Guizhou, vol. 2419, p. 012004. <https://doi.org/10.1088/1742-6596/2419/1/012004>.
- [18] Cheng, B., Yang, B., Wang, D., et al., 2023. Finite element analysis of complete structure of tower cranes. *Journal of Physics: Conference Series*, p. 012004. <https://doi.org/10.1088/1742-6596/2419/1/012004>
- [19] Zhang Y., Zhao J. Z. and Yao J. J., 2021. Static structural finite-element analysis of tower crane based on FEM. In: *2011 IEEE 2nd International Conference on Computing, Control and Industrial Engineering*, Wuhan, China, p. 220-223. <https://doi.org/10.1109/CCIENG.2011.6008106>
- [20] Lu Y., Gao M. X., Liang T., et al., 2022. Wind-induced vibration assessment of tower cranes attached to high-rise buildings under construction. *Automation in Construction*, vol.135, p.104132. <https://doi.org/10.1016/j.autcon.2022.104132>
- [21] Jiang W. G., Ding L. Y. and Zhou C., 2022. Digital twin: Stability analysis for tower crane

hoisting safety with a scale model, *Automation in Construction*, vol.138, p.104257.  
<https://doi.org/10.1016/j.autcon.2022.104257>

[22] Kenan H., Azeloğlu O., 2022. Design of scaled down model of a tower crane mast by using similitude theory, *Engineering Structures*, vol. 220, p.10985.  
<https://doi.org/10.1016/j.engstruct.2020.110985>

[23] GB/T 27547-2011. GB/T: Elevating Work Platform-Mast climbing work platform. 2011.(In Chinese)

[24] JB 5007-2011. JB: Code for design of building foundation. 2011.(In Chinese)

# EXPERIMENTAL STUDY ON QUALITY LOSS AND MICROSTRUCTURAL CHARACTERISTICS OF REINFORCED CONCRETE IN BRIDGE DECK PANELS AFTER SALT FREEZING

*Xilong Zheng<sup>1</sup>, Di Guan<sup>2</sup>, Honglei Zhang<sup>3</sup>*

- 1. School of Civil and Architectural Engineering, Harbin University, No.109 Zhongxing Road, Harbin, Heilongjiang Province, China; sampson88@126.com*
- 2. School of Civil and Architectural Engineering, Harbin University, No.109 Zhongxing Road, Harbin, Heilongjiang Province, China*
- 3. Bridge Department, Beijing New Bridge Technology Development Co., LTD, No.8 Xitucheng Road, Beijing, China*

## ABSTRACT

The reinforced concrete structure is the most widely used structural form today. In the western salt-alkali areas and in road and bridge projects in the northern regions where de-icing agents are applied, chloride ion intrusion into concrete leads to rebar depassivation and corrosion. With the occurrence and intensification of corrosion, the expansion of corrosion products leads to cracking or spalling of the concrete cover, resulting in durability damage to the reinforced concrete structure. Among all the components of the bridge, the bridge deck panels suffer the most severe and direct damage from salt freezing. Therefore, predicting the service life under salt freezing conditions is an urgent issue to address for the durability design, evaluation, and structural maintenance decision-making for reinforced concrete bridge deck panels. Concrete specimens in both water and salt solutions follow a four-stage pattern of deterioration. After 300 freeze-thaw cycles, the mass loss rates of specimens in water, NaCl solution, Solution A, and Solution B were 0.56%, 2.36%, 3.39%, and 3.71% respectively. Using Matlab analysis software, it was found that specimens in Solution B reached the failure limit first after 410 freeze-thaw cycles.

## KEYWORDS

Freeze-thaw, Salt freezing, Reinforced concrete bridge deck panel, Quality loss, Microscopic

## INTRODUCTION

The investigation conducted by relevant departments of the Ministry of Transportation on highway bridges in the high latitudes of the world revealed that the service life of urban transportation and road and bridge systems will be significantly shortened under the application of deicing agents in high latitude areas [1, 2]. The erosion and destruction of concrete by salt is the comprehensive result of physical and chemical effects. Although soluble inorganic salts such as NaCl and CaCl<sub>2</sub> scattered on the pavement can prevent icing, some studies have shown that salt will aggravate the surface erosion of concrete. The physical and chemical action and corrosion of snow melting agent are very strong, which will cause chronic damage to the bridge panel [3, 4].

In China, the old Beijing Xizhimen overpass was demolished and rebuilt due to durability problems after only 18 years of operation, and the Shenyang Wenhua Road overpass was cracked

and spalling seriously after 13 years of use due to steel corrosion [5]. The Harbin-Daqing Highway, after being in operation for only 5 years, experienced severe longitudinal cracking and spalling of the concrete [6]. It is reported that a large number of snow melting agents have been used abroad in the past few years, which has caused serious corrosion damage to buildings mainly dominated by Bridges, and huge economic losses [5]. Foreign investigations have shown that Bridges that use snowmelt agents show corrosion damage in about 15 years [6]. In the United States, a quarter of highway Bridges have been restricted due to corrosion of concrete and steel bars caused by snowmelt, of which 1% (about 5,000) are no longer open to traffic, and the maintenance cost alone is as high as \$90 billion [7]. The UK has spent 6.2 billion pounds repairing Bridges damaged by corrosion caused by snowmelt [8]. The United States has done an experiment, the original design life of an overpass is 50 years, if the use of snow melt agent snow removal, the life of the overpass may drop to 20 years, or even 15 years, which seriously hindered traffic, damage public property, the harm cannot be ignored [9,10].

There is a lack of research in China and even in developed countries regarding the assessment of the harmful effects of de-icing agents on highways and bridges. There is also a lack of reasonable methods to evaluate the corrosiveness of de-icing agents, and no rational evaluation system has been established [11-13]. Therefore, conducting technical research on the erosion mechanism of de-icing agents on reinforced concrete bridge decks, the permeation pattern of chloride ions, and the impact of de-icing agents on their durability has become an urgent issue for highway authorities. The aim is to reduce the harm caused by de-icing agents to bridges and the environmental pollution they cause [14-16].

This project adopts the method of coupling chloride salt solution and freeze-thaw cycles to explore the distribution, migration, and microstructural evolution of chloride ions in reinforced concrete bridge decks. It reveals the impact of chloride ion diffusion on the bond stress of reinforced concrete and analyzes the collaborative performance of test beams in terms of concrete quality loss after salt freezing damage. The findings will provide a theoretical basis and technical support for design departments to carry out durability design of concrete bridge decks in cold regions, as well as for transportation management departments in terms of controlling the use of de-icing materials, evaluating their harmfulness to highways and bridges, and predicting their service life. This research is of significant theoretical and practical value, as it guarantees the long-term safe operation of infrastructure in China and promotes rapid and sustained economic development. It also helps reduce maintenance costs of highways, bridges, and other infrastructure, leading to important economic and social benefits.

## **DETERMINATION OF SURFACE DELAMINATION MORPHOLOGY AND MASS LOSS OF SPECIMENS AFTER SALT FREEZING**

### **Test summary**

The concrete mass loss rate reflects the degree of erosion of the concrete protective layer during salt freezing cycles and is an important factor affecting concrete durability. It can be used as an indicator to evaluate concrete durability. It is generally considered that when the concrete mass loss reaches 5%, it is considered as failure. Concrete salt freezing damage can be roughly divided into four stages: (1) Surface without obvious damage, with minor pitting erosion. (2) With increasing freeze-thaw cycles, the surface mortar begins to erode, resulting in small pits and grooves. (3) Severe erosion of the surface mortar, deeper and larger pits and grooves, exposure of fine aggregates, and slight erosion. (4) Severe erosion of fine aggregates, exposing coarse aggregates, and the concrete texture becomes porous.

### **1. Composition of the immersion solution for freeze-thaw specimens**

There are four types of immersion solutions, including water, NaCl solution, a solution with a

mass ratio of NaCl: MgCl<sub>2</sub>: CaCl<sub>2</sub>=6:2:2, and a solution with a mass ratio of NaCl: MgCl<sub>2</sub>: CaCl<sub>2</sub>=6:3:1. The concentration of each solution is 3%. For convenience, the solution with a mass ratio of NaCl: MgCl<sub>2</sub>: CaCl<sub>2</sub>=6:2:2 is defined as solution A, and the solution with a mass ratio of NaCl: MgCl<sub>2</sub>: CaCl<sub>2</sub>=6:3:1 is defined as solution B.

**2. Translate the raw materials such as cement and aggregates**

The concrete mix ratio for casting the experimental beam is shown in Table 1. The cement used is Swan brand 42.5 ordinary Portland cement produced by Harbin Yatai Cement Co., Ltd. The coarse and fine aggregates are crushed stones with a maximum particle size of 16 mm and natural river sand with a fineness modulus of 2.5, respectively, in gradation Zone 11. The water-to-cement ratio of the concrete is 0.40, and the slump is 28 mm.

*Tab. 1 - Concrete mix ratio and mechanical properties*

W/C	Water (Kg)	Concrete (Kg)	Sand (Kg)	Stone (Kg)	28d Axial compressive strength $f_{cu}$ (N/mm <sup>2</sup> )
0.4	166	415	600	1219	52.3

The reinforcement used Grade HRB335, and the mechanical properties of the reinforcement are shown in Table 2.

*Tab. 2 - Mechanical properties of the reinforcement*

Strength grade	Steel grade	Nominal diameter (mm)	Yield strength $f_y$ (MPa)	Ultimate strength $f_u$ (MPa)	Elongation $\delta_{10}$ (%)
HRB335	Ribbed steel bar	10	335	495	≥16

**3. Sample preparation and grouping:**

The experiment uses plain concrete specimens with dimensions of 100 mm×100 mm×400 mm, formed horizontally. A total of 12 specimens are prepared and divided into 4 groups. After being left to stand at room temperature for 24 hours, the specimens are demolded and numbered as follows: Group 1, numbered A13D~B33D; Group 2, numbered A41D~A43D; Group 3, numbered A11D~A31D; Group 4, numbered A12D~A32D. Different liquids are poured into each group during the freeze-thaw test, including water, NaCl solution, Solution A, and Solution B. To meet the requirements of the control study, 3 specimens without any damage treatment are prepared, making a total of 15 specimens. Freeze-thaw test was carried out in freeze-thaw chamber. Each cycle includes 2 hours of freezing and 2 hours of thawing. Freeze-thaw cycle diagram of concrete is shown in Figure 1.



*Fig. 1 – Freeze-thaw cycle diagram of concrete*

**Experimental results and analysis**

The erosion conditions of the specimens in water and Solution B are shown in Figure 2, from top to bottom, representing specimens subjected to 50, 150, and 250 freeze-thaw cycles respectively.

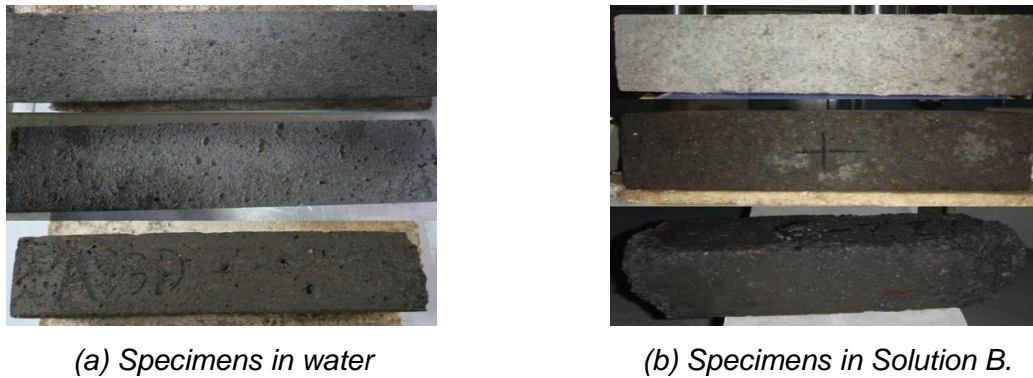


*Fig. 2 – Visual changes of the specimen’s external damage*

The mass changes of the specimens during 300 freeze-thaw cycles in water and different solutions are shown in Figure 3.

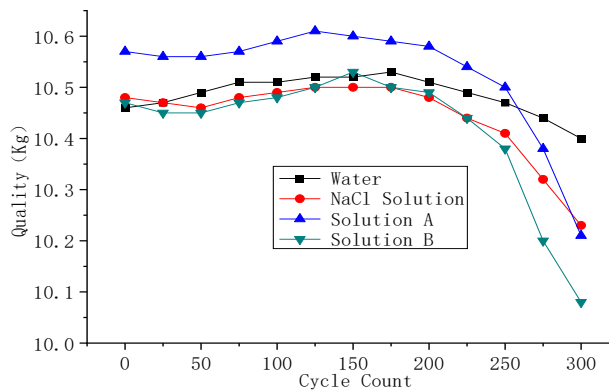


*Fig. 3 – Graph of the mass changes of the specimens*

Refer to Table 3 for the mass loss rate of the specimens as shown in Figure 4 - Figure 5.

*Tab. 3 - Statistical table of specimen mass loss rate*

Soaking liquid		Cycle count										
		0	25	50	75	100	125	150	200	225	275	300
Rate of quality loss%	Water	0	-0.14	-0.26	-0.49	-0.53	-0.60	-0.60	-0.46	-0.33	0.21	0.56
	NaCl solution	0	0.14	0.14	0.03	-0.08	-0.15	-0.17	0.01	0.34	1.56	2.35
	Solution A	0	0.05	0.04	-0.03	-0.19	-0.35	-0.28	-0.08	0.30	1.76	3.39
	Solution B	0	0.15	0.14	0.02	-0.14	-0.26	-0.54	-0.23	0.25	2.57	3.71

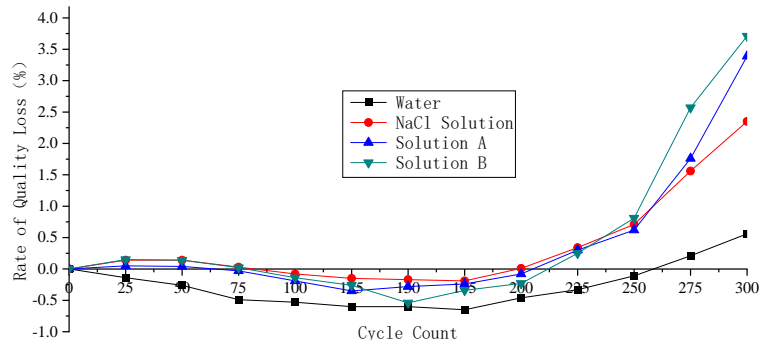


Fig. 4 – Graph of the specimen mass loss rate

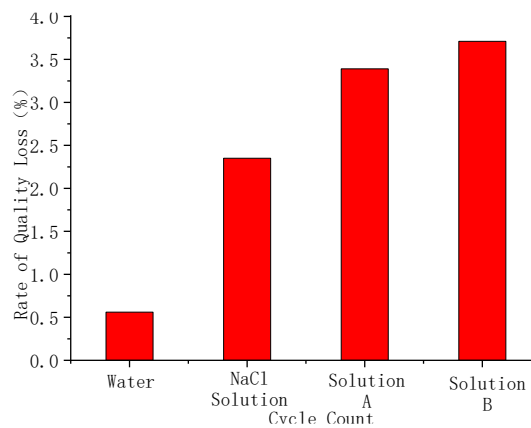


Fig. 5 – Mass loss rate of the specimens after 300 cycles

From Figure 3, it can be observed that the freeze-thaw damage test of the specimens in the salt solution follows the same four-stage failure mode. In Figure (b), the upper specimen is after 50 freeze-thaw cycles, with a smooth and flat surface. The middle specimen is after 150 cycles, and localized surface cracks and detachment of the surface mortar can be observed, but the damage is slight, with no exposed aggregates, and the local area remains smooth. The lower specimen is after 250 cycles, where the surface erosion is already severe, with pits and grooves throughout the specimen, significant loss of concrete mortar and fine aggregates, and even some detachment of coarse aggregates, exposing them. The cross-sectional area has reduced significantly, with the ends of the specimen resembling elliptical cones. When struck with a hard object, the surface feels loose, and materials may detach.

From Figure 4 and Figure 5, it can be seen that throughout the entire freeze-thaw cycle, the mass changes of the specimens do not continuously decrease. In the early stage (0-150 cycles) of the freeze-thaw test, there is a slight increase in mass for the specimens in water and different solutions, but the trend is relatively stable. In the middle and later stages, the mass loss of the specimens (especially in the different solutions) intensifies, and the mass loss curve becomes steeper. After 300 freeze-thaw cycles, the mass loss rates of the specimens in water, NaCl solution, Solution A, and Solution B are 0.56%, 2.36%, 3.39%, and 3.71% respectively.

This change in mass loss is caused by multiple factors, including temperature stress, osmotic pressure, and crystallization pressure. In the early stage, the intact concrete surface has a dense structure with low porosity and no significant cracks or defects. When the surface mortar undergoes freeze-thaw spalling, micro-pores and cracks are exposed, facilitating the penetration of ions. As the ions from the solution penetrate deep into the concrete, complex physicochemical reactions occur with the concrete materials, resulting in the formation of crystals and harmful substances. At this stage, the amount of reaction products slightly exceeds the amount of concrete spalling, leading to

a minor increase in the specimen's mass. As the mortar and fine aggregates further spall, the pore structure undergoes significant changes, which further facilitates the intrusion of ion media and intensifies the process of concrete spalling. The concrete spalling becomes much greater than the generation of physicochemical reaction products, resulting in a rapid increase in mass loss.

The experiment shows that chloride salt solution can significantly accelerate the freeze-thaw damage process of concrete structures. Taking 300 freeze-thaw cycles as an example, the mass loss rates of the specimens in NaCl solution, Solution A, and Solution B are 4.2, 6.0, and 6.5 times higher than that in water, respectively. Using Matlab analysis software fitting, it is found that the mass loss of specimens in Solution B will reach 5.02% (the limit specified in the standard is 5%) after 410 freeze-thaw cycles, reaching the failure limit first.

## MICROSCOPIC ANALYSIS OF THE INTERFACE BETWEEN STEEL AND CONCRETE IN REINFORCED CONCRETE

### Summary of the experiment

The core of modern materials science lies in the relationship between the microscopic structure inside the material and its properties. In the past, research on reinforced concrete focused on the study of macroscopic basic properties, including strength, load-bearing capacity, carbonation depth, and so on, with limited research conducted at the microscopic level. At the macroscopic scale, concrete materials are assumed to be uniform and isotropic, allowing various conventional tests to be conducted. However, this assumption does not hold at the microscopic level. Therefore, conducting only macroscopic research lacks accuracy and rigor. It is crucial and urgent to conduct in-depth research on the microscopic structure and mineral composition changes of reinforced concrete after salt freezing.

Scanning electron microscopy (SEM) can be used to observe the pore size distribution, coarse and fine aggregate morphology, hydration product structure, and the intrusion of harmful substances into the concrete and steel-concrete interface. This provides a microscopic basis for studying the salt freeze durability of reinforced concrete.

### 1. Testing apparatus

In this experiment, scanning electron microscopy (SEM) is employed to observe the microscopic morphology of the surface, interior, and steel-concrete interface of the reinforced concrete specimens. Additionally, elemental energy-dispersive spectroscopy (EDS) analysis is used to analyze the elemental content in various areas, studying the relationship between chloride (Cl-) content and changes in the concrete's microscopic structure.

In this experiment, the QUANTA200 scanning electron microscope (SEM) manufactured by Japan Electron Optics Co., Ltd. is used. The SEM operates at an accelerating voltage of 20 kV and has an instrument resolution of 3.5 nm. Elemental analysis is performed using the Oxford INCA energy-dispersive spectroscopy (EDS) analyzer. The scanning electron microscope (SEM) is shown in Figure 6.



Fig. 6 – Scanning electron microscope (SEM)

## 2. Sample preparation

In this experiment, specimens L20, L22, and L24 are used for the tensile test. After the completion of the tensile test, samples are taken from the surface of the specimen, 25 mm below the surface, and the steel-concrete interface. Three small samples are taken from each specimen, making a total of nine samples. The samples are dried to a constant weight and then undergo coating treatment before being observed under the QUANTA 200 scanning electron microscope.

All three specimens are subjected to salt freeze-thaw treatment using a solution of NaCl: MgCl<sub>2</sub>: CaCl<sub>2</sub> in a ratio of 6:3:1. The number of freeze-thaw cycles for each specimen is 50, 100, and 150 respectively.

## Experimental Results and Analysis

(1) Electron microscopy observation and elemental energy spectrum analysis of specimen L20 SEM images of the microstructure of concrete samples from specimen L20 are shown in Figure 7, and elemental energy spectrum analysis is presented in Figure 8 - Figure 10.

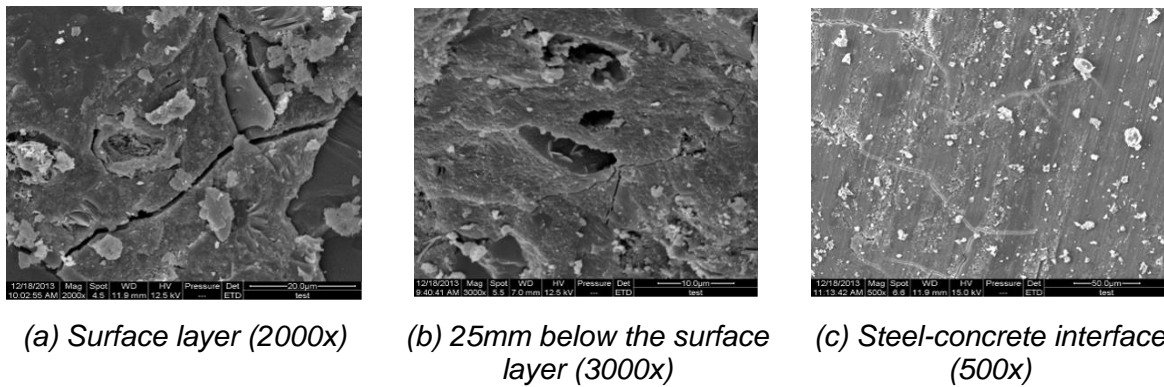


Fig. 7 – SEM images of microstructure of L20 specimen

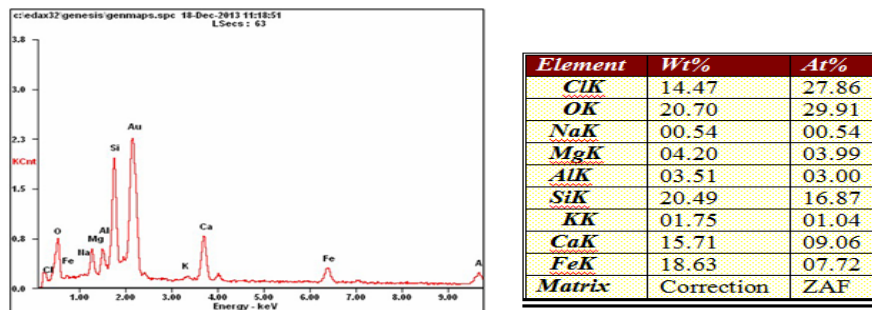
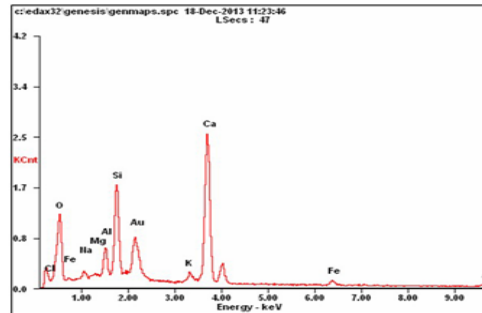
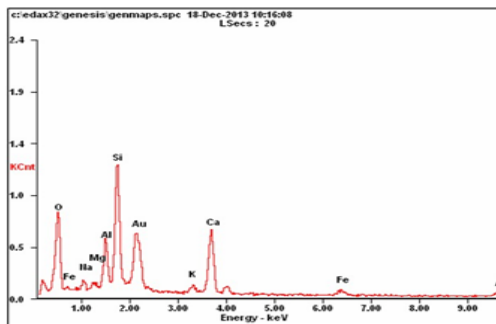


Fig. 8 – Energy-dispersive X-ray spectroscopy (EDS) analysis of surface elements of L20 specimen



Element	Wt%	At%
ClK	09.92	18.64
OK	31.71	44.75
NaK	01.22	01.19
MgK	00.47	00.43
AlK	03.29	02.75
SiK	11.45	09.21
KK	02.01	01.16
CaK	35.98	20.27
FeK	03.96	01.60
Matrix	Correction	ZAF

Fig. 9– Energy-dispersive X-ray spectroscopy (EDS) analysis of elements at a distance of 25mm from the surface of L20 specimen



Element	Wt%	At%
OK	37.40	55.41
NaK	02.02	02.08
MgK	00.92	00.89
AlK	07.02	06.17
SiK	21.76	18.36
KK	02.44	01.48
CaK	21.14	12.50
FeK	07.31	03.10
Matrix	Correction	ZAF

Fig. 10 – Energy-dispersive X-ray spectroscopy (EDS) analysis of elements at the steel-concrete interface of L20 specimen

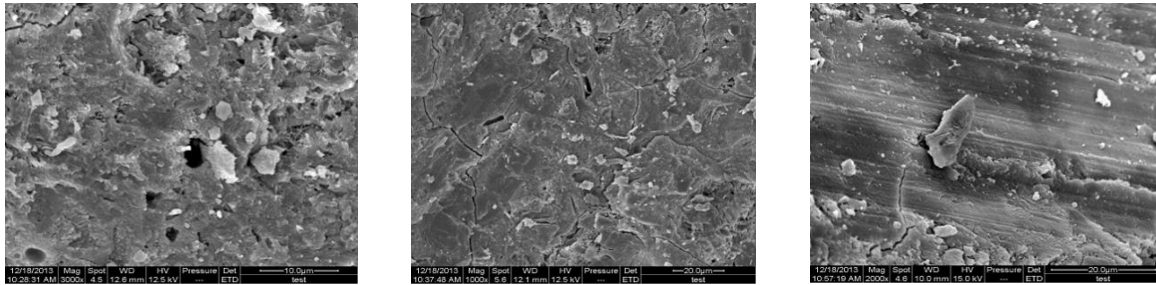
From the SEM images, it can be observed that cracks have occurred in the concrete at three different depths. Among them, the concrete cracks at the steel-concrete interface are narrow and short, mainly formed due to concrete shrinkage, and their development is limited as the internal temperature stress has little effect on them during freeze-thaw cycles. On the surface, there is a long crack in the concrete with a wider width. This crack is caused by significant strains due to temperature stress, resulting in severe damage. The concrete at a distance of 25 mm from the surface exhibits a level of damage between the two cases, with the cracks developing at the interplay of concrete shrinkage and temperature stress and showing some degree of progression.

After freeze-thaw cycles, the surface concrete becomes more porous and its permeability significantly decreases. There is also a certain development in the pore structure, and noticeable chloride salt products can be found on the surface. At a distance of 25 mm from the surface, no significant chloride salt products are detected, and the structure is relatively compact. The concrete at the steel-concrete interface appears relatively smooth and dense, exhibiting good overall integrity and resistance to permeability.

From the energy-dispersive X-ray spectroscopy (EDS) analysis, it can be observed that the distribution of Cl<sup>-</sup> varies significantly among different depths. The surface concrete has the highest content, with a mass percentage of up to 14.47% and a molar percentage of 27.86%. The concrete at a distance of 25 mm from the surface comes next, with a mass percentage of 9.92% and a molar percentage of 18.64%. No presence of Cl<sup>-</sup> is detected at the steel-concrete interface, indicating that after 50 freeze-thaw cycles, Cl<sup>-</sup> failed to effectively penetrate to the steel-concrete interface. The concrete at the steel-concrete interface is only subjected to temperature stress and has not been corroded by chloride salt media.

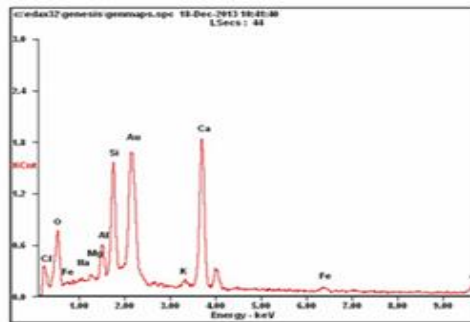
(2) Electron microscopy observation and elemental energy-dispersive X-ray spectroscopy (EDS) analysis of L22 specimen

The microstructure SEM images of the concrete specimens of L22 are shown in Figure 11, and the elemental energy-dispersive X-ray spectroscopy (EDS) analyses are shown in Figure 12 - Figure 14.



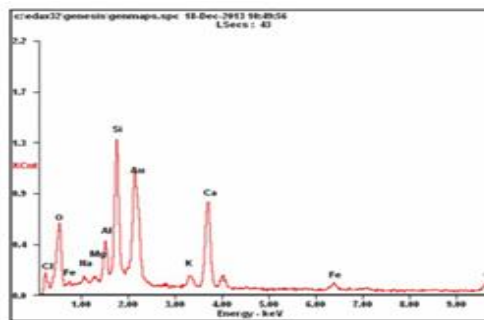
(a) Surface layer (3000x)      (b) 25mm below the surface layer (1000x)      (c) Steel-concrete interface (2000x)

Fig. 11 – SEM images of the microstructure of the L22 specimen



Element	Wt%	At%
<b>ClK</b>	15.23	29.46
<b>OK</b>	25.54	34.22
<b>NaK</b>	00.55	00.62
<b>MgK</b>	00.62	00.66
<b>AlK</b>	04.22	04.04
<b>SiK</b>	16.70	10.36
<b>KK</b>	01.70	01.12
<b>CaK</b>	31.15	17.52
<b>FeK</b>	04.28	01.98
<b>Matrix</b>	Correction	ZAF

Fig. 12 – Elemental energy-dispersive X-ray spectroscopy (EDS) analysis of the surface layer of the L22 specimen



Element	Wt%	At%
<b>ClK</b>	10.52	20.01
<b>OK</b>	24.24	37.59
<b>NaK</b>	01.41	01.53
<b>MgK</b>	00.60	00.62
<b>AlK</b>	05.05	04.70
<b>SiK</b>	19.55	15.27
<b>KK</b>	03.74	02.40
<b>CaK</b>	27.46	14.53
<b>FeK</b>	07.44	03.34
<b>Matrix</b>	Correction	ZAF

Fig. 13 – Elemental energy-dispersive X-ray spectroscopy (EDS) analysis of the L22 specimen at a distance of 25mm from the surface layer

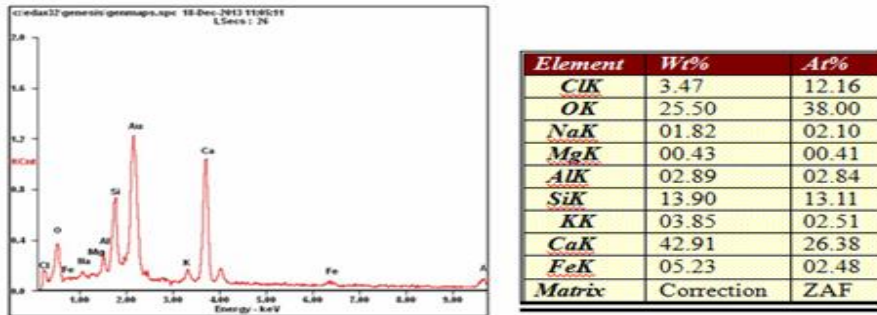


Fig. 14 – Elemental energy-dispersive X-ray spectroscopy (EDS) analysis of the steel-concrete interface of the L22 specimen

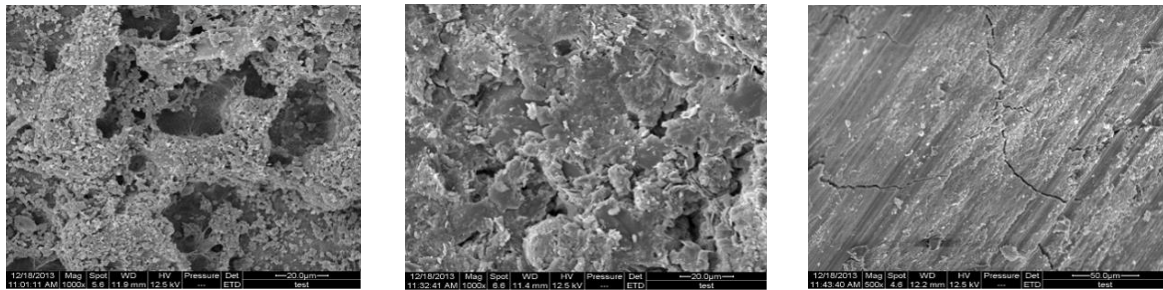
Based on the SEM images, it can be observed that cracks have developed in the concrete at different depths. The cracks at the steel-concrete interface are narrower, shorter, and more sporadic. They are mainly caused by concrete shrinkage, and the influence of internal temperature stress during freeze-thaw cycles is relatively minor. Therefore, the crack propagation is slow. The concrete at the surface layer exhibits a prominent crack with a wider width. This crack is a result of significant strain caused by temperature stress, leading to severe damage. The concrete at a distance of 25 mm from the surface layer shows intermediate levels of damage. Cracks have formed due to the combined effects of concrete shrinkage and temperature stress, with some degree of propagation.

After freeze-thaw cycles, the surface layer of the concrete becomes more porous, resulting in a significant decrease in permeability. The pore structure also develops to a certain extent, with numerous and larger-sized pores. There are visible chloride salt deposits on the surface. At a distance of 25 mm from the surface layer, a small amount of chloride salt deposits can be found, and the structure is relatively denser. The concrete at the steel-concrete interface is relatively smooth and compact, exhibiting overall integrity and good resistance to permeability.

The distribution of Cl<sup>-</sup> in different depths can be observed from the energy-dispersive X-ray spectroscopy analysis. The surface layer of the concrete has the highest concentration, with a mass percentage of 15.23% and a molar percentage of 29.46%. The Cl<sup>-</sup> content is lower at a depth of 25 mm from the surface layer, with a mass percentage of 10.52% and a molar percentage of 20.01%. The Cl<sup>-</sup> content is the lowest at the steel-concrete interface, with a mass percentage of 3.47% and a molar percentage of 12.16%, exceeding the critical value for inducing reinforcement corrosion. This indicates that Cl<sup>-</sup> has only penetrated to the steel-concrete interface after 100 freeze-thaw cycles, where the concrete is mainly affected by temperature stress and less influenced by chloride salt corrosion.

### (3) Electron microscopy observation and elemental energy-dispersive X-ray spectroscopy analysis of the L24 specimen

SEM images of the microstructures of concrete specimens for L24 specimen are shown in Figure 15, while the elemental energy-dispersive X-ray spectroscopy analyses are shown in Figure 16 - Figure 18.



(a) Surface layer (1000x)      (b) 25mm below the surface layer (1000x)      (c) Steel-concrete interface (500x)

Fig. 15 – SEM images of the microstructure of the L24 specimen

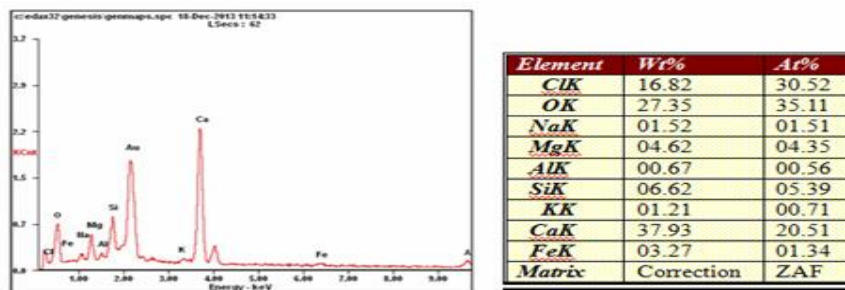


Fig. 16 – Elemental energy-dispersive X-ray spectroscopy analysis of the surface layer of the L24 specimen

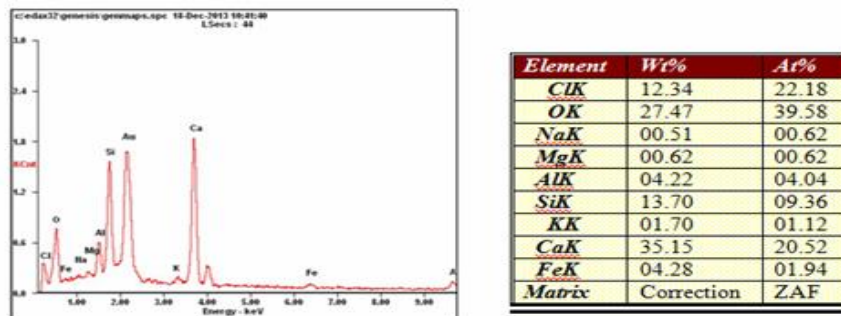


Fig. 17 – Elemental energy-dispersive X-ray spectroscopy analysis of the L24 specimen at a distance of 25mm from the surface layer

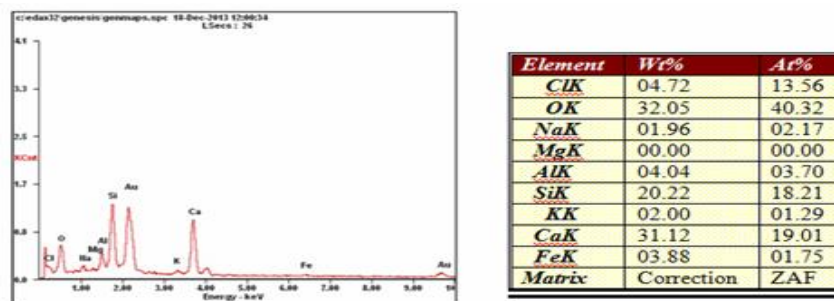


Fig. 18 – Elemental energy-dispersive X-ray spectroscopy analysis at the steel-concrete interface of the L24 specimen

According to the SEM images, it can be observed that under the combined effects of concrete

shrinkage, temperature stress, and chloride ion erosion, the surface morphology of the concrete exhibits a honeycomb-like appearance, with severe loose, porous, and fragmented characteristics. The impermeability can be considered negligible as the surface is heavily covered with chloride salt deposits, indicating the loss of its protective structural function. The concrete cracks at the steel-concrete interface have significantly developed in width compared to 50 and 100 cycles of freeze-thaw cycles, transitioning from fine mesh-like cracks to coarse, deep-through cracks. No cracks were observed at a distance of 25 mm from the surface, but the concrete still exhibited severe loose, porous, and fragmented characteristics, leading to a significant reduction in impermeability.

From the energy-dispersive X-ray spectroscopy analysis, it can be observed that the content of Cl<sup>-</sup> increases significantly in different depth layers. The surface layer of the concrete has the highest content, with a mass fraction of up to 16.82% and a molar percentage of 30.52%. The content of Cl<sup>-</sup> at a distance of 25 mm from the surface is the second highest, with a mass fraction of 12.34% and a molar percentage of 22.18%. The Cl<sup>-</sup> content at the steel-concrete interface is the lowest, with a mass fraction of 4.72% and a molar percentage of 13.56%, exceeding the critical value for inducing steel corrosion. This indicates that after 100 cycles of freeze-thaw, Cl<sup>-</sup> has just penetrated the steel-concrete interface, where the concrete is primarily affected by temperature stress and has a lesser influence from chloride salt erosion.

Through comparison, the degree of concrete damage at the same location increases with the number of freeze-thaw cycles. After 50 cycles, the concrete damage is minimal, with only noticeable cracks on the surface layer. The development of concrete porosity is slow, and the texture is relatively compact. No significant chloride salt erosion is observed in the core region of the concrete. After 100 cycles, the concrete damage intensifies, with significant increases in the width and length of cracks in various areas. The concrete exhibits severe deterioration, reduced overall integrity, and decreased impermeability. The presence of chloride elements is detected in the core region of the concrete. After 150 cycles, the concrete damage in all areas becomes highly apparent. The protective function of the surface layer concrete is largely lost, and the Cl<sup>-</sup> content in the core region far exceeds the critical value for steel corrosion.

Based on the SEM images and energy-dispersive X-ray spectroscopy analysis at different freeze-thaw cycles and depths, it can be concluded that the penetration of chloride ions in concrete follows Fick's second law, with the ion permeation from the surface to the interior gradually decreasing and the erosion damage of the concrete diminishing. The damage to the steel-reinforced concrete occurs initially at the surface. Under the influence of multiple factors such as chloride salt and freeze-thaw, the chloride salt medium in the solution infiltrates into the concrete's interior through micro-cracks in the surface, filling the pore structure during crystallization. This induces pore structure expansion under the dual action of water freezing and expansion, damaging the microstructure of the concrete and further allowing the intrusion of chloride salt medium. The development of micro-cracks is caused by internal stresses resulting from salt crystallization, while the development of the pore structure and the formation of honeycomb morphology are the combined effects of chemical reactions with chloride salt medium and freeze-thaw actions.

## CONCLUSION

The erosion and mass loss of various specimens after freeze-thaw cycles in water and different solutions were studied, and the variation patterns of mass loss rate under different freeze-thaw cycles and environments were analyzed. Through scanning electron microscopy (SEM) experiments, the morphology of hydrates, changes in micro-pore structure, and crack development in concrete at different depths after 50, 100, and 150 freeze-thaw cycles in Solution B were observed. Combined with energy-dispersive X-ray spectroscopy analysis, the permeation and distribution patterns of chloride ions were investigated. The following conclusions were primarily drawn:

- (1) Concrete specimens in both water and salt solutions follow a four-stage pattern of

deterioration. However, under the combined effects of temperature stress and osmotic pressure, the mass of the specimens does not continuously decrease but rather exhibits a trend of slight increase in the early stages followed by a sharp decrease in the later stages. Furthermore, chloride ions can accelerate the freeze-thaw damage of concrete, with a higher concentration of chloride ions resulting in more pronounced deterioration. After 300 freeze-thaw cycles, the mass loss rates of specimens in water, NaCl solution, Solution A, and Solution B were 0.56%, 2.36%, 3.39%, and 3.71% respectively.

(2) From the SEM images, it can be observed that the concrete specimens exhibit different morphologies at different stages of deterioration. Initially, the surface appears dense and smooth, then it gradually develops spalling, roughness, and discolored areas. Eventually, a significant loss of mortar, fine aggregates, and coarse aggregates occurs. The crack pattern also transitions from fine interconnected cracks to larger and deeper penetrating cracks. The development of cracks accelerates the erosion of the concrete, which explains the phenomenon of a sharp increase in the mass loss rate of the specimens in the later stages of freeze-thaw cycles.

(3) From the energy-dispersive X-ray spectroscopy analysis, it can be observed that the penetration of chloride ions in concrete follows the basic principles of Fick's second law. After 50 freeze-thaw cycles, chloride ions have not yet penetrated the steel-concrete interface. However, after 100 freeze-thaw cycles, the presence of chloride ions is detected at the steel-concrete interface, and their concentration exceeds the regulatory requirements, which can lead to corrosion of the reinforcing steel and a decrease in bond stress. After 150 freeze-thaw cycles, the chloride ion content at the steel-concrete interface far exceeds the critical threshold for inducing reinforcement corrosion. Additionally, severe concrete spalling occurs at the surface, causing a significant loss of the concrete's protective function.

(4) This corrosive effect not only affects the aesthetic and structural integrity of the concrete, but also reduces its service life and safety. Therefore, when using deicing salt, it is necessary to weigh its advantages and disadvantages and take appropriate protective measures, such as using an isolated coating system to isolate the direct contact between deicing salt and concrete to reduce damage.

## ACKNOWLEDGEMENTS

Thank you for the support provided by the Heilongjiang Province Natural Science Foundation project (ZD2021E005).

## REFERENCES

- [1] Liu D, Tu Y, Sas G, 2021. Freeze-thaw damage evaluation and model creation for concrete exposed to freeze-thaw cycles at early-age. *Construction and Building Materials*, vol. 312, 125352. <https://doi.org/10.1016/j.conbuildmat.2021.125352>
- [2] Polat R, Demirboğa R, Karakoç M B, 2010. The influence of lightweight aggregate on the physico-mechanical properties of concrete exposed to freeze-thaw cycles. *Cold Regions Science and Technology*, vol. 60, no. 1, p. 51-56. <https://doi.org/10.1016/j.coldregions.2009.08.010>
- [3] Li W, Pour-Ghaz M, Castro J, 2012. Water absorption and critical degree of saturation relating to freeze-thaw damage in concrete pavement joints. *Journal of Materials in Civil Engineering*, vol. 24, no. 3, p. 299-307. <https://doi.org/10.1016/j.coldregions.2009.08.010>
- [4] Subramaniam K V, Ali-Ahmad M, Ghosn M, 2018. Freeze-thaw degradation of FRP-concrete interface: Impact on cohesive fracture response. *Engineering Fracture Mechanics*, vol. 75, no. 13, p. 3924-3940. <https://doi.org/10.1016/j.engfracmech.2007.12.016>
- [5] Yun Y, Wu Y F, 2011. Durability of CFRP-concrete joints under freeze-thaw cycling. *Cold Regions Science and Technology*, vol. 65, no. 3, p. 401-412. <https://doi.org/10.1016/j.coldregions.2010.11.008>

- [6] Peng R, Qiu W, Teng F, 2020. Three-dimensional meso-numerical simulation of heterogeneous concrete under freeze-thaw. *Construction and Building Materials*, vol. 250, p. 118573. <https://doi.org/10.1016/j.conbuildmat.2020.118573>
- [7] Cai L, Wang H, Fu Y, 2013. Freeze-thaw resistance of alkali-slag concrete based on response surface methodology. *Construction and Building Materials*, vol. 49, p. 70-76. <https://doi.org/10.1016/j.conbuildmat.2013.07.045>
- [8] Wang Z, Zeng Q, Wu Y, 2014. Relative humidity and deterioration of concrete under freeze-thaw load. *Construction and Building Materials*, vol. 62, p.18-27. <https://doi.org/10.1016/j.conbuildmat.2014.03.027>
- [9] Xu S, Li A, Ji Z, 2016. Seismic performance of reinforced concrete columns after freeze-thaw cycles. *Construction and Building Materials*, vol. 102, p. 861-871. <https://doi.org/10.1016/j.conbuildmat.2015.10.168>
- [10] Santana Rangel C, Amario M, Pepe M, 2020. Durability of structural recycled aggregate concrete subjected to Freeze-Thaw cycles. *Sustainability*, vol. 12, no. 16, p. 6475. <https://doi.org/10.3390/su12166475>
- [11] Guo J, Sun W, Xu Y, 2022. Damage mechanism and modeling of concrete in freeze-thaw cycles: a review[J]. *Buildings*, vol. 12, no. 9, p. 1317. <https://doi.org/10.3390/buildings12091317>
- [12] Liu Y, Chen Y F, Wang W, 2016. Bond performance of thermal insulation concrete under freeze-thaw cycles. *Construction and Building Materials*, vol. 104, p. 116-125. <https://doi.org/10.1016/j.conbuildmat.2015.12.040>
- [13] Yu H, Ma H, Yan K, 2017. An equation for determining freeze-thaw fatigue damage in concrete and a model for predicting the service life. *Construction and building materials*, vol. 137, p. 104-116. <https://doi.org/10.1016/j.conbuildmat.2017.01.042>
- [14] Alsaif A, Bernal S A, Guadagnini M, 2019. Freeze-thaw resistance of steel fibre reinforced rubberised concrete. *Construction and Building Materials*, vol. 195, p. 450-458. <https://doi.org/10.1016/j.conbuildmat.2018.11.103>
- [15] Zhang K, Zhou J, Yin Z, 2021. Experimental study on mechanical properties and pore structure deterioration of concrete under freeze-thaw cycles. *Materials*, vol. 14, no. 21, p. 6568. <https://doi.org/10.3390/ma14216568>
- [16] Bao J, Xue S, Zhang P, 2021. Coupled effects of sustained compressive loading and freeze-thaw cycles on water penetration into concrete. *Structural Concrete*, vol. 22, p. E944-E954. <https://doi.org/10.1002/suco.201900200>

# POLYURETHANE CEMENT REINFORCEMENT FOR SEISMIC TESTING OF CURVED BEAM BRIDGES PIERS

*Longyi Wang<sup>1</sup> Quansheng Sun<sup>1</sup> Haoyang Zhang<sup>1</sup> and Yong Huang<sup>2</sup>*

- 1. School of Civil Engineering and Transportation, Northeast Forestry University, Harbin, 150040, China; sunquansheng@nefu.edu.cn*
- 2. Associate Researcher, Key Laboratory of Earthquake Engineering and Engineering Vibration, Institute of Engineering Mechanics, China Earthquake Administration, Harbin, China*

## ABSTRACT

The "bending and torsion coupling" effect of curved bridges increases the likelihood of shear fracture and bending collapse of curved girder bridge piers and columns under earthquake action, leading to serious consequences such as overall collapse or overturning of the bridge structure. Polyurethane cement is commonly used as a reinforcement material for structural seismic reinforcement due to its excellent performance. In this study, a three-way shaking table test was conducted on a curved girder bridge, and an OpenSees finite element software was utilized to establish a fiber unit model of the abutment specimen. The model was then used to conduct parameter sensitivity analysis in order to investigate the influence of abutment height and polyurethane reinforcement on the seismic performance of polyurethane cement-reinforced abutment specimens. The results indicate that higher abutments lead to decreased reinforcing effects of polyurethane cement, while greater thicknesses of polyurethane cement result in improved reinforcing performance. Specifically, it was found that higher abutments diminish the reinforcing effect of polyurethane cement, whereas thicker layers of polyurethane cement reinforcement yield more pronounced effects. Based on data from parameter sensitivity analysis, parameters were optimized and the most economical parameters were derived. These findings provide a sufficient theoretical basis for utilizing polyurethane cement for reinforced curved beam bridge piers.

## KEYWORDS

Curved beam Bridge piers, Polyurethane cement, Seismic Strengthening, OpenSees, Parameter optimization

## INTRODUCTION

Curved beam bridges are widely utilized in various interchanges and ramps due to their unique advantages. However, these bridges experience complex forces under seismic conditions, owing to the characteristics of pier-beam connection and continuous curvature. The bridge pier plays a crucial role in bearing the load of the bridge and providing resistance against lateral forces. Seismic data shows that damage to bridge piers is a common phenomenon, which can lead to severe structural damage and even collapse of the bridge. Despite the maturity of many current bridge pier reinforcement technologies, there is a relatively limited amount of comparative research on seismic performance. Rational reinforcement methods can not only bring economic viability but also achieve better reinforcement effects. Therefore, enhancing the seismic performance of bridge piers is crucial for addressing the insufficient seismic capacity of beam bridges. Improving the seismic performance of bridge piers has become a hot topic in academic research.

In the presence of seismic loads, bridge piers on curved beam bridges are prone to serious damage. Many scholars have conducted research on methods for strengthening bridge piers against seismic forces [1-6]. Haoyang Zhang et al. [7] utilized polyurethane cement as a reinforcing material for treating the curved beam bridge piers. They conducted scaled-down model tests using a three-way shaking table to analyze and evaluate the effectiveness of the reinforcement treatment. The test results and data analysis indicate that the use of polyurethane cement can improve the seismic performance of reinforced curved beam bridge piers. He et al. [8] employed externally bonded fiber-reinforced polymer (FRP) materials to repair severely damaged reinforced concrete (RC) piers and columns, and then subjected them to seismic performance testing using a proposed static test system. The results demonstrate that whether or not steel reinforcement is broken affects the effectiveness of fiber composites in reinforcing severely damaged RC piers and columns.

When the seismic intensity is high and the duration is prolonged, the overall integrity of the plastic hinge region of bridge piers is severely weakened, ultimately leading to its crushing and causing the pier to lose its bearing capacity. This type of failure, known as flexural crushing, poses a significant risk of collapse, and the pier becomes challenging to repair after an earthquake. Polyurethane is a block copolymer formed by polycondensation reaction with isocyanate as hard segment and polyol as soft segment. It is used as cementing material in bridge projects. Polyurethane composite materials with different engineering characteristics are prepared by mixing cement, fly ash, coarse aggregate, rubber particles, steel fibers, etc., to meet technical requirements. These include polyurethane cement composite, polyurethane fly ash composite, polyurethane emery, polyurethane concrete, elastic polyurethane concrete and steel fiber reinforced polyurethane concrete [9] ~ [11]. In recent years, polyurethane cement has gradually been applied in the reinforcement of structures due to its excellent axial compression, flexural, and shear properties. It shows broad prospects in seismic-prone areas. There have been some studies on the performance of polyurethane cement indicating its numerous advantages [12] ~ [14].

Letizia Verdolotti's team [15] conducted a study in which they blended polyurethane material with silicate cement to form polyurethane cement. They investigated the mechanical properties of this composite material and demonstrated the mutual continuity between hydrated cement and polyurethane phases. In a separate study, Wang Jianlin et al. [16] utilized polyurethane cement composite materials to reinforce hollow slab beam bridges. The results of their research indicated that this method could effectively enhance the load-bearing capacity of the bridge, and the reinforcement process could be carried out without interrupting vehicular traffic. Furthermore, Haleem K. Hussain's team [17] conducted experiments to measure material parameters. They found that the compactness of polyurethane cement composite materials had a significant impact on material strength. Additionally, compared to conventional concrete, polyurethane cement materials exhibited substantial improvements in flexural and compressive strength.

This paper focuses on the seismic retrofitting of curved beam bridge piers using polyurethane cement. The research adopts a combined approach of experimental studies and numerical simulations to investigate the advantages of polyurethane cement in enhancing the seismic performance of curved beam bridge piers. The findings aim to provide theoretical support for the seismic retrofitting of curved beam bridge piers using polyurethane cement.

## **EXPERIMENTAL STUDY ON MECHANICAL PROPERTIES OF POLYURETHANE CEMENT**

### **Materials**

Polyurethane is a composite material synthesized through the polymerization of polyols and polyisocyanates, belonging to the category of synthetic resins. Its primary raw materials include oligomeric polyols and polyisocyanates. Polyurethane cement is a novel resin concrete composed mainly of polyurethane as the base and cement as the filling material. It possesses characteristics such as fast curing, high early strength, and good viscosity. This material is suitable for rapid

concrete repair and structural reinforcement in building structures, making it a new type of high-strength, high-toughness organic-inorganic composite material.

The primary raw materials used in this study for the preparation of polyurethane cement are a two-component polyurethane (consisting of isocyanate and combined polyether) and ordinary Portland cement with a strength rating of 42.5. The key additives include catalysts, water-reducing agents, and mold release agents. The intended ratio for the preparation of polyurethane cement is as follows: black material (isocyanate): white material (combined polyether): cement = 1:1:2.

### Polyurethane Cement Cubic Compression Test

At a temperature of 20°C, uniaxial compressive strength tests were conducted on polyurethane cement using cubic specimens with dimensions of 70.7mm × 70.7mm × 70.7mm. Both the upper and lower compression surfaces were coated with Vaseline to reduce friction-induced confinement forces resulting from the free deformation of the contact surfaces. Horizontal and vertical strain gauges were affixed to the free surfaces for measuring the material's Poisson's ratio. The tests were performed on a universal testing machine at a loading rate of 0.5mm/min. Figure 1 presents the results of the uniaxial compressive strength test for polyurethane cement, while Figure 2 displays photographs of its compressive failure.

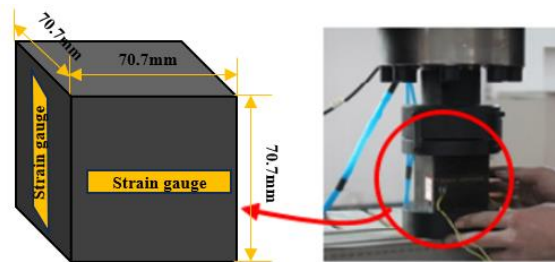


Fig. 1 - Polyurethane Cement Uniaxial Compression Test Graph



Fig. 2 - Polyurethane Cement Uniaxial Compression Failure Diagram

From Figure 2, it is evident that the compressive failure of polyurethane cement exhibits a typical plastic behavior, characterized by the formation of cracks penetrating to create a failure surface. Based on the experimental findings, the stress-strain relationship curve for uniaxial compression of polyurethane cement can be depicted, as illustrated in Figure 3.

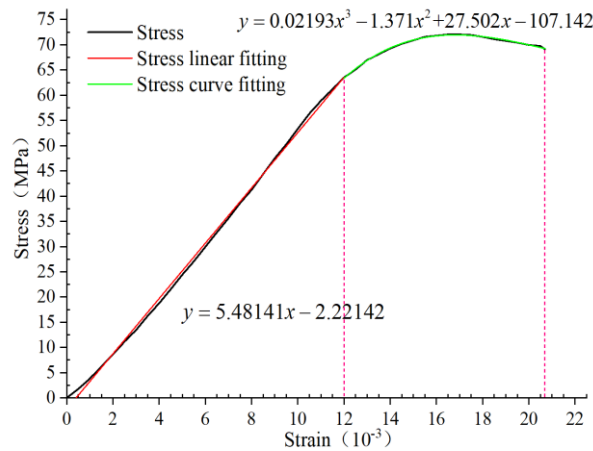


Fig. 3 - Polyurethane Cement Uniaxial Compression Stress-Strain Curve

From Figure 3, it is evident that the uniaxial compression behavior of polyurethane cement can be categorized into two distinct stages. The first stage demonstrates linear elastic behavior, with a stress-strain relationship characterized by an elastic modulus of approximately 5481.3 MPa and an elastic limit of around 63.4 MPa, corresponding to a strain of 12.1 mε. The second stage exhibits nonlinear behavior, following a higher-order curve with an ultimate compressive stress of about 72.05 MPa at a strain of 16.6 mε, and a failure strain of approximately 20.6 mε. The stress-strain fitting equations for these two stages are as follows:

$$\sigma = 5481.41\varepsilon - 2.22142, \quad \varepsilon < 12 \times 10^{-3} \quad (1)$$

$$\sigma = 2.193 \times 10^7 \varepsilon^3 - 1.371 \times 10^6 \varepsilon^2 + 27502\varepsilon - 107.142, \quad 12 \times 10^{-3} < \varepsilon < 20.6 \times 10^{-3} \quad (2)$$

### Polyurethane Cement Tensile Test

Polyurethane Cement Direct Tensile Test [18] was conducted using dumbbell-shaped thin specimens with a thickness of 12.7mm, a central width of 30mm, and side widths of 60mm. The axial tensile test was performed on a small-scale universal testing machine with a loading speed of 50N/s and a head spacing of 85mm between the upper and lower fixture heads, as illustrated in Figure 4.

Strain gauges were strategically positioned along the direction of tension at the center of the specimen to measure strain variations during the tensile process. Based on the experimental results, the uniaxial tensile curve for polyurethane cement composite material can be plotted as shown in Figure 5.

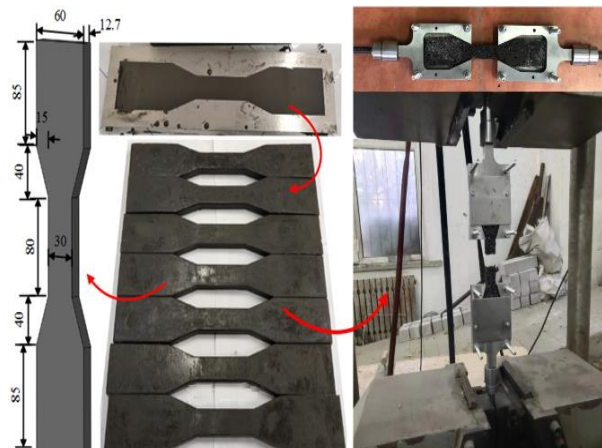


Fig. 4 - Polyurethane Cement Tensile Performance Test Graph (Unit: mm)

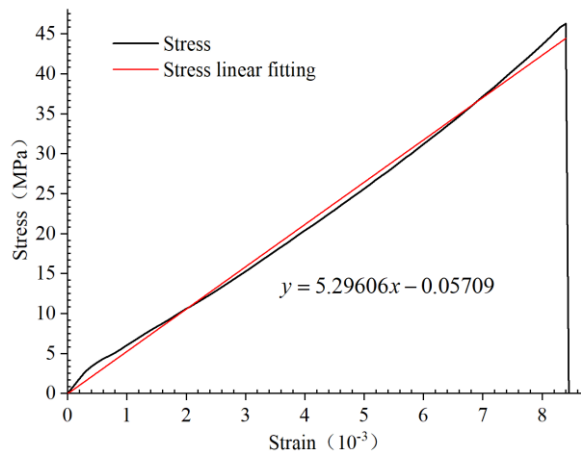


Fig. 5 - Polyurethane Cement Uniaxial Tensile Stress-Strain Curve

From Figure 5, it is evident that the uniaxial tensile curve of polyurethane cement demonstrates linear elastic behavior in the stress-strain relationship. The elastic modulus measures approximately 5296.1 MPa, which is consistent with the elastic modulus under axial compression. The ultimate tensile strength is approximately 46.25 MPa, corresponding to a strain of 8.45 mε. The fitting equation for the tensile curve is:

$$\sigma = 5296.06\varepsilon - 0.05709, \quad \varepsilon < 8.45 \times 10^{-3} \quad (3)$$

## ESTABLISHMENT OF FINITE ELEMENT MODEL FOR POLYURETHANE CEMENT STRENGTHENING CURVES OF BRIDGE PIERS

### Polyurethane Cement Reinforcement Curves Vibration Table Test of Bridge Pier

This paper presents a study on the vibration table test conducted by Haoyang Zhang et al. [7] on bridge piers reinforced with polyurethane cement as the research background. A corresponding finite element model is established using the finite element analysis software OpenSees, and the experimental data are compared with the finite element results to verify the effectiveness of the model and the correctness of the modeling approach. Based on this, a sensitivity analysis of reinforcement effects is conducted by varying various parameters of polyurethane cement material used for strengthening the bridge piers, aiming to obtain a more reasonable form of reinforcement. This study aims to provide a rational basis and reference for applying polyurethane cement reinforcement in strengthening curved girder bridge piers.

The experimental model is a continuous two-span curved bridge with unequal heights, featuring a radius of 4250 mm. The height of pier 1 is 730 mm, pier 2 is 880 mm, and pier 3 is 1030 mm. Four polytetrafluoroethylene (PTFE) laminated rubber bearings with a diameter of 150 mm and a thickness of 50 mm are utilized to connect the upper part of pier 1 and pier 3 to the main girder. For pier 2, a cast-in-place pier-beam integral form is employed. The longitudinal reinforcement for the piers consists of  $\Phi 8$  steel bars, totaling ten in number, with spiral ties using 12# galvanized iron wire at a spacing of 45 mm. The cross-section of the bridge deck is rectangular. The concrete for the piers is C15 concrete, while for the bridge deck it's C30 concrete [7]. Figure 6 shows construction photos of the experimental bridge.



*Fig. 6 - The experimental bridge construction site photos [7]*

### Introduction to the OpenSees Program

Since its formal inception in 1999, the OpenSees program has been widely adopted in research projects at advanced universities and higher research institutions in developed countries. It has successfully simulated numerous real-world engineering projects and shake table experiments, validating its excellent accuracy in the field of nonlinear numerical simulations.

The core code of OpenSees can be categorized into three major modules: 1. Model Builder: This module involves defining the model by specifying node coordinates, constraints, loads, material constitutive laws, section properties, element types, and coordinate transformations. It completes the process of model creation. 2. Analysis: This module controls numerical analysis by specifying the analysis solver type, load increment steps, iteration algorithms, and convergence tolerance. It is responsible for the overall control of numerical analysis. 3. Recorder: This module defines data and oversees the output of simulation results. It plays a crucial role in managing the output of running results. These three modules collectively form the basic structure of OpenSees, allowing for effective structural analysis and control over nonlinear numerical simulations.

### Components and Material Parameters

The selection of a suitable material constitutive model is essential for ensuring the accuracy of structural elastoplastic analysis. Conventional curved girder bridge piers are typically composed of ordinary concrete and reinforcing steel as constituent materials. In addition to these, the material properties of polyurethane cement also need to be taken into consideration for finite element analysis. The mechanical characteristics of these three materials play a significant role in determining the performance of the bridge pier, particularly during the nonlinear stage where various nonlinear features manifest to different extents in the hysteresis response of the pier columns.

The OpenSees program offers a variety of uniaxial and multiaxial material models. The use of fiber beam-column element models simplifies the selection of material constitutive models, requiring only the adoption of uniaxial constitutive models under uniaxial loading conditions.

The following presents the constitutive relationship model for polyurethane cement material used in modeling:

Based on the aforementioned experimental analyses, a constitutive relationship for the stress-strain behavior of polyurethane cement has been proposed. The complete stress-strain curve for polyurethane cement is depicted in Figure 7, and the specific parameters for the constitutive model are as follows:

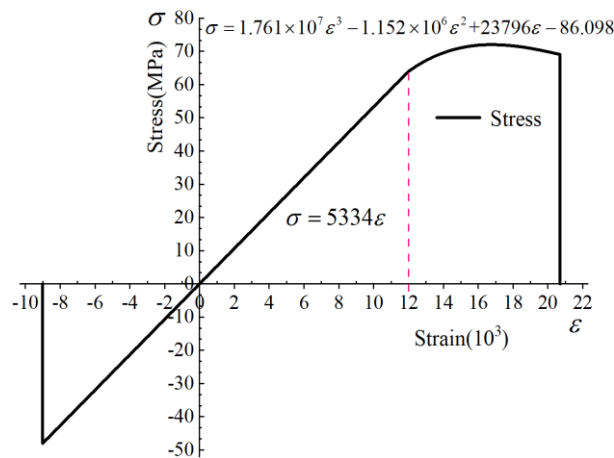


Fig. 7 - Polyurethane Cement Stress-Strain Full Curve (compression as positive)

The elastic modulus of polyurethane cement is 5334 MPa, the Poisson's ratio is 0.27, and the density is in the range of 1.51 to 1.53g/cm<sup>3</sup>. Here, a density of 1520kg/m<sup>3</sup> is used.

### Establishing Finite Element Model

Seismic loads are applied based on the seismic wave data obtained during experiments. The El-Centro seismic wave data are configured for north-south, east-west, and vertical directions, representing longitudinal, transverse, and vertical seismic excitations respectively. Two loading conditions are established: one for a seismic condition with a severity level corresponding to seismic intensity VI and another with a severity level corresponding to seismic intensity VII. These intensity levels are determined by scaling the model and converting to equivalent seismic input intensities.

Using the flexibility method, nonlinear beam-column elements are employed to simulate the experimental bridge pier components. Each component is modeled with a single element, and five Gauss integration points are set. Based on the material composition of the pier and the different constrained states experienced by concrete, the section is divided into four types of fibers: protective layer concrete, hoop-restrained concrete, restrained steel bars, and polyurethane cement. Each steel bar is treated as a fiber.

For a circular section, the core concrete is divided into at least thirty sections radially and ten fiber grids circumferentially. The protective layer concrete is divided into ten sections circumferentially and ten fiber grids radially. In total, the section is divided into 412 fibers.

The material constitutive parameters for each fiber are input based on actual material performance tests or recommended values from relevant studies.

The base nodes of the beam-column elements are fully constrained, with the constraint handling method set to "Plain". Masses, moments, and torques are applied at the top nodes of the elements to simulate the connection between the pier and the beam in the original bridge model. The solution to the nonlinear equation system will be achieved through a combination of various iterative algorithms, with a convergence tolerance criterion based on the energy method and an accuracy control of 10<sup>-5</sup>. Finally, a Recorder is utilized to output results such as displacement of the top nodes for post-processing.

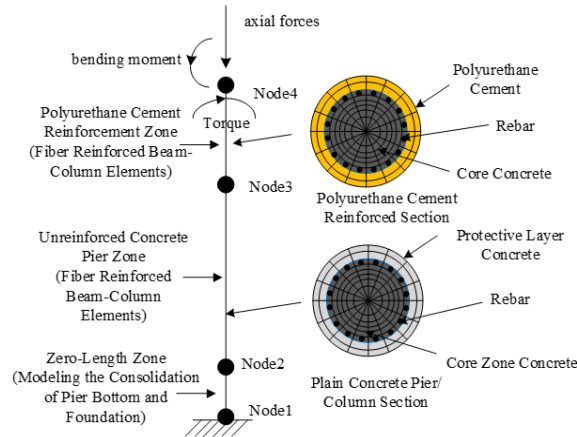
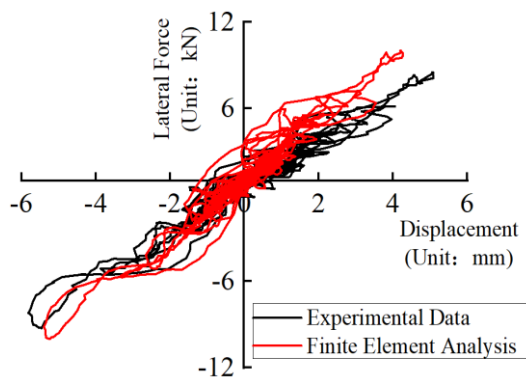


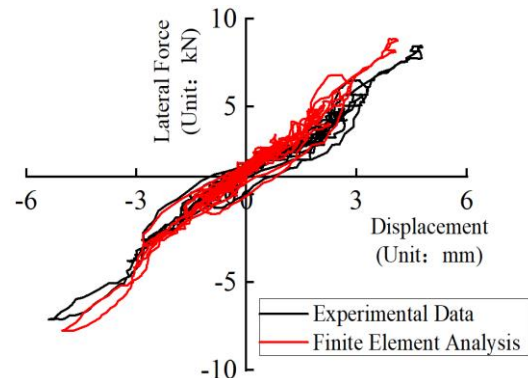
Fig. 8 - Finite Element Modeling Schematic

### Analysis Results Verification

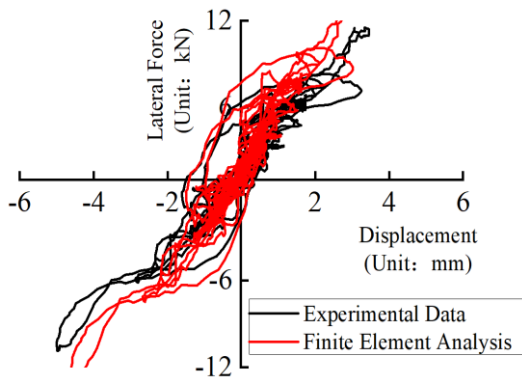
After conducting finite element simulation and obtaining the results, a comparison was made between the measured hysteresis curves of each bridge pier specimen in the shake table test. This paper presents a comparison of the experimental values and finite element data hysteresis curves, as well as the pier top displacement under intensity level VI, as shown in Figure 9. The hysteresis curves generated by the finite element numerical simulation generally coincide well with those obtained from the experimental results. The finite element simulation effectively reflects the behavior of the bridge pier during the loading process: as seismic response changes, the pier top displacement varies. Over time, significant displacement occurs in the pier, resulting in substantial lateral forces. Subsequently, due to elastic-plastic properties of materials, situations arise where seismic load is zero while displacement and lateral forces are not zero.



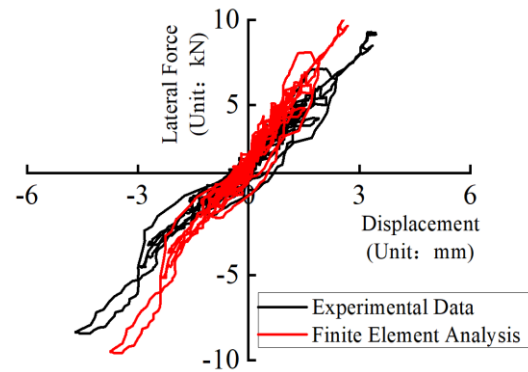
(a) Unreinforced Pier Top Longitudinal Hysteresis Curve under Intensity Level VI



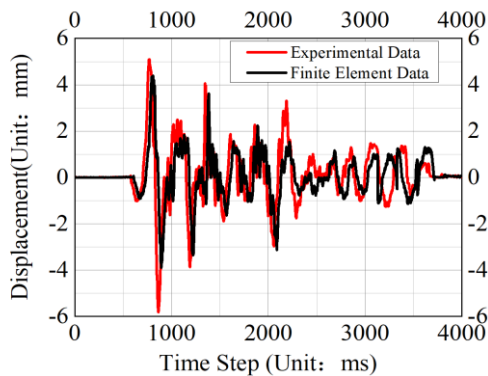
(b) Unreinforced Pier Top Transverse Hysteresis Curve under Intensity Level VI



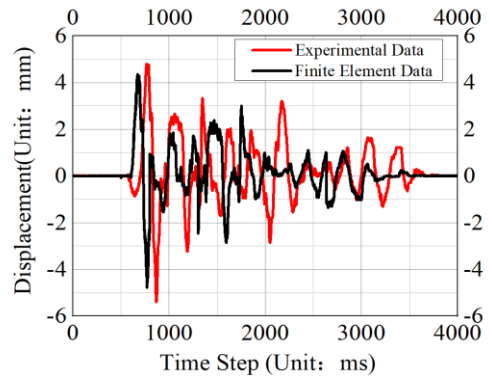
(c) Reinforced Pier Top Longitudinal Hysteresis Curve under Intensity Level VI



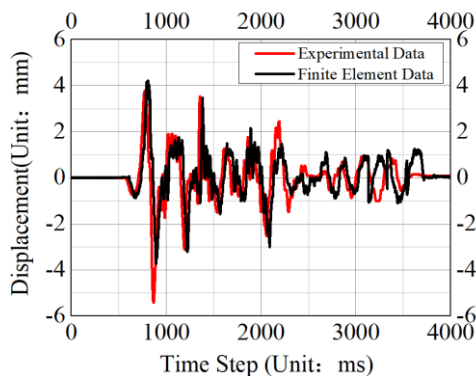
(d) Reinforced Pier Top Transverse Hysteresis Curve under Intensity Level VI



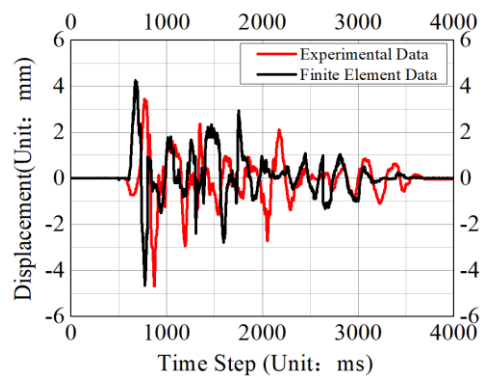
(e) Unreinforced Pier Top Longitudinal Displacement under Intensity Level VI



(f) Unreinforced Pier Top Transverse Displacement under Intensity Level VI



(g) Reinforced Pier Top Longitudinal Displacement under Intensity Level VI



(h) Reinforced Pier Top Transverse Displacement under Intensity Level VI

Fig. 9 - Comparison Chart of Measured Values and Finite Element Data for Pier Top Hysteresis Curves

The measured transverse and longitudinal displacements under different intensities and conditions consistently exceed the results obtained through finite element simulation. Specifically, at intensity level VI, the unreinforced pier top transverse and longitudinal displacement responses from the finite element model are approximately 0.78 to 0.92 times the experimentally measured data. After reinforcement at intensity level VI, the transverse and longitudinal displacement responses of the pier top from the finite element model are approximately 0.75 to 1.12 times the experimentally measured data. At intensity level VII, the unreinforced pier top transverse and longitudinal

displacement responses from the finite element model are approximately 0.65 to 0.91 times the experimentally measured data. Additionally, after reinforcement at intensity level VII, the transverse and longitudinal displacement responses of the pier top from the finite element model are approximately 0.68 to 0.97 times that of experimental measurements. The discrepancies may be attributed to: 1) deviations in control parameters of concrete and steel constitutive models during reverse loading; 2) a certain degree of discrepancy between simulating polyurethane cement material according to concrete constitutive type and actual polyurethane cement material; 3) changes in various loads acting on pier tops due to seismic load effects; 4) some error between input seismic waves and those used in experiments.

Comparison between shake table test results and OpenSees finite element simulation data under similar conditions indicates that hysteresis curves and displacement time history curves for pier tops fall within a reasonable range for both seismic intensities, suggesting that OpenSees modeling method has sufficient accuracy and reliability for this study.

## PARAMETER SENSITIVITY ANALYSIS

### The Influence of Pier Height

The height of bridge piers has a significant impact on the various natural frequencies of the overall bridge structure. As the height of bridge piers increases, the overall stiffness of the structure decreases, leading to larger overall natural periods and smaller seismic design acceleration response spectrum values. Consequently, the horizontal shear forces experienced by the piers decrease. However, taller piers result in larger moments at the base of the piers for the same shear force, leading to greater horizontal displacement at the top of the piers. Therefore, pier height has a complex influence on the seismic performance of bridges. It is necessary to analyze how polyurethane cement affects seismic performance at different pier heights.

In this study, we will consider piers with heights of 640mm, 760mm, 880mm, 1000mm, and 1120mm. Figure 10 illustrates a schematic diagram showing polyurethane cement reinforcement with only changes in pier height while keeping other parameters constant. The study aims to investigate how polyurethane cement reinforces piers of different heights under conditions where other parameters remain unchanged.

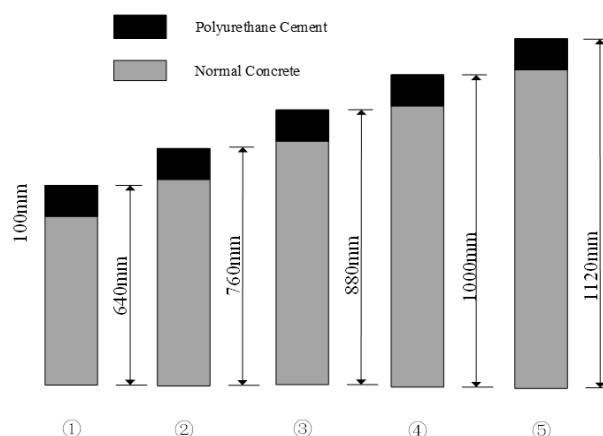


Fig. 10 - Schematic Diagram of Reinforcement by Changing Pier Height

The aforementioned models will undergo finite element analysis using the validated method. The decrease in maximum transverse and longitudinal bridge displacements at the pier top under intensity levels VI and VII will be utilized to assess the seismic effectiveness of polyurethane-reinforced piers. The collected data will be organized into Table 1.

Tab. 1 - Finite Element Model Maximum Displacements at Different Pier Heights (Unit: mm)

Model	Reinforcement Status	Intensity Level VI Transverse Maximum Displacement	Intensity Level VI Longitudinal Maximum Displacement	Intensity Level VII Transverse Maximum Displacement	Intensity Level VII Longitudinal Maximum Displacement
①	Not Reinforced	4.271	3.494	8.154	6.648
	Reinforced	4.139	3.277	4.770	3.703
	Reinforcement Effect	0.031	0.062	0.415	<b>0.443</b>
②	Not Reinforced	4.834	3.994	8.427	7.349
	Reinforced	4.704	3.802	5.262	4.319
	Reinforcement Effect	0.027	0.048	0.376	<b>0.412</b>
③	Not Reinforced	5.391	4.583	10.256	8.721
	Reinforced	5.261	4.396	6.979	5.656
	Reinforcement Effect	0.024	0.041	0.32	<b>0.352</b>
④	Not Reinforced	6.224	5.214	11.606	9.842
	Reinforced	6.087	4.976	8.613	7.12
	Reinforcement Effect	0.022	0.046	0.258	<b>0.277</b>
⑤	Not Reinforced	6.845	6.782	13.054	11.867
	Reinforced	6.715	6.572	10.208	9.090
	Reinforcement Effect	0.019	0.031	0.218	<b>0.234</b>

When all other parameters are held constant, an increase in pier height leads to a gradual increase in peak displacements in both transverse and longitudinal directions. This suggests that as the pier height increases, the stiffness of the specimen decreases, resulting in a reduced capacity to resist seismic loads. When comparing the reinforcement effects of five different height pier models at various intensity levels (the difference in displacement between reinforced and unreinforced conditions, normalized by the unreinforced displacement), it is found that the maximum reinforcement effects for the five models are 0.443, 0.412, 0.352, 0.277, and 0.234 respectively.

Therefore, within a certain range, taller piers exhibit poorer reinforcement effects with polyurethane cement. This may be attributed to increased pier height leading to decreased bridge stiffness, increased flexibility, and larger response under seismic loads. Consequently, the seismic effects on the material at the top of the pier become more pronounced, resulting in a smaller seismic resistance effect for the same polyurethane cement material. Overall, these findings suggest that taller piers may have a detrimental impact on their ability to withstand seismic forces when using polyurethane cement as a reinforcing material.

### Impact of Retrofitting Height

Polyurethane cement demonstrates high tensile strength and good tensile deformation capacity, making it a suitable material for reinforcement. Therefore, conducting a sensitivity analysis on the retrofitting height parameter for polyurethane cement is essential to understand its impact on the seismic performance of curved bridge piers. In this study, five different retrofitting schemes with polyurethane cement heights of 50mm, 100mm, 150mm, 200mm, and 250mm are proposed.

Figure 11 depicts a schematic representation of the proposed schemes where only the retrofitting height of polyurethane cement is varied while keeping other parameters constant. This analysis aims to explore the sensitivity of the seismic retrofitting effect on bridge piers concerning different polyurethane cement retrofitting heights.

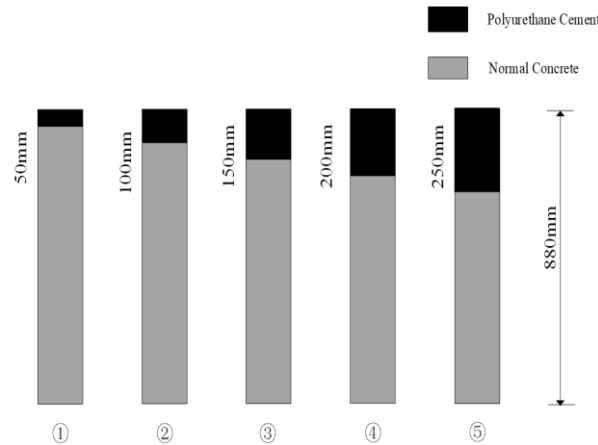


Fig. 11 - Altering Retrofitting Height Schematic

Conduct finite element analysis on the aforementioned models using the validated method. Assess the seismic resistance of the bridge piers retrofitted with polyurethane by examining the reduction in maximum horizontal and vertical bridge displacements under seismic intensities VI and VII. Present the collected data in Table 2.

Tab. 2 - Finite element model maximum displacement at different widths of polyurethane cement (Unit: mm)

Model	Reinforcement Status	Intensity Level VI Transverse Maximum Displacement	Intensity Level VI Longitudinal Maximum Displacement	Intensity Level VII Transverse Maximum Displacement	Intensity Level VII Longitudinal Maximum Displacement
①	Not Reinforced	5.391	4.583	10.256	8.721
	Reinforced	5.301	4.487	8.338	7.062
	Reinforcement Effect	0.017	0.021	0.187	<b>0.190</b>
②	Not Reinforced	5.391	4.583	10.256	8.721
	Reinforced	5.261	4.396	6.979	5.656
	Reinforcement Effect	0.024	0.041	0.32	<b>0.352</b>
③	Not Reinforced	5.391	4.583	10.256	8.721
	Reinforced	5.232	4.358	6.659	4.841
	Reinforcement Effect	0.03	0.049	0.351	<b>0.445</b>
④	Not Reinforced	5.391	4.583	10.256	8.721
	Reinforced	5.179	4.294	6.15	4.787
	Reinforcement Effect	0.039	0.063	0.4	<b>0.451</b>
⑤	Not Reinforced	5.391	4.583	10.256	8.721

Reinforced	5.172	4.281	6.107	4.714
Reinforcement Effect	0.041	0.066	0.405	<b>0.459</b>

Maintaining other parameters constant, an increase in the height of polyurethane cement reinforcement leads to a gradual decrease in peak displacements at the top of the pier in both horizontal and vertical directions. This suggests that a greater height of polyurethane cement reinforcement results in increased stiffness for the specimen. When comparing the reinforcement effects at different intensities (difference in displacement between reinforced and unreinforced states, as well as the ratio of unreinforced displacement), it is observed that the maximum values for the five models are 0.190, 0.352, 0.445, 0.451, and 0.459 respectively. Therefore, within a certain range, a higher height of polyurethane cement reinforcement leads to improved reinforcement effects on curved bridge piers. This can be attributed to the enhanced stiffness and ductility provided by polyurethane cement reinforcement, resulting in reduced response under seismic loads, particularly at the top of the pier.

However, due to its limited flexibility, high stiffness, susceptibility to plastic deformation and relatively high cost; selecting an appropriate width is crucial for optimizing economic benefits and reinforcing effects when strengthening piers.

### Parameter Optimization Analysis

Based on the sensitivity analysis of the parameters for polyurethane cement reinforced bridge piers, it is evident that the effectiveness of polyurethane cement reinforcement decreases with increasing pier height. Conversely, a thicker layer of polyurethane cement reinforcement leads to a more pronounced effect. Therefore, by optimizing the parameters of polyurethane cement reinforcement height and pier height, we can identify the most cost-effective parameter range to optimize the economic efficiency of constructing polyurethane cement reinforced bridge piers.

The ratio of polyurethane cement reinforcement height to pier height, referred to as the reinforcement ratio, is a crucial control indicator in practical engineering. By using the maximum displacement in the vertical bridge direction under Level VII intensity as a reference value for reinforcement effectiveness, we can determine an optimal reinforcement ratio based on its growth rate. The data from the finite element model is summarized in Table 3 and illustrated in Figure 12.

Tab. 3 - Parameter Optimization Analysis

Reinforcement Ratio	0.057	0.089	0.100	0.114	0.132	0.156	0.171	0.227	0.284
Reinforcement Effect	0.19	0.234	0.277	0.352	0.412	0.443	0.445	0.451	0.459

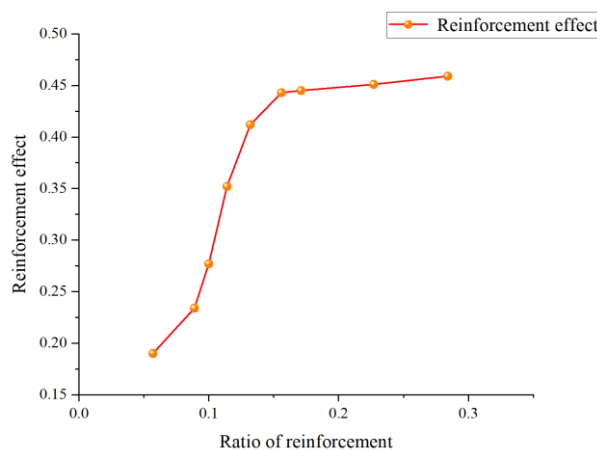


Fig. 12 - Parameter Optimization Analysis Chart

The results from finite element simulation indicate that when the reinforcement ratio is approximately 0.132, there is a greater growth rate in reinforcement effect compared to when it is around 0.156. As the reinforcement ratio exceeds 0.156, there is a gradual decrease in growth rate towards zero, potentially resulting in material waste. Thus, it can be concluded that optimal economic efficiency of reinforcement occurs at a ratio around 0.132 which provides scientific support for reinforcing bridge piers with polyurethane cement.

## CONCLUSIONS

This dissertation focuses on the reinforcement of curved bridge piers with polyurethane cement [7] and utilizes OpenSees for numerical simulation of experimental results. The numerical simulation results are compared with shake table test data, confirming a good fit between the finite element modeling and experimental results. Through finite element parameter sensitivity analysis, with bridge pier height, material thickness, and bridge pier type as variables, sensitivity patterns of corresponding reinforcement parameters are determined. Additionally, parameter optimization leads to the following conclusions:

1. Polyurethane cement has an isotropic elastic model with basic properties such as tensile strength, compressive strength, flexural strength all around 5334 MPa, and a Poisson's ratio of approximately 0.27. The ultimate tensile strain ( $\epsilon_t$ ) is  $9 \times 10^{-3}$ , and the ultimate tensile stress ( $\sigma_t$ ) is 48 MPa. In the nonlinear phase, the ultimate compressive strain ( $\epsilon_c$ ) is  $16.7 \times 10^{-3}$ , and the ultimate compressive stress ( $\sigma_c$ ) is 72.04 MPa. Polyurethane cement exhibits high compressive strength, strong toughness, elevated tensile strength, and good ductility, making it a suitable material for reinforcement.
2. Utilizing the OpenSees platform for simulations of pier specimens from a three-axis shake table experiment involving polyurethane cement-reinforced curved beam bridge piers resulted in displacement time-history curves that closely aligned with experimentally measured displacement time-history curves. This provides evidence supporting the rationality of the adopted material constitutive model and related parameter settings.
3. Sensitivity analysis of polyurethane cement-reinforced curved beam bridge pier parameters revealed that within a certain range under identical conditions, taller piers exhibit diminished effects from polyurethane cement reinforcement; similarly, thicker polyurethane cement reinforcement within a certain range yields more pronounced reinforcement effects.
4. Based on data from sensitivity analysis, the parameters of polyurethane cement reinforcement height and pier height were optimized. It was found that when the ratio of polyurethane cement reinforcement height to pier height is around 0.132, the growth rate of reinforcement effect is maximized, suggesting optimal economic efficiency for reinforcement.

The findings from this study serve as valuable reference for seismic reinforcement strategies pertaining to curved beam bridge piers, enabling practical engineering schemes to be guided towards improved economic viability.

## ACKNOWLEDGEMENTS

The authors would like to thank the Jilin Province Transportation Innovation and Development Support (Science and Technology) Project (2020-1-9) and the Heilongjiang Province Transportation Investment Group Company Limited for project support (2023-1-10).

## REFERENCES

- [1] Murugan K., Sengupta A.K., 2020. Seismic performance of strengthened reinforced concrete columns, Structures, Volume 27, Pages 487-505, ISSN 2352-0124, <https://doi.org/10.1016/j.istruc.2020.05.059>.
- [2] Zhang D.W., Zhao Y.X., Jin W.L., et al, 2017. Shear strengthening of corroded reinforced concrete columns using pet fiber based composites, Engineering Structures, Volume 153, Pages 757-765, ISSN

0141-0296, <https://doi.org/10.1016/j.engstruct.2017.09.030>.

- [3] Bousias S., Spathis A.L., Michael N.F., 2007. Seismic Retrofitting of Columns with Lap Spliced Smooth Bars Through FRP or Concrete Jackets, *Journal of Earthquake Engineering*, Volume 11, Pages 653-674, ISSN 1363-2469, <https://doi.org/10.1080/13632460601125714>.
- [4] Yuan Y., Wang Z.Y., 2019, Shear behavior of large-scale concrete beams reinforced with CFRP bars and handmade strip stirrups, *Composite Structures*, Volume 227, Pages 111253, ISSN 0263-8223, <https://doi.org/10.1016/j.compstruct.2019.111253>.
- [5] Ding F.X., Lu D.R., Bai Y., et al, 2018, Behaviour of CFRP-confined concrete-filled circular steel tube stub columns under axial loading, *Thin-Walled Structures*, Volume 125, Pages 107-118, ISSN 0263-8231, <https://doi.org/10.1016/j.tws.2018.01.015>.
- [6] Cao Y.G., Zhang Y., Liu M.Y., et al, 2020, Analysis-oriented stress-strain model for FRP-confined predamaged concrete, *Journal of Building Engineering*, Volume 36, Pages 102121, ISSN 2352-7102, <https://doi.org/10.1016/j.jobe.2020.102121>.
- [7] Zhang H.Y., Sun Q.S., Xia H.X., et al. 2022, Repair of a single pier of a continuous-curved-beam bridge with polyurethane cement. *Proceedings of the Institution of Civil Engineers -Structures and Buildings*, Volume 177, Pages 21-39, ISSN 0965-0911, <https://doi.org/10.1680/jstbu.21.00167>
- [8] He R.L., Grelle S., Sneed L.H., 2013, Rapid repair of a severely damaged RC column having fractured bars using externally bonded CFRP, *Composite Structures*, Volume 101, Pages 225-242, ISSN 0263-8223, <https://doi.org/10.1016/j.compstruct.2013.02.012>.
- [9] Yasir F.A., Kevin R.M., 2019, Polyurethane-FRP External Strengthening of RC Beams with No Steel Stirrups, *Journal of Composites for Construction*, Volume 23, Pages 04018074, ISSN 1943-5614, [https://doi.org/10.1061/\(ASCE\)CC.1943-5614.0000916](https://doi.org/10.1061/(ASCE)CC.1943-5614.0000916)
- [10] Ali A., Zhu H., Haruna S.I., et al, 2023, Impact resistance of ultra-high-performance concrete retrofitted with polyurethane grout material: Experimental investigation and statistical analysis, *Structures*, Volume 55, Pages 185-200, ISSN 2352-0124, <https://doi.org/10.1016/j.istruc.2023.06.043>.
- [11] Zhong Y.H., Xu S.J., Chi J., et al, 2023, Experimental study on the interface bonding characteristic of polyurethane and pavement materials, *Construction and Building Materials*, Volume 397, Pages 132390, ISSN 0950-0618, <https://doi.org/10.1016/j.conbuildmat.2023.132390>.
- [12] Li Y., Kong K., Wang R.J., Yang X.B., 2023, Mechanical properties and abrasion resistance of polyurethane mortar subjected to freeze–thaw cycles and sulfate attack, *Journal of Building Engineering*, Volume 78, Pages 107760, ISSN 2352-7102, <https://doi.org/10.1016/j.jobe.2023.107760>.
- [13] Ning H., Li J., Li X., et al, 2022, Study on Toughening and Temperature Sensitivity of Polyurethane Cement (PUC), *Materials*, Volume 15, Issue 12, Pages 12, ISSN 1512-4318, <https://doi.org/10.3390/ma15124318>.
- [14] Hussain H.K., Zhang L.Z., Liu G.W., 2013, An experimental study on strengthening reinforced concrete T-beams using new material poly-urethane-cement (PUC), *Construction and Building Materials*, Volume 40, Pages 104-117, ISSN 0950-0618, <https://doi.org/10.1016/j.conbuildmat.2012.09.088>.
- [15] Verdolotti, L D.M., E., et al, 2012, Hydration-induced reinforcement of rigid polyurethane–cement foams: mechanical and functional properties. *Journal of Materials Science*, Volume 47, Pages 6948–6957, ISSN 1573-4803, <https://doi.org/10.1007/s10853-012-6642-5>.
- [16] Wang J.L., Liu J.B., Ye L.S., 2013, Research on the application technology of hollow slab girder bridge reinforcement using MPC composites, *Highway*, Volume 08, Pages 39–43, ISSN 0451-0712, <https://doi.org/10.3969/j.issn.0451-0712.2013.08.008>.
- [17] Hussain H.K., Liu G.W., Yong Y.W., 2014, Experimental study to investigate mechanical properties of new material polyurethane–cement composite (PUC), *Construction and Building Materials*, Volume 50, Pages 200-208, ISSN 0950-0618, <https://doi.org/10.1016/j.conbuildmat.2013.09.035>.
- [18] Guan P.W., Tu Y.Z., Zhang P., et al, 2019, Study on uniaxial tension-compression principal relationship of ultra-high performance concrete, *Journal of Composite Materials*, Volume 36, Pages 1295–1305, ISSN 1000-3851, <https://doi.org/10.13801/j.cnki.fhclxb.20180703.004>.

# PREVENTION AND DRAINAGE TECHNOLOGY FOR ANTI-STUCK AND DISCHARGING DURING SHIELD TUNNELING IN COMPLEX RED ROCK STRATA WITH ULTRA-LARGE DIAMETER UNDER NORMAL AND PRESSURIZED CONDITIONS

*Xin Dong<sup>1</sup>, Qingcheng Zeng<sup>1</sup>, Jian Ouyang<sup>1</sup>, Dawei Hu<sup>2</sup>, Xingwei Xue<sup>3</sup> and Kexin Zhang<sup>4</sup>*

1. Engineering Department, Guangzhou Expressway Co., LTD, Guangzhou, China
2. Tunnel Engineering Department, China Railway Fourth Survey and Design Institute Group Co., LTD, Wuhan, China
3. Shenyang Jianzhu University, School of Traffic Engineering, Department of Bridge Engineering, Shenyang, China;
4. Shenyang Jianzhu University, School of Traffic Engineering, Department of Bridge Engineering, Shenyang, China; [jt\\_zkx@sjzu.edu.cn](mailto:jt_zkx@sjzu.edu.cn)

## ABSTRACT

During the construction process of shield tunnelling with ultra-large diameter under normal and pressurized conditions, problems such as mud cake formation on the cutterhead, stagnation of mud in the chamber, blockage of slurry discharge chute, high cutterhead torque, and slow excavation speed are prone to occur. In severe cases, these issues can impact construction progress and pose a threat to construction safety. Taking the Guangzhou Haizhu Bay Tunnel project as a case study, this paper proposes prevention and drainage technology for anti-stuck and discharging during shield tunnelling in complex red rock strata with ultra-large diameter under normal and pressurized conditions, focusing on mud slurry control, optimization of cutterhead flushing system, excavation parameter control, and cutter tool optimization.

## KEYWORDS

Red rock strata, Normal and pressurized cutterhead, Mud-water balance, Anti-stuck and discharging

## BACKGROUND

In recent years, with the development of economy and society, the number of ultra-large diameter shield tunnelling projects constructed in China has been increasing day by day [1-4]. Stuck discharging has a significant impact on shield tunnelling construction. On the one hand, it can cause damage to the shield machine, such as cutterhead wear, main bearing seal damage, excessive wear of the screw conveyor, etc [5,6]. On the other hand, it will lead to difficulties in shield tunnelling, severe over-excavation, difficult control of settlement, and even collapse [7-9].

The shield cutterhead clogging with muck is a common challenge encountered during shield tunnelling in cohesive soil layers such as weathered (full, middle) mudstone, muddy siltstone, muddy sandstone, silty soil, silty clay, etc [10]. It is a phenomenon in which the shield cutterhead cuts through the soil in the above-mentioned layers during tunnelling, causing the excavated muck to

become trapped between the cutterhead and the tunnel face. Under the squeezing action of the shield machine, this muck forms solid or semi-solid block-like material that adheres to the cutterhead [11,12]. When the shield cutterhead clogs with muck, the cutter tools on the cutterhead will gradually get stuck in the hardened clay, resulting in reduced penetration depth when cutting through the soil layers. When the tools are completely covered by the muck cake, the cutterhead effectively becomes a cylindrical shield. If tunnelling continues in this state, the friction between the shield machine cutterhead and the tunnel face converts kinetic energy into heat, leading to a physical and chemical process similar to “clay burning pottery.” This will completely compromise the cutting ability of the shield cutterhead and significantly decrease the controllability of tunnelling risks, posing a major threat to equipment safety [13-15]. Therefore, research on the mechanism, prevention, and control technology of muck cake formation is particularly important [16].

This article takes the Haizhuwan Tunnel in Guangzhou as an example to analyze the prevention and treatment of muck cake formation during shield tunnelling with large-diameter EPB (Earth Pressure Balance) and pressurized cutterhead. The composite bottom layers crossed by the tunnel are mainly composed of highly weathered and strongly weathered mudstones and mud siltstones, which are rich in clay mineral particles and powdery materials. These debris and powdery materials with sticky particles serve as the basic materials for muck cake formation during tunnel construction. Mudstones and mud siltstones with clay and debris content exceeding 30% are highly prone to muck cake formation. In order to compare the formation and prevention of muck cakes during shield tunnelling with large-diameter EPB and pressurized cutterheads, the East-West Line Tunnel employed EPB and pressurized cutterhead EPB tunnel boring machines for construction. A systematic study was conducted on the causes and risks of muck cake blockage and accumulation with large-diameter EPB and pressurized cutterheads, summarizing the experience of shield tunnelling with large-diameter EPB and pressurized cutterheads to mitigate the risks of blockage, improve tunnelling efficiency, and provide references for similar projects.

## INTRODUCTION TO ENGINEERING BACKGROUND

This project is the Haizhuwan Tunnel project, with the main line design mileage ranging from EK0-415.730 to EK3+933.057, totaling 4348.787 m in length. The starting point of the main line design of this project connects to the existing Dongxiaonan Viaduct, and the route extends southward in the form of a double-tube single-layer shield tunnel, passing under the Pearl River Likeng Waterway, Luoxi Island, and Sanzhixiang Waterway. After the shield tunnel ends at the north end of Nanpu Avenue, it continues in the form of a buried tunnel to cross Nanpu Avenue and connect to the ground, linking up with the bridges of the southern section of the project.

The centerline design adopts the revised planned centerline based on the urban planning and starts with a two-way 4-lane bridge connecting to the Dongxiaonan Viaduct. After crossing Nanzhou Road, it goes underground, with a shield tunnel passing under the Pearl River Likeng Waterway, Luoxi Island, and Sanzhixiang Waterway. Heading south, it transitions to an underground tunnel to cross Nanpu Avenue, then emerges at the surface to connect with the bridges of the southern section of the project. The tunnel has a total length of 3463.057 m, with the shield tunnel section totaling 2077 m and the cut-and-cover section totaling 1386.057 m. The outer diameter of the shield tunnel is 14.5 m, providing a double 6-lane configuration. The minimum horizontal radius of the shield tunnel section is 1000 m, while the onshore section has a minimum horizontal radius of 450 m, and the minimum radius for the Dongxiaonan Viaduct is 160 m. The net distance between adjacent tunnel sections is generally not less than 1.0 D, with the connection between the starting and receiving sections controlled at 0.6-0.7 D. The minimum distance between the slope change points inside the tunnel is 342.467 m, all meeting the standard requirements. The main line has a minimum gradient of 0.3% and a maximum longitudinal slope of 4%. The vertical curve minimum radius for the viaduct section is 3000 m, meeting the requirement for a design speed of 60 km/h; while for the tunnel

section, the minimum vertical curve radius is 3800 m, also meeting the design speed requirement of 60 km/h.

The strata mainly crossed by the shield tunnel section are composed of strong, medium, and slightly weathered silty sandstone. The longitudinal section layout is shown in Figure 1.

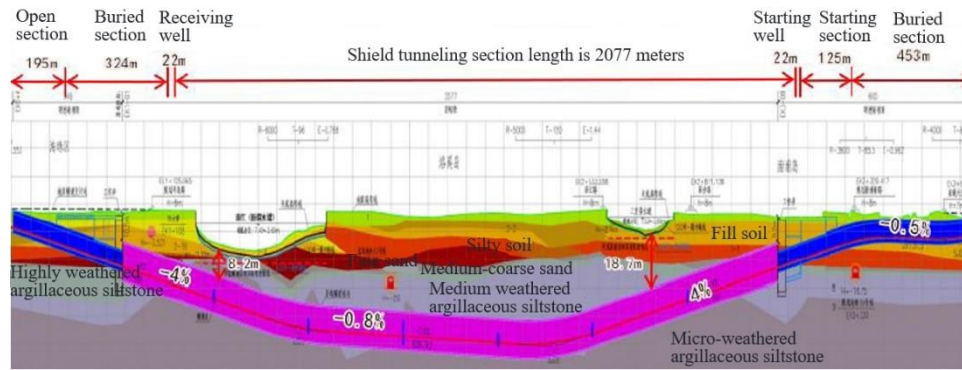


Fig. 1 – Schematic Diagram of Geological Conditions in the Hai Zhu Wan Tunnel Shield Section

The middle section of the tunnel is constructed using the shield tunnelling method, with a circular cross-section for the shield tunnel section. The outer diameter is 14.5 m, inner diameter is 13.3 m, and the thickness of the segment is 0.6 m. The cross-section layout is shown in Figure 2.

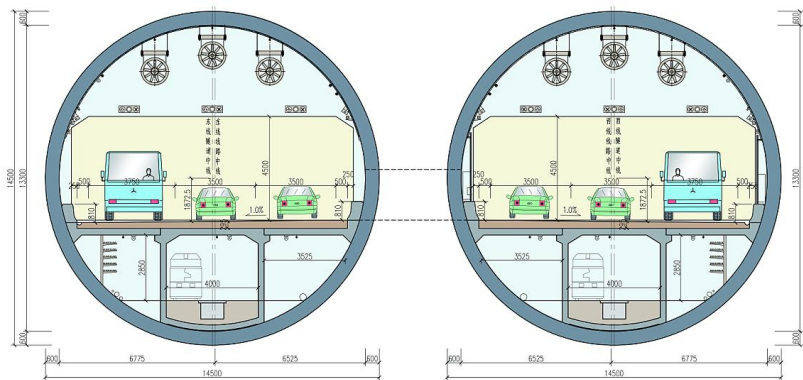


Fig. 2 – Diagonal Splitting of Bridge Abutment Cap Beam Block

## OVERVIEW OF THE SHIELD TUNNELING MACHINE

Two slurry balanced shield tunnelling machines are used in the shield tunnelling section. The excavation diameter of the shield machine is 15.07 m. The shield machine on the east line consists of a shield machine main body and 4 trailing gantries; the shield machine on the west line consists of a main body and 5 trailing gantries, with a maximum excavation speed of 50 mm/min.



Fig. 3 – Layout Drawing of the Cutterhead (Atmospheric) on the West Line



Fig. 4 – Layout Drawing of the Cutterhead (Pressurized) on the East Line

The West Line features a Herrenknecht slurry balanced shield tunnelling machine with a cutterhead diameter of 15.07 m, a total machine length of 152 m, a machine weight of approximately 4495 t, and a total machine power of about 11200 kW. The main drive power is around 5600 kW, with a rated torque of 42972 kN.m at 1.13 rpm. The working pressure of the shield machine is 9 bar. The cutterhead excavation diameter is 15.07 m, and the cutterhead is equipped with a pressure-controlled tool changing function, featuring a panel structure with an opening rate of 30%. The cutterhead is equipped with a total of 246 cutting tools and 12 sets of edge scraping blade components, with the specific tool configuration including 50 replaceable scraping blades for atmospheric pressure, 12 replaceable center disc cutters for atmospheric pressure, 60 replaceable face disc cutters for atmospheric pressure, 4 replaceable edge disc cutters for atmospheric pressure, 150 standard scraping blades, and 12 sets of standard edge scraping blades, achieving “full coverage” of the cutterhead excavation trajectory, as shown in Figure 3.

The East Line features a CREG slurry balanced shield tunneling machine with a cutterhead diameter of 15.07 m, a total machine length of 128 m, a machine weight of approximately 4300t, and a total machine power of about 9755 kW. The main drive power is around 5600 kW, with a rated torque of 42784 kN.m. The maximum total thrust is 222173 kN, and the shield machine is designed with a maximum pressure capacity of 8 bar. The cutterhead excavation diameter is 15.07 m, and the cutterhead does not have a pressure-controlled tool changing function. It has a star-shaped spoke structure with an opening rate of 35%. The cutterhead is equipped with a total of 387 cutting tools and 16 sets of edge scraping blade components. The specific tool configuration includes 6 center disc cutters with a height of 160 mm and a spacing of 101.5 mm, 77 face disc cutters with a height of 160mm and a spacing of 75 mm, 22 edge disc cutters, 180 wide cutting knives with a height of 115 mm and a spacing of 220 mm, 16 sets of edge scraping blades, and 2 overcutting knives with an overcut of 50 mm, achieving “full coverage” of the cutterhead excavation trajectory as shown in Figure 4.

## ANALYSIS OF SLURRY BALANCE SHIELD TUNNELING MACHINE WITH SUPER LARGE DIAMETER FOR MUCK DISCHARGE

The geological strata that the shield tunnel passes through in the middle section of the river mainly consist of strong, medium, and slightly weathered mudstone sandstone. Locally at both ends, it passes through silty clay, medium-coarse sand, and powdery clay layers. The cutterhead at the

center of the shield tunnel on the west line has no opening, with a small opening rate of 30%. The cutterhead opening rate for the east line with a pressurized cutterhead is 35%. In the mudstone sandstone formations, the cutterhead and cutter barrel are prone to mud cake formation, leading to blockages in the muck discharge chute and causing muck stagnation. In complex formations such as fractured zones and heterogeneous strata, as well as in formations with developed joint fissures, there may be issues with inadequate muck discharge or blockages, which, if not properly addressed, could lead to serious consequences.

According to the types of muck accumulation, there are three types of muck stagnation in super large-diameter slurry balance shield tunnelling machines: bottom-type, mud cake-type, and middle-type stagnation.

1. High-strength muck chunks are prone to form bottom-type muck stagnation

The muck consists of large particle size and high-strength muck chunks that accumulate at the bottom of the shield tunnel, blocking the muck discharge chute and outlet, affecting the circulation of the slurry, preventing timely muck removal, resulting in increased tunnelling torque, thrust, decreased speed, abnormal tunnelling parameters, leading to tunnelling difficulties, and causing wear on the surrounding cutter tools, forming bottom muck stagnation.

2. Mud cake-type muck stagnation

The muck is in the form of mud cakes, which adhere to the cutterhead and cutter barrel, causing mud cake buildup in the central area of the cutterhead and cutter barrel, leading to the loss of rock-breaking and soil-cutting functions of the cutter tools. If the mud cakes are severe, it can also result in abnormal shutdown of the tunnel boring machine.

3. Soft on top and hard below easily form midsection muck stagnation

Midsection muck stagnation primarily accumulates in uneven formations with soft on top and hard below, leading to midsection muck stagnation at the cutterhead, unbalanced shield thrust, difficult excavation, and challenging posture control.

## **MUCK SLURRY ANTI-STAGNATION TECHNOLOGY**

### **Enhancing slurry carrying capacity of muck**

1. Principle of mud treatment

This project mainly crosses the mudstone layer, with strong agitating ability and quick density increase, which easily causes mud-cake formation on the cutter head and tool adhesion. For high-density waste slurry, it is first pretreated through a separation system, and then subjected to secondary treatment through a centrifuge and filter press to achieve the purpose of reducing mud performance indicators. To expedite the density reduction process, a suitable coagulant solution for this density is prepared in advance and mixed in the pipeline before centrifugation or filtration. By operating the centrifuge at high speed, the soil and coagulant are separated, thereby achieving the desired density reduction effect. The mud treatment process is shown in Figure 5.

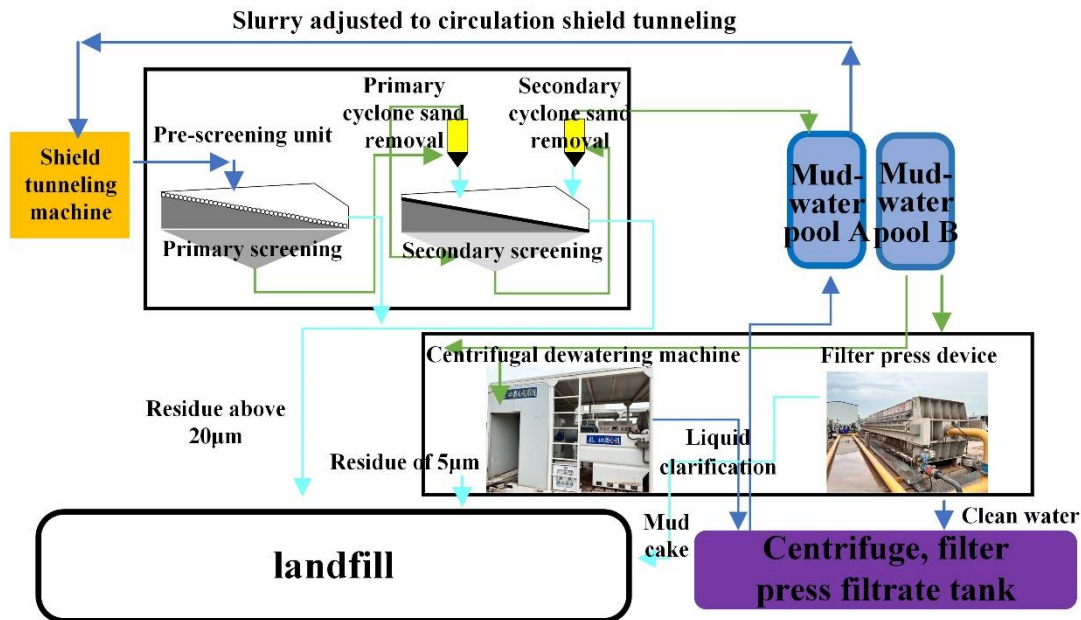


Fig. 5 – Mud-water Treatment Process

## 2. Pre-treatment of mud separation system

After the mud discharged by the shield tunnelling machine is pre-separated by a 2-layer coarse sieve vibrating screen in the mud separation system, the slag with particle size  $>3\text{mm}$  is separated, and the screened mud enters the primary slurry tank. The project is equipped with 12 sets of slurry pump feeding into 12 sets of primary cyclone units (6 sets for the east line and 6 sets for the west line), where the mud undergoes sand removal through the cyclone desander. The fine mud and sand are discharged from the lower end sand nozzle into the lower fine sieve of the mud removal screen. The overflow from the cyclone desander enters the primary intermediate tank, where it is discharged via the drainage pipe or enters the primary and secondary slurry tanks. The thick slurry from the bottom outlet of the secondary cyclone desander enters the upper fine sieve of the mud removal screen. The underflow from the primary and secondary cyclones is dewatered and sieved, separating the dried fine slag material, while the screened slurry liquid enters the primary slurry tank. The overflow from the secondary cyclone enters the settling tank, slurry conditioning tank, or secondary sand removal system. During the shield tunnelling process, if the primary sand removal system is insufficient to reduce the mud density and sand content to a reasonable range, the slurry outlet valve can be switched to allow the mud to enter the secondary sand removal system (which operates on the same principle as the primary sand removal system). Clusters of small diameter cyclone desanders can remove residual powder particles with a particle size  $>20\ \mu\text{m}$  in the mud. If the secondary sand removal system also cannot reduce the mud density to a reasonable range, chemical coagulants from the chemical tank can be pumped into the slurry conditioning tank for viscosity reduction treatment.

## 3. Waste pulp centrifuge + filter press treatment

In this project, polyacrylamide is used as a coagulant, and the solute and solvent are added quantitatively. After fully dissolving through stirring with a stirrer, the expansion time is  $>15\ \text{min}$ , and the settling time is  $\leq 12\ \text{h}$ . After the solution is fully expanded, the solution and high concentration slurry are mixed at the pipeline before the centrifuge using a diaphragm pump. The flow rate of the solution is dynamically adjusted according to the slurry density and flow rate.

The amount of excavation slurry for one ring (2 m) of shield tunnelling in this project is  $360\ \text{m}^3$ ,

which will be treated using a centrifuge. Calculated based on the assumption that particles with a particle size  $<20\ \mu\text{m}$  account for 30% of the total volume of the excavated stratum,  $3000\ \text{m}^3$  of mud circulation is required during normal excavation to increase the mud density by  $0.05\ \text{t/m}^3$ . If the adjusted density of the standby mud is  $1.10\ \text{t/m}^3$ , then a maximum of two rings can be excavated, and the mud density will rise to  $1.2\ \text{t/m}^3$ . Calculated based on the efficiency of one centrifuge processing mud at  $60\text{-}80\ \text{m}^3/\text{h}$ , it will take 50 h to process  $3000\ \text{m}^3$  of mud. Assuming each ring of shield tunnelling takes 4 h, excavating two rings would require 8 h. Therefore, it can be calculated that 6 centrifuges are needed to meet the normal excavation requirements of the shield tunneling.

#### 4. Dynamic control of mud parameters

During each circulation, mud parameters are tested at least twice to ensure that the mud performance meets the excavation requirements. Simultaneously, mud particle analysis should be conducted to understand the separation capabilities of the mud equipment and the distribution of various particle soils in the strata. Mud control indicators include density, viscosity, and sand content. In the shield tunnelling process, mud density is the main control parameter, and its value should neither be too high nor too low. An excessively high density will affect the mud carrying capacity, while an excessively low density will affect the stability of the face. According to the actual excavation conditions of this project, the mud density should be controlled between  $1.1$  and  $1.2\ \text{g/cm}^3$ . Mud viscosity is also a key control parameter in the shield tunnelling process. In terms of suspended soil particles, higher mud viscosity is preferred, but excessively high viscosity can lead to mud cake formation on the cutterhead and blockage of the cutter. Based on the actual excavation conditions of this project, the mud viscosity should be controlled between  $16.5$  and  $26.3\ \text{Pa}\cdot\text{s}$ . In highly permeable strata, the formation speed of the mud film is directly related to the sand content in the mud. This is because sand particles play a role in plugging the pores of the soil mass; therefore, the sand particles should have larger grain sizes compared to the soil mass pores, and the content should be moderate. Therefore, when excavating in mudstone with a shield, attention should be paid to the formation speed of the mud film, and the sand content should be controlled at  $10\text{-}20\%$ . The control range of mud parameters in the red bed geology is shown in Table 1.

*Tab. 1 - Mud Parameters in Red Bed Geology*

Mud Parameters	Density	Viscosity	Sand content
Range	$1.1\sim 1.2\ \text{g/cm}^3$	$16.5\sim 26.3\ \text{Pa}\cdot\text{s}$	$10\sim 20\%$

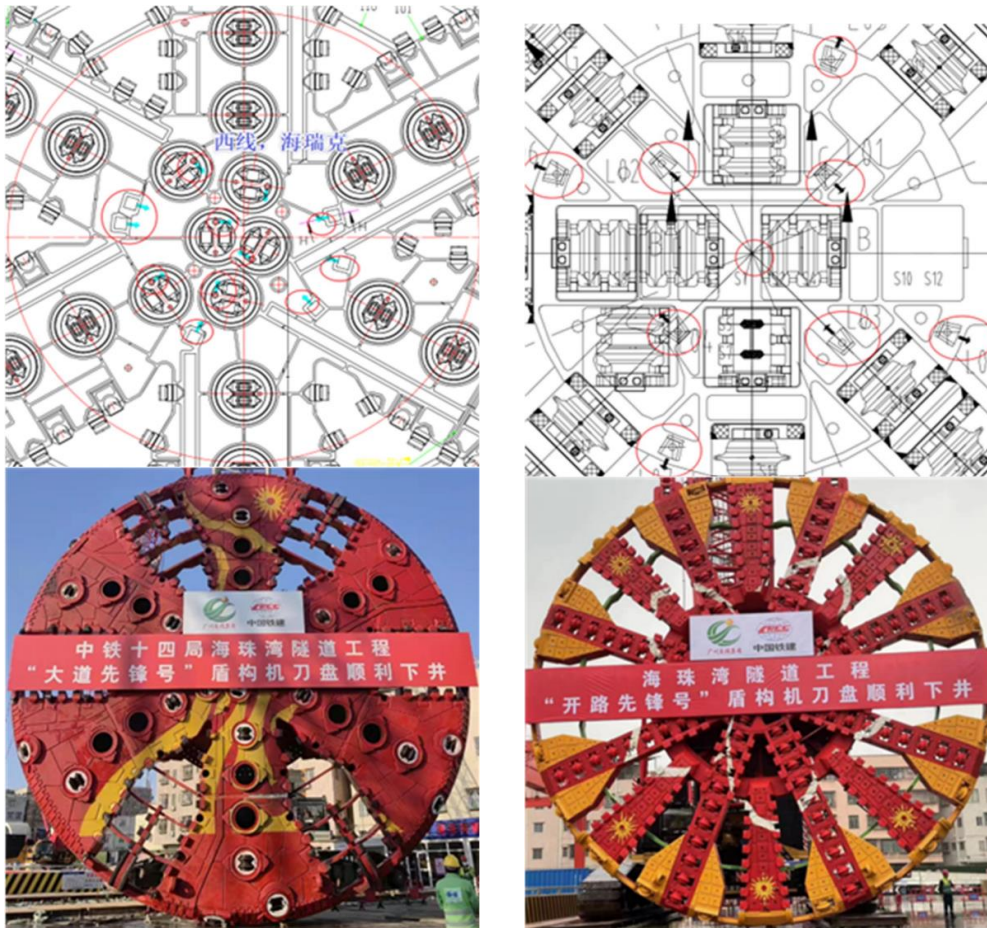
#### Enhanced layout of high-flow radial flushing system at the center of the cutter disc.

Utilize the cutter disc's built-in flushing system to perform high-pressure flushing on the slurry discharge chute, central area of the cutter disc, and cutterhead during shield tunnelling or downtime, strengthen the layout of the high-flow radial flushing system at the center of the cutter disc to prevent mud cakes in the central area of the cutter disc.

During shield tunnelling, ensure constant slurry flow and strengthen the bottom and center flushing of the cutter disc, while other pipelines can be alternately flushed. The number of center flushes on the cutter disc is shown in Table 2. During the manufacturing process of the cutter disc, 12 and 9 flushing holes are respectively designed at the center positions of the normal pressure cutter disc and the pressurized cutter disc panel (see Figure 6). To prevent tool wear caused by mud sticking to the cutter disc, cyclic flushing of the panel is carried out continuously during shield tunnelling.

Tab. 2 - Number of Center Flushes on the Cutter Disc

Cutter disc type	Normal pressure cutter disc	Pressurized cutter disc
Center brush (each)	12	9



(a) West Line Normal Pressure Cutter Disc (b) East Line Pressurized Cutter Disc

Fig. 6 – Cutter Disc Flushing Port Setting

### Handling cutter disc mud cakes.

In this project, the west line is operated with normal pressure for unloading. It was found that the cutter disc center was clogged with mud cakes and all 6 slag discharge slots at the cutter disc edge were completely blocked. The east line has fewer blockages. The following measures were taken to solve the issue. A comparison of mud cake handling methods for normal pressure and pressurized cutter discs is shown in Table 3.

1. Reduce the mud density, the slurry density during excavation must be  $< 1.15 \text{ t/m}^3$ .  
Add a central flushing port in the center of the cutter disc, increase the flushing pressure to generate a pressure difference of 0.3 MPa between the flushing pressure and the mud water tank

pressure.

2. Add a flushing port to the center cutter barrel, realize real-time flushing by branching off from the central flushing pipeline. At the same time, cut off the failure wear monitoring blade near the center of the cutter disc.

3. Weld cutting teeth on the cutter barrel to timely scrape away the uncut debris from the roller cutter, reducing the probability of cutter head clogging.

*Tab. 3 - Mud Cake Treatment Methods for Atmospheric Pressure and Pressurized Cutter Discs*

Type	Method
Earth Pressure Balance Shield	Increase scouring pressure and flow rate
	Move the suction port forward
	Add swelling agent
	Clean with high-pressure water gun arm by arm
	Remove with a pickaxe
Pressure Balance Shield	Cut off the spokes
	Clean arm by arm with a high-pressure water gun
	Cut off the spokes

### Control the excavation parameters

#### 1. Optimize the excavation parameters

Based on the geological conditions of shield tunnelling, changes in tunnel depth, etc., control the construction process. By using advanced geological coring, mud particle detection, monitoring of the quality of formed tunnel segments, and measurement data, make timely adjustments and optimizations to various excavation parameters. Recommended values for excavation parameters and control measures are shown in Table 4.

*Tab. 4 - Recommended Values of Excavation Parameters and Control Measures*

Tunnelling parameters	Recommended values	Control measures
Mud-water tank top pressure /MPa	Tunnel burial depth /10+0.02 MPa, Burial depth unit: m	The pressure fluctuation control range for each cycle is $\pm 0.01$ MPa, Strictly prohibited to make large adjustments to the pressure
Slurry density / (g /cm <sup>3</sup> )	1.1~1. 2 g/cm <sup>3</sup>	Comprehensively considering the ability to carry slag and the ability to maintain stable tunnel face pressure with slurry shield
Slurry viscosity / (Pa·s)	16.5~26.3 Pa·s	Adjust accordingly based on the slurry carrying capacity
Discharge slurry density / (g/cm <sup>3</sup> )	1.2~1. 3 g/cm <sup>3</sup>	After the slurry discharged by the shield tunneling machine is treated by the separation equipment, centrifugal treatment is conducted for the slurry with a density greater than 1.18 g/cm <sup>3</sup>
Discharge slurry viscosity / (Pa·s)	17.3~26.8/ Pa·s	Adjust the slurry with viscosity not meeting the requirements based on previous experience
Excavation speed / (mm/min)	8~16	The fluctuation of the speed per ring should not be too large
Total thrust	—	Combine torque with advance rate, and make appropriate adjustments based on the pressure situation of the cutterhead
Cutterhead torque	—	Strictly control the torque fluctuation, and the torque fluctuation of a single ring should be $\leq 500$ kN·m
Cutterhead rotational speed / (r/min)	2.0~2.4	Match with the torque fluctuation value
Penetration rate	3.1~5.2	Control the penetration depth
Cutterhead thrust force	—	Control the fluctuation value within 5000 kN

## 2. Excavation parameters management

Control the pressure in the slurry chamber, strictly control the slurry balance during the excavation process, calculate the pressure based on the tunnel depth using hydrostatics, and make dynamic adjustments during actual construction by combining past construction experience and monitoring data.

During shield tunnelling, strictly control the performance of the slurry, conduct tests on slurry density, viscosity, and sand content, and make dynamic adjustments to ensure the quality of slurry film formation and its ability to transport debris. Sample the excavated soil and compare it with the survey and design report to guide the optimization of excavation parameters.

During shield tunnelling, use torque fluctuation and cutterhead thrust as reference parameters to match thrust, torque, and speed, ensuring uniform advancement.

Increase the center flushing flow rate of the cutterhead to 1200-1500 m<sup>3</sup>/h.

## **PREVENT STICKING AND BLOCKING DURING TUNNELING IN SOFT UPPER AND HARD LOWER STRATA**

### **1. Utilize a hydraulic breaker to crush rock blocks**

Increase the operational frequency of the crusher to crush the rock blocks accumulated at the slag discharge outlet, prevent the rocks from getting stuck at the slag discharge outlet or crusher position. At the same time, increase the circulation flow rate of the mud to flush the rock blocks crushed at the slag discharge outlet position and bottom, preventing blockage at the slag discharge outlet.

Extend the circulation time to completely discharge the sediment in the silo, maintaining the liquid level in the silo as close to zero as possible. Increase the flushing flow rate at the bottom of the mud, while adjusting the viscosity of the mud to a higher level to enhance the slurry's carrying capacity of slag.

### **2. Increase the pressure in the mud-water tank appropriately**

Slightly increase the pressure in the mud-water tank to prevent the dropping of rock blocks from the top. The pressure set value of the mud-water tank is the calculated theoretical pressure value + 0.02 MPa, with the pressure fluctuation range per cycle controlled within  $\pm 0.01$  MPa. It is strictly prohibited to make significant adjustments to the pressure.

### **3. Increase the mud indices appropriately**

Appropriately increase the mud indices, using high-performance mud to fill the cracks on one hand and enhance the mud carrying capacity of slag on the other hand, which is beneficial for slag discharge. The slurry density control is set at 1.1~1.2 g/cm<sup>3</sup>, the slurry viscosity control is maintained between 16.5~26.3 Pa·s, the discharge density control is set at 1.18~1.19 g/cm<sup>3</sup>, and the discharge viscosity control is maintained between 17.3~26.8 Pa·s.

### **4. Targeted flushing**

Enhance the flushing of the mud circulating at the bottom of the cutterhead, strengthen the flushing of the bottom of the cutterhead and the slag discharge chute, use reverse flushing to prevent silting and blockage that may cause stagnant discharge.

### **5. Tool optimization**

Uneven formation rock strength with soft top and hard bottom can easily lead to abnormal tool damage. Rational selection and configuration of tools, as well as control of cutterhead torque and pressure, are prerequisites for protecting the tools.

The cutterhead is equipped with a single-axis dual-blade roller cutter that can be replaced under normal pressure, with the scraper to break rocks. The red formation has a certain strength, and the smooth blades are prone to wear and impact damage during excavation. Due to the inability to simultaneously meet the wear resistance and impact resistance requirements of the tools based on the hardness and toughness of the metal materials, single-edge and double-edge toothed roller cutters are used after experiments (refer to Figure 7), with wear-resistant tungsten carbide hardfacing on the cutter ring and tooth bed. The embedded teeth enhance impact resistance, while the hardfaced tungsten carbide improves wear resistance, thereby enhancing rock breaking capability and increasing excavation efficiency.



(a) Single-edge toothed roller cutter (b) Double-edge toothed roller cutter

Fig. 7 – Toothed roller cutter

## 6. Blade blockage prevention

After the mudstone is crushed, it forms mud powder with a free expansion rate of up to 30%, and a cohesive strength of up to 3 MPa, and a saturated water absorption rate of 2%. During the excavation of the mudstone section, the mud powder enters the cutter barrel with the rotation of the tool. With the increase of excavation time, the tool temperature rises, which makes it easy to cause residue accumulation in the cutter barrel.

Based on the shape of the cutter barrel for the shield tunnel boring machine under normal pressure during the mud-water balance and the condition of debris monitoring pipeline in the cutter barrel during excavation, the inside and outside of the cutter barrel are treated with rubber rings. By installing rubber rings, the accumulation of debris in the cutter barrel is reduced to ensure the normal operation of the tool rotation monitoring system.

## CONCLUSION

1. An analysis of anti-blocking and discharge measures in the construction of red bed geology is conducted in terms of improving the slurry carrying capacity. It is found that by dynamically controlling the slurry density, viscosity, and sand content index, the slurry carrying capacity can be enhanced to prevent slurry blockage. High slurry density affects the slurry carrying capacity, while low density affects the stability of the face of the cutterhead.
2. The higher the slurry viscosity, the better the carrying capacity of debris, but excessively high viscosity can lead to mud cake formation on the cutterhead and blockage of the cutter barrel. The formation speed of mud film is directly related to the sand content of the slurry, which should be moderate. According to the actual excavation conditions of this project, the slurry density should be controlled within the range of 1.1 to 1.2 g/cm<sup>3</sup>, the slurry viscosity should be controlled between 16.5 and 26.3 Pa.s, and the sand content should be maintained at 10 to 20%.
3. An analysis of anti-blocking and discharge measures in the construction of red bed geology is carried out from the aspects of strengthening the layout of high-flow radial flushing system at the center of the cutterhead and dealing with mud cake on the cutterhead. It is found that during shield tunnelling, maintaining a constant slurry flow rate and enhancing bottom and center flushing of the cutterhead are essential. For the center positions of the cutterhead with normal pressure and pressurized face plates, 12 and 9 flushing holes are respectively designed to prevent tool wear due to muddy cutterhead. Measures such as increasing flushing pressure and flow rate, moving the suction mouth forward, adding bentonite, arm-by-arm cleaning with high-pressure water gun, removing ribs, and chiseling with pneumatic picks are implemented to prevent and control mud cake

formation.

4. Research on anti-blocking and discharge in the upper soft and lower hard strata shows that measures such as breaking rock blocks with a hydraulic hammer, moderately increasing the pressure in the mud chamber, adjusting mud parameters appropriately, targeted flushing, and optimizing tools can effectively prevent blockages.

## REFERENCE

- [1] He X C, Xu Y S, Shen S L, et al. Geological environment problems during metro shield tunnelling in Shenzhen, China[J]. *Arabian Journal of Geosciences*, 2020, 13: 1-18.
- [2] Chen J, Min F, Chen J, et al. Cutting, Wear and replacement of cutting tools during shield tunneling[J]. *Shield tunnel cutter replacement technology*, 2022: 11-76.
- [3] Chen J, Min F, Chen J, et al. Stabilization Technology and Tool Change Technology for Open Face with Pressure Open[J]. *Shield Tunnel Cutter Replacement Technology*, 2022: 197-266.
- [4] Kou L, Zhao J, Lian F, et al. Experimental study on the formation and characteristics of mud filtration cake in large-diameter slurry shield tunneling[J]. *Advances in Civil Engineering*, 2021, 2021: 1-10.
- [5] Li X, Yang Y, Li X, et al. Criteria for cutting head clogging occurrence during slurry shield tunneling[J]. *Applied Sciences*, 2022, 12(3): 1001.
- [6] Zhang M, He H, Liu Y. Technical Measures of Shield Tunnel Construction in Alternating Hard and Soft Rock Strata[M]//Challenges and Advances in Sustainable Transportation Systems. 2014: 524-531.
- [7] Yang N, Nie Q, et al. Driving Parameter Trends and a Safety Evaluation Method Based on the Composite Ratio for Shield Tunneling in Complex Strata[J]. *ASCE-ASME Journal of Risk and Uncertainty in Engineering Systems, Part A: Civil Engineering*, 2023, 9(2): 04023007.
- [8] Liu F, Wang Q, Ji Z, et al. Performance assessment and structural design of the atmospheric cutterhead of slurry shield machine[J]. *Journal of Mechanical Science and Technology*, 2022, 36(11): 5611-5624.
- [9] Gao Y, Chen R, Qin W, et al. Learning from explainable data-driven tunneling graphs: A spatio-temporal graph convolutional network for clogging detection[J]. *Automation in Construction*, 2023, 147: 104741.
- [10] Li T, Liu B, Li Y, et al. Properties of Foam and Soil Improvements for Earth-Pressure Balance Shield Construction in Red Soils[J]. *Advanced Materials Research*, 2011, 243: 2834-2841.
- [11] Lu H, Qi J, Li J, et al. Multi-agent based safety computational experiment system for shield tunneling projects[J]. *Engineering, Construction and Architectural Management*, 2020, 27(8): 1963-1991.
- [12] Liu W, Ding L. Global sensitivity analysis of influential parameters for excavation stability of metro tunnel[J]. *Automation in Construction*, 2020, 113: 103080.
- [13] Menchini G L, Liti M. Ismailia: The first tunnels to be constructed under the Old and New Suez Canals—a case history[M]//Tunnels and Underground Cities. *Engineering and Innovation Meet Archaeology, Architecture and Art*. CRC Press, 2019: 4039-4048.
- [14] Chen J, Min F, Chen J, et al. Conventional Cutterhead and Tool-Changing Under Normal Pressure Technology[J]. *Shield Tunnel Cutter Replacement Technology*, 2022: 77-155.
- [15] Dai Z, Li P, Zhu M, et al. Dynamic prediction for attitude and position of shield machine in tunneling: A hybrid deep learning method considering dual attention[J]. *Advanced Engineering Informatics*, 2023, 57: 102032.

- [16] Exadaktylos G, Stavropoulou M. A spatial estimation model for continuous rock mass characterization from the specific energy of a TBM[J]. Rock mechanics and rock engineering, 2008, 41: 797-834.

# DYNAMIC PERFORMANCE ANALYSIS OF CABLE DAMAGE IN PRESTRESSED $\pi$ -SHAPED BEAM CABLE-STAYED BRIDGE

*Xilong Zheng<sup>1</sup> and Honglei Zhang<sup>2</sup>*

1. School of Civil and Architectural Engineering, Harbin University, No.109 Zhongxing Road, Harbin, Heilongjiang Province, China; sampson88@126.com
2. Bridge Department, Beijing New Bridge Technology Development Co., LTD, No.8 Xitucheng Road, Beijing, China

## ABSTRACT

This paper takes a prestressed  $\pi$ -shaped beam cable-stayed bridge in China as an engineering case, and conducts relevant research on the overall and local parameter sensitivity of the structure and the stress characteristics under cable damage. The main factors causing cable damage in the prestressed  $\pi$ -shaped beam cable-stayed bridge are analyzed, and the selection of elastic modulus as a damage variable is determined. Based on the finite element model analysis of the actual bridge, different inclined cables are selected for damage simulation, and the dynamic variation characteristics of the main beam, cables, and other structures under one-sided, symmetrical, and asymmetrical cable damage are analyzed. This provides a reference for the dynamic performance analysis of prestressed  $\pi$ -shaped beam cable-stayed bridges under similar cable damage conditions in the future.

## KEYWORDS

Cable-stayed bridge,  $\pi$ -shaped beam, Finite element analysis, Static performance

## INTRODUCTION

Currently, in the design of cable-stayed bridges, the maximum span exceeds 400m, and the main beam form is mainly steel or composite beams, while for spans below 400m, the preferred main beam forms are prestressed concrete box girders or  $\pi$ -shaped beams [1-3]. The development of cable-stayed bridges has become increasingly mature, but it also brings more and more challenging problems. Currently, the detection and maintenance of cable-stayed bridges are not yet in a mature stage. As the lifeline of cable-stayed bridges, the cable plays a crucial role and is also the most susceptible to damage. Therefore, scholars at home and abroad have conducted in-depth research on this important structure [4,5].

Not only do structural parameters have a significant impact on the stress performance of cable-stayed bridges, but also certain external accidental factors during operation can lead to changes in their stress performance [6-8]. As the lifeline of cable-stayed bridges, the cables are generally in good operational condition, but a few cable-stayed bridges have experienced varying degrees of issues. Due to the existence of cables, the main beam belongs to a multiple point elastic support system, and its stress characteristics are similar to those of a multi-span continuous beam bridge, which significantly reduces the bending moment of the main beam. The cables, as critical components of the whole system, bear most of the load acting on the main beam [9-12]. However, in daily operation, factors such as damaged sheathing, wire corrosion, and vibration fatigue can

cause varying degrees of damage to the cables. Cable damage leads to a redistribution of cable forces across the entire bridge and can result in varying degrees of deflection changes in the main beam, directly influencing the bridge's service life. Currently, the research on cable damage is mainly focused on integral box girder cable-stayed bridges, and there is relatively less research on the impact of cable damage on  $\pi$ -shaped beam cable-stayed bridges [13,14].

There is still no definitive standard for the causes of cable damage, the impact on cable-stayed bridge performance, and how to accurately determine the location and degree of cable damage. Cable damage is inevitable during normal operation due to various reasons. How to make accurate assessments of cable damage and develop effective testing methods is a difficult problem that cable-stayed bridges face [15]. In this article, a prestressed  $\pi$ -shaped beam cable-stayed bridge engineering example is used to identify the impact of parameter changes and cable damage on the stress performance of the bridge. By changing the elastic modulus of the cables to simulate cable damage, the trend of changes in cable tension, main beam vertical displacement, and overall structural frequency under various cable damage conditions were analyzed, and the influence of cable damage on the structural mechanics performance of the prestressed  $\pi$ -shaped beam cable-stayed bridge was obtained.

## INTRODUCTION TO ENGINEERING BACKGROUND

The engineering background of this article is a prestressed  $\pi$ -shaped beam single-tower cable-stayed bridge in Jilin Province. The total length of the prestressed  $\pi$ -shaped beam cable-stayed bridge is 617.06 m, with a span combination of  $(4 \times 30) \text{ m} + (39.9 + 89.1 + 151) \text{ m} + (4 \times 30) \text{ m} + (3 \times 30) \text{ m}$ , and the main bridge section for study is the second section. The main bridge adopts an "H" shaped single-tower double-cable-plane PC beam cable-stayed bridge, with a span combination of  $39.9 \text{ m} + 89.1 \text{ m} + 151 \text{ m}$ . The main bridge structure is a fixed system, with a 2.0% bi-directional transverse slope and a design load of Class-A city. There are a total of 18 pairs of spatial cables arranged in a fan shape on the main tower. The cables are arranged on the main beam cross-section at a distance of 0.8m from the edge of the main beam. The layout of the prestressed  $\pi$ -shaped beam cable-stayed bridge is shown in Figure 1. Cross section diagram of the main bridge is shown in Figure 2.

### 1. Main beam structure

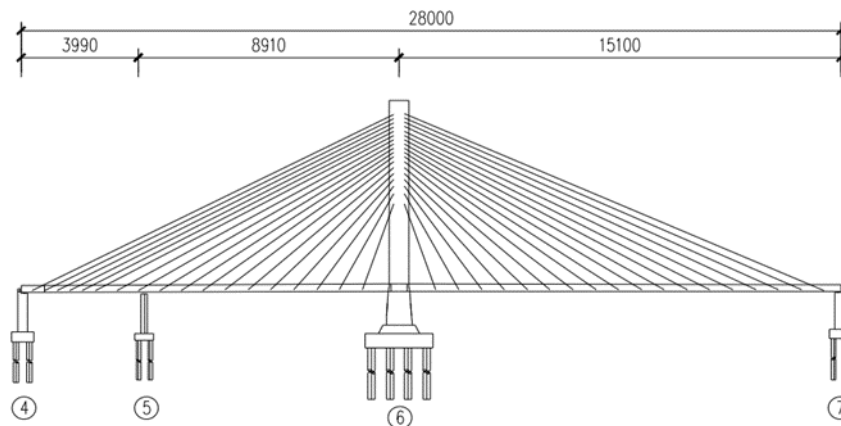


Fig. 1 – Layout diagram of the main bridge (unite: cm)

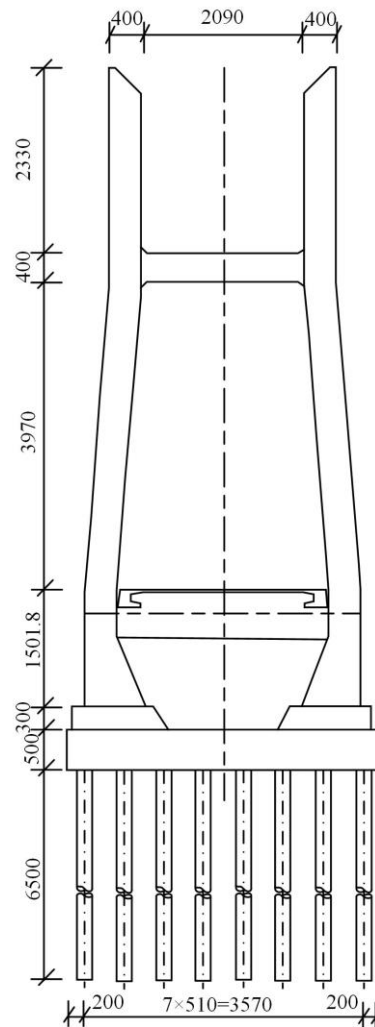


Fig. 2 – Cross section diagram of the main bridge (unite: cm)

The main beam adopts a pre-stressed concrete "π" shaped cross-section. The width of the main beam section is 26.5 m, and the height is 2.3 m. It is designed with a bidirectional 2% cross slope. The basic spacing of the transverse beams is 3.9 m, 3.65 m, and 4.25 m. The transverse beams are all equipped with pre-stressed steel hinge lines. The main beam is connected to the main tower using a fixed system, and both the main beam and the transverse beams are made of C55 concrete.

## 2. Main tower

The main tower of the cable-stayed bridge adopts an H-shaped main tower. The height of the main tower is 117.318 m. The cross-section of the tower column is a hollow rectangular shape, with a full width of 6.8 m in the middle and upper tower columns longitudinally, and a width of 4.0 m in the transverse bridge direction. The upper part of the lower tower column gradually increases from a width of 6.8 m to a full width of 8.8 m longitudinally, and the width in the transverse bridge direction gradually increases to 7.5 m.

The cross-section of the transverse beam is a hollow rectangular shape. The upper transverse beam has a rectangular cross-section of 6.2 m × 4 m, while the lower transverse beam has a width of 6.4 m and a height ranging from 6 m to 6.27 m. A tower pedestal with a height of 3 m is provided at the top of the main tower's bearing platform. Except for the lower transverse beam, which is made

of C55 concrete, the rest of the main tower structures are made of C50 concrete.

### 3. Stay cable

The main tower is equipped with a total of 72 stay cables, with each cable spaced at a designed interval of 7.8 m. The cable spacing changes to 7.8 m, 7.3 m, and 4.25 m corresponding to the length variations of the main span's cast-in-place segments. The stay cables are positioned 0.8 m away from the edge of the main beam cross-section. The stay cables are all made of  $\Phi$ s 15.2 steel strand with a standard strength of 1860 MPa. The stay cable numbering is shown in Figure 3.

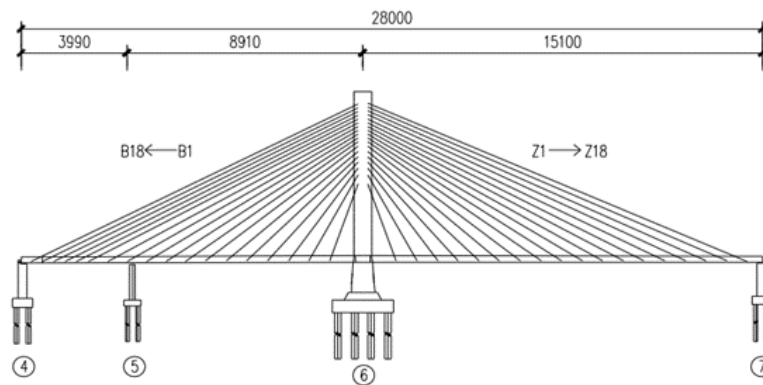


Fig. 3 – Stay cable numbering diagram

### FINITE ELEMENT ANALYSIS MODEL

The finite element model of this prestressed  $\pi$ -type girder cable-stayed bridge is established and analyzed using the specialized bridge analysis software, Midas Civil. The main beam and main tower are simulated using 2D beam elements, with section dimensions set to match the actual conditions. The overall finite element model of the prestressed  $\pi$ -type girder cable-stayed bridge consists of 483 nodes and 399 elements, with 327 beam elements, including 235 main beam elements and 92 main tower elements. There are 72 truss (stay cable) elements that only experience tension. The complete bridge finite element model is shown in Figure 4.

The main beam and main tower are simulated in the cable-stayed bridge using the shared node approach to model the fixed support system. The auxiliary piers and main beam are rigidly connected, and the connection between the stay cable anchorage points, main beam, and main tower is simulated using rigid connections as well. The transverse beams on the main beam and main tower are made of C55 concrete. The lower transverse beam of the main tower, upper tower columns, middle tower columns, lower tower columns, and tower base are made of C50 concrete. The 5# auxiliary pier is made of C40 concrete.

Both longitudinal and transverse prestressing tendons are made of high-strength low-relaxation prestressing strand with a single strand diameter of  $\Phi$ s 15.2 mm. The standard strength of the strand is 1860 MPa, with an elastic modulus of  $1.95 \times 10^5$  MPa, and a cross-sectional area of 140 mm<sup>2</sup>.

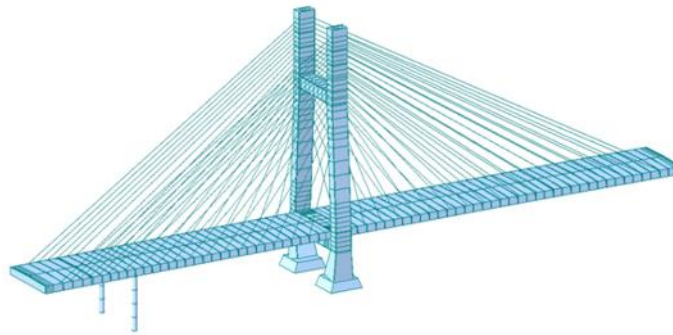


*Fig. 4 – The finite element model of the main bridge*

### **DYNAMIC PERFORMANCE ANALYSIS OF PRESTRESSED $\pi$ -TYPE BEAM CABLE-STAYED BRIDGE UNDER SIMILAR CABLE DAMAGE CONDITIONS**

In this section, the first 10 vibration modes of the prestressed  $\pi$ -type beam cable-stayed bridge model were obtained through the finite element software Midas Civil. By modifying the elastic modulus of the cable, simulations were conducted on the cable damage location and degree under different working conditions, and the changes in dynamic characteristics of the prestressed  $\pi$ -type beam cable-stayed bridge were studied. As a result, the relationship between cable damage location and degree and changes in dynamic characteristics was derived. The first 10 vibration modes of the cable in undamaged condition are shown in Figure 5 - Figure 14, with frequencies and periods listed in Table 1.

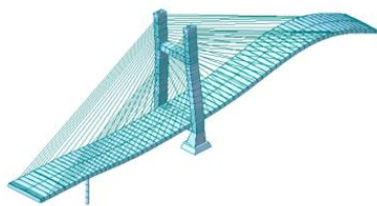


*Fig. 5 – The first-order array diagram*

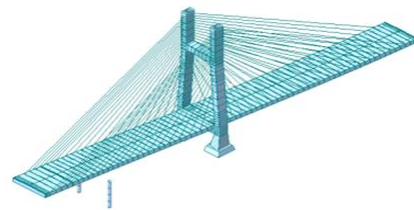


*Fig. 6 – The second-order array diagram*

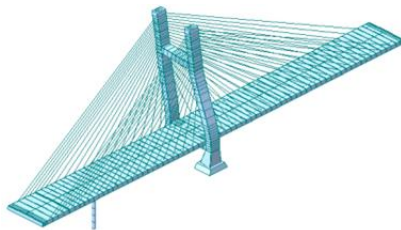


*Fig. 7 – The third-order array diagram*

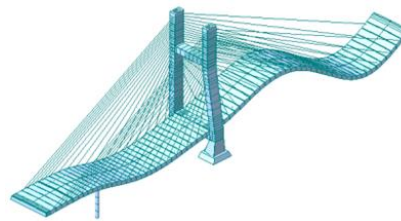


*Fig. 8 – The fourth-order array diagram*

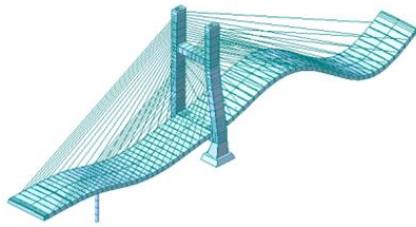


Fig. 9 – The fifth-order array diagram

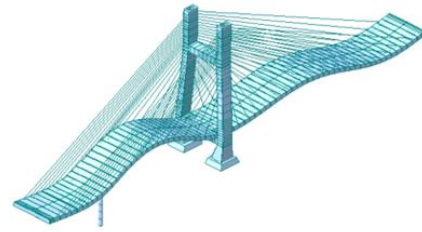


Fig. 10 – The sixth-order array diagram

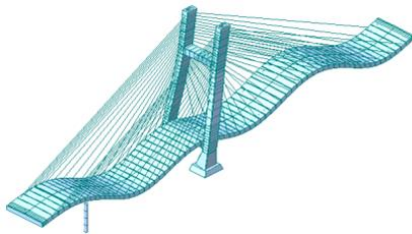


Fig. 11 – The seventh-order array diagram

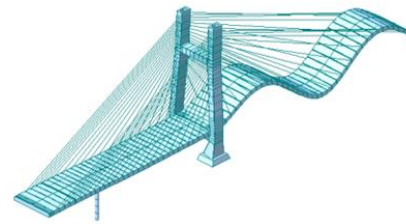


Fig. 12 – The eighth-order array diagram

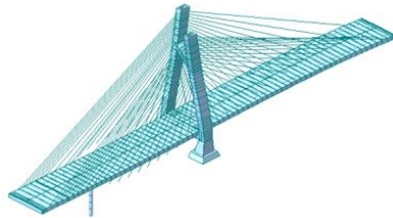


Fig. 13 – The ninth-order array diagram

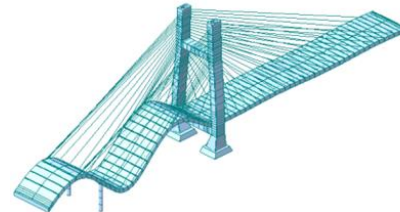


Fig. 14 – The tenth-order array diagram

Tab. 1 - Dynamics characteristics table of a prestressed  $\pi$ -Type beam cable-stayed bridge

Order	Frequency (Hz)	Period (s)	Description of the waveform
1	0.643	1.556	Main tower right side main girder first-order vertical bending
2	0.988	1.012	Main girder lateral deflection
3	1.139	0.876	Tower column lateral bending
4	1.271	0.787	Main tower right side main girder second-order vertical bending
5	1.298	0.770	Main girder vertical oscillation
6	1.428	0.700	Main tower both sides main girder first-order symmetric vertical bending
7	1.839	0.544	Main tower both sides main girder second-order symmetric vertical bending
8	2.131	0.469	Main tower right side main girder third-order vertical bending
9	2.401	0.416	Tower column lateral symmetric bending
10	2.727	0.367	Main tower left side main girder third-order vertical bending

**Dynamic Performance Analysis of Single-Side Cable-Stayed Bridge with Similar Damage Level**

For the analysis of different cable-stayed bridges with varying damage levels of 60% on auxiliary spans and short main spans, eight scenarios are selected: B1, B3, B6, B8, B10, B12, B16, and B18. The definition of each scenario is provided in Table 2.

*Tab. 2 - Table of Natural Frequencies and Mode Shapes of Structures with Different Cable Damage Levels on Auxiliary Spans and Short Main Spans*

Order	Non-destructive	B1 60%	B3 60%	B6 60%	B8 60%	B10 60%	B12 60%	B16 60%	B18 60%	Theoretical model mode of vibration
1	0.642	0.642	0.642	0.642	0.641	0.639	0.638	0.636	0.636	First-order vertical bending of the main beam on the right side of the main tower
2	0.987	0.987	0.987	0.987	0.987	0.987	0.987	0.987	0.987	Lateral deflection of the main beam
3	1.138	1.136	1.136	1.136	1.136	1.136	1.136	1.136	1.136	Lateral bending of the tower column
4	1.270	1.269	1.266	1.266	1.269	1.269	1.268	1.268	1.268	Second-order vertical bending of the main beam on the right side of the main tower
5	1.298	1.297	1.297	1.297	1.297	1.297	1.297	1.297	1.297	Vertical deflection of the main beam
6	1.42	1.423	1.406	1.398	1.418	1.427	1.425	1.424	1.425	First-order symmetrical vertical bending of the main beam on both sides of the main tower
7	1.83	1.830	1.826	1.817	1.821	1.82	1.828	1.828	1.827	Second-order symmetrical vertical bending of the main beam on both sides of the main tower
8	2.130	2.129	2.129	2.129	2.129	2.129	2.129	2.129	2.129	Third-order vertical bending of the main beam on the right side of the main tower
9	2.401	2.399	2.399	2.399	2.396	2.383	2.377	2.371	2.367	Symmetrical lateral bending of the tower column
10	2.726	2.713	2.699	2.725	2.714	2.721	2.726	2.725	2.726	Third-order vertical bending of the main beam on the left side of the main tower

Due to the difficulty of directly observing the frequency variations in each damaged scenario, calculating the frequency variations for each scenario can provide a more intuitive understanding of the frequency and mode shape changes. To facilitate a more direct comparison of the frequency variations on the cable-stayed bridge's auxiliary spans and short main spans in different damaged scenarios, the eight scenarios mentioned above are compared separately based on cable position.

Please refer to Figure 15 - Figure 18 for the graphical representation of these comparisons.

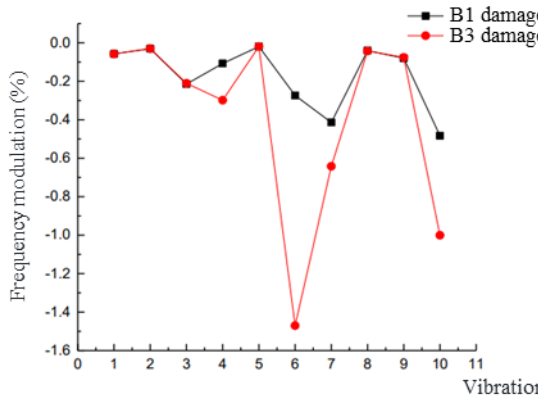


Fig. 15 – The location of the auxiliary span and the inner side of the short main span

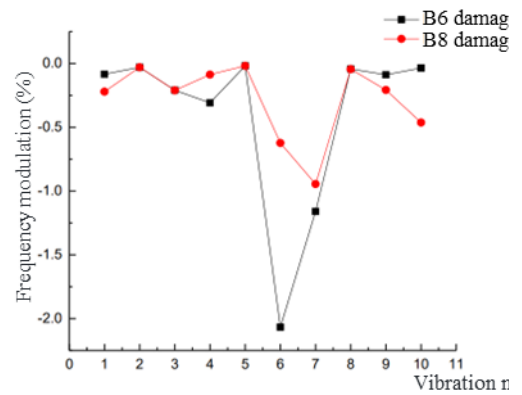


Fig. 16 – The position of 1/3L to 1/2L of the auxiliary span and the short main span

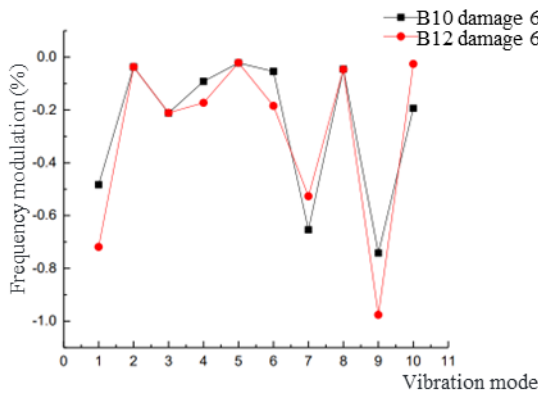


Fig. 17 – The position of 1/2 to 2/3L of the auxiliary span and the short main span

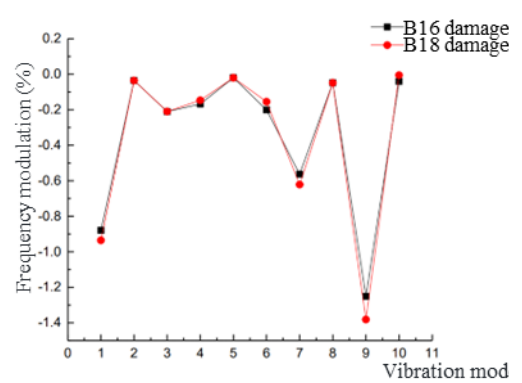


Fig. 18 – The outermost position of the auxiliary span and the short main span

Damage to the diagonal cables of the auxiliary span and short main span has almost no effect on the lateral or vertical deflection of the main beam or the high-order vertical bending of the right main beam of the main tower. Damage to the diagonal cables within 1/2 L near the auxiliary span and short main span will have a relatively large impact on the sixth-order natural frequency of the structure, with a maximum value of 2.06%. At the same time, it can be observed that the influence of diagonal cable damage on the sixth-order natural frequency within the auxiliary span and short main span increases with distance from the main tower, but the trend is opposite within the range of 1/3 L~1/2 L.

Damage to the diagonal cables within the range of 1/2 L near the auxiliary span and short main span shows a consistent trend, all of which have a significant impact on the ninth-order natural frequency. The further the damaged diagonal cables are from the main tower, the greater the impact on the ninth-order natural frequency.

To compare the frequency variations under different levels of 60% damage to the diagonal cables of the long main span, eight different scenarios (Z1, Z3, Z6, Z8, Z10, Z12, Z16, Z18) were selected for analysis. The definition of each scenario can be found in Table. 4 - Table. 10.

In order to visually compare the frequency changes under different damage conditions, the eight scenarios are compared separately according to the position of the diagonal cables, as shown in

Figure19 - Figure 22.

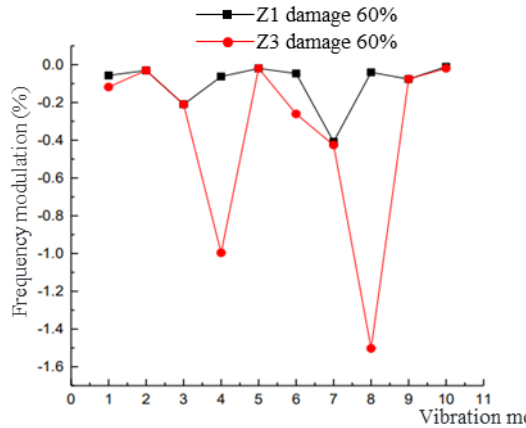


Fig. 19 – The inner side of the long main span

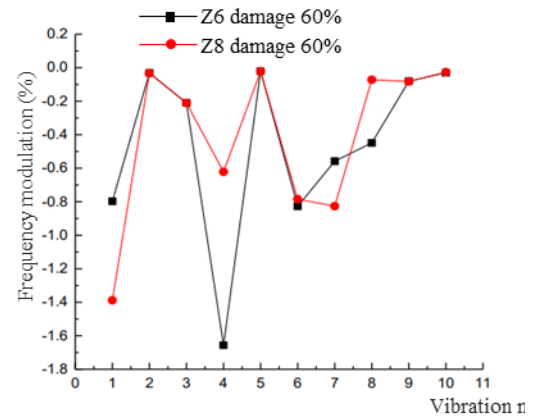


Fig. 20 – The position of 1/3L to 1/2L of the long main span

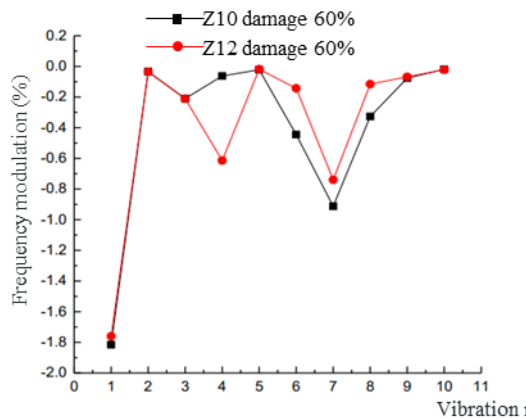


Fig. 21 – The position of 1/2 to 2/3L of the long main span

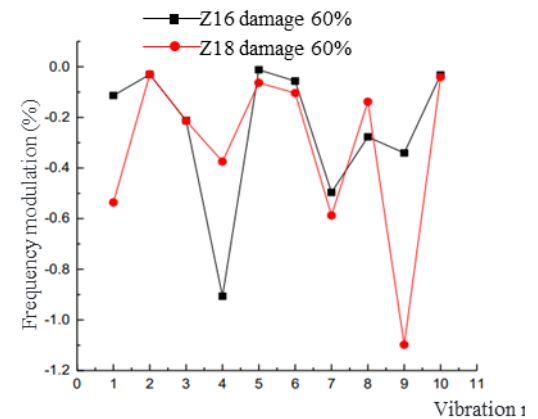


Fig. 22 – The outer side position of the long main span

Damage to the inclined cables at the outer position of the long main span has almost no impact on the lateral and vertical deflection of the main beam and the higher-order vertical bending of the main tower's left side. The damage to the innermost Z1 inclined cable has a minimal effect on the dynamic characteristics of the cable-stayed bridge, with the greatest impact observed on the 7th mode frequency, which is only 0.41%.

Within the range of 1/2 to 2/3L of the long main span, the trend of damage to the inclined cables remains consistent. It has a similar impact on the first mode frequency of the structure, with a maximum frequency variation of 1.82%. However, as the damaged inclined cables are farther from the main tower, they have a greater influence on the 4th mode frequency. The farther the damaged inclined cables are from the tower, the more pronounced the lateral symmetric bending of the tower columns becomes, with a maximum frequency variation of 1.1%.

### Analysis of Dynamic Performance under the Same Level of Damage in Symmetric Stay Cables

For the level of damage being equal to 60% in symmetrically positioned cables on both sides of

the main tower, four scenarios, namely B3+Z3, B6+Z6, B12+Z12, and B18+Z18, were selected for analysis, with each scenario described in Table 3.

Tab. 3 - Table of dynamic characteristics for a prestressed  $\pi$ -type girder cable-stayed bridge

Order	Non-destructive	B3+Z3 60%	B6+Z6 60%	B12+Z12 60%	B18+Z18 60%
1	0.643	0.643	0.642	0.637	0.627
2	0.988	0.988	0.987	0.987	0.987
3	1.139	1.139	1.136	1.136	1.136
4	1.271	1.271	1.256	1.248	1.261
5	1.298	1.298	1.298	1.298	1.298
6	1.428	1.428	1.403	1.387	1.424
7	1.839	1.839	1.826	1.814	1.823
8	2.131	2.131	2.099	2.121	2.128
9	2.401	2.401	2.399	2.399	2.378
10	2.727	2.727	2.699	2.725	2.726

The frequencies of the first 10 mode shapes for the aforementioned four damage scenarios are shown in Figure 23. The frequency variations of the first 10 modes for all scenarios are depicted in Figure 24. It can be observed from Figure 23 that after the symmetric stay cables are damaged, the variation in frequencies for each mode shape is very small, with the maximum frequency change amplitude being only 2.89%.

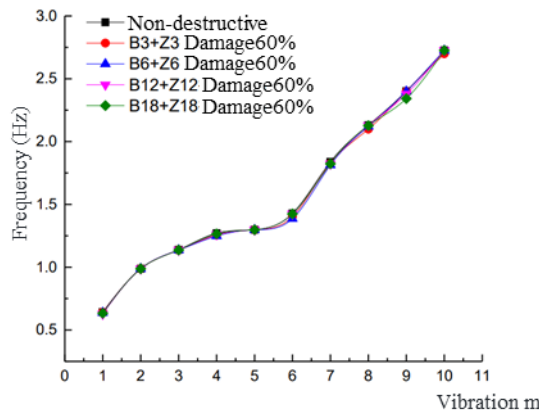


Fig. 23 – The frequency variation graph of symmetrical cable damage

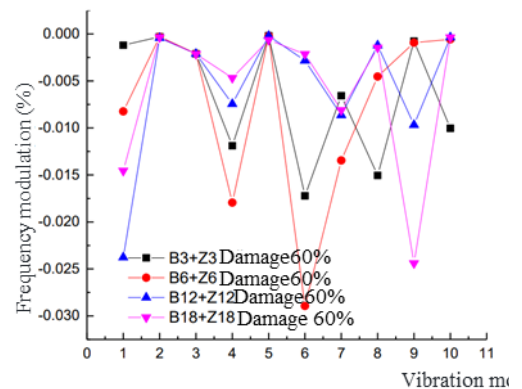


Fig. 24 – The frequency and amplitude variation graph of symmetrical cable damage

The symmetric cable damage on the entire bridge has little effect on the lateral and vertical deflection of the main girder. When symmetrical cable damage occurs on the diagonal cables at  $1/3 L \sim 1/2 L$  of both sides of the main tower, the 6th-order frequency is affected the most, with a frequency variation of up to 2.89%. When symmetrical cable damage occurs on the diagonal cables at  $1/2 L \sim 2/3 L$  of both sides of the main tower, the 1st-order fundamental frequency is affected the most, with a frequency variation of up to 2.38%. Only when the diagonal cables on the inner side of the main tower are symmetrically damaged, the 10th-order frequency is affected.

### Dynamic Performance Analysis of Non-symmetric Diagonal Cables with the Same Degree of Damage

For the non-symmetric diagonal cables on both sides of the main tower with the same degree of damage (60%), 12 working conditions are selected for analysis: B3+Z6, B3+Z12, B3+Z18, B6+Z3,

B6+Z12, B6+Z18, B12+Z3, B12+Z6, B12+Z18, B18+Z3, B18+Z6, B18+Z12. The definition of each working condition is shown in Table. 4 - Table. 12. To make a more intuitive comparison of the frequency changes of the non-symmetric diagonal cables under different damage conditions, the 12 damage conditions are merged into 4 working conditions for comparison, as shown in Figure 25 - Figure 28.

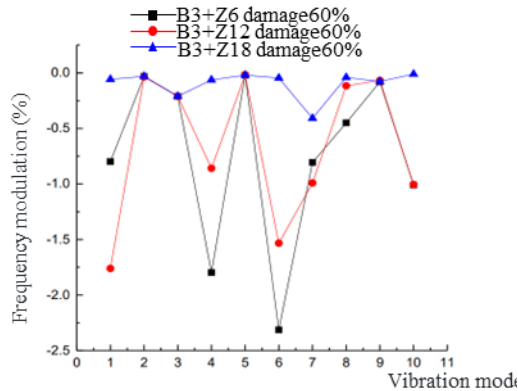


Fig. 25 – Asymmetric cable damage combination condition 1

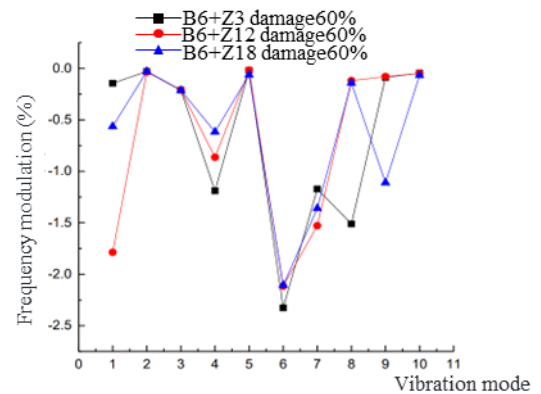


Fig. 26 – Asymmetric cable damage combination condition 2

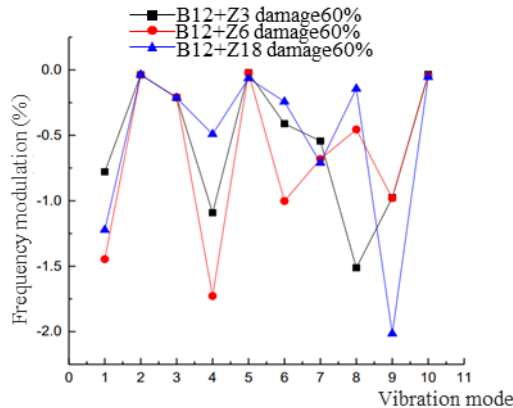


Fig. 27 – Asymmetric cable damage combination condition 3

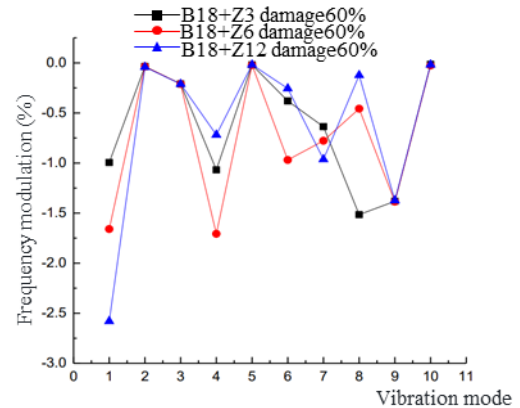


Fig. 28 – Asymmetric cable damage combination condition 4

According to Figure 24, it can be concluded that when there is damage to the inner inclined cable of the auxiliary span and the main span inclined cable is damaged at any position, it will have an impact on the vertical bending of the entire bridge structure. However, it has almost no effect on main beam lateral displacement, main beam vertical displacement, tower column lateral bending, and tower column lateral symmetric bending. Except for the first-order natural frequency of the structure, the farther the damaged position of the main span inclined cable is from the main tower, the smaller the impact on the various natural frequencies of the structure. When there is damage to the inclined cable at 1/3 position of the main span, it has the greatest influence on the sixth-order natural frequency of the structure—main beam first-order symmetric vertical bending, with a maximum change amplitude of 2.31%.

According to Figure 25, it can be concluded that when the inclined cable of the auxiliary span and the short main span at the position of  $1/3L \sim 1/2L$  is damaged, it will have almost no impact on the main beam lateral displacement, tower column lateral bending, and main tower left side main

beam third-order vertical bending, regardless of where the inclined cable of the main span is damaged. When there is damage to the inclined cable at any position of the main tower, the impact on the first and second-order symmetric vertical bending of the main beam on both sides of the main tower is basically the same, with change amplitudes of about 2.30% and 1.50%, respectively. When there is damage to the inner inclined cable of the long main span, it has the greatest influence on the sixth-order natural frequency of the structure—main beam first-order symmetric vertical bending, with a maximum change amplitude of 2.32%.

According to Figure 26, it can be concluded that when the inclined cable of the auxiliary span and the short main span at the position of  $1/2L \sim 2/3L$  is damaged, it will have almost no impact on the main beam lateral displacement, tower column lateral bending, main beam vertical displacement, and main tower left side main beam third-order vertical bending, regardless of where the inclined cable of the main span is damaged. When there is damage to the outer inclined cable of the long main span, it has a significant impact on the ninth-order natural frequency of the structure—tower column lateral symmetric bending, compared to the damage of other inclined cables, with a maximum change amplitude of 2.01%.

Based on Figure 27, it can be concluded that when the inclined cable of the auxiliary span and the outer inclined cable of the short main span is damaged, it will have almost no impact on the main beam lateral displacement, tower column lateral bending, main beam vertical displacement, and main tower left side main beam third-order vertical bending, regardless of where the inclined cable of the main span is damaged. The closer the damaged inclined cable is to the outer side of the main span, the greater the impact on the first-mode vibration of the entire bridge structure, with a maximum change amplitude of 2.58%. When there is damage to any position of the inclined cable of the long main span, the impact on the lower-order frequencies of the entire bridge structure shows a similar trend.

### Dynamic Performance Analysis of Pre-stressed $\pi$ -type Girder Cable-stayed Bridge under Different Cable Damage Conditions

The study aims to investigate the impact of symmetrical damage in different cable locations on the dynamic characteristics of the bridge by selecting four different levels of damage (B3+Z3, B6+Z6, B12+Z12, B18+Z18). The simulation of cable damage is conducted by reducing the elastic modulus of the simulated cable. The dynamic analysis results under different levels of damage for each combination of damaged cables can be seen in Figure 29 - Figure 32.

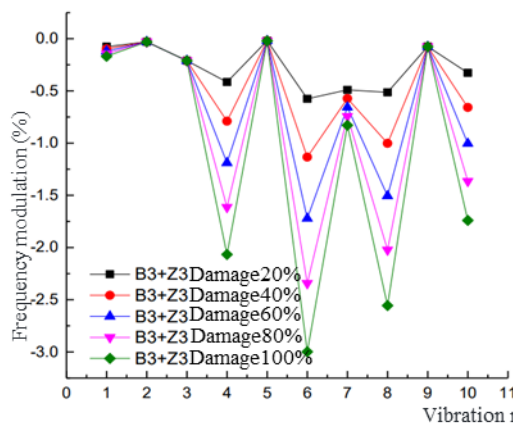


Fig. 29 – Frequency-Amplitude Variation of Symmetrical Cable Damage Condition 1

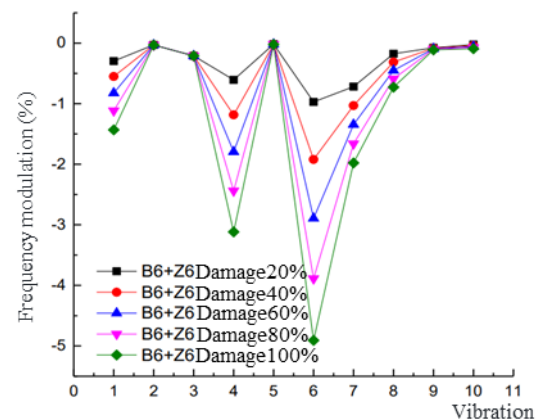


Fig. 30 – Frequency-Amplitude Variation of Symmetrical Cable Damage Condition 2

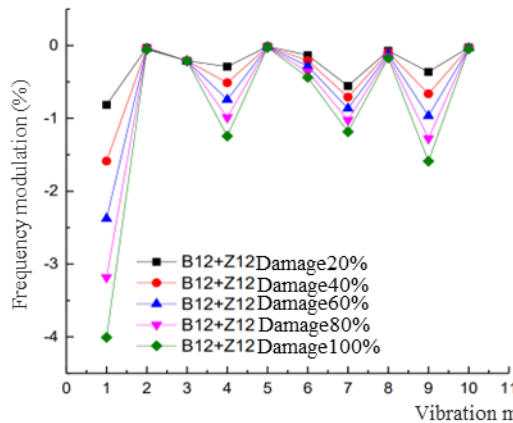


Fig. 31 – Frequency-Amplitude Variation of Symmetrical Cable Damage Condition 3

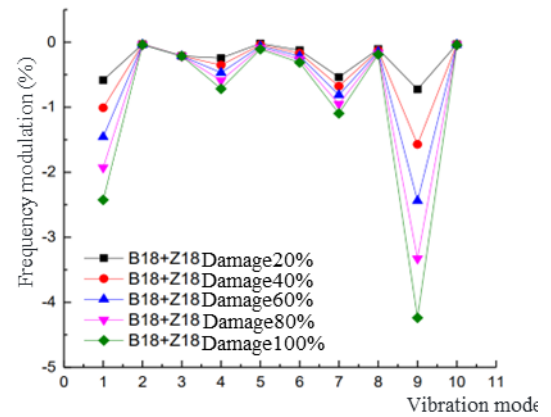


Fig. 32 – Frequency-Amplitude Variation of Symmetrical Cable Damage Condition 4

The symmetric damage in the inner side of the main tower does not significantly affect the first-order natural frequency of the structure, and the frequency-amplitude increases with the increase of damage level. However, it has different impacts on the tenth-order natural frequency of the structure. The impact of symmetric damage of cable-stayed bridge on the dynamic performance is greater than that of damage to a single-side cable or non-symmetric cable; the frequency-amplitude increases by about 2%.

Symmetric damage to cables at various locations will have varying degrees of impact on the vertical bending of the main girder. The effects of symmetric cable damage at different locations are similar to those of non-symmetric and single-side cable damage, and they will not have a significant impact on the lateral deflection of the main girder and the lateral bending of the tower column.

## CONCLUSION

1. Damage to the full bridge cables will almost always have varying degrees of impact on the vertical bending of the main girder, but it generally does not affect the lateral and vertical bending modes of the main girder. The varying degree of damage to the cable-stayed bridge has a consistent trend in impacting the dynamic performance of the structure, which is only reflected in the changes in frequency-amplitude. As the level of damage increases, the frequency-amplitude of a certain mode continues to increase.
2. The impact of symmetric damage to cable-stayed bridge on the dynamic performance of the structure is much greater than that of single-side cable damage or non-symmetric damage. Particularly, special attention should be paid to the cases where the outermost cable and the cables located at  $1/3L$  to  $1/2L$  from both sides of the main tower are damaged. When the damage level reaches 100%, the maximum impact on the structural frequency can be around 5%.

## REFERENCES

- [1] Li H, Ou J. The state of the art in structural health monitoring of cable-stayed bridges[J]. Journal of Civil Structural Health Monitoring, 2016, 6: 43-67.
- [2] Martins A M B, Simões L M C, Negrão J H J O. Optimization of cable-stayed bridges: A literature survey[J]. Advances in Engineering Software, 2020, 149: 102829.
- [3] Ren W X, Peng X L, Lin Y Q. Experimental and analytical studies on dynamic characteristics of a large span cable-stayed bridge[J]. Engineering Structures, 2005, 27(4): 535-548.

- [4] Janjic D, Pircher M, Pircher H. Optimization of cable tensioning in cable-stayed bridges[J]. *Journal of bridge engineering*, 2003, 8(3): 131-137.
- [5] Calvi G M, Sullivan T J, Villani A. Conceptual seismic design of cable-stayed bridges[J]. *Journal of Earthquake Engineering*, 2010, 14(8): 1139-1171.
- [6] Mehrabi A B. In-service evaluation of cable-stayed bridges, overview of available methods and findings[J]. *Journal of Bridge Engineering*, 2006, 11(6): 716-724.
- [7] Wang P H, Tang T Y, Zheng H N. Analysis of cable-stayed bridges during construction by cantilever methods[J]. *Computers & Structures*, 2004, 82(4-5): 329-346.
- [8] Cho S, Yim J, Shin S W, et al. Comparative field study of cable tension measurement for a cable-stayed bridge[J]. *Journal of Bridge Engineering*, 2013, 18(8): 748-757.
- [9] Zhang L, Qiu G, Chen Z. Structural health monitoring methods of cables in cable-stayed bridge: A review[J]. *Measurement*, 2021, 168: 108343.
- [10] Casciati F, Cimellaro G P, Domaneschi M. Seismic reliability of a cable-stayed bridge retrofitted with hysteretic devices[J]. *Computers & Structures*, 2008, 86(17-18): 1769-1781.
- [11] Sung Y C, Chang D W, Teo E H. Optimum post-tensioning cable forces of Mau-Lo Hsi cable-stayed bridge[J]. *Engineering Structures*, 2006, 28(10): 1407-1417.
- [12] Xu Z D, Wu Z. Simulation of the effect of temperature variation on damage detection in a long-span cable-stayed bridge[J]. *Structural Health Monitoring*, 2007, 6(3): 177-189.
- [13] Cao D Q, Song M T, Zhu W D, et al. Modeling and analysis of the in-plane vibration of a complex cable-stayed bridge[J]. *Journal of Sound and Vibration*, 2012, 331(26): 5685-5714.
- [14] Wang H, Tao T, Li A, et al. Structural health monitoring system for Sutong cable-stayed bridge[J]. *Smart structures and systems*, 2016, 18(2): 317-334.
- [15] Tang E K C, Hao H. Numerical simulation of a cable-stayed bridge response to blast loads, Part I: Model development and response calculations[J]. *Engineering Structures*, 2010, 32(10): 3180-3192.

# FRACTURE ENERGY OF UNSTABILIZED RAMMED EARTH: INFLUENCE OF CLAY TYPE AND CONTENT IN THE MIXTURE

*Barbora Mužíková, Tereza Plaček Otcovská and Pavel Padevět*

*Czech Technical University in Prague, Faculty of Civil Engineering, Department of  
Mechanics, Thákurova 7, 166 29 Praha 6, Czech Republic; barboramuzikova@seznam.cz*

## ABSTRACT

This study explores the fracture energy of unstabilized rammed earth, focusing on the influence of different types and amounts of clay within the mixtures. Utilizing a three-point bending test, this research evaluates the fracture energy of rammed earth to better understand how variations in clay type and content affect its structural integrity. The findings reveal significant differences in fracture energy values correlated with the clay's molecular structure and the interlayer chemical bonds. Clays such as illitic-kaolinitic, montmorillonite, and illite were tested, each demonstrating unique responses to mechanical stress based on their respective chemical bonds. Mixtures containing illitic-kaolinitic clay exhibited the highest fracture energy values, attributed to the presence of kaolinite due to its robust interlayer bonds. The results contribute insights into the selection and optimization of rammed earth materials for sustainable construction, aligning with the growing emphasis on ecological and durable building resources.

## KEYWORDS

Rammed earth, Clay, Fracture energy, Three-point bending test, Sustainable construction

## INTRODUCTION

The construction and materials engineering industry is grappling with the challenge of sourcing sustainable materials that also fulfill strict standards for durability and environmental impact. Unfired earth, traditionally perceived as an obsolete material, holds significant potential for modern applications. This article examines unstabilized rammed earth, a material with a rich historical legacy. As global focus on sustainability escalates, especially after 2023, the hottest year on record [1], this ancient construction technique is resurfacing as a promising solution due to its low energy production, recyclability, and positive influence on indoor climate.

Earthen construction has deep roots in human history. Ancient civilizations utilized locally available resources such as stone, earth, and plant materials to build shelters, resulting in the construction of earthen structures across all continents and climate zones. Some of the oldest preserved structures date back to the Neolithic period at sites like Catalhoyuk in Turkey and Mohenjo-Daro in India. In Egypt, large earthen blocks were used for structures with Nubian vaults (circa 3500 BCE). In Morocco, the 11th-century Ait Ben Haddou stands as a prominent example of rammed earth architecture [2].

The cradle of earthen construction also includes America. In South America, Peru is home to some of the largest and most significant unfired clay structures, including the pyramids of Túcume in the Lambayeque Valley. These pyramids, built around 1100 AD, comprise 26 structures spread over 200 hectares. Constructed from adobe bricks, these pyramids served as important cultural and religious centers for the civilizations. The construction technique involved mixing clay with water and organic materials, forming bricks, and allowing them to dry naturally in the sun [3]. Similarly, in the southwestern United States, the Ancestral Puebloans (formerly known as the Anasazi) built

impressive pueblos using similar techniques. An example is the Taos Pueblo in New Mexico, which has been continuously inhabited for over a thousand years [4].

In Europe, the earliest known building using earth is a Bronze Age half-timbered house with clay wall infill. The oldest earthen wall in northern Europe was found at the Heuneburg fortification in Germany, dating back to the 6th century BCE [5]. In the Czech Republic, earth construction gained traction in the 13th and 14th centuries as it became a primary building material. The popularity increased after devastating fires in the 16th and 17th centuries, which spurred the use of fire-resistant earth structures. This led to widespread use of earth buildings in both rural and urban architecture. Many traditional earth structures in Moravia remain intact, along with half-timbered houses in northwestern Bohemia, combining wooden frames and earth infill [6].

Modern rammed earth construction meets stringent housing standards and offers numerous benefits. Known for its excellent thermal mass, rammed earth helps regulate indoor temperatures, reducing the need for artificial heating and cooling, and is inherently fire-resistant. Studies by Bui [7] and Reddy [8] show that rammed earth walls exposed to natural weathering for 20 years have minimal erosion, demonstrating their long-lasting nature. These walls also provide good acoustic insulation, creating a quieter indoor environment, and their unique natural aesthetic blends well with various surroundings. Moisture absorption is a significant concern for rammed earth. Stabilizing agents like lime or cement are often added to reduce absorbency and improve moisture resistance. Stabilized rammed earth walls can effectively manage moisture levels, preventing mold growth and structural weakening [2]. Additionally, properly composed unfired clay can regulate indoor humidity between 40–60%, which is optimal for human health, and can bind harmful substances from the air (phthalates, formaldehyde, cigarette smoke) [9]. Stabilized rammed earth walls with hydraulic lime prevent moisture ingress, ensuring a healthier living environment [10].

For example, a family home in Santa Fe, New Mexico, features two substantial rammed earth walls (see Figure 1, left) [11]. In Plavy, Czech Republic, a traditional timber barn was reconstructed using stone and earth blocks, demonstrating the material's adaptability (see Figure 1, right) [12].



*Fig. 1 – Modern rammed earth buildings: on the left, a house in Santa Fe [11] and on the right, in Plavy [12]*

## Regulatory Challenges and Objectives

The adoption of earthen construction techniques in the EU is stymied by the absence of cohesive regulatory standards, partly due to its historical decline in the 19th century. During that period, the method of firing bricks in a circular kiln was discovered, dramatically reducing their cost. This regulatory gap relegated earthen construction mainly to enthusiasts and environmentally conscious individuals [13, 14]. Meanwhile, non-EU countries like Australia [15], New Zealand [16], and the USA (New Mexico) [17] have established specific regulations, though standards, particularly regarding mechanical properties, vary significantly. The required compressive strength ranges from 0.30 to 2.07 MPa, and tensile strength ranges from 0.00 to 0.35 MPa. In the EU, old standards for

earthen construction in Germany [18] and Switzerland [19] are no longer valid. This article seeks to bridge this knowledge gap by investigating how the composition of rammed earth - the type and quantity of clay, affects its fracture energy – one of crucial mechanical properties.

## MATERIALS AND METHODS

### Composition of the earth mixture

Earth forms through rock erosion due to mechanical movements like glaciers, wind, water, thermal expansion, and contraction, as well as chemical reactions with acids and oxygen. This results in clay, a mix of weathered rocks and organic components. The composition and properties of clay are influenced by local factors such as parent rock and climate. Thus, understanding the characteristics of a specific clay is crucial for construction use [2].

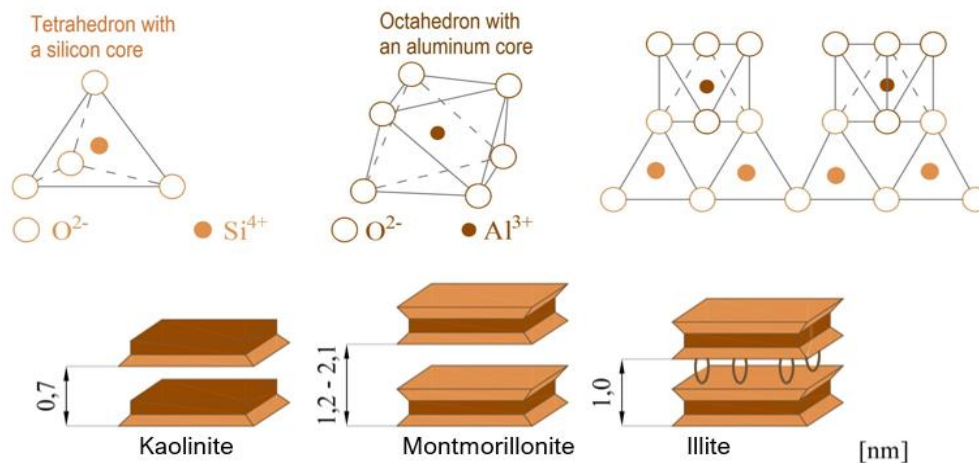


Fig. 2 – Tetrahedron with a silicon core and octahedron with an aluminum core

The earth is a mixture of fine particles like clay minerals, silt, sand, and other materials (gravel, stones, water). Silt, sand, and gravel are different from clay in that they are fillers bound by cohesive forces, consisting of eroded or water-transported aggregates. Their mutual ratio, known as granularity, is identified through sieve analysis, which determines the proportions and plots the grain-size curve [13]. In the mixture, clay acts as a binder, while larger particles act as fillers, and water activates clay's binding properties. The proportion and type of these components influence the earth's construction properties. "Clay is a natural material primarily composed of fine-grained minerals, generally plastic with adequate water content, and hardens upon drying or firing" [20]. Clay consists mainly of the phyllosilicate group, where large ions form layers, and smaller cations (Si, Al, Mg, Fe) occupy spaces between. These layers are structured as tetrahedra and octahedra (Figure 2). A structure composed of one tetrahedral and one octahedral layer is referred to as 1:1. The 2:1 layer type has two tetrahedral layers with one octahedral layer. Tetrahedral networks surround the octahedral one in the middle [20], see Figure 2.



*Fig. 3 – The pure clays used in the mixtures, images of the manufacturing test specimens, the process of ramming, and the manufactured specimens*

There are three main groups of clay minerals – kaolinite, smectite minerals, and illite. Kaolinite minerals, such as kaolinite, are hydrated aluminium silicates and are part of the 1:1 layered silicates. Adjacent layers of kaolinite are shifted by 0.7 nm and linked through hydrogen bonds and van der Waals forces, preventing swelling between layers and resulting in strong bonds. Smectite minerals, like montmorillonite, have a 2:1 layered structure and are characterized by weak van der Waals forces between layers, allowing water to penetrate between layers, causing swelling. Montmorillonite contains exchangeable cations that offset the negative charge of the layers. Illite, a 2:1 mineral, is structurally similar to montmorillonite but has stronger interlayer bonds and does not expand upon contact with water, although its bonds are not as strong as those in kaolinite [20].

Clay type is determined through methods like X-ray diffraction, which identifies clay minerals [2]. Next method is the methylene blue test, measuring dye absorption based on microstructure [21]. Atterberg limits define changes in clay properties with moisture, identifying transitions between liquid, plastic, and semi-solid states [22].

### **Manufacturing of Specimens**

The first step before manufacturing was to design the composition of the earth mixtures. The key objective during the development of the formulas was to investigate the effect of different types and amounts of clay, as well as adjusted water content, on the mechanical and physical properties of the manufactured specimens. Mixtures with different types of clay, various clay contents, and water contents were designed to enable comparison and to evaluate the impact of composition changes on the properties. The rammed earth was without stabilizers or other additives. The proposed sand-to-clay ratio was expressed as  $s/c$  in weight percentage of the mixture. The total sum of  $s$  and  $c$  was 100 %. The water coefficient  $w$  was then determined, representing the ratio of the water weight used in the mixture to the weight of the clay. The weight percentages of water in the mixture  $h$  were also determined for each mix, indicating the water content as a percentage of the total mixture weight.

Tab. 1 - The chemical composition of clays used to produce test specimens. The percentage representation of individual compounds is given [29]

Type of clay	SiO <sub>2</sub> [%]	Al <sub>2</sub> O <sub>3</sub> [%]	Fe <sub>2</sub> O <sub>3</sub> [%]	TiO <sub>2</sub> [%]	CaO [%]	MgO [%]	NA <sub>2</sub> O [%]	K <sub>2</sub> O [%]
Illitic-kaolinitic (IK)	59.31	24.71	3.37	1.09	0.19	0.40	0.30	2.82
Illitic (I)	56.57	18.40	9.72	1.16	1.12	2.54	0.18	2.91
Montmorillonitic (M)	50.51	31.20	3.37	0.86	0.40	0.42	0.08	1.62

Three types of clays were used (illitic-kaolinitic S and KR, illitic AGL, and montmorillonite GEM), all supplied in powder form (see Figure 3) by LB Minerals. The exact chemical composition of the clays used is in Table 1. (except clay S, which did not have the exact chemical composition listed). The clays were mixed with sand of known grain-size distribution in predefined ratios, and the grain-size curves of each mixture were then calculated, there are shown in Figure 4. Along with the grain-size curves of the mixtures used in this paper, some grain-size curves of rammed earth mixtures used in the literature are included in the Figure 4 for a better general idea. For producing the test specimens, the mixture components were weighed according to predetermined formulations. First, the exact amount of sand and water was weighed, then 2/3 of the water was added to the sand and mixed. Finally, the clay and the remaining water were added, and the entire mixture was thoroughly blended. Water for the mixture was sourced from the municipal water supply.

The mixtures were compacted into steel molds, using both mechanical and manual compaction methods to ensure material homogeneity. There were two basic specimen sizes: 40×40×60 mm and 20×20×100 mm. After being removed from the molds, the prepared specimens were transferred to a controlled drying process in a climate chamber to ensure a stable environment before measuring their properties. Nineteen mixtures were produced, and 3 to 6 specimens from each were tested in the three-point bending test.

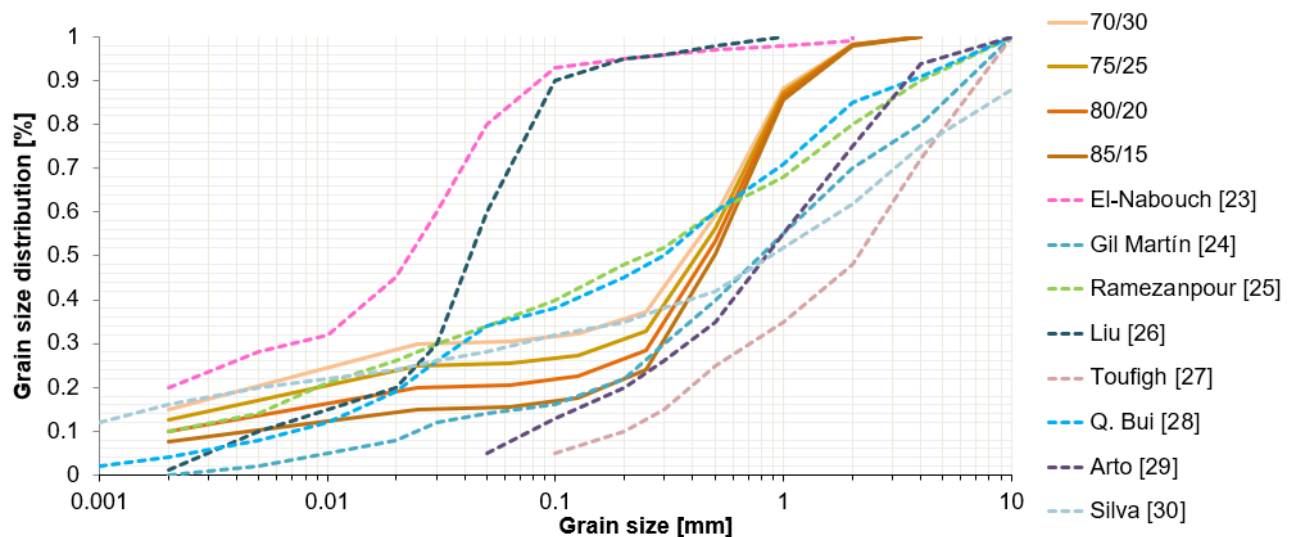


Fig. 4 – Grain size distribution curves of the used mixtures, marked sand/clay ratio (solid lines) and comparison with grain size curves from the literature (dashed lines)

Due to laboratory constraints, such as the limited force of the testing machine, smaller samples of rammed earth with reduced layer height compared to real-world structures were used in this study. The maximum grain size in the mixture was set to 4 mm. Based on this grain size, the number of compacted layers at a height of 40 mm was set to 4-5 (at least 8 mm each), and at a height of 20 mm to 3 layers (at least 6 mm each). The layer thickness was ensured to be at least 1.5 times greater than the maximum grain size to maintain structural integrity and layer representativeness. The mechanical properties of larger structures can be effectively replicated at a

smaller scale if layering principles are followed. The authors believe that these conditions still provide a valid approximation of the behaviour of rammed earth.

### Fracture Energy of Rammed Earth: State of the Art

Fracture mechanics examines the failure of materials beyond traditional strength analysis, focusing on the energetic analysis needed for crack formation. There are three main types of fracture mechanics: linear, which applies to brittle materials with inelastic deformation at the crack tip; elastic-plastic, for ductile materials like steel that develop a plastic, strengthening, nonlinear zone around the crack tip; and nonlinear fracture mechanics for quasi-brittle materials like concrete or unstabilized rammed earth, which develop a nonlinear process zone with gradual damage in the form of microcracks and microslips. This can be seen in Figure 4 [31, 32]. For clarification, mode I fracture, where the crack opens, is depicted in Figure 4.

Before conducting experimental measurements, a review of current studies on fracture energy in unstabilized rammed earth was performed. Table 2 lists fracture energy values from the literature, including the author's name, the country of research, and the publication reference. It provides bulk density  $\rho$ , flexural tensile strength  $f_t$ , and its standard deviation (if reported). Another column indicates the method used to determine fracture energy, followed by the fracture energy value  $G_f$  and its standard deviation (if reported).

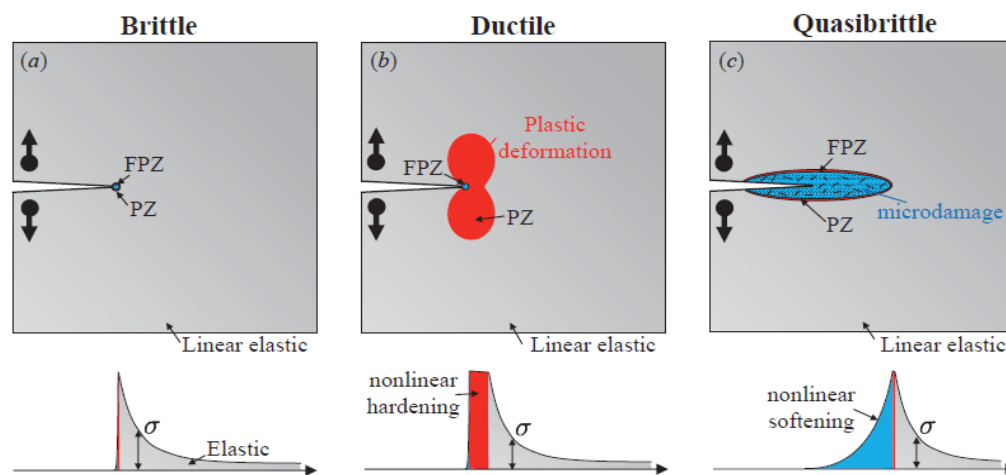


Fig. 4 – Types of structural fracturing behaviour: (a) brittle, (b) ductile and (c) quasi-brittle. Trends of the stress distributions along the crack line are shown at the bottom of each figure [31]

Since rammed earth is classified as a quasi-brittle material, fracture energy is a critical property alongside compressive and tensile strength and the modulus of elasticity. Despite its importance for understanding material behaviour and potential mathematical modelling, it has received relatively little research attention.

Tab. 2 - Fracture energy values reported in the literature

Source	$\rho$ [kg/m <sup>3</sup> ]	$f_t$ [MPa]	Type of test	$G_f$ [J/m <sup>2</sup> ]
Q. Bui (VN) [28]	2300	0.130	Calculated of $f_c$ , depends on grain size	12
Arto (ES) [29]	2010	0.440 ± 0.050	Three-point bending test	23
Silva (PT) [30]	1830	0.126	Estimated as 29 $f_t$	4
Miccoli (DE) [33]	2190	0.370	Estimated as 29 $f_t$	11
Corbin (GB) [34]	-	-	Wedge splitting test	2 ± 1
Hussaini (IR) [35]	1946	0.240	Wedge splitting test	19

## Method for Measuring and Calculating Fracture Energy

The three-point bending method was chosen to measure the fracture energy. Literature identifies two types of tests for obtaining fracture energy: three-point bending tests and wedge splitting tests. However, a challenge arises with the three-point bending of rammed earth due to difficulties in notch creation on the specimens. The specimens tend to crumble and break during cutting, thereby degrading the sample. Consequently, a modification of the standard methodology recommended was implemented, and the tests were performed without notches. Given that the mixture under test is fine-grained, a crack was anticipated to form under the applied load at mid-span without notching. This occurrence was confirmed experimentally (visible cracks are shown in Figure 5).

Rammed earth is generally assumed to be an anisotropic material. Tests, therefore, are conducted perpendicular to the rammed layers, aligning with the actual loading conditions of structural elements. This orientation posed challenges in test feasibility because the top edge was uneven due to the compaction process. This irregularity created difficulties in achieving a flat surface necessary for the load cylinder of the test rig. This led to the consideration of testing the samples in a rotated orientation, parallel to the compaction layers. In this setup, the two opposite sides of the body are flat, thanks to the steel mold used for specimen preparation.

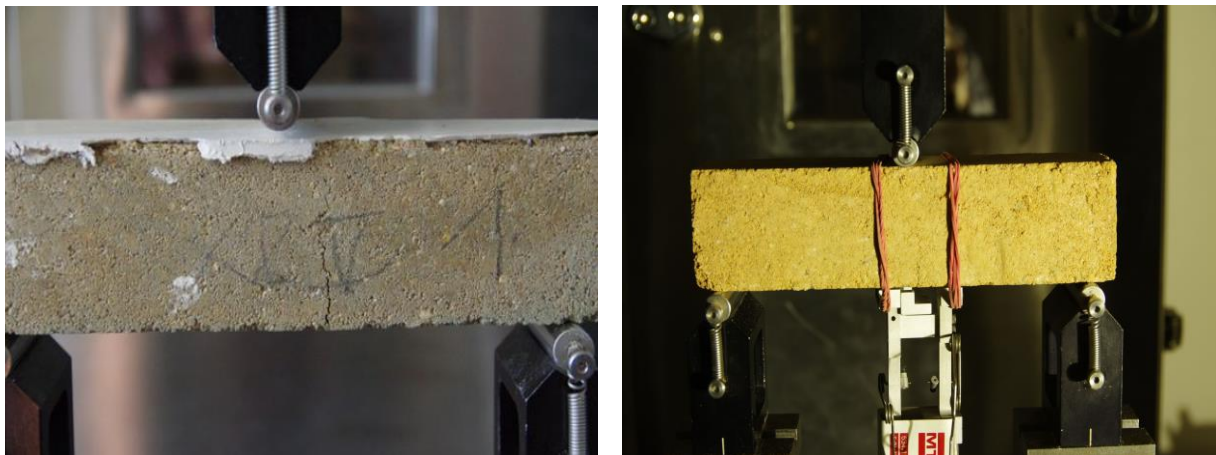


*Fig. 5 – Left: perpendicular [43], Right: parallel orientations of specimens*

Research on the anisotropy and isotropy of materials, such as the studies by T. Bui [36] and Q. Bui [37], were consulted. These studies, which investigated samples both perpendicular and parallel to the layers, demonstrated only a 5 % difference in compressive strength between these directions. Based on these findings, it was hypothesized that, assuming adequate adhesion between the layers, the material could be considered effectively isotropic for the purposes of this study, as reflected by the similar measured properties in both orientations. This assumption also supports the development of numerical models, such as those used by Silva [30] to model rammed earth as a homogeneous material.

Experimentally, this hypothesis was tested by analyzing samples from one mixture both perpendicular and parallel to the layers (see Figure 5 left for perpendicular and Figure 5 right for parallel). For perpendicular testing, the top edge of the specimens was smoothed with a thin layer of gypsum to create a flat surface, which did not affect the flexural strength. The differences in flexural tensile strength between the perpendicular and parallel orientations fell within the standard deviations of the measurements, aligning with the research findings where deviations were within 5 %. Additionally, no delamination occurred during the tests. Further bending tests were conducted on rotated specimens to avoid the need for plastering.

The fictitious crack model methodology was employed to determine fracture energy. This model addresses mode I (i.e., crack opening) where the crack is located on the axis of symmetry of the specimen and the load attempts to open the crack symmetrically [38]. For this determination, a

working diagram from a three-point bending test is essential. The tests were conducted using an MTS Alliance RT 30kN machine with a loading rate of 0.5 mm/min. The entire working diagram, including the descending branch, was recorded to capture the complete behaviour until specimen failure [38].

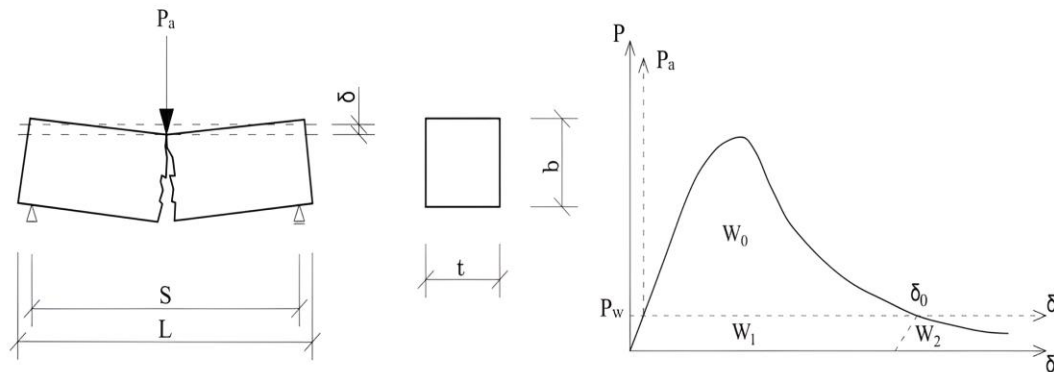


Fig. 6 – Left: three-point bending arrangement, Right: obtained  $P-\delta$  diagram

The area that appears under the diagram is called the fracture work and from this the fracture energy  $G_f$  can be calculated. Figure 6 shows a schematic of the test and the resulting working diagram with the added consideration of the self-weight. The area  $W_0$  is the work done in three-point bending by the external loading force  $P_a$ . The force  $P_w$  represents the equivalent force to the self-weight of the specimen. The areas  $W_1$  and  $W_2$  are due to the self-weight of the specimen. The area  $W_1$  can be derived as  $W_1 = P_w \cdot \delta_0$  [36]. The areas of  $W_1$  and  $W_2$  are equal according to [38].

Before calculating the fracture energy, the necessity of considering the stresses imposed on the crack by the specimen's own weight was evaluated. The stress over the midspan from the dead weight was compared to the tensile strength of the specimen, expressed as a percentage. This value, assessed across three different mixes, varied between 1.04–2.20 %. In the literature, it is recommended to include the self-weight in the fracture energy calculations for concrete, typically around 10 % [32]. Given the significantly lower values, the effect of self-weight was excluded from the fracture energy calculations in this study. The fracture work was then calculated using the area under the working diagram:

$$A_F = \int_0^{\delta_{max}} P(\delta) d\delta \quad (1)$$

Fracture energy was calculated by dividing the fracture work by the area of the crack created, expressed in units of N/m, or more specifically for this study, N/mm:

$$G_f = \frac{A_F}{b \cdot t} \quad (2)$$

## RESULTS

Fracture energy values are presented in Table 3. Each mixture is identified by a label provided by the clay manufacturer. Table columns include mixture number, number of specimens measured, specimen size, sand-to-clay ratio ( $s/c$ ), water coefficient ( $w$ ), clay content by weight percentage of the mixture ( $j$ ), water content by weight percentage of the mixture ( $h$ ), bulk density ( $\rho$ ), bending tensile strength ( $f_t$ ), fracture energy ( $G_f$ ), and the standard deviation of the fracture energy ( $\sigma_{Gf}$ ).

Tab. 3 - Fracture energy measurement results

Mix.	No	Pcs	Size [mm]	s / c - w [% / % - -]	Clay j [%]	Water h [%]	$\rho$ [kg/m <sup>3</sup> ]	$f_t$ [MPa]	$G_f$ [J/m <sup>2</sup> ]	$\sigma_{Gf}$ [J/m <sup>2</sup> ]
S	3	6	20×20×100	75/25 - 0.295	23.3	6.9	2185	0.812	19.112	0.023
S	4	6	20×20×100	85/15 - 0.370	14.2	5.3	2064	0.373	7.438	0.037
S	5	6	20×20×100	75/25 - 0.335	23.1	7.7	2133	0.623	15.705	0.008
GEM	1	6	20×20×100	80/20 - 0.370	18.6	6.9	2097	0.344	17.335	1.460
GEM	2	6	20×20×100	75/25 - 0.370	22.9	8.5	2078	0.401	17.111	3.415
GEM	3	4	20×20×70	75/25 - 0.295	23.3	6.9	1932	0.361	16.577	1.804
AGL	1	3	40×40×160	80/20 - 0.370	18.6	6.9	2122	0.334	5.712	1.073
AGL	2	3	40×40×160	75/25 - 0.295	22.9	8.5	2082	0.330	8.389	1.141
AGL	3	3	40×40×160	80/20 - 0.400	18.5	7.4	2096	0.310	4.261	0.434
AGL	5	3	40×40×160	85/15 - 0.370	14.2	5.3	1982	0.146	1.933	0.308
AGL	6	3	40×40×160	85/15 - 0.400	14.2	5.7	1998	0.224	3.062	0.818
AGL	7	3	40×40×160	80/20 - 0.290	18.9	5.5	2098	0.133	3.571	1.410
AGL	10	3	40×40×160	75/25 - 0.295	23.3	6.9	2125	0.328	7.410	0.634
AGL	11	3	40×40×160	75/25 - 0.400	22.7	9.1	2095	0.386	9.776	0.787
AGL	12	3	40×40×160	70/30 - 0.295	27.6	8.1	2097	0.458	10.997	1.475
KR	2	3	40×40×160	75/25 - 0.370	22.9	8.5	2098	0.695	21.944	4.702
KR	8	3	40×40×160	80/20 - 0.290	18.9	5.5	2052	0.551	11.613	2.302
KR	11	3	40×40×160	75/25 - 0.400	22.7	9.1	2115	0.638	20.746	6.057
KR	14	3	40×40×160	70/30 - 0.400	26.8	10.7	2112	0.678	14.069	1.256

Mixture KR 2 exhibited the highest fracture energy, measuring  $21.944 \pm 4.702$  J/m<sup>2</sup>, whereas the lowest was observed in AGL 3 at  $1.933 \pm 0.308$  J/m<sup>2</sup>. These results, discussed in further detail in the subsequent chapter, correspond well with the mixture's composition. The observed values align with the range reported in the literature, as referenced in Table 2. For instance, the minimum value closely matches the 2 J/m<sup>2</sup> reported by Corbin [39] and the 4 J/m<sup>2</sup> by Silva [30], adjusted to equivalent units. The maximum value of 23 J/m<sup>2</sup> from Arto work [34] aligns with our highest measurements. Average values noted by Q. Bui [28] at 12 J/m<sup>2</sup> and Miccoli [33] at 11 J/m<sup>2</sup> correspond to our mean measurements, underscoring the consistency of our data with existing studies. The graph in Figure 7 compares the measured fracture energies of the different mixtures. Each clay is indicated by a different colour of the bars. The orange markers plot the percentage of clay in the mixture and the blue markers plot the water content. For a detailed analysis of the impact of composition, the mixtures were divided into two groups. These groups were defined so that each group shared a common characteristic in the composition:

*Type of Clay:* Mixtures in this group have identical composition except for the type of clay used. The sand-to-clay ratio (s/c) and the water coefficient  $w$  are the same.

*Different Clay Content:* Mixtures here have the same water coefficient  $w$ , but the clay content varies among the mixtures. However, all mixtures in this group utilize the same type of clay.

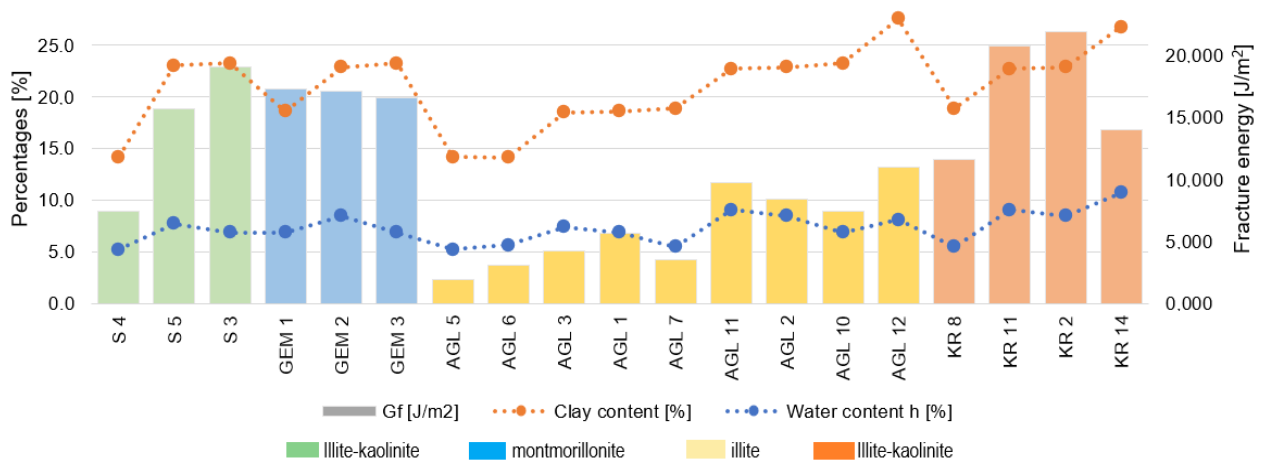


Fig. 7 – Results of fracture energies with indicated percentages of clay and water in the mixture

### Type of Clay

The first comparative set includes mixtures with the same sand-to-clay ratio (s/c) and water coefficient but different types of clay. For the KR mixture, the clay is illitic-kaolinitic (IK, S), while the AGL group contains illitic clay (I), montmorillonite (M).

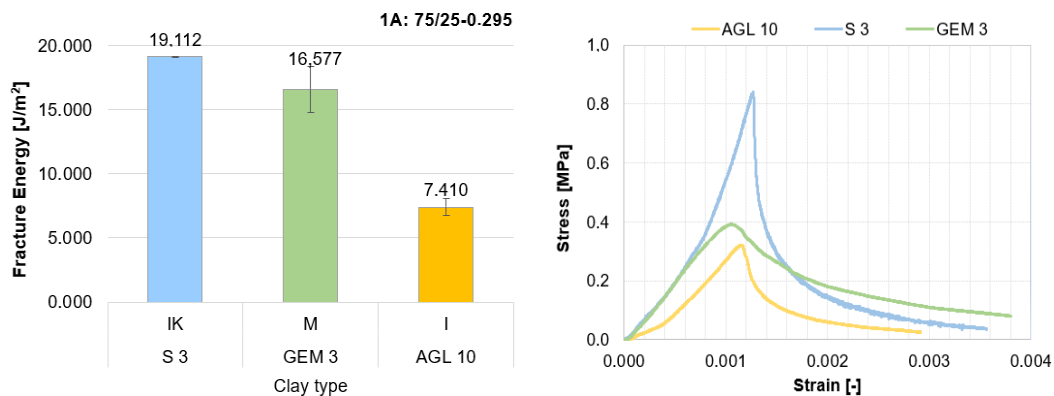


Fig. 8 – Left: Fracture energy for group 1A, Right: Stress-Strain diagrams of 1A

1A: 75/25–0.370: The highest fracture energy was measured in the S3 mixture containing illitic-kaolinitic clay, reaching  $19.112 \pm 0.023 \text{ J/m}^2$ . The mixture with montmorillonite clay, GEM 3, followed with  $16.577 \pm 1.804 \text{ J/m}^2$ . The lowest value was observed in the AGL10 mixture with illite, recording  $7.410 \pm 0.634 \text{ J/m}^2$ . The results are graphically compared in Figure 8.

1B: 75/25–0.400: Mixtures in this group have a higher water coefficient than group 1A with the same sand/clay ratio. Again, the highest value was observed in the KR 2 mixture with illitic-kaolinitic clay, amounting to  $21.944 \pm 4.702 \text{ J/m}^2$ . The mixture with montmorillonite, GEM 2, showed slightly lower values at  $17.111 \pm 3.415 \text{ J/m}^2$ , and the smallest value was recorded in the AGL 2 mixture with illite, showing  $8.389 \pm 1.141 \text{ J/m}^2$ . The values are displayed graphically in Figure 9.

1C: 80/20–0.290: In this group, the highest fracture energy value was measured in the GEM 1 mixture with montmorillonite, which was  $17.355 \pm 1.460 \text{ J/m}^2$ . The smallest value was recorded in the AGL 1 mixture with illitic-kaolinitic clay, measuring  $5.712 \pm 1.073 \text{ J/m}^2$ .

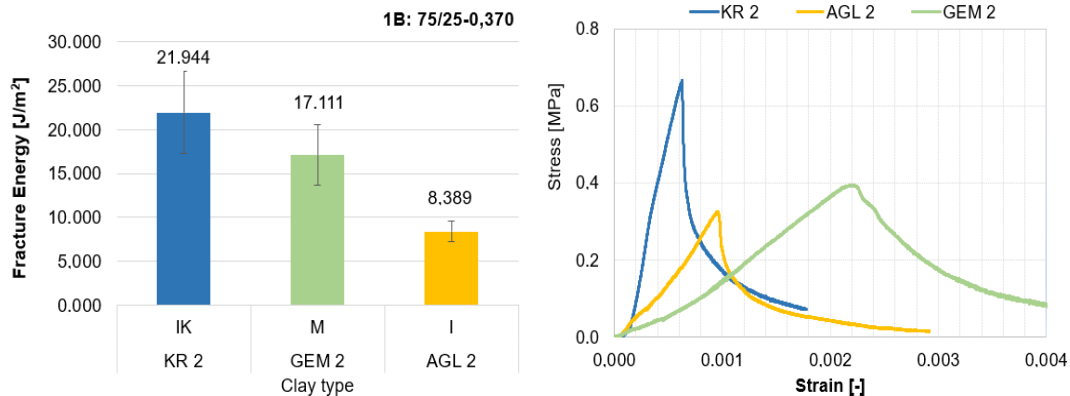


Fig. 9 – Left: Fracture energy for group 1B, Right: Stress-Strain diagrams of 1B

1D: 85/15–0.370: Higher values were measured in the S 4 mixture with IK clay,  $7.4385 \pm 0.037 \text{ J/m}^2$ , while the smaller value was observed in the AGL 5 mixture with I clay, at  $1.933 \pm 0.308 \text{ J/m}^2$ .

Across all comparative groups, the highest values were observed in mixtures with illitic-kaolinitic clay, followed by montmorillonite clay, with the lowest values consistently recorded in mixtures with illitic clay.

### Different Clay Content

In Group 2, mixtures with the same water coefficient, same type of clay but differing in the clay content are compared.

2A:  $w=0.295$ , Illite Clay: There are two mixtures, AGL 10 with 23.3 % clay and AGL 12 with 27.6 % clay. The higher fracture energy value was observed in mixture AGL 12 with a higher clay content ( $10.997 \pm 1.475 \text{ J/m}^2$ ), while a lower value was measured for mixture AGL 10 with less clay ( $7.410 \pm 0.634 \text{ J/m}^2$ ).

2B:  $w=0.370$ , Illite Clay: A similar trend is found in group 7B again with illite, but with a higher water coefficient  $w=0.370$ . The lowest value is in mixture AGL 5 with 14.2 % clay ( $1.933 \pm 0.308 \text{ J/m}^2$ ), followed by mixture AGL 1 with 18.6 % clay ( $5.712 \pm 1.073 \text{ J/m}^2$ ), and the highest value was measured in mixture AGL 2 with 22.9 % clay ( $8.389 \pm 1.141 \text{ J/m}^2$ ), see Figure 10.

2C:  $w=0.400$ , Illite Clay: Group 7C is the last with illite and the highest water coefficient  $w=0.400$ . Graphical comparison of the measured values is shown in Figure 11. Again, a trend is observed where the fracture energy increases with the clay content. The lowest fracture energy value of  $3.062 \pm 0.818 \text{ J/m}^2$  was measured for AGL 6 with 14.2 % clay, followed by mixture AGL 3 with  $4.261 \pm 0.434 \text{ J/m}^2$  and 18.5 % clay, and the highest value of  $9.776 \pm 0.787 \text{ J/m}^2$  was for mixture AGL 11 with the highest clay content of 22.7 %.

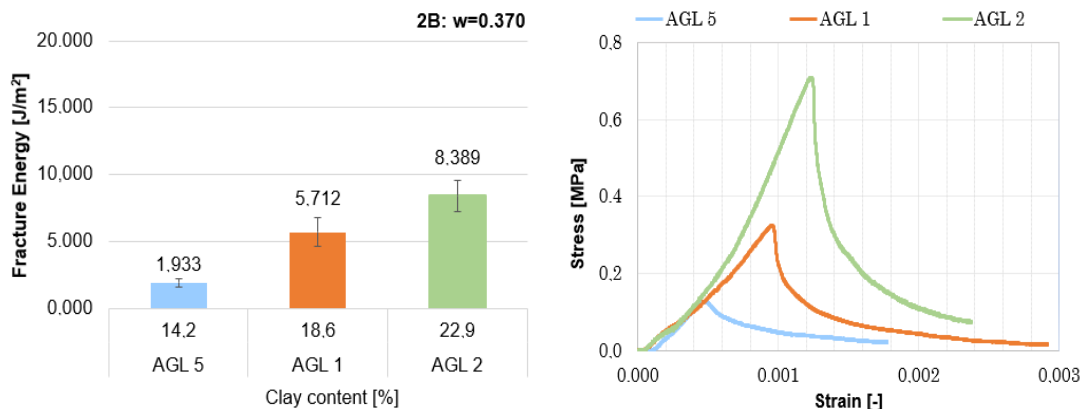


Fig. 10 – Left: Fracture energy for group 2B, Right: Stress-Strain diagrams of 2B

**2D:  $w=0.400$ , Illitic-Kaolinitic Clay:** Unlike the previous groups with illite, the highest fracture energy value of  $20.746 \pm 6.057 \text{ J/m}^2$  was measured for mixture KR 11 with a lower clay content of 22.7%, while a lower value of  $14.069 \pm 1.256 \text{ J/m}^2$  was measured for mixture KR 14 with a higher clay content of 26.8 %.

**2E:  $w=0.400$ , Montmorillonite Clay:** The last group consists of mixtures with montmorillonite. Two mixtures, GEM 1 with 18.6 % clay and GEM 2 with 22.9 % clay, had comparable fracture energy values of  $17.355 \pm 1.460 \text{ J/m}^2$  and  $17.111 \pm 3.415 \text{ J/m}^2$ , respectively.

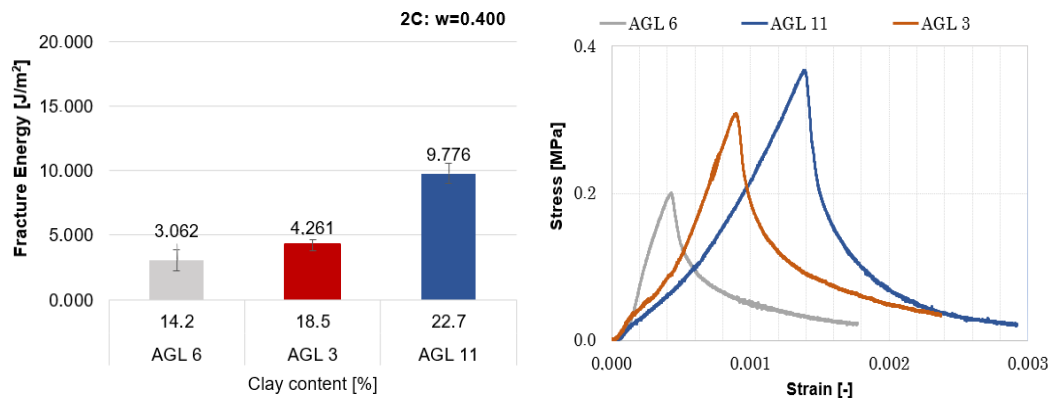


Fig. 11 – Left: Fracture energy for group 2C, Right: Stress-Strain diagrams of 2C

Across all tested groups with illite, an increasing trend in fracture energy was noted with the rising clay content. However, the results for illitic-kaolinitic clay deviated from the expected trend; surprisingly, mixtures with a lower content of this clay type showed higher fracture energy, suggesting an influence of kaolinite's properties enhancing the material's performance even at lower concentrations. This unexpected outcome highlights the complex interplay of clay composition on mechanical properties. For montmorillonite mixtures, the fracture energy values were relatively uniform, indicating that the impact of varying clay content is less pronounced due to the clay's inherent susceptibility to water-induced swelling, aligning with its known properties.

### Fracture Energy and Tensile Strength in Bending Relationship

From the measured data on fracture energy and tensile strength in bending, a correlation coefficient of  $R = 0.77$  was established, indicating a strong correlation. The relationship derived from the data is as follows:  $G_f = 24f_t$ . However, this relationship may not be universally applicable, as it is only a calculation based on the measured data, serving as a rough estimate of the dependence of fracture energy on flexural tensile strength. Interestingly, the work by Silva [30] and Miccoli [33], who did not measure fracture energy experimentally but inferred it from tensile strength, used the relationship  $G_f = 29f_t$ , which is close to the results obtained from the experiments presented in this article.

### DISCUSSION

Mixtures containing illitic-kaolinitic clay demonstrated the highest fracture energy values, influenced by the strong interlayer bonds of kaolinite. These strong bonds, formed via hydrogen bonds and van der Waals forces, prevent moisture-induced swelling and enhance the mechanical stability of the material [2]. In contrast, montmorillonite mixtures exhibited lower fracture energy due to their naturally weaker van der Waals bonds. These bonds facilitate water penetration and swelling, compromising structural integrity under load [20]. Although montmorillonite contains exchangeable cations that provide cohesion and resistance, they do not sufficiently counteract the mechanical weakening associated with its structural properties. While illite has stronger interlayer bonds than montmorillonite [20], it showed the lowest fracture energy values among the tested clays. This suggests that although illite bonds resist water-induced expansion better than montmorillonite, they

are significantly weaker than kaolinite bonds, limiting their effectiveness in enhancing the fracture energy of rammed earth.

When comparing clay content in the mixtures, an increasing trend in fracture energy was observed for illite across all test groups with rising clay content. However, results for illitic-kaolinitic clay deviated from this expected trend. Mixtures with a lower content of this clay demonstrated higher fracture energy, indicating kaolinite properties that improve material performance even at lower concentrations. This unexpected result emphasizes the complex interplay between clay composition and mechanical properties. In montmorillonite mixtures, fracture energy values were relatively consistent, suggesting that varying clay content has a less pronounced impact. These measurement results indicate the significant impact of both the type and content of clay on the fracture energy of rammed earth. While previous studies typically focused on individual clay types, such as Corbin [36] with kaolinite, or mixtures of multiple types of clay (Miccoli [33], el Nabouch [23]), other articles do not specify the exact type and chemical composition of clay. Instead, they measure only the clay content based on the particle size distribution curve (e.g., Silva [30], Arto [29]). This article examines three specific types of clay and shows that the clay type significantly influences the mechanical properties of rammed earth.

## CONCLUSION

This study confirms the critical impact of the type and amount of clay on the fracture energy of unstabilized rammed earth. It was found that mixtures containing illitic-kaolinitic clay exhibit the highest fracture energy values, attributed to the presence of kaolinite. The robust interlayer bonds of kaolinite enhance the structural integrity and resilience of the earth. Montmorillonite, with its weaker bond structure, showed lower fracture energy values. Illite, despite having stronger bonds than montmorillonite but weaker than those of kaolinite, still displayed the lowest fracture energy.

Unexpectedly, the study revealed that even the low mechanical properties of earth can be optimized by adjusting the content and type of clay in the mixture. This finding differs from traditional approaches that do not differentiate between the types of clays contained in the mixture. Given these insights, further research should focus on exploring the detailed mechanical behaviours of different types of clays under various environmental conditions and stresses, to develop more accurate predictions and models for the behaviour of rammed earth.

## ACKNOWLEDGEMENTS

This research was supported by project SGS22/089/OHK1/2T/11 Building Materials and Construction through the Eyes of Experiment and from the project GACR No. 18-10884S Unfired and Rammed Clay for Construction.

## REFERENCES

- [1] Copernicus, 2024. Global Climate Highlights 2023: Copernicus - 2023 is the hottest year on record, with global temperatures close to the 1.5°C limit. <https://climate.copernicus.eu/copernicus-2023-hottest-year-record> [cited 2024-09-01]
- [2] Reddy, B.V.V., 2022. Compressed Earth Block & Rammed Earth Structures (Springer Nature Singapore, Singapore) Springer Transactions in Civil and Environmental Engineering. 331-345 pp. ISBN: 9789811678776.
- [3] Taos Pueblo, 2024. About. <https://taospueblo.com/about/> [cited 2024-07-16].
- [4] Peru Hop, 2024. Tucume: Valley of the Pyramids, Peru. <https://www.peruhop.com/tucume-valley-of-pyramids-peru/> [cited 2024-07-16].
- [5] Minke, G., 2006. Building with Earth: Design and Technology of a Sustainable Architecture (Birkhäuser - Publisher for Architecture). 11-18 pp. ISBN: 9783764374778.
- [6] Žabičková, I., 2002. Earthen Buildings (ERA Publishing). 1-15 pp. ISBN: 8086517217.

- [7] Bui, Q. B., Morel, J.-C., Reddy, B., Ghayad, W., 2009. Durability of rammed earth walls exposed for 20 years to natural weathering. *Building and Environment*, vol. 44, 912-919 pp. DOI: 10.1016/j.buildenv.2008.07.001.
- [8] Reddy, V. B. V., Kumar, P. P., 2011. Cement stabilized rammed earth Part B: Compressive strength and stress-strain characteristics. *Materials and Structures*, vol. 44, 695-707 pp. DOI: 10.1617/s11527-010-9644-7.
- [9] Růžička, J., Diviš, J., 2019. The Influence of Building Materials on Relative Humidity of Internal Microclimate. *IOP Conference Series: Earth and Environmental Science*, vol. 290, 012029 pp. DOI: 10.1088/1755-1315/290/1/012029
- [10] Hall, M., & Djerbib, Y., 2004. Rammed earth sample production: context, recommendations and consistency. *Construction and Building Materials*, vol. 18, no. 4, 281-286 pp. DOI: 10.1016/j.conbuildmat.2004.02.006.
- [11] Nk'Mip Desert Cultural Centre, 2023. Southeast Wyoming Welcome Center. <https://sirewall.com/portfolio/nkmip-desert-cultural-centre/> [cited 2023-05-15]
- [12] Mutl, J., 2023. Implementation - Family House in Plavy. <http://janmutl.cz/realizace/> [cited 2023-05-16]
- [13] Houben, H., Guillaud, H., 1994. *Earth Construction: A Comprehensive Guide* (ITDG Publishing). 145-158 pp. ISBN: 1-85339-193-X.
- [14] Keable, J., Keable, R., 1996. *Rammed Earth Structures* (Practical Action Publishing). 16-28 pp. ISBN: 978-1-85339-727-1.
- [15] Walker, P., Standards Australia, 2002. HB 195 - 2002: *The Australian Earth Building Handbook* (Standards Australia). 40-45 pp. ISBN: 0-7337-4000-6.
- [16] Council New Zealand, 1998. NZ 4297: *Engineering design of earth buildings*. [http://www.eastue.org/project/linea-adobe/norme/NZD4297-1998-Engineering\\_Design\\_of\\_Earth\\_Buildings.pdf](http://www.eastue.org/project/linea-adobe/norme/NZD4297-1998-Engineering_Design_of_Earth_Buildings.pdf) [cited 2023-05-22]
- [17] Construction Industries Division of the Regulation and Licensing Department, 2016. 2015 New Mexico Earthen Building Materials Code. <https://www.srca.nm.gov/parts/title14/14.007.0004.html> [cited 2023-05-22]
- [18] Deutscher Normenausschuss Fachnormenausschuss Bauwesen, 1956. *Lehmbau: Ausführung von Lehmbauten: Richtlinien: DIN 18954* (Beuth).
- [19] Schweizerischer Ingenieur- und Architekten-Verein, 1994. D 0111: *Regeln zum Bauen mit Lehm*. [https://www.iglehm.ch/application/files/2515/1696/9453/SIA\\_D0111\\_Lehmbauregeln.pdf](https://www.iglehm.ch/application/files/2515/1696/9453/SIA_D0111_Lehmbauregeln.pdf) (cited 30-3-2024)
- [20] Weiss, Z., Kužvart, M., 2005. *Clay Minerals and Their Nanostructure and Uses* (Karolinum, Prague). ISBN: 80-246-0868-5.
- [21] Otcovská, T., Mužíková, B., Padevěť, P., 2022. Methylene blue test and adsorption capacity of clays. *Acta Polytechnica CTU Proceedings*, vol. 34, 63 pp. DOI: 10.14311/APP.2022.34.0063
- [22] Mitchell, J.K., Soga, K., 2005. *Fundamentals of Soil Behavior* (John Wiley & Sons, Inc.). 15-16 pp. ISBN: 978-0-471-46302-7.
- [23] El-Nabouch, R., Bui, Q.-B., Plé, O., Perrotin, P., 2017. Assessing the in-plane seismic performance of rammed earth walls by using horizontal loading tests. *Engineering Structures*, vol. 145, pp. 153-161. DOI: 10.1016/j.engstruct.2017.05.027.
- [24] Gil-Martín, L.M., Fernández-Ruiz, M.A., Hernández-Montes, E., 2022. Mechanical characterization and elastic stiffness degradation of unstabilized rammed earth. *Journal of Building Engineering*, vol. 56. DOI: 10.1016/j.jobee.2022.104805
- [25] Ramezanpour, M., Eslami, A., Ronagh, H., 2021. Seismic performance of stabilised/unstabilised rammed earth walls. *Engineering Structures*, vol. 245. DOI: 10.1016/j.engstruct.2021.112982
- [26] Liu, Q., Tong, L., 2017. Engineering properties of unstabilized rammed earth with different clay contents. *Journal of Wuhan University of Technology-Mater. Sci. Ed.*, vol. 32, 914-920 pp. DOI: 10.1007/s11595-017-1690-y
- [27] Toufigh, V., Kianfar, E., 2019. The effects of stabilizers on the thermal and the mechanical properties of rammed earth at various humidities and their environmental impacts. *Construction and Building Materials*, vol. 200, 616-629 pp. DOI: 10.1016/j.conbuildmat.2018.12.050
- [28] Bui, Q.B., Bui, T.T., Tran, M.P., Bui, T.L., 2019. Assessing the Seismic Behavior of Rammed Earth Walls with an L-Form Cross-Section. *Sustainability*, vol. 11, issue 5. DOI: 10.3390/su11051450

- [29] Arto, I., Gallego, R., Cifuentes, H., Puertas, E., Gutiérrez-Carrillo, M.L., 2021. Fracture Behavior of Rammed Earth in Historic Buildings. *Construction and Building Materials*, vol. 289. DOI: 10.1016/j.conbuildmat.2021.123196
- [30] Silva, R., Oliveira, D., Schueremans, L., Lourenco, P., Miranda, T., 2014. Modelling of the Structural Behaviour of Rammed Earth Components. *Proceedings of the 9th International Conference on Civil, Structural and Environmental Engineering Computing*. DOI: 10.4203/ccp.106.112
- [31] Bažant, Z., Le, J.L., Salviato, M., 2021. *Quasibrittle Fracture Mechanics and Size Effect: A First Course* (Oxford University Press, Oxford). 3-6 pp. ISBN: 978-0-19-284624-2.
- [32] Shah, S., Carpinteri, A., 1991. *Fracture Mechanics Test Methods For Concrete* (Taylor and Francis, London). 162-165 pp. ISBN: 0-412-41100-8.
- [33] Miccoli, L., Oliveira, D., Silva, R., Mueller, U., Schueremans, L., 2014. Static Behaviour of Rammed Earth: Experimental Testing and Finite Element Modelling. *Materials and Structures*, vol. 48. DOI: 10.1617/s11527-014-0411-7
- [34] Corbin, A., Augarde, C., 2014. Fracture Energy of Stabilised Rammed Earth. *Procedia Materials Science*, vol. 3. DOI: 10.1016/j.mspro.2014.06.217
- [35] Hussaini, S.M.S., Toufigh, V., 2019. Strength and Fracture Behavior of Rammed-Earth Materials. *Journal of Materials in Civil Engineering*, vol. 31, issue 10. DOI: 10.1061/(ASCE)MT.1943-5533.0002923
- [36] Bui, T.T., Bui, Q.B., Limam, A., Maximilien, S., 2014. Failure of rammed earth walls: From observations to quantifications. *Construction and Building Materials*, vol. 51, 295-302 pp. DOI: 10.1016/j.conbuildmat.2013.10.053
- [37] Bui, Q.B., Morel, J.C., 2009. Assessing the anisotropy of rammed earth. *Construction and Building Materials*, vol. 23(9), 3005-3011 pp. DOI: 10.1016/j.conbuildmat.2009.04.011
- [38] Vydra, V., 2005. Habilitation thesis: Fracture characteristics of concrete exposed to high temperatures (Czech Technical University in Prague).

# DUST DISTRIBUTION PATTERN AND OPTIMIZATION OF TUNNEL VENTILATION SYSTEM

*Xuhui Zhang<sup>1,2</sup>, Hanwen Lai<sup>1</sup>, Zeren Peng<sup>1</sup>, Hengxing Zhong<sup>1</sup>, Yashi Liao<sup>1</sup>, Lian Lian Tan<sup>3</sup> and Jingping Liao<sup>4,5</sup>*

- 1. University of Engineering and Design, Hunan Normal University, Changsha, 410081, China*
- 2. University of Mechanical and Electrical Engineering, Central South University, Changsha Hunan 410083, China*
- 3. Hunan Lianzhi Technology Co.,Ltd. Changsha Hunan 410219, China*
- 4. Beijing Technology Research Branch, CCTEG Tiandi Science & Technology Co., Ltd, Beijing 100013, China*
- 5. Intelligent Mining Research Institute, CCTEG Chinese Institute of Coal Science, Beijing 100013, China; woshiliao1989@163.com*

## ABSTRACT

This paper focuses on examining the effectiveness of a long-pressure and short-pumping ventilation system in a tunnel construction project. Utilizing computational fluid dynamics theory and ventilation system design principles, the study involves numerical simulations through finite element method to analyze dust distribution within the tunnel. The research investigates the effect of the distance of the duct from the working face and pumping ratio on dust concentration. The results indicate that optimal ventilation and dust removal occur when  $L_{\text{pressure}}$  set at 20m,  $L_{\text{pumping}}$  set at 3m, and pumping ratio is 0.7, the dust concentration can be reduced to less than 250 mg/m<sup>3</sup> within 10m of the tunnel face which ensures the requirement of dust reduction in the main working area of workers and ensure a safer working environment.

## KEYWORDS

Tunnel ventilation system, Dust concentration, Long-pressure and short-pumping, Pumping ratio, Duct

## INTRODUCTION

The rapid development of underground engineering machinery has led to widespread use of roadheaders across various fields [1]. However, the full-section hard rock roadheader produces significant amounts of dust during tunnel construction, posing risks to workers such as pneumoconiosis and safety hazards [2-3]. Dust accumulation can also interfere with equipment operation. Therefore, the ventilation and dust removal system is crucial to ensure worker safety, equipment functionality, and control of environmental conditions within the tunnel [4-6]. Numerous scholars have conducted research on this issue, proposing innovative solutions. For instance, Ni et al. [7] introduced a pseudo-concentrated particle population model that views dust as a "two-phase

flow" of gas and solid particles, revealing the spatial distribution of particle concentration. Hargreaves et al. [8] employed a kinetic approach to develop tunnel ventilation models, enhancing auxiliary ventilation systems to mitigate hazards.

Scholars have also fine-tuned dust removal system models to optimize dust elimination based on dust characteristics. The studies by Parra et al. [9], Wang et al. [10], Lai et al. [11], Hussein et al. [12], Klemens et al. [13], SA et al. [14] and Ashrafi et al. [15] demonstrate various approaches to addressing dust control challenges in tunnel construction, showcasing the importance of efficient ventilation systems and dust management protocols in ensuring worker health and safety.

Several scholars have conducted research on ventilation methods for different terrain conditions. Lee et al. [16] conducted a comparative analysis of the pitch angle of the jet fan in a jet fan ventilation system. Torano et al. [17] ultimately identified the optimal pitch angle for enhancing ventilation efficiency. Liu et al. [18] utilized CFD numerical simulation to investigate the effects of ventilation and dust removal systems on dust dispersion distance and average concentration within the excavation area. Meanwhile, Xie et al. [19] explored 16 distinct ventilation conditions, determining effective dust suppression parameters through numerical simulation and field measurements. Yang et al. [20] proposed a modular airflow diversion system that integrates ventilation and dust removal, analyzing airflow-dust coupling behaviors under various conditions and identifying optimal airflow rate ratios and distances between working faces and airflow outlets. Additionally, Von Glehn et al. [21] analyzed the impact of ventilation systems on the thermal working environment and driving equipment in TBM tunnel boring, devising an optimal ventilation scheme for controlling tunnel temperatures. In a separate study, Xia et al. [22] examined the effects of main vent position, main baffle plate, and exhaust air volume on flow field distribution and dust flow characteristics during open-type TBM tunnel boring. Liu et al. [23] investigated dust control in TBM construction tunnels under varying dust extraction flow rates. Lastly, Li et al. [24] developed a cartridge filter to address dust pollution issues during TBM tunnelling in submarine tunnels, successfully reducing dust concentrations within the tunnels following practical tests.

Existing studies have pointed out the hazards associated with high concentrations of dust generated during tunnel construction, the dispersion patterns of dust under varying working conditions, and effective strategies to mitigate tunnel dust concentration. These findings not only advance the field of tunnel construction and dust control but also lay the groundwork for enhancing the tunnel construction environment and guiding the design of ventilation and dust removal systems. Currently, the absence of standardized design approaches for ventilation and dust removal in specific tunnels poses a challenge. Given the diversity in tunnel structures and working environments, as well as variations in the characteristics and operational conditions of comprehensive excavation faces across regions, a one-size-fits-all solution is unattainable. Furthermore, existing research predominantly focuses on the impact of individual factors on tunnel dust removal efficiency, overlooking the combined effects of multiple factors. Thus, a more comprehensive investigation into ventilation and dust removal system design is warranted in diverse tunnel environments. Through a detailed analysis of dust migration within the ventilation system of a tunnel, as illustrated in Figure 1, this study advocates for the adoption of a long-pressure and short-pumping ventilation system. The combination of pressure and pumping satisfies the air supply needs, while also directing dust particles into the dust removal device for purification. By optimizing the configuration of ventilation and dust

removal ducts, and adjusting the distance between the duct and working face while controlling the pumping air volume, a strong circulating flow field will be formed in front of the working face. This approach aims to enhance the efficiency of dust removal and ventilation while maintaining a safe and stable working environment, which keeps the tunnel dust concentration below 250mg/m<sup>3</sup>. The insights gained from this study are expected to inform best practices in the construction and operation of tunnels.

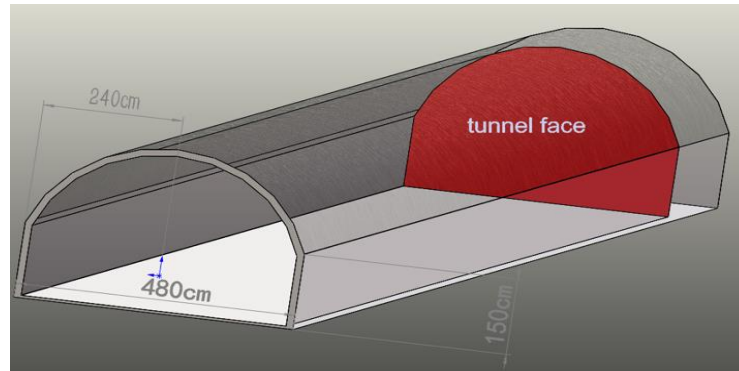


Fig. 1 – Structure of a road tunnel

## FINITE ELEMENT MODELLING

### Hypothetical condition

In this paper, the physical model of the tunnel is based on several key assumptions. Firstly, it is assumed that the density of air within the tunnel is uniform and that the air itself behaves as an incompressible fluid. Additionally, it is assumed that the air ducts are effectively sealed, with no consideration given to flow and pressure losses within the ducts. Moreover, the wind flow induced by the fan at the inlet or outlet of each property is assumed to remain constant over time, in terms of both pressure and direction. Finally, the flow field within the tunnel is assumed to exhibit steady-state turbulence.

### Basic control equations

The law of conservation of mass in a flow field containing incompressible gas, where the gas density is assumed to remain constant over time, can be simplified:

$$\frac{\partial v_x}{\partial x} + \frac{\partial v_y}{\partial y} + \frac{\partial v_z}{\partial z} = 0 \quad (1)$$

Energy in a fluid system:

$$E = i + K + P \quad (2)$$

$$i = cT \quad (3)$$

$$K = \frac{1}{2}(V_x + V_y + V_z) \quad (4)$$

In the formula:  $E$ : total energy;  $i$ : internal energy of a fluid system;  $c$ : specific heat capacity of a fluid;  $K$ : internal energy of a fluid system;  $P$ : potential energy of a fluid system;  $T$ : fluid temperature.

In fluid dynamics, the total energy ( $E$ ) in the system consists of internal energy, kinetic energy,

and potential energy of the fluid. Typically, the focus is on the conservation of internal energy ( $i$ ), with the deduction of kinetic energy ( $K$ ) in the conservation equation. Internal energy ( $i$ ) is directly proportional to the temperature ( $T$ ), leading to the formulation of an energy conservation equation with temperature ( $T$ ) as the variable. The system's energy equation yields insights into the composition and conservation of energy within the fluid in practical fluid problems [25]:

$$\frac{\partial}{\partial t}(\rho T) + \text{div}(\rho \vec{v} T) = \text{div}\left(\frac{k}{c} \text{grad} T\right) + S_T \quad (5)$$

In the formula:  $\rho$ : fluid density;  $k$ : fluid heat transfer coefficient;  $S_T$ : viscous dissipative term (in fluid mechanics).

The conservation of momentum law is widely applied, stating that the magnitude of an external force acting on a small fluid element is equal to the rate of change of momentum with time. This law forms the basis for deriving an equation that conserves momentum of the microelement in the  $x$ ,  $y$ , and  $z$  directions. This conservation equation can be expressed as follows:

$$\begin{aligned} & \frac{\partial(pu)}{\partial t} + \frac{\partial(puu)}{\partial x} + \frac{\partial(puv)}{\partial y} + \frac{\partial(puw)}{\partial z} \\ &= \frac{\partial}{\partial x}\left(\mu \frac{\partial u}{\partial x}\right) + \frac{\partial}{\partial y}\left(\mu \frac{\partial u}{\partial y}\right) + \frac{\partial}{\partial z}\left(\mu \frac{\partial u}{\partial z}\right) - \frac{\partial p}{\partial x} + S_u \end{aligned} \quad (6)$$

$$\begin{aligned} & \frac{\partial(pv)}{\partial t} + \frac{\partial(pvu)}{\partial x} + \frac{\partial(pvv)}{\partial y} + \frac{\partial(pvw)}{\partial z} \\ &= \frac{\partial}{\partial x}\left(\mu \frac{\partial v}{\partial x}\right) + \frac{\partial}{\partial y}\left(\mu \frac{\partial v}{\partial y}\right) + \frac{\partial}{\partial z}\left(\mu \frac{\partial v}{\partial z}\right) - \frac{\partial p}{\partial y} + S_v \end{aligned} \quad (7)$$

$$\begin{aligned} & \frac{\partial(pw)}{\partial t} + \frac{\partial(pwu)}{\partial x} + \frac{\partial(pwv)}{\partial y} + \frac{\partial(pww)}{\partial z} \\ &= \frac{\partial}{\partial x}\left(\mu \frac{\partial w}{\partial x}\right) + \frac{\partial}{\partial y}\left(\mu \frac{\partial w}{\partial y}\right) + \frac{\partial}{\partial z}\left(\mu \frac{\partial w}{\partial z}\right) - \frac{\partial p}{\partial z} + S_w \end{aligned} \quad (8)$$

In the formula:  $\mu$ : dynamic viscosity coefficient of the fluid,  $\text{N}\cdot\text{s}/\text{M}^2$ ;  $p$ : Pressure on the fluid,  $\text{pa}$ ;  $S_u$   $S_v$   $S_w$ : Generalised source terms for the dynamical equations in the  $x$ ,  $y$  and  $z$  directions.

### Geometric modelling of ventilation systems

The simplified tunnel model, as depicted in Figure 2, has a length of 30 m. The tunnel arch has a height of 3.6 m and a width of 4.8 m, resulting in a tunnel section area ( $A$ ) of  $15.15 \text{ m}^2$ , with detailed dimensions illustrated in Figure 3. Ventilation and dust removal ducts are suspended on both sides of the tunnel. These ducts are positioned with their axis centers  $1.7 \text{ m}$  from the vertical center axis and  $1.5 \text{ m}$  from the ground. Both ducts have a diameter of  $0.8 \text{ m}$

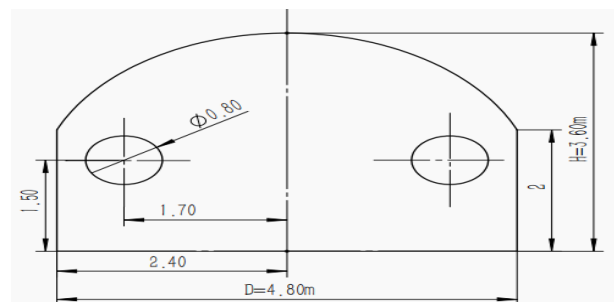
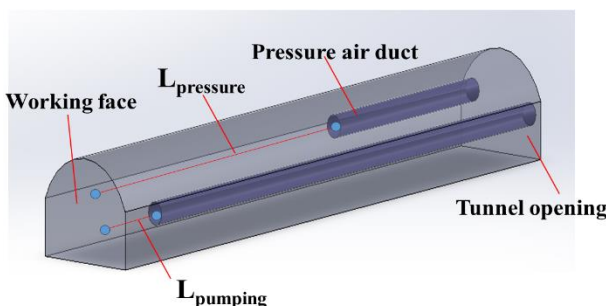


Fig. 2 – Tunnel model sketch

Fig. 3 – Tunnel cross-section dimensions

When the tunnel section area ( $A$ ) is  $15.15 \text{ m}^2$ , the duct distance from the working face can be determined by the empirical formulas working face [30]:

$$L_{pressure} \geq (4\sim 5)\sqrt{A}$$

$$L_{pumping} \leq 1.5\sqrt{A} \quad (12)$$

In above formulas, the  $L_{pressure}$  denotes the range of 15.56m to 19.45m and the  $L_{pumping}$  below 5.84 m.

In this paper, the geometric model of the tunnel includes both the tunnel and air ducts. The mesh division size is set at 0.1m, and the resulting mesh model is depicted in Figure 4.

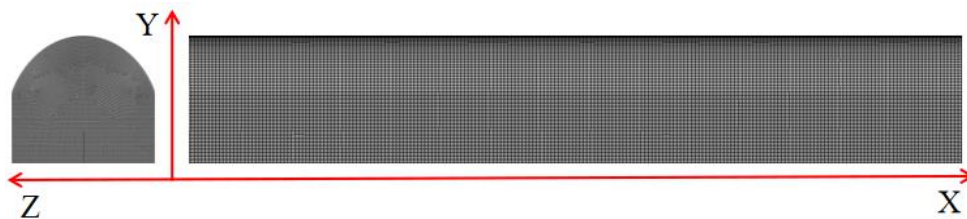


Fig. 4 – Cell mesh diagram of the tunnel

The physical model of the tunnel, as depicted in Figure 5, was established with specific directional indicators: X representing the length direction, Z representing the width direction, and Y representing the height direction. The ZX section of the tunnel model denotes the vertical measurement above the tunnel's ground, set at a height of 1.5m. The XY section corresponds to the center plane of the tunnel's vertical axis, while the ZY section illustrates the tunnel profile at various distances from the tunnel-faced end. Five cross-sections were selected along the negative X-axis direction of the tunnel within the 10m from the working face, specifically at intervals of 1m, 3m, 5m, 7m, and 9m. Subsequently, the Dust Par Mass Concentration (DPM-C) of these five cross-sections was analyzed to conduct data statistics.

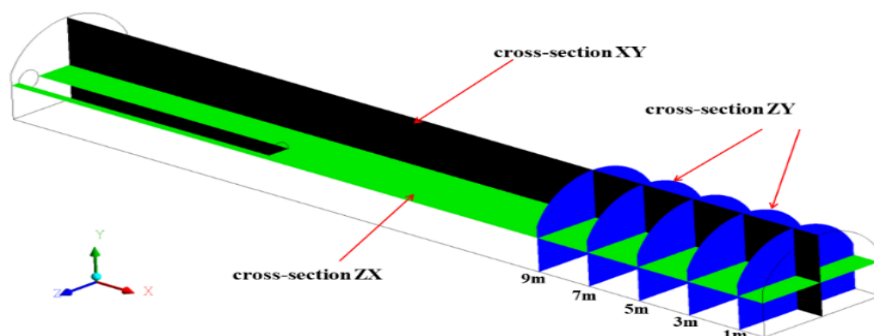


Fig. 5 – Schematic diagram of the physical model of the tunnel

### Numerical simulation models

Individual dust particles are used in constructing the Discrete Phase Model (DPM) in an Eulerian-Lagrangian approach [27]. Table 1 shows the specific computational model and Table 2 displays the parameter settings for the Discrete Phase Model.

Tab. 1 - Computational modelling

Calculate Model		Define
Solver		Pressure Based
Space		3D
Time		Steady
Viscous Model		K-epsilon
Energy		Off
Pressure-Velocity Coupling		Coupled
Discrete Phase Model		On
Acceleration of gravity	X	0
	Y	-9.81m/s <sup>2</sup>
	Z	0

Tab. 2 – Discrete phase model parameters

Discrete Model	Phase	Define
Interaction		Interaction with Continuous Phase
Number of Continuous Phase Iterations per DPM Iteration		10
Max Number of Steps		5000
Length Scale		0.01
Drag Law		Spherical

The tunnel construction ventilation standards specify Q as 600 m<sup>3</sup>/min, with duct diameters of 0.8m and a calculated duct cross-sectional area of 0.503 m<sup>2</sup>. Per the air volume and velocity conversion formula [28]:

$$V = \frac{Q}{60A} \quad (13)$$

In the formula: V: Velocity Air volume Cross-sectional area (m/s); Q: Air volume; m<sup>3</sup>/min; A: Cross-sectional area (m<sup>2</sup>).

Setting the specific boundary conditions: Inlet Boundary Type is set to velocity-inlet; Hydraulic Diameter is set to 0.8 m; Outlet Boundary Type is set to Outflow; the DPM Condition of Wall is set to reflect; the Shear Condition is set to no slip and the velocity V<sub>1</sub> at the pressing air volume is calculated to be 19.89 m/s by substituting the air volume and the cross-sectional area of the duct into Equation 1. Similarly, the velocity V<sub>2</sub> at the pumping air volume is determined to be 13.93 m/s.

## SIMULATION RESULT ANALYSIS

### Effect of the position of pressure duct on dust distribution

The dust concentration distribution in the ZX plane at a height of 1.5m from the ground (the average breathing height of the workers) is intercepted and analyzed. Prior to analysis, distance between the pumping duct and the working face (L<sub>pumping</sub>), with a pumping ratio (r) of 0.7, was set at 3m, and the height distance between the centres of the two ventilation ducts was established at 1.5m. Subsequently, the L<sub>pressure</sub> was varied at 16m, 18m, 20m, 22m, 24m, and 26m for numerical simulation. The simulation results, shown in Figure 6, provide significant insights into the ventilation system's effectiveness in controlling dust concentration levels.

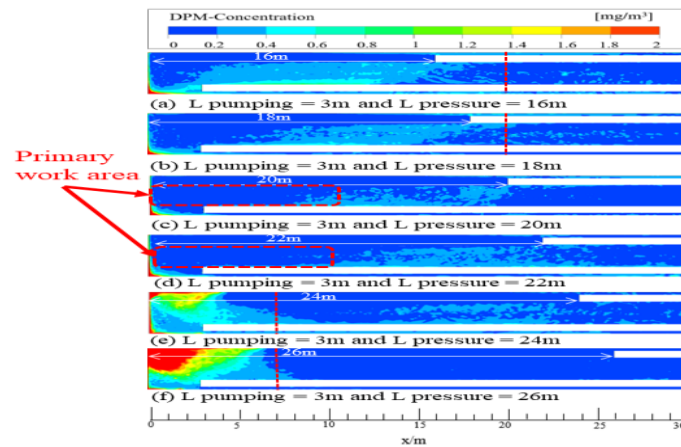


Fig. 6 – Distribution of dust concentration at a height of 1.5m above the ground at different locations of pressure air outlets: (a)  $L_{pumping} = 3m$  and  $L_{pressure} = 16m$ ; (b)  $L_{pumping} = 3m$  and  $L_{pressure} = 18m$ ; (c)  $L_{pumping} = 3m$  and  $L_{pressure} = 20m$ ; (d)  $L_{pumping} = 3m$  and  $L_{pressure} = 22m$ ; (e)  $L_{pumping} = 3m$  and  $L_{pressure} = 24m$ ; (f)  $L_{pumping} = 3m$  and  $L_{pressure} = 26m$

As depicted in Figure 6, the distribution of dust accumulation is influenced by the distance of the pressing air outlets to the working face. When the  $L_{pressure}$  is in the range of 16m to 18m, denoted in Figure 6(a) and (b), the close distance between the pressing air outlet and the working face results in a significant dispersion of dust beyond the jet area, rendering the pumping duct less effective in controlling the dust concentration. Consequently, the secondary dust spreading distance extends up to about 20m, covering a substantial area of the construction site with higher dust concentrations near the pumping duct compared to the pressing duct. Moreover, as the  $L_{pressure}$  is in the range of 20m to 22m, denoted in Figure 6(c) and (d), a well-balanced airflow pattern is achieved with a moderate distance between the pressing air inlet and the working face, facilitating efficient dust flow towards the suction air inlet and restricting dust dispersion to within a 5m. The concentration of dust is primarily confined to the main construction area, emphasizing the effectiveness of ventilation and dust removal in this scenario. However, when the  $L_{pressure}$  extends to 24m or 26m, as shown in Figure 6(e) and (f), dust predominantly locates approximately 10m from the working face, leading to high dust concentrations. It can be explained that the large  $L_{pressure}$  will diminish wind speed and restrict effective dust discharge, resulting in dust retention near the working face. Consequently, the tunnels experience suboptimal ventilation and dust removal efficacy under these large  $L_{pressure}$ .

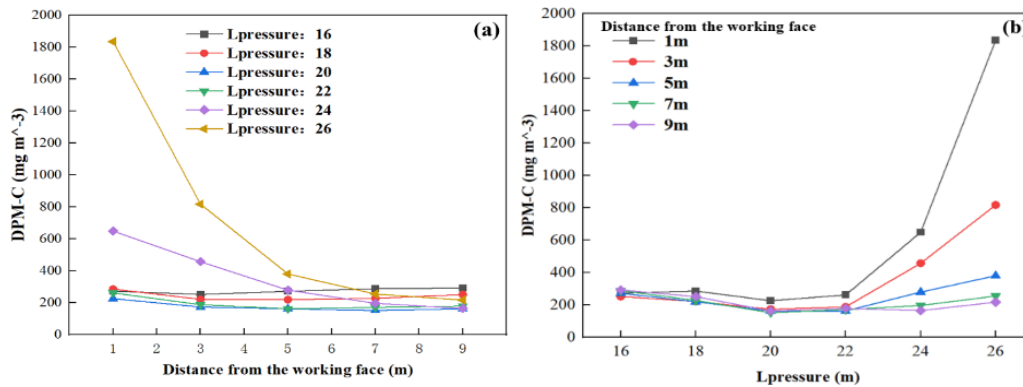


Fig. 7 – Comparison of along-track distribution of dust concentration at different locations of the pressure air outlets: (a) different locations of the pressure air outlet; (b) different distances from the working face.

Upon examining Figure 7(a), it is evident that different  $L_{\text{pressure}}$  yield varying dust concentrations within the vicinity of the working face. For instance, when the  $L_{\text{pressure}}$  ranges from 24 to 26m, within 5m from the working face ( $0 < X < 5\text{m}$ ), the dust concentration experiences a sharp decrease as the distance from working face increases, yet the DPM-C remains above 600 mg/m<sup>3</sup>, designating this region as critical for dust control measures. Conversely, with an  $L_{\text{pressure}}$  between 16 and 18m, at a distance of 5-10m from the working face ( $3 < X < 10\text{m}$ ), the dust disperses rearward as the distance from working face increases, leading to a gradual increase in concentration, eventually reaching 300 mg/m<sup>3</sup> on average. Subsequently, an  $L_{\text{pressure}}$  of 20 to 22m results in a diminishing dust mass concentration within a 10m from the working face compared with the  $L_{\text{pressure}}$  equals 24 and 26m, with the DPM-C being effectively lowered to 250mg/m<sup>3</sup>. Notably, the optimum reduction in the DPM-C to 250 mg/m<sup>3</sup> and enhanced dust removal efficiency are achieved at an  $L_{\text{pressure}}$  of 20m. This outcome not only benefits construction personnel by providing a conducive environment for construction operations but also enhances the overall effectiveness of dust control measures.

### Effect of the position of pumping duct on dust distribution

To investigate the effect of the pumping duct position on dust distribution, the  $L_{\text{pressure}}$  is set at 20m, with a pumping ratio of 0.7 and the height of the center position of the two ventilation ducts at 1.5m. The  $L_{\text{pumping}}$  is selected as a variable with value of 1m, 2m, 3m, 4m, 5m, and 6m. Figure 8 presents the simulation results under different  $L_{\text{pumping}}$ .

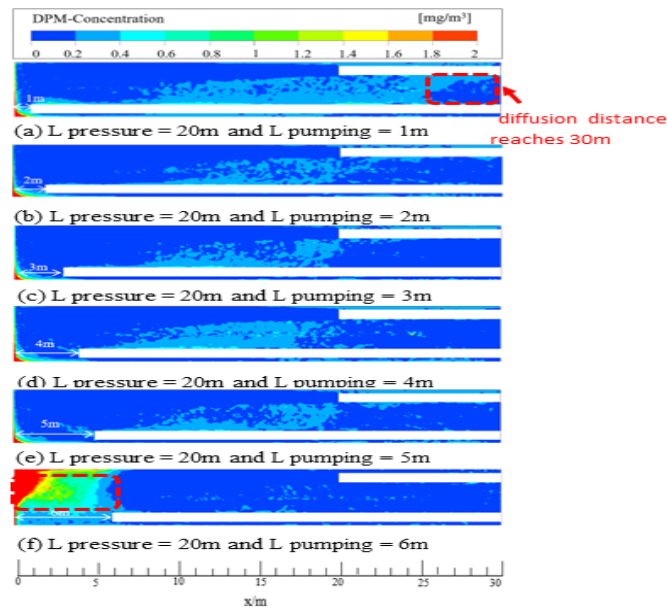


Fig. 8 – Distribution of dust concentration at a height of 1.5m above the ground at different locations of the air pumping outlets: (a)  $L_{pressure} = 20m$  and  $L_{pumping} = 1m$ ; (b)  $L_{pressure} = 20m$  and  $L_{pumping} = 2m$ ; (c)  $L_{pressure} = 20m$  and  $L_{pumping} = 3m$ ; (d)  $L_{pressure} = 20m$  and  $L_{pumping} = 4m$ ; (e)  $L_{pressure} = 20m$  and  $L_{pumping} = 5m$ ; (f)  $L_{pressure} = 20m$  and  $L_{pumping} = 6m$

When the position of the air pressure outlet is fixed, the distance of the air pumping outlet from the face has a significant impact on the spread of dust. For instance, at a distance of 1m ( $L_{pumping} = 1m$ ) as depicted in Figure 8(a), the proximity of the air pumping port to the working face results in the dust being influenced by the impact airflow from the rock breaking activity at the head of the roadheader. Consequently, the dust is driven outward, with some particles escaping the airflow control mechanism of the air pumping system, leading to diffusion into other areas of the tunnel up to a distance of 30m. In contrast, at distances of 2-5m ( $L_{pumping} = 2\sim 5m$ ) as illustrated in Figure 8(b), (c), (d), (e), the location of the air pumping duct in relation to the working face creates a moderate airflow field that effectively controls the dust generated at the working face. The airflow limits the diffusion distance of the dust within the tunnel, resulting in a relatively reduced coverage area and improving the overall ventilation and dust removal efficiency at the operating face. Conversely, when the distance is 6m ( $L_{pumping} = 6m$ ) as shown in Figure 8(f), the air pumping duct is too distant from the working face, leading to the airflow being insufficient to drive the dust towards the pumping point effectively. Consequently, a significant accumulation of dust occurs within a 5m from the working face, resulting in high dust concentrations and poor ventilation and dust removal efficacy in that area.

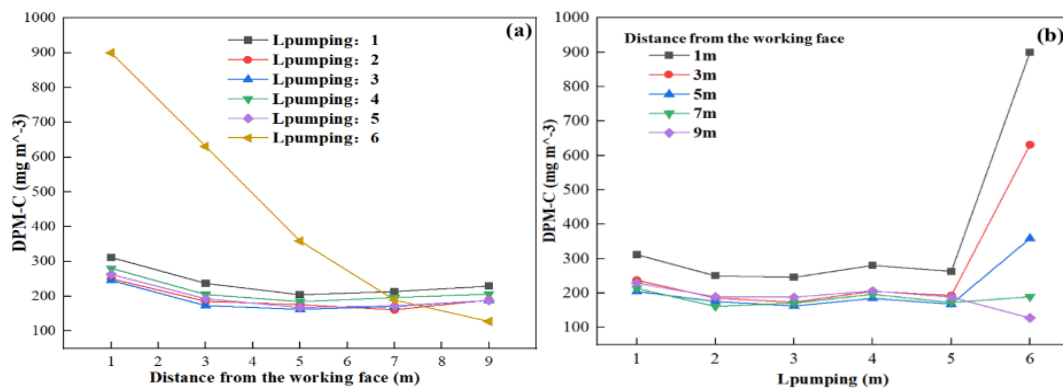


Fig. 9 – Comparison of along-track distribution of dust concentration at different pumping positions: (a) different pumping positions; (b) different distances from the working face.

After analyzing Figure 9, it is observed that when the  $L_{\text{pumping}}$  distance is 6m, there is a sharp decline as the distance from working face increases in dust concentration trends, with the highest average concentration exceeding  $900\text{mg}/\text{m}^3$ . Conversely, for  $L_{\text{pumping}}$  distances ranging from 1 to 5m, the dust distribution tends to stabilize, effectively controlling the DPM-C within the range of  $300\text{mg}/\text{m}^3$ . Specifically, at 1m  $L_{\text{pumping}}$ , the DPM-C of dust reaches  $310\text{mg}/\text{m}^3$ , while at 3m  $L_{\text{pumping}}$ , the dust removal efficiency is optimal, reducing the DPM-C to  $250\text{mg}/\text{m}^3$ . This reduction is beneficial for the overall well-being, health, and safety of construction workers. Further comprehensive analysis of the simulation results and data comparison reveals that with a fixed pressure outlet location, if the distance between the air pumping port is small, a significant amount of dust remains unsucked and diffuses throughout the entire tunnel area. Conversely, when the distance between the air pumping duct is large, a substantial portion of dust cannot be effectively removed and is instead diffused due to the wind flow impact, leading to higher dust concentrations near the working face. Therefore, it is concluded that the optimal parameter for the air pumping port location and distance from the working face is  $L_{\text{pumping}}$  at 3m. By implementing this parameter in the primary roadheader construction area, the DPM-C can be effectively controlled within the range of  $250\text{mg}/\text{m}^3$ , thereby enhancing the overall construction operation environment within the boring tunnel.

### Effect of pumping air volume on velocity distribution and dust distribution

Selecting the optimal pumping air volume can lower the fan's energy consumption, as long as the tunnel's flow requirements are met. To study the effect of pumping air volume on dust concentration, the simulation involved setting fixed parameters for  $L_{\text{pumping}}$  at 3m and  $L_{\text{pressure}}$  at 20m, while fixing the pressure air volume at  $600\text{ m}^3/\text{min}$ . The pumping air volume was adjusted to achieve a pumping ratio( $r$ ) of less than 1. Subsequently, different pumping ratio ( $r$ ) were selected at 0.4, 0.5, 0.6, 0.7, 0.8, and 0.9 for numerical simulation. This corresponded to pumping air volumes of  $240\text{ m}^3/\text{min}$ ,  $300\text{ m}^3/\text{min}$ ,  $360\text{ m}^3/\text{min}$ ,  $420\text{ m}^3/\text{min}$ ,  $480\text{ m}^3/\text{min}$ , and  $540\text{ m}^3/\text{min}$ . The simulation results, depicted in Figure 10 and 11.

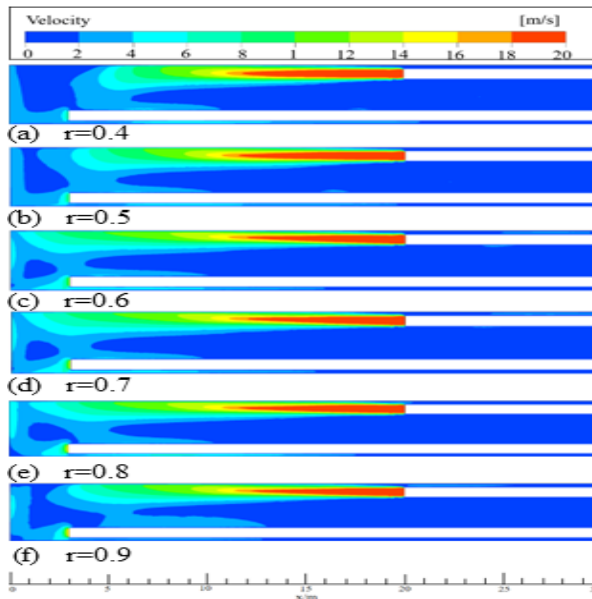


Fig. 10 – Velocity distribution of flow field at 1.5m above ground level for different pumping ratio and less than 1: (a) $r=0.4$ ; (b) $r=0.5$ ; (c) $r=0.6$ ; (d) $r=0.7$ ; (e) $r=0.8$ ; (f) $r=0.9$

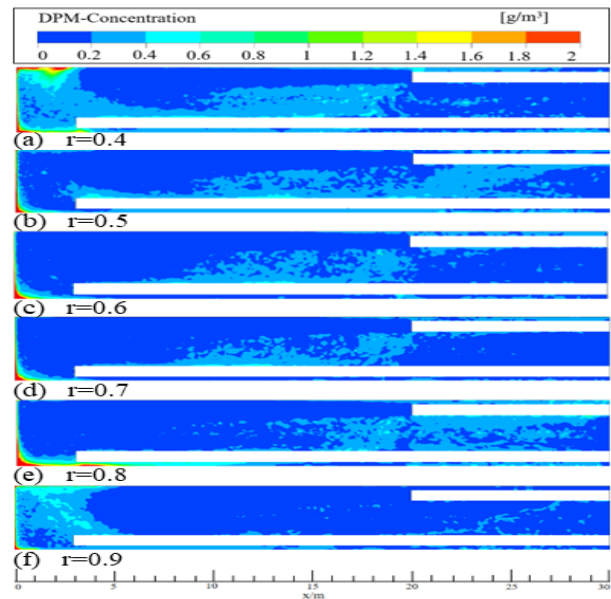


Fig. 11 – Distribution of dust concentration at 1.5m above ground level for different pumping ratio and less than 1: (a) $r=0.4$ ; (b) $r=0.5$ ; (c) $r=0.6$ ; (d) $r=0.7$ ; (e) $r=0.8$ ; (f) $r=0.9$

Upon comparison of Figure 10 and 11, it is evident that a decrease in the value of  $r$ , signifying a reduction in the pumping air volume, leads to the continuous dispersion of dust throughout the tunnel due to the influence of the wind flow. When the pumping air volume is significantly lower than the pressing air volume, the pressing air outlet generates wind that disperses dust within the tunnel. For  $r$  values of 0.4 and 0.5, depicted in Figure 10(a), (b) and Figure 11(a), (b), the insufficient pumping air volume fails to capture dust emitted from the working face during construction, resulting in low wind flow rates at the duct overlap. Consequently, unsucked dust drifts towards the tunnel opening, causing dust accumulation at the duct overlap and throughout the tunnel area, including the corners adjacent to the working face. In contrast, for  $r$  values of 0.6, 0.7, and 0.8 shown in Figure 10 (c), (d), (e) and Figure 11(c), (d), (e), the pumping air volume adequately matches the dust volume produced, facilitating effective dust removal via the pumping duct. When  $r$  equals 0.6, 0.7, and 0.8, the dust distribution in the tunnel remains similar, with lower dust concentrations diffusing up to 15-20m from the working face. and up to 30m for  $r$  equals 0.8. Additionally, limited diffusion of lower dust concentrations occurs along the tunnel wall due to pressure-induced airflow into the ducts. For  $r$  equals 0.9, as depicted in Figure 10(f) and Figure 11(f), the pumping and pressing air volumes are approximately equivalent, resulting in reduced airflow velocity around the pumping duct. Consequently, a substantial accumulation of dust occurs at the working face, leading to high dust concentration and decreased dust suction efficiency by the pumping duct.

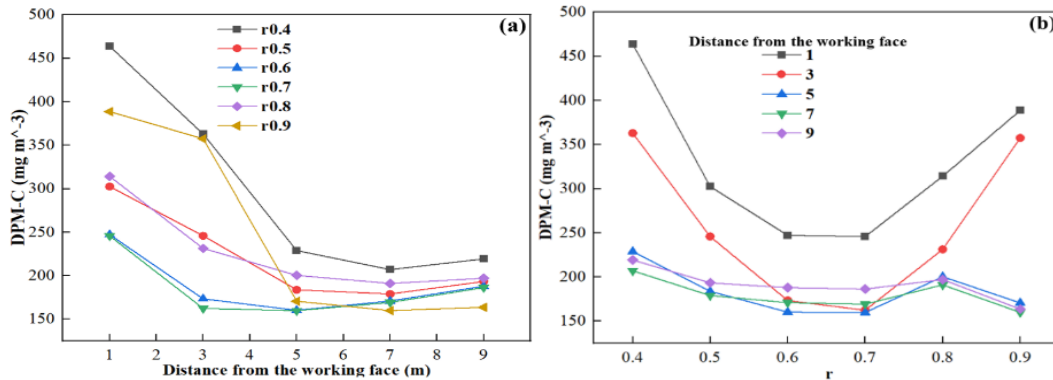


Fig. 12– Comparison of along-track distribution of dust concentration for different pumping ratio: (a) pumping ratio less than 1; (b) different distances from the working face.

When examining Figure 12(a), it is evident that when  $r$  falls below 1, the overall dust concentration demonstrates a declining pattern as the distance from the working face increases within the range of 0m to 5m ( $0 < X < 5$ m) from the working face. Progressively, the concentration then tends to stabilize between the distances of 5m to 10m ( $5 < X < 10$ m) from the working face. Figure 12(b) illustrates that in the primary construction operational zone, the highest average dust concentration surpasses  $350\text{mg}/\text{m}^3$  for  $r$  values of 0.4 and 0.9. Similarly, for  $r$  values of 0.5 and 0.8, the highest average concentration of dust exceeds  $300\text{mg}/\text{m}^3$ . Conversely, for  $r$  values of 0.6 and 0.7, the average dust concentration remains below  $250\text{mg}/\text{m}^3$ . Furthermore, the average concentration of dust can be diminished notably when  $r$  equals 0.7, as depicted in Figure 12 (b). Remarkably, the reduction in average dust concentration is more pronounced at  $r$  equal to 0.7, as clearly illustrated in the figure.

Base on the comprehensive analysis of the simulation results and data comparison, it is inferred that when the pumping air volume is less than the pressing air volume ( $r < 1$ ), the optimal  $r$  equals 0.7. Maintaining this pumping ratio facilitates effective coordination between the pressure and pumping airflows, thereby enhancing the performance of the ventilation system for tunnel ventilation and dust removal.

### **Effect of pressure air volume on velocity distribution and dust distribution**

To study the effect of pressure air volume on dust concentration, fixed  $L_{\text{pumping}}$  was maintained for 3 m and  $L_{\text{pressure}}$  for 20 m. Fixed pumping air volume at  $600\text{ m}^3/\text{min}$ . The pressure air volume was adjusted to achieve a pumping ratio( $r$ ) greater than 1. Following this, numerical simulations were conducted with different pumping ratio ( $r$ ) of 1.1, 1.2, 1.5, 1.6, 1.8, and 2. As a result, the simulated pumping air volumes were  $660\text{ m}^3/\text{min}$ ,  $720\text{ m}^3/\text{min}$ ,  $900\text{ m}^3/\text{min}$ ,  $960\text{ m}^3/\text{min}$ ,  $1080\text{ m}^3/\text{min}$ , and  $1200\text{ m}^3/\text{min}$  respectively. The simulation outcomes, depicted in Figure 13 and 14.

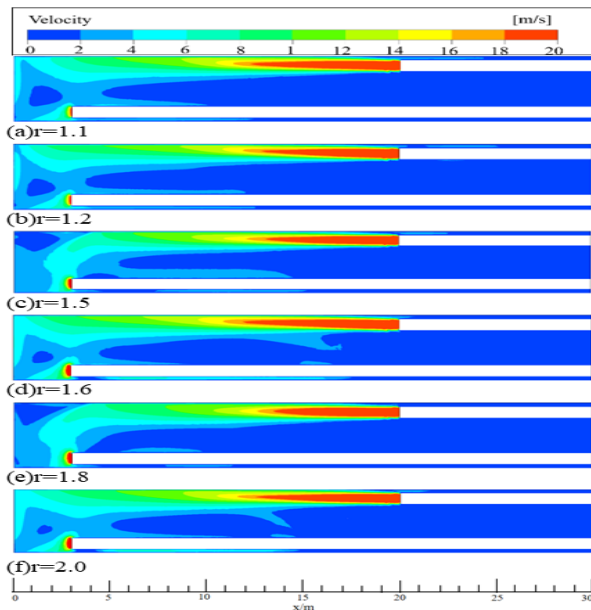


Fig. 13 – Velocity distribution of the flow field at different pumping ratio and greater than 1: (a)  $r=1.1$ ; (b)  $r=1.2$ ; (c)  $r=1.5$ ; (d)  $r=1.6$ ; (e)  $r=1.8$ ; (f)  $r=2.0$

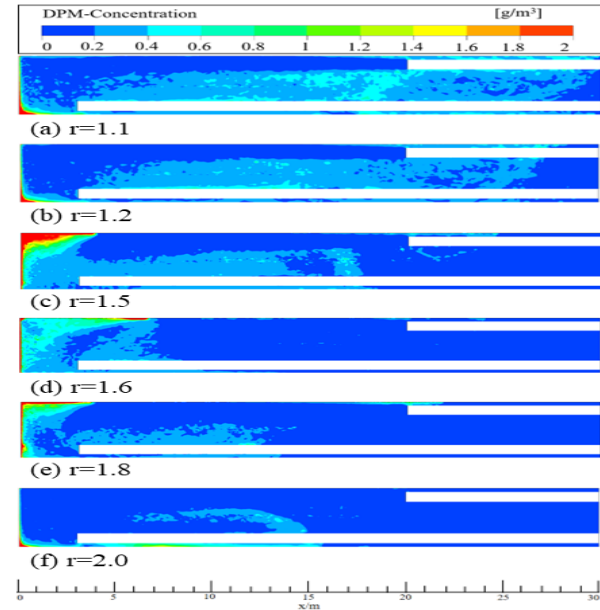


Fig. 14 – Distribution of dust concentration at different pumping ratio greater than 1: (a)  $r=1.1$ ; (b)  $r=1.2$ ; (c)  $r=1.5$ ; (d)  $r=1.6$ ; (e)  $r=1.8$ ; (f)  $r=2.0$

Upon comparing Figure 13 and 14, it is evident that with an increase in  $r$ , signifying an increase in the pumping air volume, the diffusion distance of the dust decreases gradually due to the influence of wind flow. When  $r$  values are at 1.1 and 1.2, illustrated in Figure 13(a) and (b), and Figure 14(a) and (b), the pumping air volume slightly surpasses the pressing air volume. There is a smaller discrepancy between the air volumes in the two ducts and a noticeable impact of the pumping air on the dust concentration around the working face, leading to lower dust concentration levels. Despite this, the pumping air fails to establish an effective flow field interaction with the pressing air, causing ineffective dust suction at the outlet. Consequently, the dust is inadequately removed, leading to its widespread distribution throughout the tunnel space and a diminished ventilation effect. As  $r$  increases to 1.5, 1.6, and 1.8, depicted in Figure 13(c), (d), and (e), and Figure 14(c), (d), and (e), the dust diffusion distance diminishes gradually due to the escalating difference between the pumping and pressing air volumes. The enhanced suction effect of the pumping propels the pressing air flow and the tunnel air towards the working face. This leads to the accumulation of dust primarily in the vicinity of the working face, resulting in higher dust concentration levels, confined within a range of approximately 5m from the working face. As  $r$  equals 2, showcased in Figure 13(f) and 14(f), the pumping air volume markedly surpasses the pressing air volume. The potent suction effect of the pumping successfully removes most of the dust, transferring it to the pumping air duct. Simultaneously, the pressing air conveys the remaining low-concentration dust towards the pumping air outlet, with some minor amounts spreading towards the pumping air duct's side and the tunnel wall within a range of 10-15m from the working face. Consequently, the expansion distance and

coverage area are relatively few, enhancing the efficiency of dust removal in this scenario.

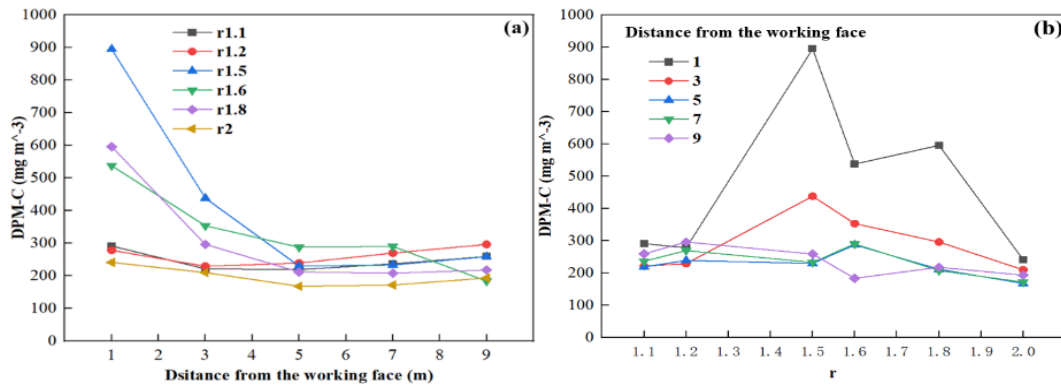


Fig. 15 – Comparison of along-track distribution of dust concentration for different pumping ratio greater than 1: (a) pumping ratio greater than 1; (b) different distances from the working face.

As can be seen from Figure 15, in the main construction work area, the dust concentration within 5m ( $0 < X < 5m$ ) from the working face exhibits a sharp decline as the distance from the working face increases when r values are 1.5, 1.6, and 1.8, followed by a tendency to stabilize. However, despite this trend, the highest DPM-C of dust exceeds  $530 \text{ mg/m}^3$ , indicating that the dust removal effectiveness is not optimal. On the other hand, for r values of 1.1, 1.2, and 2, the dust concentration remains relatively stable, hovering around  $300 \text{ mg/m}^3$  within 10m ( $0 < X < 10m$ ) from the working face. Notably, when r equals 2, the DPM-C of dust can be effectively maintained within the range of  $250 \text{ mg/m}^3$ .

It is concluded, based on a comprehensive analysis of the simulation results and data comparisons, that when the pumping air volume exceeds the pressing air volume ( $r > 1$ ), the optimal parameter for r is 2. However, under these circumstances, the pumping air duct also draws in fresh air, leading to an inadequate supply of fresh air in the tunnel, which necessitates a higher level of performance for the dust fan. Furthermore, fans with large air volumes typically consume more energy, resulting in higher production costs for manufacturers and potential wastage. As a result, in practical working conditions, a higher pumping ratio is generally not recommended.

### 3.5 Simulation verification

Based on several sets of simulation results, the optimal values of the tunnel ventilation system layout parameters are obtained: the  $L_{\text{pumping}}$  is 3 m, the  $L_{\text{pressure}}$  is 20 m, and the pumping ratio (r) is 0.7. Further numerical simulations are carried out to verify the accuracy of the ventilation layout parameters by simulating the ventilation and dust removal effects of the tunnel ventilation system under these layout parameters. The simulation results are shown in Fig. 16.

As depicted in Figure 16, the majority of the dust is effectively removed by the suction duct or carried away by the tunnel wind flow, resulting in optimal ventilation and dust removal efficiency. It is evident that only a minor fraction of dust disperses to the tunnel between the distances of 12-30m from the working face, exhibiting low concentration levels. Conversely, in the crevices and corners of the working face adjacent to the duct and the tunnel wall, there is a small area of significant dust accumulation with high concentration levels.

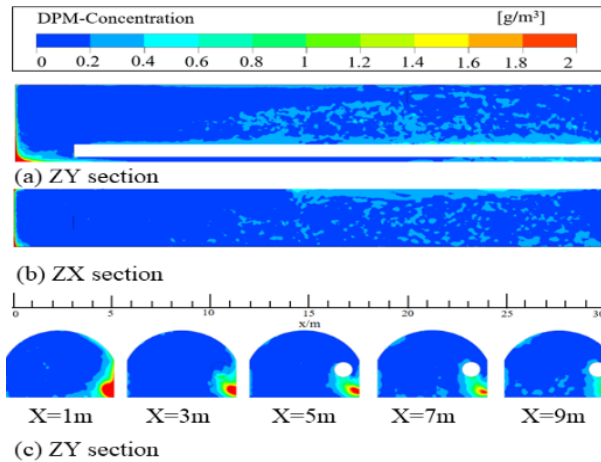


Fig. 16 – Distribution of dust concentration in different cross sections after optimal design: (a) ZY section; (b) ZX section; (c) ZY section

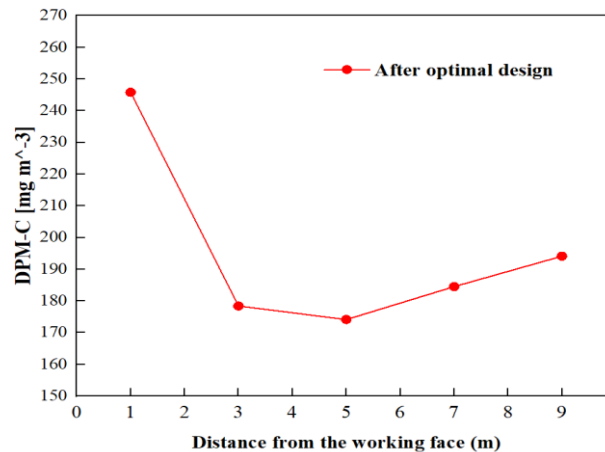


Fig. 17 – Distribution of dust concentration along the course of the optimal design

Figure 17 illustrates the effective control of dust mass concentration in the main construction area of the tunnel, remaining within the range of 250mg/m<sup>3</sup>. Specifically, the highest DPM-C of 245.8mg/m<sup>3</sup> is observed within 3m (0<X<3m) from the tunnel's face, while the mass concentration remains below 200mg/m<sup>3</sup> within 3-10m (3<X<10m) from the tunnel's face. This controlled environment is conducive for construction workers to carry out their tasks efficiently. Therefore, the data accuracy and credibility of the optimal arrangement parameter can be substantiated.

## CONCLUSION

The optimal values for the tunnel ventilation system parameters were found to be 20m for  $L_{\text{pressure}}$ , 3m for  $L_{\text{pumping}}$ , and a pumping ratio of 0.7, as revealed by the results. Specifically, under these parameters, the dust particulate matter concentration (DPM-C) can be successfully controlled within the range of 250mg/m<sup>3</sup>. Therefore, the numerical simulation outcomes not only provide a theoretical foundation but also offer guidance for the appropriate arrangement of air ducts and management of dust concentration in the tunnel ventilation system when similar operating conditions are encountered.

In this paper, only the condition of ventilation duct arrangement has been considered, and

whether the duct length should be proportionally increased for longer tunnels as well as adjusting the angle of the air duct and the working face still needs to be explored in the future.

## ACKNOWLEDGEMENT

This research is supported by the National Natural Science Foundation of China (Granted No. 52005179), the Scientific Research Project of Hunan Education Department (Granted No. 20C1153), the Natural Science Foundation of Hunan Province (Granted No.2020JJ5365).

## REFERENCE

- [1] Zhou W, Nie W, Liu X, et al. Optimization of dust removal performance of ventilation system in tunnel constructed using shield tunneling machine[J]. *Building and Environment*. 2020, 173: 106745.
- [2] Hua Y, Nie W, Liu Q, et al. The development and application of a novel multi-radial-vortex-based ventilation system for dust removal in a fully mechanized tunnelling face[J]. *Tunnelling and Underground Space Technology*. 2020, 98: 103253.
- [3] Menéndez J, Fernández-Oro J M, Merlé N, et al. Auxiliary ventilation systems in mining and tunnelling: Air leakage prediction and system design to optimize the energy efficiency and operation costs[J]. *Tunnelling and Underground Space Technology*. 2023, 140: 105298.
- [4] Ates U, Copur H. Investigation of parameters affecting vibration patterns generated during excavation by EPB tbms[J]. *Tunnelling and Underground Space Technology*. 2023, 138: 105185.
- [5] Lehmann G, Käsling H, Hoch S, et al. Analysis and prediction of small-diameter TBM performance in hard rock conditions[J]. *Tunnelling and Underground Space Technology*. 2024, 143: 105442.
- [6] Li J, Guo D, Chen Z, et al. Transfer learning for collapse warning in TBM tunneling using databases in China[J]. *Computers and Geotechnics*. 2024, 166: 105968.
- [7] Ni S, Chao B T, Soo S L. Particle diffusivity in fully developed, turbulent, horizontal pipe flow of dilute air—solid suspensions[J]. *International Journal of Multiphase Flow*. 1990, 16(1): 43-56.
- [8] Hargreaves D M, Lowndes I S. The computational modeling of the ventilation flows within a rapid development drivage[J]. *Tunnelling and Underground Space Technology*. 2007, 22(2): 150-160.
- [9] Parra M T, Villafruela J M, Castro F, et al. Numerical and experimental analysis of different ventilation systems in deep mines[J]. *Building and Environment*. 2006, 41(2): 87-93.
- [10] Wang H, Cheng W, Sa Z, et al. Experimental study of the effects of air volume ratios on the air curtain dust cleaning in fully mechanized working face[J]. *Journal of Cleaner Production*. 2021, 293: 126109.
- [11] Lai A C K. Modeling indoor coarse particle deposition onto smooth and rough vertical surfaces[J]. *Atmospheric Environment*. 2005, 39(21): 3823-3830.
- [12] Hussein T, Hruška A, Dohányosová P, et al. Deposition rates on smooth surfaces and coagulation of aerosol particles inside a test chamber[J]. *Atmospheric Environment*. 2009, 43(4): 905-914.
- [13] Klemens R, Kosinski P, Wolanski P, et al. Numerical study of dust lifting in a channel with vertical obstacles[J]. *Journal of loss prevention in the process industries*. 2001, 14(6): 469-473.
- [14] Sa Z, Li F, Qin B, et al. Numerical simulation study of dust concentration distribution regularity in cavern stope[J]. *Safety Science*. 2012, 50(4): 857-860.
- [15] Ashrafi K, Shafie-Pour M, Kalhor M, et al. Numerical Simulation of Air Pollutant Distribution in Urban

- Tunnels[J]. *Environmental Modeling & Assessment*. 2012, 17(5): 555-564.
- [16] Toraño J, Torno S, Menéndez M, et al. Auxiliary ventilation in mining roadways driven with roadheaders: Validated CFD modelling of dust behaviour[J]. *Tunnelling and Underground Space Technology*. 2011, 26(1): 201-210.
- [17] Lee S, Lee S, Lee J. CFD analysis on ventilation characteristics of jet fan with different pitch angle[J]. *KSCCE Journal of Civil Engineering*. 2014, 18(3): 812-818.
- [18] Liu Q, Nie W, Hua Y, et al. A study on the dust control effect of the dust extraction system in TBM construction tunnels based on CFD computer simulation technology[J]. *Advanced Powder Technology*. 2019, 30(10): 2059-2075.
- [19] Xie Z, Ruan C, Zhao Z, et al. Effect of ventilation parameters on dust pollution characteristic of drilling operation in a metro tunnel[J]. *Tunnelling and Underground Space Technology*. 2023, 132: 104867.
- [20] Yang X, Yu H, Wang Y, et al. Investigation of dust pollution control rules in tunnel excavation based on modularized airflow diverging system[J]. *Building and Environment*. 2022, 221: 109356.
- [21] Von Glehn F H, Bluhm S J. Practical aspects of the ventilation of high-speed developing tunnels in hot working environments[J]. *Tunnelling and underground space technology*. 2000, 15(4): 471-475.
- [22] Xia Y, Yang D, Hu C, et al. Numerical simulation of ventilation and dust suppression system for open-type TBM tunneling work area[J]. *Tunnelling and Underground Space Technology*. 2016, 56: 70-78.
- [23] Liu X, Nie W, Zhou W, et al. The optimization of a dust suppression and clean production scheme in a TBM-constructed tunnel based on an orthogonal experiment[J]. *Process Safety and Environmental Protection*. 2020, 136: 353-370.
- [24] Li S, Jin H, Hu S, et al. Experimental investigation and field application of pulse-jet cartridge filter in TBM tunneling construction of Qingdao Metro Line 8 subsea tunnel[J]. *Tunnelling and Underground Space Technology*. 2021, 108: 103690.
- [25] Eftekharian E, Dastan A, Abouali O, et al. A numerical investigation into the performance of two types of jet fans in ventilation of an urban tunnel under traffic jam condition[J]. *Tunnelling and Underground Space Technology*. 2014, 44: 56-67.
- [26] Wang J, Levy E K. Particle motions and distributions in turbulent boundary layer of air-particle flow past a vertical flat plate[J]. *Experimental Thermal and Fluid Science*. 2003, 27(8): 845-853.
- [27] Chang P, Xu G, Huang J. Numerical study on DPM dispersion and distribution in an underground development face based on dynamic mesh[J]. *International Journal of Mining Science and Technology*. 2020, 30(4): 471-475.
- [28] van Wachem B G M, Almstedt A E. Methods for multiphase computational fluid dynamics[J]. *Chemical Engineering Journal*. 2003, 96(1-3): 81-98.
- [29] Cai P, Nie W, Chen D, et al. Effect of air flowrate on pollutant dispersion pattern of coal dust particles at fully mechanized mining face based on numerical simulation[J]. *Fuel*. 2019, 239: 623-635.
- [30] Wan W, Li X, An N. Study on the reasonable position of the wind pipe of the long-pressure-short-drawing ventilation system of the comprehensive excavation working face [J]. *Coal Technology*. 2019, 38(04): 123-125. (in Chinese)